Reactions of [FeFe]-Hydrogenase with Carbon Monoxide and Formaldehyde

A thesis submitted to the Board of the Faculty of Physical Sciences, for the degree of Doctor of Philosophy, University of Oxford

Carina E. Foster

Jesus College

Trinity Term 2012

Abstract

Reactions of [FeFe]-Hydrogenase with Carbon Monoxide and Formaldehyde

Carina E. Foster, Jesus College

A Thesis Submitted for the degree of DPhil, Trinity Term 2012

The use of H_2 as an energy carrier has in recent years been identified as a promising future solution to the current energy crisis. Hydrogenases are metalloenzymes found in many microorganisms and are used to catalyse the reversible inter-conversion of protons and H_2. These enzymes and their synthetic analogues have been recognised as a way to facilitate the use of H_2 as a fuel. A major challenge to the future use of these catalysts is their reactions with small molecule inhibitors, such as oxygen and carbon monoxide. Detailed understanding of the structure and catalytic mechanism of these highly efficient catalysts is vital for the design of bio-inspired functional analogues for use in technological applications.

In this thesis electrochemical studies of three [FeFe]-hydrogenases are presented, performed using the technique of protein film electrochemistry. The strong potential dependence of the reaction of these hydrogenases with carbon monoxide and formaldehyde is characterised and rationalised. These studies provide compelling evidence for the formation of a previously ambiguous super-reduced state of [FeFe]-hydrogenase at low potential. This state is shown to be active and stable, and it is proposed that this state is involved in catalytic H_2 production.

This super-reduced state is shown to have a high affinity for the reversible binding of formaldehyde, but a very low affinity for both carbon monoxide and oxygen. Activation of carbon monoxide inhibited [FeFe]-hydrogenase can be very rapidly induced by the application of a sufficiently reducing potential. These enzymes, considered to be oxygen

sensitive, are shown to be extremely tolerant to irreversible oxygen damage at very reducing potentials where the super-reduced state is formed.

Acknowledgements

Firstly I would like to thank Prof. Fraser Armstrong for giving me the opportunity to work in his group, and for providing so much help and support throughout my DPhil.

In the Armstrong group, special thanks go to Dr. Alison Parkin and Dr. Rhiannon Evans for their endless support, both academic and emotional throughout the last few years. I also thank all the ladies of 'lunch club' for the welcome daily distraction and gossip. Thank you to all my proof readers – Dr. Rhiannon Evans, Suzannah Hexter, Andreas Bachmeier and Dr. Maxie Roessler, I really appreciate all the time and effort you put in to it. A huge thank you to all the other members of the Armstrong group, past and present, who have provided so much help to me and have, most importantly, made my time in the group so enjoyable.

I could not have performed any of the experiments in this thesis without the help of the support staff in the Chemistry department, in particular Ashleigh, Terri, Nenad, Paul, Charlie, Les, and Tom. I also thank Jesus College and the EPSRC for the financial support they have provided.

Finally a massive thank you to all my friends, in particular my fellow Oxonians Jon, Jessie and Kate, and my family for their ongoing support throughout my time in Oxford. I wouldn't have made it through without you all.

Publications

[1] **Foster, C. E.;** Kramer, T.; Wait, A. F.; Parkin, A.; Jennings, D. P.; Happe, T.; McGrady, J. E.; Armstrong, F. A., Inhibition of [FeFe]-Hydrogenases by Formaldehyde and Wider Mechanistic Implications for Biohydrogen Activation. *Journal of the American Chemistry Society* **2012** 134, (17), 7553-7557

[2] Knoerzer, P.; Silakov, A.; **Foster, C. E.;** Armstrong, F. A.; Lubitz, W.; Happe, T., Importance of the protein framework for catalytic activity of [FeFe]-hydrogenases. *Journal of Biological Chemistry* **2012**, 287, (2), 1489-1499

[3] Blanford, C. F.; **Foster, C. E.;** Heath, R. S.; Armstrong, F. A., Efficient electrocatalytic oxygen reduction by the 'blue' copper oxidase, laccase, directly attached to chemically modified carbons. *Faraday Discussions* **2008**, 140, 319-335, discussion 417-37.

Symbols and Abbreviations

A	amperes
Å	Angstrom
ATP	Adenosine diphosphate
ATR	attenuated total reflectance
°C	degrees centigrade
Ca	*Clostridium acetobutylicum*
Cp	*Clostridium pasteurianum*
Cr	*Chlamydomonas reinhardtii*
cm	centimeter
Cys	cysteine
Da	Dalton(s)
Dd	*Desulfovibrio desulfuricans*
Dg	*Desulfovibrio gigas*
DFT	density functional theory
e^-	electron
E	electrode potential
E°	Standard reduction potential
E. coli	*Escherichia coli*
EGTA	ethylene glycol tetraacetic acid
EPR	electron paramagnetic resonance
ET	Electron transfer
F	Faraday's constant = 9.648×10^4 C mol^{-1}
Fe_d	iron distal to the [4Fe4S] cluster in the [FeFe]-hydrogenase active site
Fe_p	iron proximal to the [4Fe4S] cluster in the [FeFe]-hydrogenase active site
FeS	iron sulphur cluster
FTIR	Fourier transform infrared (spectroscopy)
h	Planck's constant = 6.62×10^{-34} J s
i	current
i_{lim}	Limiting current
IR	infrared
j	flux of electrons
K	Kelvin
K	equilibrium constant
k	rate constant
L	litre
Lys	lysine
M	moles $litre^{-1}$
m	Milli or meter
min	minute
MV	methyl viologen

n	number of electrons
NAD^+/NADH	nicotinamide adenine dinucleotide (oxidised/reduced form)
NMR	nuclear magnetic resonance
PDB	protein data bank
PFE	protein film electrochemistry
R	ideal gas constant = 8.314 J K^{-1} mol^{-1}
rpm	revolutions per minute
s	second
SHE	standard hydrogen electrode
t	time
T	temperature
V	volts
vs.	versus
W	watt
α	electron transfer coefficient
ΔG	Gibbs free energy change
μ	micro
τ	time constant
ω	rotation rate, given in rpm

Contents

Chapter 1

Introduction

1.1 Hydrogen in Sustainable Energy Future

In the last few decades interest has dramatically increased in the search to find alternative energy options to fossil fuels. In 2008 more than 75% of the total world energy consumption was through the use of oil, coal and gas;[1] problematic because in addition to their limited availability, their extraction, purification and combustion are polluting. The current high rate of fossil fuel consumption causes considerable damage to our environment due to the emission of carbon dioxide upon combustion; increased carbon dioxide in the atmosphere can cause global climate changes.[2,3]

In the current search for alternative sustainable energy sources di-hydrogen (H_2) has been identified as a possible 'clean' fuel of the future.[4-6] Energy obtained from renewable resources such as solar, wind and wave can be stored as chemical potential energy in hydrogen and hydrogen-rich materials, and released by oxidation, generating only water as a by-product.[3,7] Unlike fuels such as gas, coal and oil, H_2 is not a primary energy source, but acts as an 'energy-carrier'. Energy from another source is used to generate H_2, which can then transported before the energy stored in the chemical (H-H) bond is released. As long as renewable energy sources are used, H_2 production is sustainable.

In order for H_2 to become a useful energy carrier there are several limitations that must be overcome. These include the safe and efficient transport of highly combustible H_2 and the further development of methods for the mass production of H_2.[3,7] Currently mass production of H_2 is largely by steam reformation of fossil fuels[7,8] which releases the harmful greenhouse gas carbon dioxide.

In nature microorganisms utilise metalloenzymes called hydrogenases to exploit H_2 as an energy source. These enzymes catalyse the inter-conversion of protons and H_2 and the possibility of using hydrogenases to facilitate the use of H_2 as a fuel has been recognised in recent years. This thesis focuses on the reactions and mechanism of catalytic H_2 production by [FeFe]-hydrogenases.

The energy stored in H_2 can be utilised using fuel cells, internal combustion engines or turbines.[6,7,9] In a traditional fuel cell, precious metal electrodes (eg. platinum) are used to generate electricity by coupling the reduction of O_2 at the cathode to the oxidation of H_2 at the anode, importantly water is the only by-product. The limitations of these cells include the expense and limited availability of the precious metals used, and catalyst poisoning by impurities such as carbon monoxide. Fuel cells have already been incorporated into vehicles allowing H_2 to be used as an alternative to petrol.[10,11] The H_2 is stored under pressure, and combined with atmospheric O_2 to generate electricity and power the motor.

Electrolysis of water, essentially the reverse of the process carried out in a fuel cell, uses two electrodes (Pt or Pd) to generate O_2 at the anode and high purity H_2 at the cathode at ambient temperature and pH.[12] Electricity is required to drive electrolysis, so for this to be a viable method of 'clean' H_2 production, this electricity would need to be produced by a renewable source. The efficiency of this process however is limited by the cost and availability of the noble metal catalysts required. The more abundant metal nickel can be used as an electrode material, however this requires greater reaction temperatures and strongly alkaline conditions.[12]

Scientists have been inspired by the efficient capture of energy from sunlight by plants and the storage of this energy in chemical bonds. A vast area of research now focuses on the development of systems where light is used to produce H_2 by 'artificial photosynthesis'.[13-16]

The aim is to use sunlight to photocatalytically split water to generate H_2 and O_2. Photochemically excited electrons are donated to a H_2 evolving catalyst ($2H^+ \rightarrow H_2$), and the electrons are replenished by water oxidation ($O^{2-} \rightarrow O_2$). These systems can be limited by the activity of the H_2 and O_2 production catalysts used. The development of artificial catalysts is often based on the structure and function of the biological, highly specific and efficient H_2 production catalysts hydrogenases.

1.2 Hydrogen in Biology

Nature has evolved highly efficient catalysts for H_2-cycling, known as hydrogenases, and these enzymes are the focus of the work in this thesis. Hydrogenases are a group of metalloenzymes abundant in the microbial world that catalyse the reversible interc-onversion of protons and dihydrogen (H_2) with minimal overpotential. Cellular respiration is essentially a series of redox reactions that take place in a cell to convert the energy from nutrients into ATP. Many microorganisms utilise H_2 as a fuel source, for example *Desulfovibrio vulgaris* can grow using H_2 and sulfate as the sole energy source.[17] The atmospheric H_2 concentration is very low, meaning that these organisms have to be very adept at scavenging H_2 from their surroundings. Additionally H_2 can be generated by a variety of processes within organisms. Hydrogen is produced photochemically in photosynthetic bacteria, cyanobacteria and green algae such as *Chlamydomonas reinhardtii*; solar energy is captured and used to produce H_2 from water, reduced sulfur compounds or organic acids.[18] Nitrogen-fixing microorganisms, such as *Rhizobium leguminosarum*, generate H_2 in the root nodules of plants in a side-reaction during nitrogen fixation.[19] Bacteria such as *Clostridium acetobutylicum* are able to produce H_2 during the process of fermentation of sugars; protons are reduced to form H_2 as a way to remove the electrons produced during the fermentation process.[20]

Although many hydrogenases are capable of both H_2 oxidation and proton reduction, *in vivo* they tend to operate in only one direction. Hydrogenases are found in various locations in the cell; from cytoplasmic soluble hydrogenases to periplasmic membrane-associated (or membrane-bound) hydrogenases. Hydrogenases can play a crucial role in cell metabolism and are often coupled to the respiratory chain in the cell.

1.3 Classification of Hydrogenases

There are three distinct classes of hydrogenases classified according to the structure of their active sites; [NiFe], [FeFe] and [Fe]-hydrogenases. The [NiFeSe]-hydrogenases are a sub-class of the [NiFe]-hydrogenases where one of the cysteine ligands to the Ni atom of the active site is replaced by a selenocysteine. The [Fe]-only hydrogenases are found only in methanogens, and split H_2 at a mononuclear iron-carbonyl active site, releasing a proton and transferring a hydride.[21] [NiFe]-hydrogenases tend to be more biased towards H_2 oxidation and exhibit naturally higher oxygen tolerance[22] than [FeFe]-hydrogenases. [FeFe]-hydrogenases are of particular interest when considering a future 'hydrogen energy economy' as they tend to be more biased towards H_2-production, and are the main focus of this study.

1.4 Hydrogenase Structure

This thesis focuses mainly on the reactions of [FeFe]-hydrogenases, however experiments were also performed on a [NiFe]-hydrogenase from *Escherichia coli* (*E.coli* Hyd-2) for comparison purposes. For this reason the structural and mechanistic differences between [NiFe] and [FeFe]-hydrogenases are described here.

1.4.1 [NiFe]-Hydrogenases

1.4.1.1 Overall Structure

The structure of *E. coli* Hyd-2 remains unsolved at this time, but the general structure of a 'standard' O_2 sensitive hydrogenases is described (such as *Allochromatium vinosum*[23] and *Desulfovibrio gigas*[24]). These hydrogenases are heterodimeric proteins, consisting of a large and a small subunit. The two subunits interact strongly with one another through hydrophobic interactions.[23] The active site is buried within the large subunit and the small subunit contains a chain of FeS clusters. These FeS clusters act as an electron relay chain, effectively 'wiring' the active site to the protein surface. There are three FeS clusters; proximal, medial and distal with respect to the active site. In a 'standard' (or O_2 sensitive) [NiFe]-hydrogenase the proximal and distal clusters are [4Fe4S]-clusters while the medial cluster is a [3Fe4S]-cluster. The distances between the active site and proximal cluster, the distal cluster and protein surface, and between each of the clusters, are all less than 14 Å. This ensures that electron tunnelling is fast and does not limit the rate of catalysis.[25]

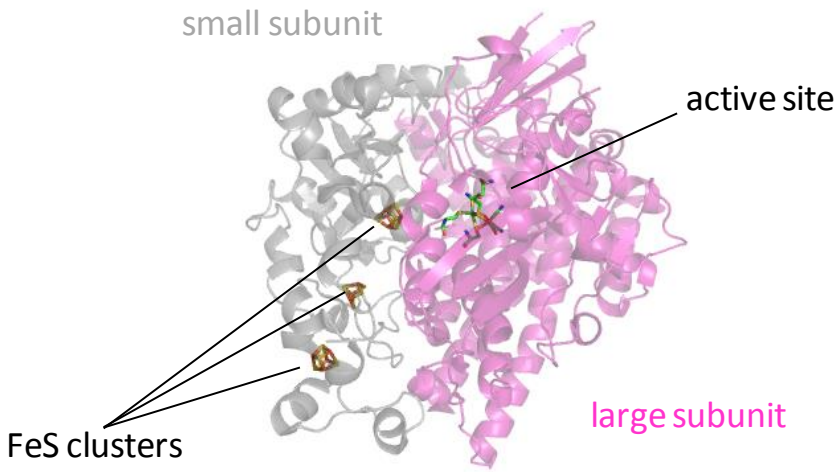

Figure 1: Cartoon representation of the oxidised form of the [NiFe]-hydrogenase from *Desulfovibrio gigas* (*Dg*H-PBD code: 1YG926) showing the large and small subunits, FeS cluster relay chain, and buried active site.

1.4.1.2 Active Site

The active site of [NiFe]-hydrogenase consists of one Ni and one Fe atom, bridged by two cysteine ligands.[22] The Ni atom is also coordinated to two further cysteine ligands, while the iron atom is coordinated to the biologically unusual diatomic ligands CO and CN as shown in Figure 2.[27,28]

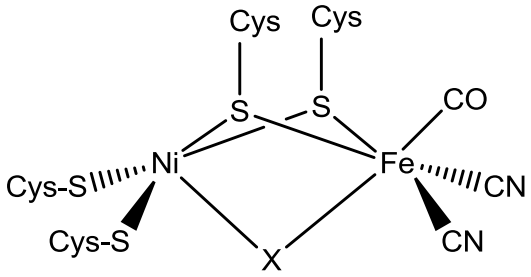

Figure 2: The active site of a [NiFe]-hydrogenase. The nature of the bridging ligand X varies between states of the enzyme.

Hydrogenases are the only class of protein to contain the toxic molecules CO and CN as intrinsic ligands.[29,30] These ligands are good π-acceptors, favouring low oxidation states and low spin iron centres. The two CN and one CO ligands are grouped around the iron atom in such a way as to maximise overlap of the t_{2g} d-orbitals of the metal with the empty π^* orbitals of the ligand, to maximise the strength of the interaction. In the +2 oxidation state the iron atom has only 16 valence electrons. The 18 valence electron rule[31] dictates that metal complexes containing metal ions with 18 valence electrons are the most thermodynamically stable, as this maximises the number of electrons in bonding orbitals. More than 18 electrons means that electrons are put into orbitals of non- or anti-bonding character, which results in a less stable complex. The iron atom of the [NiFe]-hydrogenase active site (16 electrons) is therefore susceptible to attack, and for this reason a ligand usually exists in the bridging position, denoted 'X' in Figure 2. This ligand is considered to be a hydride in the active states

of the enzyme where this position is occupied (but this is too small to be resolved crystallographically) and an oxygen-based ligand in the inactive states of the enzyme.[26,32,33]

1.4.2 [FeFe]-Hydrogenases

1.4.2.1 Overall Structure

So far the [FeFe]-hydrogenases from only two different organisms have been studied crystallographically. The first is the cytoplasmic, monomeric [FeFe]-hydrogenase I from *Clostridium pasteurianum* (*Cp*I)[34] while the second is the periplasmic, heterodimeric [FeFe]-hydrogenase HydAB from *Desulfovibrio desulfuricans* (*Dd*HydAB).[35] Both structures contain the active site (H-cluster) discussed below, and a series of FeS-clusters that form the electron transport chain (*c.f* [NiFe]-hydrogenases). The number of clusters in this chain varies between hydrogenases from different organisms, but the H-cluster is highly conserved. As discussed for [NiFe]-hydrogenases, the distances between the FeS clusters must be less than 14 Å in order for electron transfer to be rapid, and not limit the rate of catalysis.

The [FeFe]-hydrogenases from three different organisms are studied in this thesis; *Dd*HydAB and *Ca*HydA from the bacteria *Desulfovibrio desulfuricans* and *Clostridium acetobutylicum* and *Cr*HydA1from the green algae *Chlamydomonas reinhardtii.* The overall structures of these three hydrogenases are shown and compared in Figure 3.

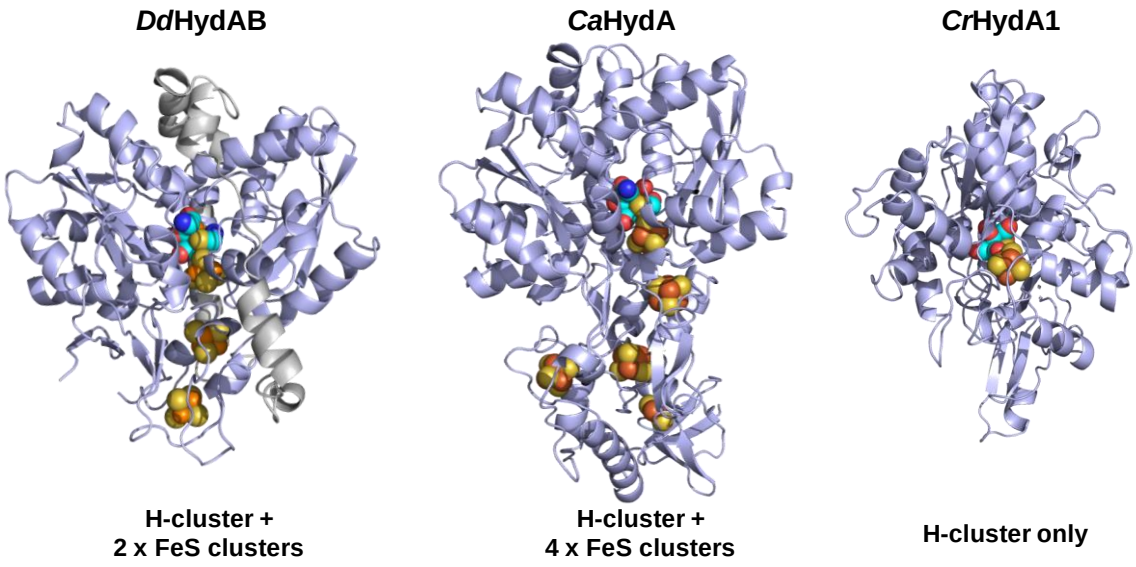

Figure 3: A comparison of the overall protein structures of the three [FeFe]-hydrogenases studied in this thesis. The structure of *Dd*HydAB was resolved by X-ray crystallography[35] (PDB code 1HFE), the structure for *Ca*HydA was obtained by homology modelling using Modweb software,[36] and the model structure of *Cr*HydA1 was generated by Sven T. Stripp via Swiss Prot. The latter two models are both based on the structure of *Clostridium pasteurianum* hydrogenase-1 (PDB code 3C8Y). The grey ribbon in the structure of *Dd*HydAB is the small subunit.

Desulfovibrio desulfuricans (*Dd*) is a sulfate-reducing bacterium that derives energy from anaerobic respiration.[37] *Desulfovibrio* species are commonly found in polluted waters or anaerobic water-logged soils rich in organic material and are considered to be an anaerobes, although these bacteria have been isolated close to oxic habitats.[38] These bacteria are able to use a wide variety of inorganic compounds, including sulfate and nitrate, as terminal electron acceptors in respiration.[39,40] Although considered an anaerobe this bacterium is capable of growing in almost atmospheric O_2 levels (18% O_2).[38]

The [FeFe]-hydrogenase from *Dd* (*Dd*HydAB) is a soluble periplasmic hydrogenase whose physiological role is hydrogen uptake.[41] The protons generated in the cell periplasm create a gradient across the membrane, thought to be coupled to synthesis of ATP in the cytoplasm.[41] The electrons generated are also thought to be transferred to the cytoplasm where they are either used to generate reducing power for the cell, or to reduce sulfate to sulfide. The

hydrogenase *Dd*HydAB is heterodimeric, consisiting of a large subunit (43 kDa) and a small subunit (10 kDa).[35] The H-cluster is housed in the large subunit, along with two ferredoxin-like [4Fe4S]-clusters that act as the electron relay chain, electrically connecting the active site to the protein surface. The small subunit (grey ribbon, Figure 3) is not considered as a separate domain, as it wraps around the large subunit completely embracing it. The *Dd*HydAB samples used in this thesis were purified aerobically, from cells grown anaerobically.[42]

Clostridium acetobutylicum (*Ca*) is a soil dwelling bacterium that generally grows under strictly anaerobic conditions and obtains energy via substrate phosphorylation by fermentation.[43] The substrates of fermentation are organic molecules which act as the electron donor and acceptor; thus this bacterium requires a carbohydrate source capable of undergoing fermentation in order to survive. The solvents acetone, acetate, butanol, butyrate and ethanol are all produced from the common precursor acetyl-CoA, and a hydrogenase is used to convert the excess protons generated into H_2.[44,45] In 2005 it was shown that this strict anaerobe is capable of growing in microoxic conditions (< 5% O_2[46]); it contains many enzymes that allow it to survive, such as superoxide dismutase, and these enzymes are up-regulated in the presence of oxygen, contributing to the short term cell survival in these conditions.

Unlike *Dd*HydAB the [FeFe]-hydrogenase *Ca*HydA is monomeric (64.3 kDa)[47]. Although the structure of this hydrogenase is not known, it shares 71% sequence identity with the crystallographically characterised *Clostridium pasteuranium* hydrogenase-1 (*Cp*I).[48] The structure is divided into two ‘domains’; the H-domain where the H-cluster is located, and the F-domain (ferredoxin like), which contains the FeS-cluster relay chain. The clusters in this chain are considered to be the same as in *Cp*I: three [4Fe4S]-clusters and one

[2Fe2S]-cluster.[34] To acquire the *Ca*HydA samples used in this thesis both the cell growth and protein purification were carried out under strictly anaerobic conditions.[47]

Chlamydomonas reinhardtii (*Cr*) is a unicellular eukaryotic green alga that is able to perform solar-driven H_2 production under anoxic conditions using an [FeFe]-hydrogenase (*Cr*HydA1).[49] The hydrogenase is localised in the chloroplast[50] and is coupled to the photosynthetic electron transfer chain. In the cell, energy from light is used to oxidise water and the electrons generated are transported from photosystem I to the *Cr*HydA1 hydrogenase via a ferredoxin partner (PetF).[51,52]

There is not yet a crystal structure of *Cr*HydA1, but it is known to share 34% sequence identity with *Cp*I and 33% with the large subunit of *Dd*H. Like *Ca*HydA this enzyme is monomeric, but is much smaller (47.5 kDa).[53] This hydrogenase contains no electron relay chain; the only FeS cluster present is the [4Fe4S]-cluster at the active site; in *vivo* electron transfer is coupled to the ferredoxin partner.[54,55] To obtain the *Cr*HydA1 samples used in this thesis both the cell growth and protein purification were carried out under strictly anaerobic conditions. [47]

1.4.2.2 Active Site

The active site of [FeFe]-hydrogenases, known as the H-cluster, is highly conserved across enzymes from different species. The H-cluster consists of 2 sub-clusters as shown in Figure 4: a cubane, $[4Fe4S]_H$, connected via the sulfur ligand of a cysteine to the proximal iron (Fe_p) of a binuclear iron cluster, $[2Fe]_H$. Both irons in the $[2Fe]_H$ are coordinated by CO and CN ligands, and are bridged by an unusual SCH_2XCH_2S dithiolate ligand, with the bridgehead atom X now widely considered to be a nitrogen atom.[56,57] In the +2 oxidation state the distal

iron atom has only 16 valence electrons and is therefore vulnerable to attack. The vacant binding site at Fe_d is denoted with an asterisk in Figure 4.

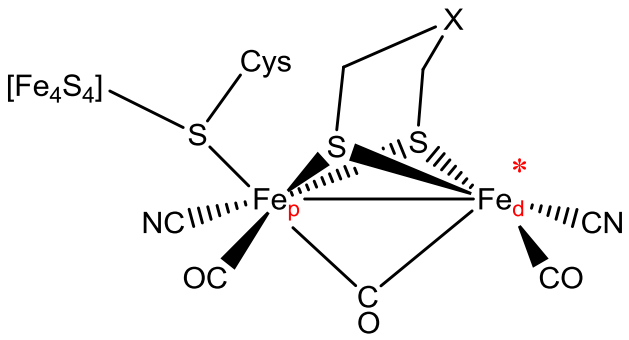

Figure 4: Active site (H-cluster) of an [FeFe]-hydrogenase in the oxidised state. The exchangeable binding site at the distal iron (Fe_d) is marked by an asterisk.

1.5 Redox States and the Catalytic Cycle

During activation and catalysis the active site of hydrogenases cycle through a number of different redox states. In some states the enzyme is inactive, and unable to perform catalytic turnover. The reactivity of the enzyme with substrates and inhibitors can vary for the different redox states of the active site.

1.5.1 [NiFe]-Hydrogenases

1.5.1.1 Redox States

For [NiFe]-hydrogenases the different redox states of the active site have been characterised through various EPR and FTIR studies and are summarised in Figure 5.[58-60] It has been found that only the oxidation state of the Ni atom changes between the different states, the Fe remains in the low spin Fe^{2+} state, favoured by the strong field CO and CN^- ligands.[28,59,61] There are two catalytically inactive oxidised states (Ni-A and Ni-B) that can be reductively activated. Activation of the Ni-A state is much slower than that of Ni-B, and for this reason these states are also referred to as ‘unready’ and ‘ready’ respectively. Both of these states are

EPR active and are characterised by a different set of g values.[58,59] One electron reduction of Ni-A and Ni-B results in the formation of the EPR silent states Ni-SU (silent unready) and Ni-SIr (silent ready). Under sufficiently reducing conditions the Ni-SIr state is converted to the EPR silent state Ni-SIa (silent active), which can be further reduced to generate the EPR and catalytically active Ni-C state believed to contain Ni^{3+} and a bridging hydride ligand.[62] This state is light sensitive;[63] under illumination the hydride is lost to form the Ni-L state, stable only at low temperatures, where Ni is in the +1 oxidation state. Reduction of the Ni-C state in the presence of H_2 generates the active Ni-R state, where the Ni is in the +2 oxidation state and retains the bridging hydride ligand.[58,59]

The inactive Ni-A and Ni-B states are generated when [NiFe]-hydrogenases are exposed to O_2.[64] The Ni-B state can also be generated anaerobically at high potential and is thought to contain a bridging hydroxyl ligand in the active site,[65,66] while it is believed that the Ni-A state contains a peroxide bridging ligand.[67]

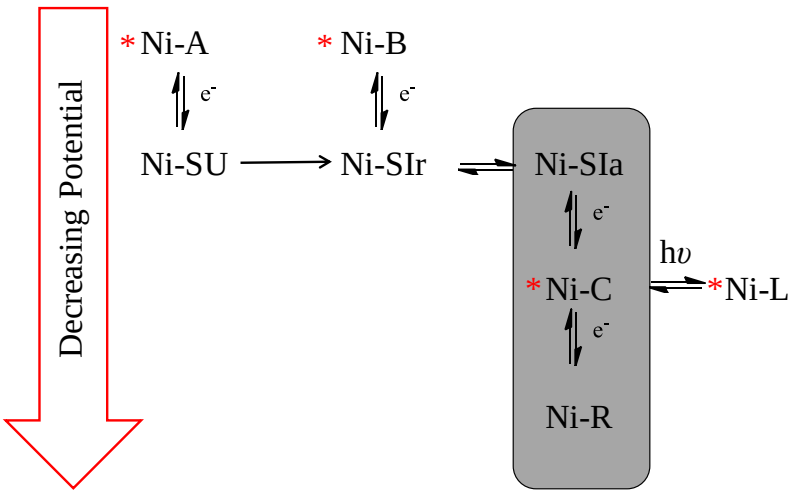

Figure 5: A schematic representation of the different redox states of a 'standard' [NiFe]-hydrogenase. The states within the grey box are active states believed to be involved in the catalytic cycle and those states with an asterisk are paramagnetic and therefore EPR-active. Figure adapted from references 58 and 59.

1.5.1.2 Catalytic Mechanism

The three states Ni-SIa, Ni-C and Ni-R, inter-converted by one electron/one proton equilibria, are all thought to be involved in the catalytic cycle of [NiFe]-hydrogenases.[59,68,69] In Ni-SIa there is no bridging ligand present and it is this state that is thought to bind H_2, but it is not certain whether H_2 binds to the Ni or Fe atom.[70] Recent studies using Density Functional Theory (DFT) suggest that the mechanism may be explained by a two-state model in which H_2 can bind to both the Ni and Fe atoms.[70,71] After H_2 binding catalysis is thought to proceed via base assisted hetereolytic cleavage, generating a hydride that bridges the Ni and Fe metal centres.[72-74] This base may be a nearby cysteine ligand, or alternatively a water molecule bound to the Fe. One possible mechanism, proposed by Siegbahn *et al*.[72] and proceeding via H_2 binding to the Fe, is shown in Scheme 1.

Scheme 1: A suggested catalytic cycle for [NiFe]-hydrogenase, proceeding via H_2 binding to the Fe atom, adapted from reference 72. The Ni-SIa, Ni-R and Ni-C states are labelled in red.

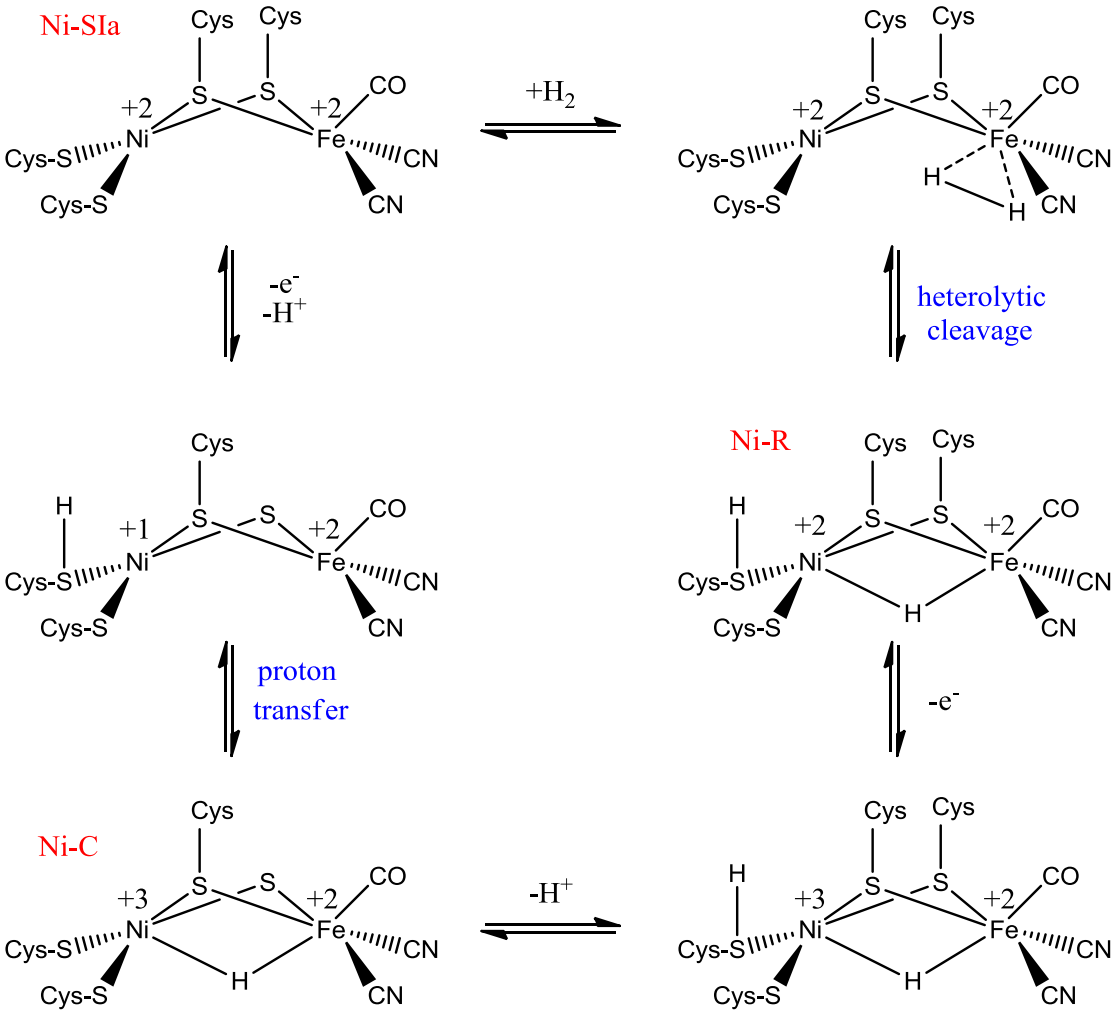

In the mechanism shown above, heterolytic cleavage of H_2 generates a proton, which is transferred to one of the terminal cysteine residues on Ni, and a hydride which moves to the bridging position, forming the Ni-R state. An electron is then transferred to the proximal [4Fe4S]-cluster and the cysteine deprotonated via the proton transfer pathway (discussed later) to generate the Ni-C state. Finally the Ni-SIa state is regenerated by loss of the hydride as a proton (transferred via the terminal cysteine) and a one electron oxidation of the Ni.

1.5.2 [FeFe]-Hydrogenases

1.5.2.1 Redox States

The active site of [FeFe]-hydrgenase is able to cycle through a range of redox states with the Fe atoms in the $[2Fe]_H$ sub-cluster in either the +1 or +2 oxidation state. The binding of ligands at Fe_d and Fe_p varies between the different states as shown in Figure 6. The diamagnetic H_{ox}^{inact} state is a highly oxidised inactive form of the enzyme that is obtained during the aerobic purification of some [FeFe]-hydrogenases, such as *Dd*HydAB.[42,75] This state can also be formed from active states of the hydrogenase under highly oxidising conditions.[76-78] In the H_{ox}^{inact} state both iron atoms are oxidised to Fe(II) and the FeS cluster moiety is in the $[4Fe4S]^{2+}$ state. According to X-ray crystallography[34,57] there is a bridging CO ligand between the two iron atoms, and a bound oxygenic species (OH^-/H_2O) at the distal iron site. This state can undergo irreversible one electron reduction to transiently form a paramagnetic (EPR active) state, H_{trans}, with a reduced FeS cluster $[4Fe4S]^{1+}$.[79-81] In this state the oxygenic species is still assumed to be bound at Fe_d and the CO ligand remains in a bridging position.

At more reducing potentials the H_{trans} state undergoes an irreversible conformational change that favours transfer of the electron from the $[4Fe4S]_H$ cluster to the $[2Fe]_H$ moiety to form the active oxidised state H_{ox}.[59,82] Spectroscopic studies favour an oxidation state assignment of $[4Fe\text{-}4S]^{2+}Fe_p(I)Fe_d(II)$ for H_{ox}.[59,82,83] In this state Fe_p still shares a bridging CO with Fe_d but the oxygenic ligand at Fe_d is lost.[34,84] One electron reduction of the H_{ox} state generates the active reduced state H_{red}.[82,85] In the structure of the [FeFe]-hydrogenase from *Desulfovibrio desulfuricans* (*Dd*HydAB), which was crystallised in the H_{red} form, the bridging CO moves to a terminal position on Fe_d[35] and the state is assigned as either $[4Fe\text{-}4S]^{2+}Fe(I)Fe(I)$ or the hydrido species $[4Fe4S]^{2+}Fe(II)Fe(II)H^-$.[59,83]

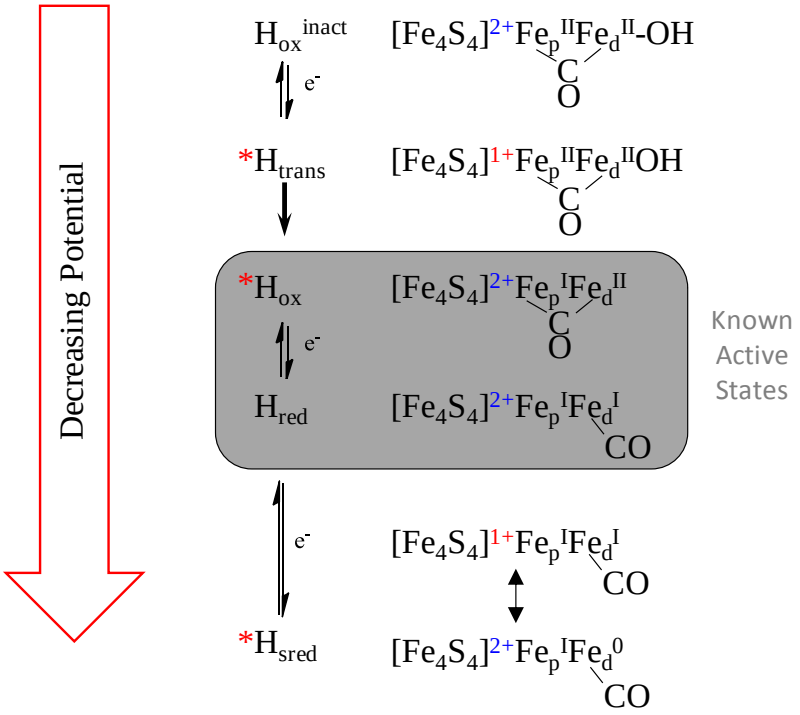

Figure 6: The different possible redox states of [FeFe]-hydrogenases, showing the change in oxidation state and ligand binding. EPR active states are denoted by an asterisk.

A two-electron 'super-reduced' state symbolised as H_{sred} remains poorly characterised – not surprising, since such a species should be highly reactive, rapidly evolving H_2 and escaping detection. In this state the additional electron is thought to reside on the $[4Fe4S]_H$ cluster, giving the state $[4Fe\text{-}4S]^{1+}Fe(I)Fe(I)$, although it is possible that instead, one of the Fe atoms is reduced to Fe(0). This species is expected to be EPR-active, although it has not been observed using this technique to date.

FTIR studies of *Dd*HydAB by Roseboom *et al.*[82] revealed that at low potentials the signals from the H_{red} state are lost, and replaced with a variety of new, weak bands, attributed to formation of the super-reduced state. The midpoint potential of the H_{red}/H_{sred} transition, as measured by the disappearance of the H_{red} band at 1894 cm^{-1}, was measured as -540mV at pH 8. Formation of this state was largely irreversible; minimal H_{red} and H_{ox} bands were regained upon oxidation, and it was suggested that the $[2Fe]_H$ subcluster is destroyed at low

potential (< 500 mV).[82] This is consistent with studies on *Cp*I,[86] for which the H_2 production activity was found to increase as the potential was lowered until -425 mV (at pH 7), after which activity decreased greatly. This loss of activity was attributed to formation of an inactive $[4Fe4S]^{1+}$ state at low potentials.[86] In contrast FTIR studies of *Cr*HydA1 carried out by Silakov *et al*. showed that a super-reduced state is formed *reversibly* at low potentials, and this state is stable.[87] The midpoint potential for the H_{red}/H_{sred} transition was found to be -460 mV (at pH 8) for *Cr*HydA1, 90mV higher than for *Dd*HydAB, while the H_{ox}/H_{red} transition occurs at a very similar potential for both enzymes.[82,87] As previously discussed, the H-cluster is conserved between these two enzymes, while the overall structures are quite different. Formation of the H_{sred} state is thought to involve the addition of an electron at the $[4Fe4S]_H$-cluster, a position affected by the greater differences in the surrounding protein environment compared to the $[2Fe]_H$ site, explaining the greater variation observed in the H_{red}/H_{sred} transition potential.[87]

1.5.2.2 Catalytic Mechanism

The mechanisms proposed so far for catalysis by [FeFe]-hydrogenases include only the well characterised active states, H_{ox} and H_{red}, as stable intermediates in the cycle, one such mechanism is shown below in Scheme 2.[58,59] Electron and proton transfer are assumed to take place in almost simultaneous steps. Although various DFT studies have revealed that both the binding of a hydride in a bridging or a terminal position results in a stable complex, in all cases the isomer with the hydride in the bridging position is more thermodynamically favoured.[88-91] It has been demonstrated by Hall *et al*.[92] however that the bridging amine group can act as a proton acceptor, facilitating H_2 cycling initiated by terminal hydride binding at the distal iron site. Reaction of the terminal-hydride species with electrons and protons (to form H_2) must therefore be considerably more rapid than isomerisation to the bridging

hydride form for H_2 cycling to proceed via this mechanism. It has been suggested that a highly conserved lysine residue (Lys237) may play a role in stabilising the terminal hydride species.[93-95] The electrostatic interaction between this positively charged group and the negatively charged CN ligand at Fe_d might limit rotation of the distal iron group, thus hindering formation of the bridging hydride.[93]

Scheme 2: A proposed mechanism for H_2 cycling by [FeFe]-hydrogenases adapted from reference 59.

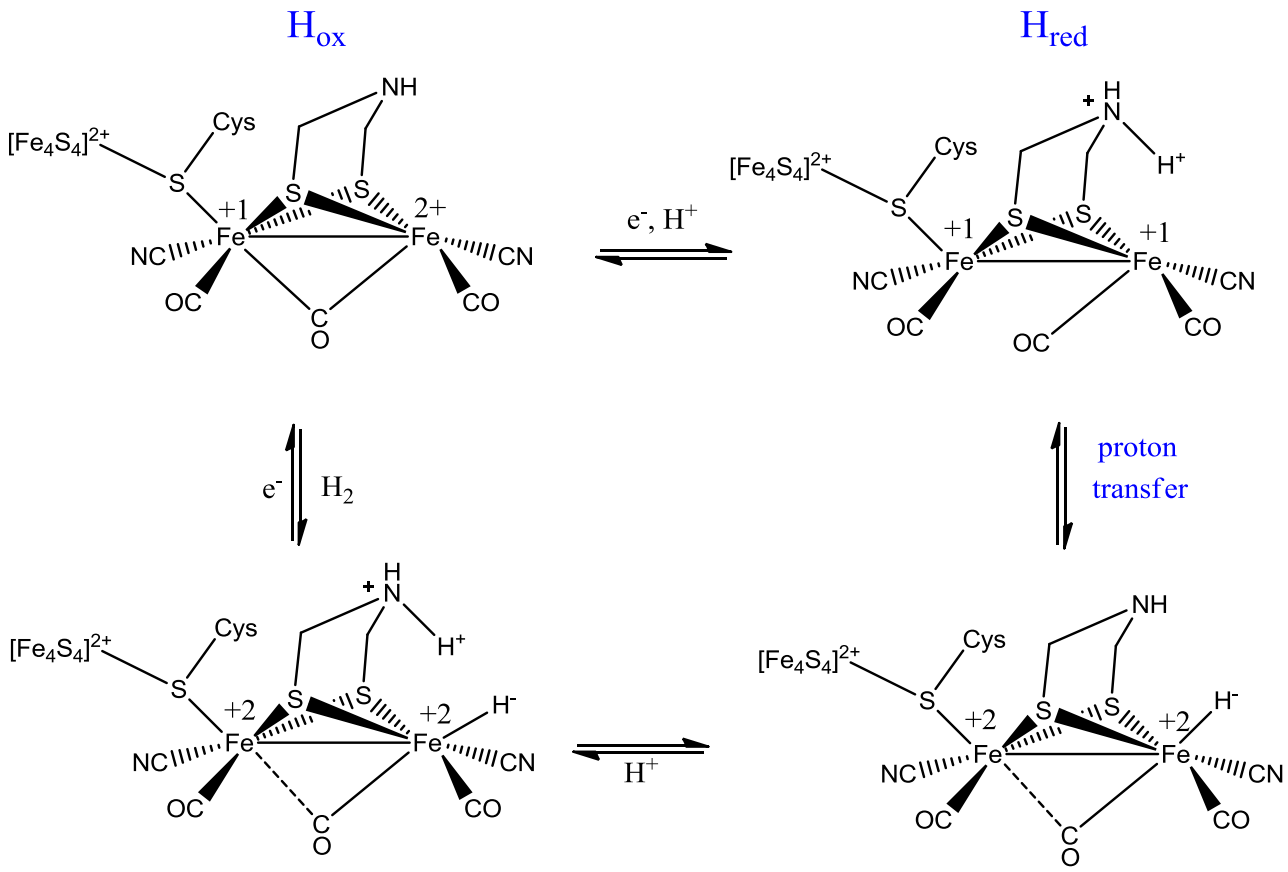

In this mechanism H_2 production is initiated by protonation and one electron reduction of the H_{ox} state to form the H_{red} state (top right). The proton is then transferred to the distal iron, where it binds as a hydride, and the iron atoms are both formally in the +2 oxidation state. The bridgehead nitrogen is then re-protonated and this proton combines with the hydride on Fe_d. The H_{ox} state is regenerated by release of H_2 and the concomitant addition of one electron.

This mechanism however is not fully understood, and it is not clear whether proton reduction and H_2 oxidation follow the same mechanism. Additionally, this mechanism does not assign any role to the $[4Fe4S]_H$ cluster, it remains as $[4Fe4S]^{+2}$ throughout the cycle. The states H_{ox} and H_{red}, are only separated by one electron, while H_2 cycling is a two electron process. It is possible that the FeS cluster is involved in providing or removing sufficient electrons to catalyse H_2 production or oxidation. Recent DFT studies[93,96] that involve the $[4Fe4S]_H$ moiety in the model structure have determined that H_2 evolution by protonation of the super-reduced state $[4Fe4S]^{1+}Fe(II)Fe(II)\text{-}H^-$ is exothermic. Hydrogen evolution by this state is predicted to be more thermodynamically favoured than for the corresponding H_{red} state ($[4Fe4S]^{2+}Fe(II)Fe(II)\text{-}H^-$), indicating that the super-reduced state could reasonably be involved in the catalytic cycle of [FeFe]-hydrogenases.[93,96] It should be noted however that this model did not consider the contributions of the bridgehead amine group, this was replaced by a CH_2 bridge in the model.

The involvement of a super-reduced state in catalysis is investigated in this thesis using protein film electrochemistry (PFE).

1.5.2.3 Catalysis and Bias

Representative voltammograms of the three [FeFe]-hydrogenases studied in this thesis, using PFE, are shown in Figure 7. All three hydrogenases are bidirectional, catalysing both H_2 oxidation (positive current) and H_2 production (negative current). The gradient of the voltammogram reflects the increased rate of catalysis with the increased driving force for electron transfer as the potential is swept to more oxidising (for H_2 oxidation) or more reducing (for H_2 production) values. All three voltammograms cut the zero-current axis (blue lines) at the thermodynamic potential of the $2H^+/H_2$ couple under these conditions.

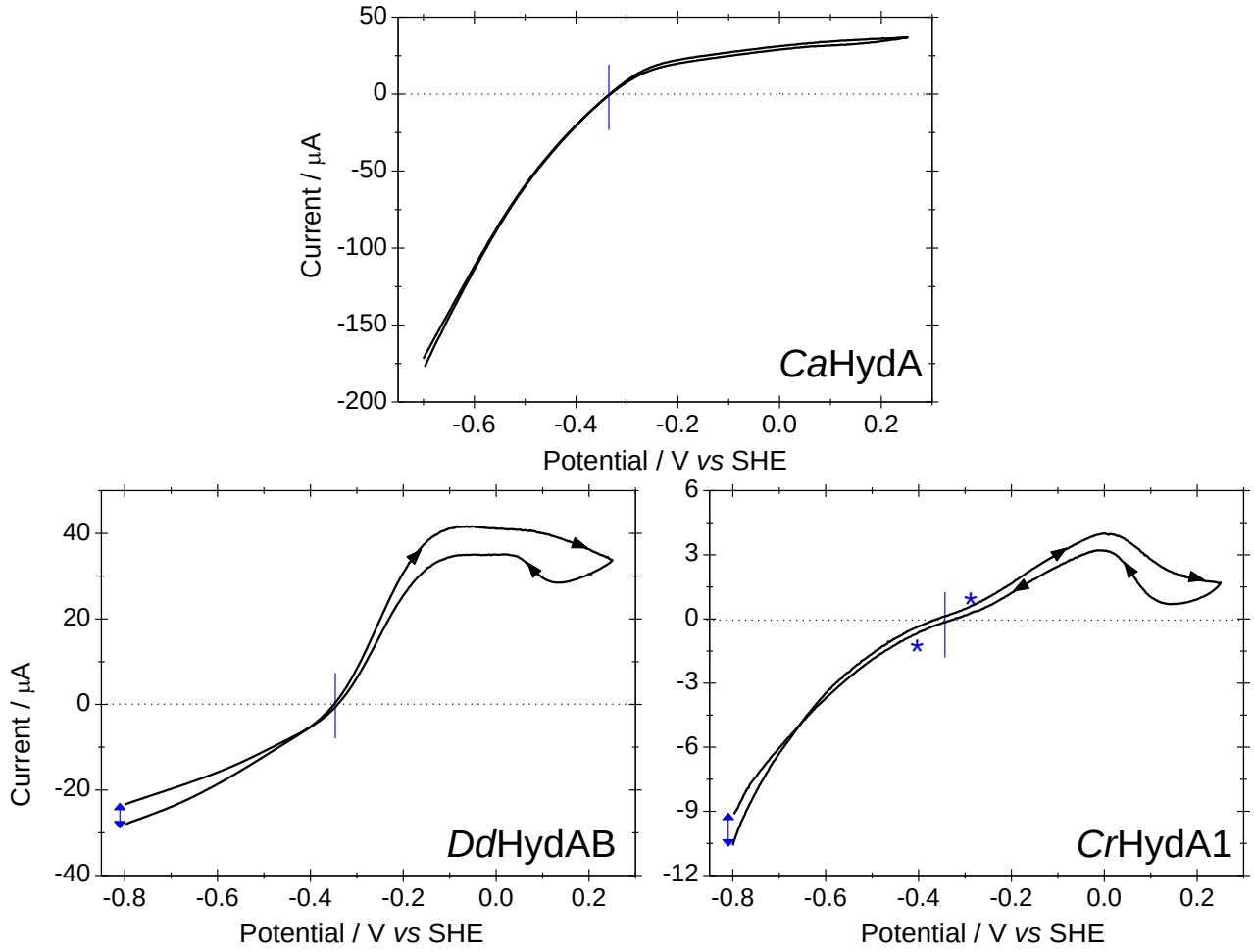

Figure 7: Representative cyclic voltammograms of three [FeFe]-hydrogenases *Ca*HydA (top), *Dd*HydAB (bottom, left) and *Cr*HydA1 (bottom, right). Conditions: 100% H_2, 10 °C, ω = 3000 rpm, pH 6 phosphate buffer, 20 mV/s scan rate. The 'bend' in the voltammogram of *Cr*HydA1 around the zero current axis is marked by asterisks. Black arrows show the scan direction, blue arrows highlight the current lost over the duration of the voltammogram.

The voltammograms of both *Ca*HydA and *Dd*HydAB cut the x-axis cleanly (Figure 7, blue line); only minimal driving force is required to drive the reaction in either direction. The voltammogram of *Cr*HydA1 however does not cut the axis smoothly; it appears slightly 'bent' in this region (marked by asterisks). This reflects an overpotential requirement for catalysis in either direction. This may be related to the lack of an FeS cluster relay chain in this enzyme; the electron tunnelling distance between the electrode surface and the H-cluster may be greater, resulting in slower electron transfer kinetics.

Both *Ca*HydA and *Dd*HydAB show strong catalytic bias as previously reported, while *Cr*HydA1 does not.[76,97] For *Cr*HydA1 the magnitude of the H_2 oxidation and H_2 production current is almost the same for any given driving force (difference between the potential and $E(2H^+/H_2)$. It can be seen in the voltammogram of *Ca*HydA that this enzyme strongly favours H_2 production; the negative current is approximately three times the magnitude of the positive current. The voltammogram of *Dd*HydAB shows the opposite bias, H_2 oxidation is favoured; the positive current is more than twice as great as the negative current. All three hydrogenases show significant H_2 production activity in 100% H_2; as previously reported, product inhibition for these enzymes is minimal compared to [NiFe]-hydrogenases.[76]

The voltammograms differ quite dramatically at high potential for the three enzymes. At potentials greater than -0.25 V the H_2 oxidation current of *Ca*HydA reaches a plateau. The current is expected to increase as the potential is raised, as the rate of electron transfer increases with additional driving force. The plateau reflects the point at which a process other than electron transfer becomes rate limiting. This is likely to be a chemical process, possibly the formation of the Fe_d-H_2 bond or breakage of the H-H bond. For both *Dd*HydAB and *Cr*HydA1 the oxidative current does not reach a plateau, in fact the current stops increasing and begins to decrease as the potential is swept above -0.1 V for *Dd*HydAB and 0 V for *Cr*HydA1. This is attributed to electrochemical formation of the highly oxidised, inactive state H_{ox}^{inact}.[77,98] This process is very slow for *Ca*HydA, and minimal attenuation in the voltammograms is observed only at very slow scan rate ($< 5\ mVs^{-1}$).[76,97] This anaerobic inactivation is largely reversible for both *Dd*HydAB and *Cr*HydA1 under the conditions used in these voltammograms, seen by the increase in current in the reductive scan (0.1→0 V) even though the driving force for oxidation is decreased. Previous studies however have shown that formation of the H_{ox}^{inact} state of *Cr*HydA1 is not always completely reversible.[98] The

voltammogram of *Dd*HydAB is complicated by the fact that there are two maxima at high potential, one at ~ -0.1 V and one at 0 V. The peak at 0 V is attributed to the formation of H_{ox}^{inact}, but the identity of the second is not understood.[77] It is possible that there are two separate inactivation processes that occur at high potential for this enzyme, or that there is a great dispersion of enzyme orientations on the electrode surface, and the second maxima results from different rates of electron transfer for enzymes in different orientations. The stability of an enzyme film on the electrode surface is much greater for *Ca*HydA and *Cr*HydA1 than *Dd*HydAB, and experiments of the latter are often complicated by the high rate of enzyme film loss over the course of the experiment. Film loss is seen in the voltammograms in Figure 7 as the difference in the current at -0.8 V at the start and end of the voltammogram cycle (blue arrows) and is most significant for *Dd*HydAB.

1.6 Proton and Gas Transport

1.6.1 Proton Transport

For both [NiFe]- and [FeFe]-hydrogenases it is essential that the transfer of protons between the active site and the exterior of the protein is efficient to ensure that catalysis is rapid.

In [NiFe]-hydrogenases protons are believed to be transferred between amino acid residues via a protonation/deprotonation mechanism.[99] Given the prevalence of suitable residues throughout the protein it is difficult to study this pathway using crystallographically, however it is fairly well defined close to the active site. Crystal structures of the [NiFe]-hydrogenases show there is a Mg^{2+} cation close to the C-terminus of the large subunit.[23] This cation is coordinated to the active site via a network of hydrogen bonds, and this network is considered to be involved in the proton transport chain.[23,58]

In [FeFe]-hydrogenases, the bridgehead nitrogen atom is widely believed to be involved in the transfer of protons, as shown in Scheme 2.[57] This amine is sufficiently close to a conserved cysteine residue (Cys178 in *Dd*HydAB or Cys299 in *Cp*I) for protons to be transferred between the two sites.[57] Crystal structures of *Dd*HydAB and *Cp*I have identified a proton pathway between the protein surface and Cys178 or Cys299 repspectively.[34,57] Computational studies performed by Hong e*t al*. suggest that the mechanism of proton transfer in both *Dd*HydAB and *Cp*I is concerted, protons being transferred between glutamic acid (Glu), serine (Ser) and cysteine (Cys) residues; from Glu159 to Ser198 to Glu156 to Cys 178 in *Dd*HydAB.[96]

1.6.2 Gas Transport

For both [NiFe] and [FeFe]-hydrogenases gaseous H_2 must diffuse to and from the solution outside of the enzyme, through the protein structure, to the buried active site, in order for catalytic H_2 cycling to occur. Additionally other diatomic gaseous molecules, such as CO and O_2 are able to access the active site and inhibit catalysis. The locations of hydrophobic channels, which may allow the transport of gaseous molecules through the enzyme to the active site, have been investigated for various hydrogenases. X-ray diffraction studies, where the protein is crystallised after exposure to xenon under pressure, have been used to elucidate the position of these channels by mapping the location of the Xe atoms inside the enzyme.[100] These locations can then be used as starting points for molecular dynamics simulations of transport of Xe and H_2 through the protein.

Studies of several different [NiFe]-hydrogenases have revealed that a hydrophobic channel from the enzyme surface opens up near the Ni atom of the active site.[59,100,101] Genetic modification of *Df*H to narrow the opening of the putative gas channel, near the active site,

resulted in a dramatic decrease in the rate of inactivation by O_2.[102] Modification to widen this channel in the regulatory hydrogenase of *Ralstonia eutropha*, has the opposite effect; increasing its sensitivity to O_2.[103]

There are three putative pathways believed to extend from the solvent to the active site (H-cluster) of [FeFe]-hydrogenases. Xenon crystallography studies of *Dd*HydAB, such as those described above, also revealed the existence of a central cavity in close proximity to the H-cluster.[35] The first channel (A), comprises an elongated 'static' cavity that connects the central cavity to the protein surface.[35] A 'dynamic' pathway (B), identified from computational studies of *Cp*I,[104,105] also extends from the protein surface to the central cavity. This channel consists of cavities that open transiently due to fluctuations of the protein. This pathway (B) has previously been suggested to be the dominant pathway of O_2 diffusion through the protein,[104] although recent computational studies point to O_2 diffusion proceeding via channel A.[106] A third, hydrophilic channel (W) has also been identified, and diffusion of water via this channel has been observed during molecular dynamics simulations of *Cp*.[106] The amino acids that line the central cavity are conserved in most [FeFe]-hydrogenases,[107] while this is not true for channels A and B. The different rates of reaction of [FeFe]-hydrogenases from different organisms with small molecules such as CO and O_2 cannot therefore be attributed to differences at this site. It has been proposed that the lower rate of O_2 inhibition of *Ca*HydA compared to *Dd*HydAB can be explained by the presence of bulkier residues in channel A in the structure of *Cp* (and therefore *Ca*HydA) than *Dd*HydAB.[106] Additionally genetic mutations of channel A in both *Cr*HydA1[105] and *Ca*HydA[107] to introduce bulkier residues have been found to slow the rate of O_2 inhibition. Such mutations however have no effect on the rate of CO binding, or the Michaelis constant

for H_2,[107] and as yet the exact channels or pathways used by gaseous molecules use to access the active site are not fully understood.

1.7 Technological Applications

As previously discussed, for H_2 to become a viable energy alternative to fossil fuels there are various limitations to overcome, namely development of efficient, renewable methods of large scale H_2 production, safe storage and transport of H_2 and the efficient extraction of energy from H_2. In recent years the possibility of using hydrogenases (or synthetic active site mimics) to facilitate the use of H_2 as a fuel has been recognised. Both the H_2 oxidation properties of [NiFe]-hydrogenases and the H_2 production properties of [FeFe]-hydrogenases can be utilised.

1.7.1 Synthetic Analogues

The synthesis of structural and functional analogues of hydrogenases is an area of interest that has grown rapidly since the discovery of hydrogenase structures using X-ray crystallography.[108] This area of research serves several functions; firstly, to develop bio-inspired H_2 cycling catalysts for a future 'H_2 economy', but this research also helps us to further our understanding of how the active sites of hydrogenases function so efficiently. Production of [FeFe]-hydrogenase mimics is most common, partly because they are easier to synthesis than a [NiFe] complex, as they contain only one type of metallic ion. Additionally the first row transition metals nickel and iron have low affinities for H_2, so proton reduction catalysts are easier to synthesise than H_2 oxidation catalysts.[109] Many analogues of [FeFe]-hydrogenases start from the simply derived complex $(\mu\text{-}S(CH_2)_3S)[Fe^I(CO)_3]_2$. Modifications to this general structure has resulted in advancement towards the synthesis of a structural, spectroscopic and functional model of the $[Fe_2]_H$ moiety of the H-cluster. The most

recent reported model capable of catalytic H_2 oxidation is that of Rauchfuss and Camara,[110] shown in Figure 8a.

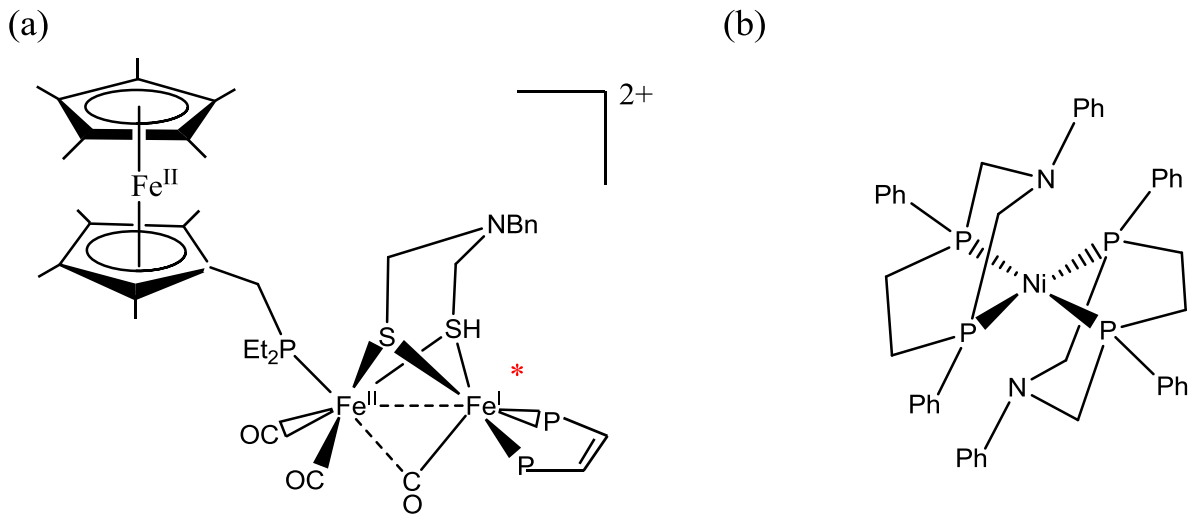

Figure 8: The structure of two synthetic H_2 cycling catalysts: (a) A H_2 oxidation catalyst based on the H-cluster of [FeFe]-hydrogenase[110] (b) A nickel based H_2 production catalyst.[111]

A diphosphine ligand is substituted in place of the electron rich cyanide ligands in the enzyme, necessary to stabilise the oxidised form of the complex. Additionally an amine group is present at the head of the dithiloate bridge, as in the H-cluster, which is able to participate in proton transfer. Importantly, the $[4Fe4S]_H$ moiety has been approximated using a the one electron redox molecule $Cp^*Fe(C_5Me_4CH_2Pet_2)$.

In general the H_2 production activity of most synthetic catalysts does not approach that of hydrogenases, and they generally require large overpotentials to drive the reaction. The poor performance of active site mimics highlights the important role of the surrounding protein structure in enabling enzymes to carry out efficient catalysis. One notable exception to the low H_2 production rate of synthetic catalysts is the DuBois catalyst[111] (Figure 8b), a nickel based complex that also includes a pendant amine base to facilitate proton transfer. A H_2 turnover frequency of 100,000 s^{-1} has been reported for catalysis, however a large overpotential is required (-1.13 V).[111]

1.7.2 Enzymatic Fuel Cells

The use of H_2/O_2 fuel cells for energy production is regarded as 'clean' as there is no production of any harmful greenhouse gases, such as CO_2. In enzymatic bio-fuel cells biological catalysts (enzymes) replace the expensive, toxic precious metals often used in traditional fuel cells (Pt and Pd).[112] Enzymes are adsorbed onto inexpensive electrode materials such as carbon, as shown in Figure 9. Hydrogenase can be used to coat the anode and catalyse the oxidation of H_2. This reaction is coupled to the reduction of O_2 by a multicopper enzyme such as bilirubin oxidase or laccase adsorbed on to the surface of the cathode.[112] Electricity is produced with water as the only by-product. [NiFe]-hydrogenases are more suited to this role than [FeFe]-hydrogenases, as they tend to be more biased towards H_2 oxidation, and are more tolerant to O_2, vital for a system such as the one shown in Figure 9.

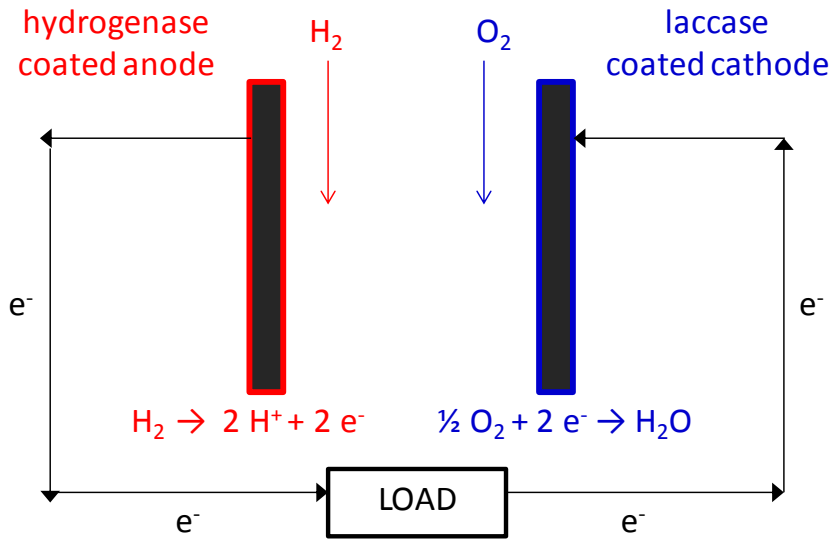

Figure 9: Illustration of a bio-fuel cell consisting of a hydrogenase coated anode (red) and a laccase coated cathode (blue).

One major benefit of using enzymes instead of precious metals as fuel cell catalysts is the increased specificity: enzymes usually only catalyse one reaction, with fewer or no by-products. In contrast, platinum catalyses both the reduction of O_2, and the oxidation of H_2,

requiring a proton exchange membrane to separate the anode and cathode compartments. This costly separation is not required when an O_2 tolerant hydrogenase is utilised.[113] The preparation of enzymes however is time consuming and expensive and enzyme-coated electrodes are only stable for a limited time period. They are also less stable at high temperatures than Pt.

1.7.3 Photochemical H_2 Production

Both hydrogenase enzymes themselves and various active site mimics have been used to produce H_2 photochemically.[114-117] In many systems the H_2 production catalyst is immobilised on particles of a semi-conductor material and a photosensitiser is co-attached to the nanoparticles. This system allows the energy from visible light to be captured by the photosensitiser, and then used to drive the production of H_2 by the catalyst.

One such system, developed within the Armstrong group[115,118], uses TiO_2 particles coated with the [NiFeSe]-hydrogenase from *Desulfomicrobium baculatum* as shown in Figure 10. A tris(bipyridyl)ruthenium (RuP) photosensitiser is also attached to the particles and the system is able to produce H_2 from neutral water at room temperature. Upon illumination with visible light the ruthenium complex becomes excited, and ejects a high energy electron into the conduction band of TiO_2. This electron is then transferred to the hydrogenase active site via the [FeS]-cluster relay chain, and used to reduced protons to form H_2. The ruthenium complex is then reduced by a sacrificial electron donor (EDTA in Tris buffer), and the cycle continues. Turnover frequencies of 50 s^{-1} have been reported for this system.[115]

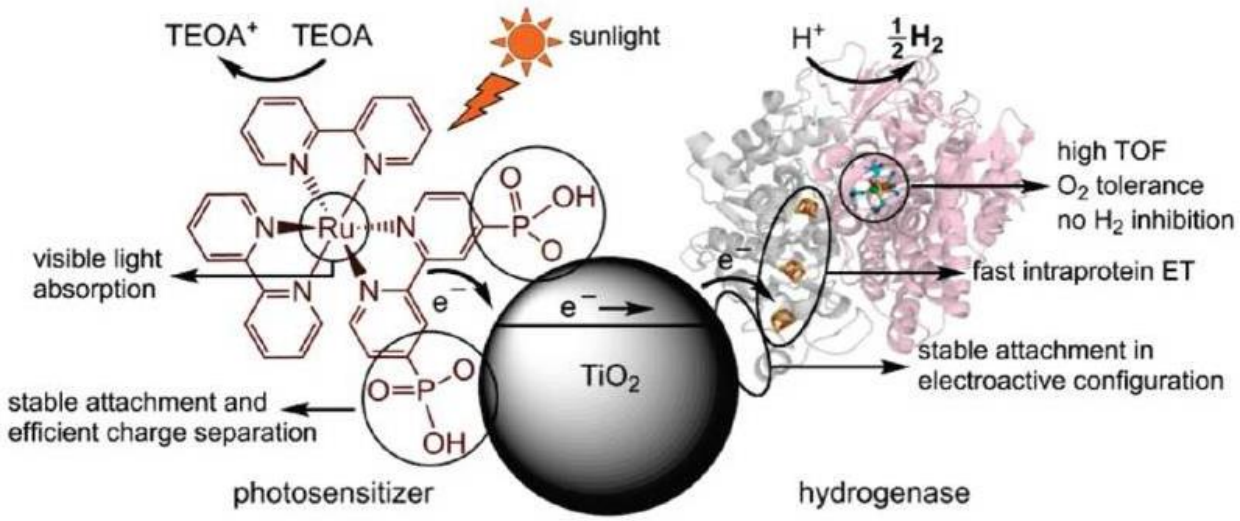

Figure 10: Cartoon representation of a hybrid (enzyme−TiO_2) nanoparticle system showing aspects that are desirable for efficient and practical H_2 production from sunlight. The system is shown with a hydrogenase (*Db* [NiFeSe]-H) as the H_2 production catalyst and the complex (RuP) that proved to be the most suitable photosensitiser. Figure reprinted with permission from reference 115 (*J. Am. Chem. Soc.* 2009, *131*, 18457-18466). Copyright (2009) American Chemical Society.

1.7.4 Enzyme Modified Particles

Other systems involving immobilisation of enzymes on small particles have been developed utilising particles of conductive materials. In 2012 Vincent *et al.*[119] developed a reversible regeneration system for NADH or NAD^+ involving particles of pyrolytic graphite modified with a mixture of hydrogenase (*E. coli* Hyd-2) and the NAD^+-reducing subunit of the soluble hydrogenase from *Ralstonia eutropha* (HoxFU).

Given that the thermodynamic potentials $E(2H^+/H_2)$ and $E(NAD^+/NADH)$ are very closely spaced, the reaction can proceed in both directions under suitable conditions; electrons can be transferred either from H_2 to NAD^+ or from NADH to H^+. Oxidoreductases, electron transfer enzymes, are utilised to transfer reducing equivalents in the form of hydride (H^-) in many industrial biocatalysis applications, including stereoselective generation of chiral alcohols. NAD cofactors are essential redox agents used for a wide range of oxidoreductases. The

particle system shown above is a promising future alternative to homogeneous enzyme regeneration systems, using H_2 as a clean, cheap electron donor or easily separated product.

The industrially relevant water-gas shift reaction ($CO + H_2O \leftrightarrow CO_2 + H_2$) has been performed using a similar graphite particles system.[120] The oxidation of CO is catalysed by a carbon monoxide dehydrogenase from *Carboxydothermus hydrogenoformans* (CODH I) while reduction of protons is carried out by a hydrogenase (*E. coli* Hyd-2). The system operates at a far lower temperature (30 °C) than the industrial process (> 200 °C) and is highly efficient. A turnover frequency of at least 2.5 s^{-1} per minimum functional unit (one CODH/Hyd-2 pair) is reported, comparable to conventional high-temperature catalysts used industrially. It is vital that the H_2 producing hydrogenase employed in this system is stable in the presence of CO. This means that although [FeFe]-hydrogenases are more catalytically active towards H_2 production than [NiFe]-hydrogenases, they are unsuitable due to their high sensitivity to inhibition by CO.

1.8 Aims of this Thesis

The main aim of this thesis was to elucidate information regarding the catalytic mechanism of hydrogen production by [FeFe]-hydrogenases. Investigations were particularly focussed on gaining evidence for the existence, electronic structure and activity of a super-reduced state of the H-cluster. Additionally the reaction of these hydrogenases with various inhibitors (CO, O_2 and HCHO) was investigated, revealing information about their potency as inhibitors and their mechanism of reaction. This understanding is important when considering the uses of hydrogenases (and their synthetic analogues) in technical applications, as described above, where the presence of such inhibitors may be unavoidable. In Chapters 3 and 4 the reactions of three structurally diverse [FeFe]-hydrogenases *Ca*HydA, *Dd*HydAB and *Cr*HydA1 with

the inhibitors carbon monoxide (CO) and formaldehyde (HCHO) were investigated using protein film electrochemistry. Carbon monoxide is known to be a competitive inhibitor of [FeFe]-hydrogenases, targeting the same binding site as H_2 and for this reason it is a good probe of the catalytic mechanism.

In Chapter 3 the effect of illumination on enzyme catalysis and stability was studied, in addition to the potential dependence of light activated CO release. Electrochemical experiments are also presented performed at very low potentials to probe catalysis of [FeFe]-hydrogenases under these conditions, and gain information about the generation and activity of the super-reduced state. A detailed investigation of the potential dependence of CO inhibition was also conducted in this chapter.

In Chapter 4 experiments to probe the potential dependence of inhibition of [FeFe]-hydrogenases by formaldehyde were carried out over a wide potential range. This inhibitor is also thought to bind at the H-cluster, and the strong potential dependence of inhibition provides insight into the nature of reduced states of these enzymes.

In Chapter 6 the development and use of spectroscopic techniques, including infrared (IR), electron paramagnetic resonance (EPR) and nuclear magnetic resonance (NMR) are described. These techniques were used in order to study the different redox states of [FeFe]-hydrogenases and their reaction with formaldehyde.

Chapter 2

Experimental Theory and Experimental Methods

2.1 Experimental Methods

2.1.1 Introduction to Protein Electrochemistry:

Early electrochemical studies on enzymes involved the use of redox mediators (small, redox-active molecules) to shuttle electrons between an electrode and a redox protein. These studies were limited by the slow diffusion of the protein and mediator to the electrode, and by the high protein concentration required. In 1977 Hill[121] and Kuwana[122] demonstrated the use of electrodes modified with electron donor/acceptor groups, which allowed the voltammetry of cytochrome *c* to be studied without the use of mediators in solution. In 1989 the high protein concentration requirement was eliminated by the development of protein film electrochemistry (PFE) by Armstrong *et al.*[123-125] The technique of PFE involves the direct absorption of very small quantities of redox proteins to the surface of an electrode to form an enzyme 'film'.

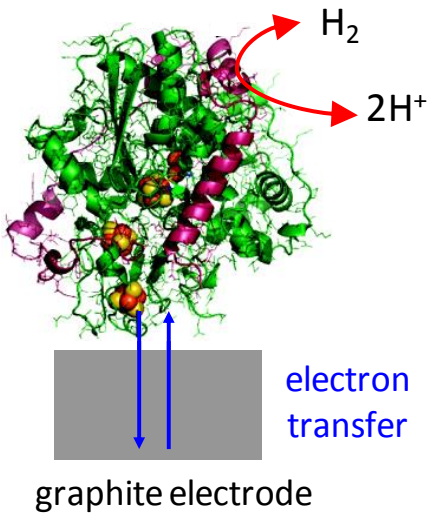

Figure 11: Cartoon illustrating the concept of protein film electrochemistry for hydrogenase adsorbed to a graphite electrode.

In a PFE experiment the immobilised enzyme is effectively wired to the electrode; the electrons can be exchanged between the electrode and protein without the use of mediators and the recorded current is a direct measure of the catalytic turnover rate of the enzyme. There are many benefits of using PFE over traditional solution protein electrochemistry; however the technique does present some limitations.

Benefits:

- The rate of interfacial electron transfer between the electrode surface and the enzyme is very high, meaning that the enzyme can be probed with considerable precision; the oxidation state of the entire enzyme sample can be changed instantly by a change in the applied potential.
- Proteins containing redox centres with potentials outside the range accessible to mediators can still be studied.
- The protein requirement is very low; studies are carried out with less than a picomole of enzyme adsorbed to the electrode, compared to more than nanomole quantities required for spectroscopic techniques such as EPR.
- The enzyme is immobilised on the electrode meaning that:
  - (i) the voltammetry is not complicated by diffusion effects of enzyme in solution.
  - (ii) it is possible to study the reversibility of reactions with inhibitors simply by solution or gas exchange.

Limitations:

- The protein must have an acceptor (redox centre or relay) within the electron tunnelling distance (~14Å) of the enzyme surface and must be immobilised on the

electrode in an orientation that brings this acceptor in to close proximity of the electrode surface.

- There must be good surface interactions between the protein and the electrode surfaces to facilitate adsorption of the enzyme film.

2.1.1.1 Electrode Surfaces and Enzyme Binding

There are many factors to consider when deciding upon an electrode material, most importantly good conductivity. It is of great importance that the electrode is chemically inert over the potential range of study and does not exhibit redox signals that would mask those of the protein under investigation. The material must interact favourably with the enzyme surface, ideally facilitating strong adsorption without causing any denaturation of the protein. Both carbon and gold electrodes have been widely used for PFE studies, however carbon electrodes have been utilised in this thesis as the surface does not require modification for enzyme adsorption, and carbon is chemically inert over a larger potential window (-1 to +0.7 V *vs.* SHE).[126]

2.1.1.1.2 Pyrolytic Graphite

One of the most abundant allotropes of carbon is graphite, of which there are a number of forms varying in density and degree of order. Pyrolytic graphite (PG) is formed by heating hydrocarbons to their decomposition temperature, when the graphite crystallises. It comprises a series of ordered layered graphene sheets, with some covalent bonds between the layers caused by imperfections in the production process. The layered structure means that there are two distinct orientations, basal (PGB) and edge (PGE) as shown in Figure 12. The PGB plane runs parallel to the plane of aromaticity, whereas PGE plane surfaces are formed by cutting

the graphite in such a way that the layers of graphite lie perpendicular to the surface. The edge plane surface is therefore more reactive than basal plane due to the severed bonds created by cleaving perpendicular to the plane of aromaticity. Many enzymes will adsorb directly onto PGE surfaces but not to PGB surfaces, due to the greater density of acidic C-O functional groups on the PGE surface. These acidic functionalities are generated by oxidation of the unsaturated carbon centers formed by graphene ring cleavage. Electrons flow parallel to the graphene sheets via delocalised p-orbitals.

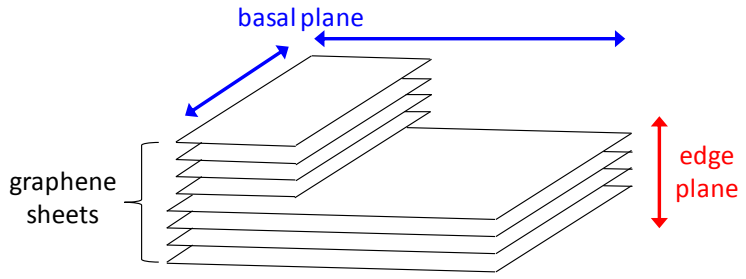

Figure 12: Schematic diagram of pyrolytic graphite, showing the basal and edge planes.

2.1.2 The Three-Electrode System

In a simple two-electrode system, as electrons are passed between a working electrode and the adsorbed protein active site, a potential difference is set up between the electrode/solution interface, $\Delta\Phi_{e/s}^{work}$. This can be monitored by reading the potential difference between the working electrode and a reference electrode for which the $\Delta\Phi_{e/s}$ is known. The applied voltage *E* can then be defined:

$$E = \Delta\Phi_{e/s}^{work} + \Delta\Phi_{e/s}^{ref} + iR \qquad [1.01]$$

The term *iR* describes the drop in voltage in the solution caused by resistance to the passage of electrons between the electrodes through the solution. The current (*i*) can be measured as a function of $\Delta\Phi_{e/s}^{work}$.

In a three electrode system, employed when *iR* is large, the current flows between the working electrode and a third, counter electrode. The potentiostat functions by maintaining the potential of the working electrode at a constant level with respect to the reference electrode by adjusting the current at the counter electrode. The potential of the working electrode, relative to that of the reference electrode, is monitored using a device with a high internal resistance, so that the current drawn through the reference electrode remains negligible, and its potential remains constant.

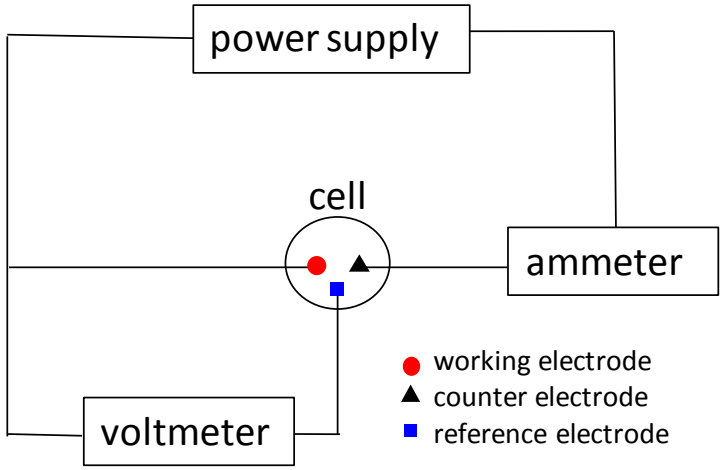

Figure 13: Schematic diagram showing the three-electrode system.

2.1.3 Cyclic Voltammetry

In cyclic voltammetry (CV) experiments the working electrode potential is varied linearly versus time at a set scan rate. In contrast to linear sweep voltammetry, once the set potential is reached, the potential scan is reversed. This can be done multiple times in a single experiment. The current flowing at the working electrode is plotted against the applied potential to give the CV trace or 'scan'. The current recorded in a cyclic voltammogram is made up from both Faradaic and non-Faradaic components.

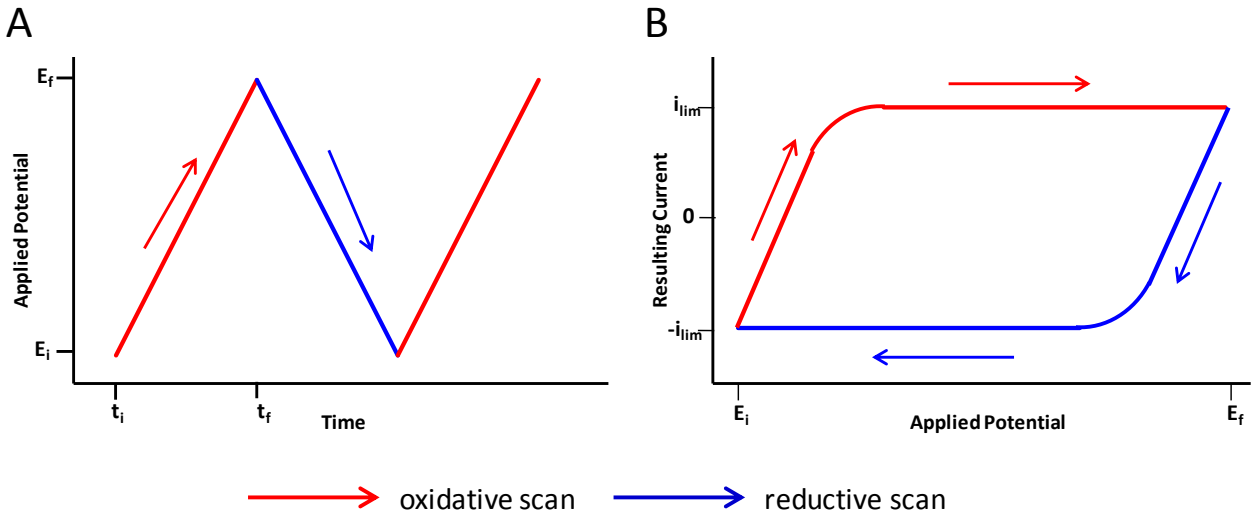

Figure 14: (A) The variation in applied potential (between E_i and E_f) with time. (B) The non-Faradaic current produced by a blank, unmodified pyrolytic graphite edge-plane rotating disk electrode, as a function of potential over the same range.

Cyclic voltammetry is often employed when studying proteins using PFE; information can be gathered about the potential at which processes occur.

2.1.3.1 Non-Faradaic Current

Non-Faradaic current arises from non-redox processes at the electrode, and in cyclic voltammetry appears as a background current. The current arises from polarisation of the solution at the electrode surface. The electrode-solution interface behaves as a capacitor, for which charge (q) is governed by Equation 1.02:

$$q = CE \qquad [1.02]$$

where C = capacitance and E = the potential across the capacitor.

At a given potential there is a charge on the electrode surface (q^M), representing an excess or deficiency of electrons, and a charge in the solution (q^S), caused by an excess of either anions or cations in a thin layer close to the electrode surface. This layer is formed due to favourable

electrostatic interactions between the charged electrode and electrolyte ions. The two charges are equal and opposite ($q^M = - q^S$) and there is a potential difference established across the two layers of charge. As the potential is modulated in a cyclic voltammogram there is rearrangement of the charges at the electrode-surface interface, resulting in current flow.

The current (*i*) is equal to the change in charge with time (dq/dt):

$$i = \frac{dq}{dt} = C\frac{dE}{dt} = C\vartheta \qquad [1.03]$$

In a cyclic voltammogram the change in potential with time (dE/dt) is simply the scan rate (υ). This non-Faradaic current is recorded in a control scan on a bare graphite electrode and is known as a 'blank' scan. The appearance of the blank scan depends on a number of factors, including the scan rate, surface area of electrode, potential range scanned and the composition of the cell solution.

2.1.3.2 Faradaic Current

The Faradaic current arises from oxidation or reduction of a redox-active species, caused by the donation of electrons to, or the withdrawal of electrons from, the electrode. These processes are governed by Faraday's law: the amount of chemical reaction caused by the flow of current is proportional to the amount of electricity passed. This is the current contribution of interest during a PFE experiment; a potential is applied which induces a current to flow, this current provides a direct measure of the catalytic activity of the enzyme.

2.1.4 Enzyme Electrochemistry

In PFE the enzyme molecules are adsorbed directly to the electrode surface and electrons are transferred between the electrode surface and the enzyme molecule. The Faradaic current

measured can be limited by several processes as shown below (Figure 15Figure 15), any of which can be rate limiting.

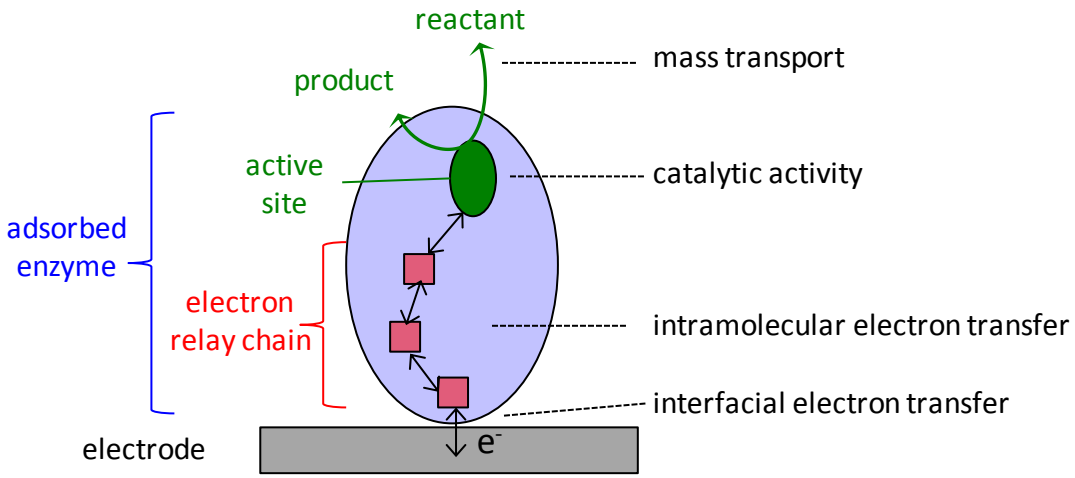

Figure 15: Cartoon showing an adsorbed enzyme molecule on a carbon electrode. The flow of electrons between the electrode, enzyme and active site are shown by arrows and the processes that limit catalysis are labelled.

Each of the processes can be considered as a resistor, the total resistance (R_{tot}) being the sum of each.

(i) Electron transfer (**R_{ET}**)

- Interfacial: between the electrode surface and the enzyme relay chain
- Intramolecular: between the electron relay chain and the active site

(ii) Catalytic turnover (**R_{cat}**)

(iii)Mass transport (**R_{trans}**), of reactant molecules *to* the enzyme, and of product molecules *away*.

$$R_{tot} = R_{ET} + R_{cat} + R_{trans} \qquad [1.04]$$

2.1.4.1 Electron Transfer

Usually the rate of intramolecular electron transfer (between an FeS-cluster relay chain and the active site) is extremely rapid[25], and contributes little to the total resistance, making catalytic turnover at the active site the rate limiting step within the enzyme. Interfacial electron transfer has also been shown to be rapid in many cases.[22,127] The potential dependence of the rate of electron transfer can be modelled by the Butler-Volmer equation, which is based on transition-state theory. For the system:

$$O + ne^- \underset{k_{ox}}{\overset{k_{red}}{\rightleftharpoons}} R$$

where O and R are oxidised and reduced species that are interconverted by the transfer of n electrons from the electrode. k_{ox} and k_{red} are the 1st order rate constants for the oxidation and reduction processes at the electrode surface. The current recorded is dependent on the electrode surface area (A), flux of reactant molecules to the electrode surface (j), and the charge being transported (represented by Faraday's constant, F).

$$i_{ox} = FAj_{ox} \qquad i_{red} = FAj_{red} \qquad [1.05]$$

$$i_{tot} = i_{ox} - i_{red} \qquad [1.06]$$

The flux can be represented as:

$$j_{ox} = nk_{ox}\Gamma_R \qquad j_{red} = nk_{red}\Gamma_O \qquad [1.07]$$

where Γ_O and Γ_R are the electroactive coverages of the oxidised or reduced species per unit area and *n* is the number of electrons. Substituting these expressions for flux into Equation 1.06 gives:

$$i_{tot} = nFA[k_{ox}\,\Gamma_R - k_{red}\,\Gamma_O] \qquad [1.08]$$

Transition state theory assumes that an activated complex (transition state) is formed from the reactants before the product is produced. This transition state is assumed to be in equilibrium with the reactants, with equilibrium constant $K^{\neq}$. Using $\Delta G^{\neq}=-RTlnK^{\neq}$, transition state theory predicts the rate of reaction to be:

$$k = A_p \exp\left(\frac{-\Delta G^{\neq}}{RT}\right) \qquad [1.09]$$

where A_p is a constant pre-exponential factor and $\Delta G^{\neq}$ is the Gibbs free energy of activation.

At equilibrium (potential = E_{eq}), zero current flows. For a reaction to be induced and current to flow a different potential must be applied; the difference between the applied potential and the equilibrium potential is known as the overpotential (η), $(E-E_{eq}) = \eta$. The rate of electron transfer increases exponentially with overpotential and also depends on the transition coefficient (α), which is a measure of the sensitivity of the transition state to the applied potential ($0 < \alpha < 1$).

The rates of electron transfer can therefore be expressed:

$$k_{red} = A_p \exp\left(\frac{-\Delta G^{\neq}}{RT}\right) \exp\left(\frac{-\alpha n F(E - E^{\theta})}{RT}\right) \qquad [1.10]$$

[1.11]

$$k_{ox} = A_p \exp\left(\frac{-\Delta G^{\neq}}{RT}\right) \exp\left(\frac{(1-\alpha)nF(E-E^{\theta})}{RT}\right)$$

These equations can be simplified by defining the pre-exponential terms as $k_{0,ox}$ and $k_{0,red}$:

$$k_{red} = k_{0,ox} \exp\left(\frac{-\Delta G^{\neq}}{RT}\right) \exp\left(\frac{-\alpha nF(E-E^{\theta})}{RT}\right) \quad [1.12]$$

$$k_{ox} = k_{0,red} \exp\left(\frac{-\Delta G^{\neq}}{RT}\right) \exp\left(\frac{(1-\alpha)nF(E-E^{\theta})}{RT}\right) \quad [1.13]$$

Under standard equilibrium conditions $k_{0,ox} = k_{0.red} = k_0$ and $k_{0,ox}$ and $k_{0,red}$ are potential independent. Equations 1.12 and 1.13 can be substituted back into the expression for current (Equation 1.08) to give:

$$i_{tot} = nFA\left[k_0 \Gamma_R \exp\left(\frac{(1-\alpha)nF(E-E^{\theta})}{RT}\right) - k_0 \Gamma_O \exp\left(\frac{-\alpha nF(E-E^{\theta})}{RT}\right)\right] \quad [1.14]$$

At equilibrium $i = 0$, therefore:

$$nFAk_0 \Gamma_R \exp\left(\frac{(1-\alpha)nF(E-E^{\theta})}{RT}\right) = nFAk_0 \Gamma_O \exp\left(\frac{-\alpha nF(E-E^{\theta})}{RT}\right) = i_0 \quad [1.15]$$

where i_0 is the exchange current, which is the Faradaic current of the oxidation and reduction processes at equilibrium, corresponding to zero *net* current. The Butler-Volmer equation can be obtained by dividing both sides of the above equation by the exponential term, to get values for $nFAk_0\Gamma_R$ and $nFAk_0\Gamma_R$ in terms of i_o, and substituting these into Equation 1.14, giving:

$$i_{tot} = i_0\left[\exp\left(\frac{(1-\alpha)nF\left(E-E_{eq}\right)}{RT}\right) - \exp\left(\frac{-\alpha nF\left(E-E_{eq}\right)}{RT}\right)\right] \quad [1.16]$$

Since: $E - E_{eq} = \eta$

$$i_{tot} = i_0\left[\exp\left(\frac{(1-\alpha)nF\eta}{RT}\right) - \exp\left(\frac{-\alpha nF\eta}{RT}\right)\right] \quad [1.17]$$

This is the Butler-Volmer equation, which is fundamental to electrochemical kinetics.[128] A more detailed expression can be determined using Marcus theory,[129] although this is considerably more complex and unnecessary for the experiments presented in this thesis.

2.1.5 Mass Transport

For the adsorbed enzyme molecules in a PFE experiment to perform catalytic turnover it is vital that reactant molecules are brought to the electrode surface from the bulk solution. It is also important that the product molecules, once formed, are quickly removed. In order for these transport processes to not be a rate limiting step, the electrode is rotated rapidly in solution. The rotation spins the solution outwards from the electrode surface in a radial direction due to centrifugal forces; this movement then draws in fresh solution towards the surface of the electrode, ensuring a constant supply of reactant.

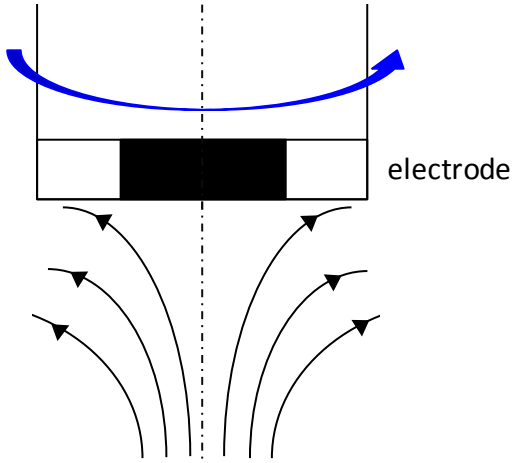

Figure 16 Laminar flow lines at a rotating electrode.

The rotation rate dependence of the transport limited current (*i*) at a rotating electrode is described by the Levich equation[129]:

$$i = 0.62nFAD^{2/3}\nu^{-1/6}\omega^{1/2}[reactant] \qquad [1.18]$$

where *n* is the number of electrons involved in the reaction, *F* is Faraday's constant, *A* is the electrode surface area, *D* is the diffusion coefficient of the diffusing species, υ is the kinematic viscosity of the solution and ω is the rotation rate. As the limited current depends linearly on the square root of the rotation rate, a plot of the transport-limited current against the square root of the rotation rate should give a straight line which passes through the origin. The rotation rate can be increased until a maximum limiting current is reached, *i.e.* the current is no longer limited by mass transport, but is under enzymatic control. At this point the relationship between current and the rotation rate breaks down and is then given by the Koutecky-Levich equation:

$$\frac{i}{i_{lim,\omega}} = \frac{1}{i_{lim}} + \frac{1}{0.62nFAD^{2/3}\nu^{-1/6}\omega^{1/2}[reactant]} \qquad [1.19]$$

where $i_{lim,\omega}$ is the maximum limiting current achieved at rotation speed ω and i_{lim} is the maximum limiting current achieved at infinite rotation rate. The limiting current at infinite rotation speed can be calculated from a plot of $1/i_{lim,\omega}$ against $1/\omega^{1/2}$, which yields a straight line with y-intercept of $1/i_{lim}$.

All PFE experiments in this thesis were carried out with the electrode rotated at high speeds, $2500 < \omega < 3000$ rpm, unless otherwise stated. This speed was sufficient to ensure that the rate of catalysis was under enzymatic rather than mass transport control.

2.1.6 Catalytic Voltammetry

The catalytic current was measured in the PFE experiments in this thesis; reversible electron transfer is coupled to the catalytic oxidation or reduction of substrate by the adsorbed enzyme molecules. The catalytic current response to change in the applied potential is predicted to be sigmoidal.

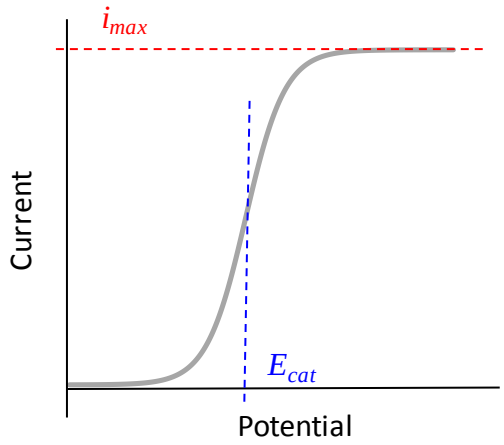

Figure 17: Ideal sigmoidal current trace corresponding to the oxidation of substrate by an enzyme film adsorbed on an electrode.

Initially the current is potential dependent; the rate of catalysis is limited by the rate of electron transfer to form the oxidised state of the enzyme. Enzyme in this state then oxidises substrate, meaning that the current increases with increased driving force

(overpotential). The gradient of the slope is steepest at the catalytic potential (E_{cat}), which corresponds to the potential up to which electron transfer between the enzyme and the electrode surface is rate-determining.

At potentials greater than E_{cat} the current becomes potential independent and plateaus at i_{max}; the rate of electron transfer is no longer rate limiting. When the electrode is rotated fast enough to ensure that mass transport of substrate is also not rate limiting, i_{max} reflects the maximum turnover frequency of the enzyme, ${k_{cat}}^{max}$:

$$i_{max} = nFA\Gamma {k_{cat}}^{max} \quad [1.20]$$

If the electroactive coverage of the enzyme is known, the maximum current can be used to calculate ${k_{cat}}^{max}$.

In some cases, for example the hydrogenase *Dd*HydAB from *Desulfovibrio desulfuricans*, a maximum current is not reached at high potential. As the potential is swept to higher values the enzyme forms an inactive state which cannot oxidise substrate (H_2), and the current actually decreases at high potential. Another reason for deviation from the ideal sigmoidal potential dependence is enzyme dispersion. The enzyme molecules adsorbed on the electrode surface may not be uniformly distributed; there will be a range of enzyme molecule orientations. The rate of interfacial electron transfer will not be the same for all of the molecules; some will be oriented in such a way that electron transfer will be very efficient between the electrode and the active site, whereas others may have very slow electron transfer. This dispersion of electron transfer rates can result in cyclic voltammograms that do not conform to the ideal sigmoidal shape and have residual slope remaining even at high driving forces.

2.1.7 Chronoamperometry

Chronoamperometry (CA) is an alternative method that can be used to study the catalytic activity of enzyme films. In CA experiments the potential of the working electrode is held constant, and the current is measured as a function of time. This technique can be used to study the stability of an enzyme film over time as well as the effect of various conditions, such as cell temperature, substrate concentration, inhibitor concentration and rotation rate, on the catalytic activity of an enzyme film at a particular potential. An example CA experiment is illustrated in Figure 18. The potential is held constant throughout and the effect of an inhibitor is being investigated. Both the extent and the rate of inhibition can be measured, as can the recovery of activity after removal of the inhibitor.

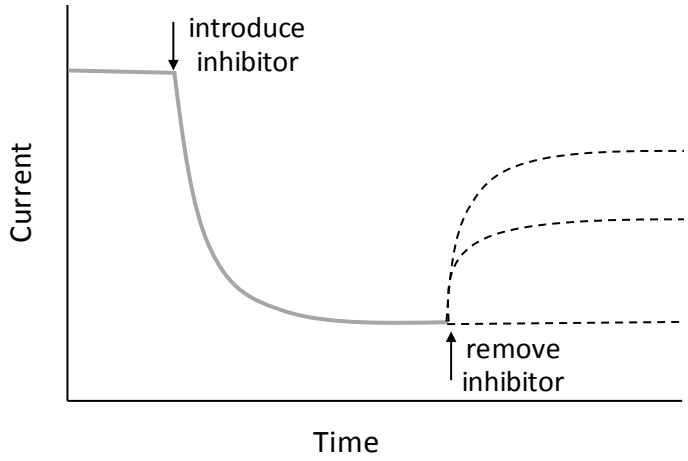

Figure 18: Example chronoamperometry experiment. The potential is held constant throughout the experiment. The effect of the introduction of inhibitor, and subsequent removal, on the catalytic activity is measured.

Several chronoamperometry potential 'steps' can be pieced together in a single experiment to monitor the rate of potential dependent reactions (for example high potential inactivation) by stepping the potential from a value where this process does not occur to a potential where this process is favoured. The applied potential is changed extremely rapidly meaning that the rate of reaction can be determined accurately. In these experiments the contribution of non-

Faradaic current must be considered. As shown in Figure 19, the non-Faradaic current of an unmodified 'blank' electrode peaks immediately upon a change in applied potential, and then decays exponentially. Figure 19 illustrates that the current recorded in the first 10-15 s after a potential step in a CA experiment should be disregarded; the non-Faradaic contribution to the current is significant over this time period.

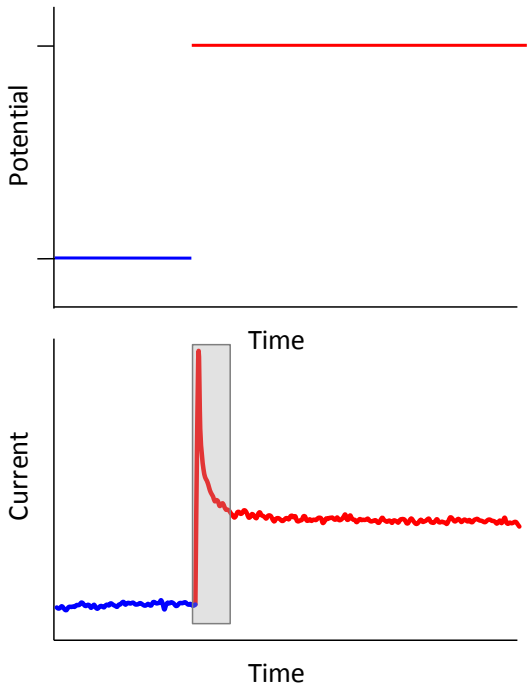

Figure 19: Example potential-step chronoamperometry experiment on an unmodified 'blank' electrode. The grey box shows the 15 seconds after the potential step, where the non-Faradaic contribution to the current is large.

2.1.8 Film Loss

One limitation of PFE experiments on graphite electrodes is the phenomenon of 'film loss'; the gradual decrease in catalytic current in the absence of any change (inhibitor, pH, temperature etc.). This loss can be attributed to several factors, including desorption, denaturation and reorientation of the enzyme molecules on the electrode surface. The progression of film loss is extremely difficult to predict, as the rate and extent varies between enzymes and even between enzyme samples.[130]

For some chronoamperometry experiments in this thesis it was necessary to correct the data for film loss; for example to study the extent of inhibition. In these cases the film loss was fitted to a simple exponential (Equation 1.20) using the Microsoft Excel Solver tool, with the current at time *t* (i_t) dependent on a time constant τ:

$$i_t = (i_{t=0} - i_{t=\infty})exp\left(\frac{t_o - t}{\tau}\right) + i_{t=\infty} \quad [1.20]$$

Figure 20 shows an example chronoamperometry experiment; the raw data is shown on the left, with the exponential fit for film loss overlaid in red. The film loss-corrected, normalised data is shown on the right.

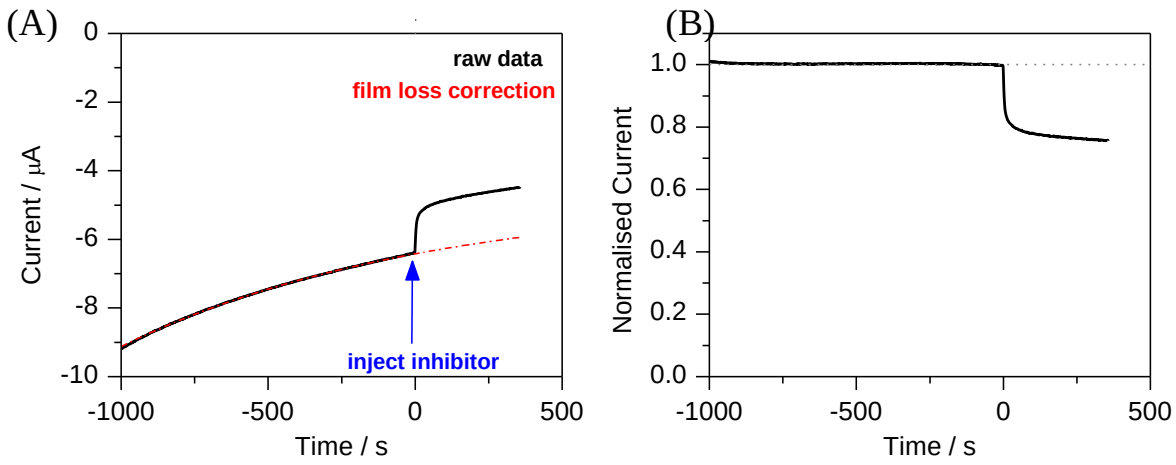

Figure 20: Example chronoamperometry experiment with an inhibitor introduced at t = 0. The raw data is shown in (A), with the exponential fit for film loss overlaid in red. The film loss corrected, normalised current is shown in (B).

Successive scans in cyclic voltammetry experiments can also be corrected for film loss, although this technique is slightly more involved.

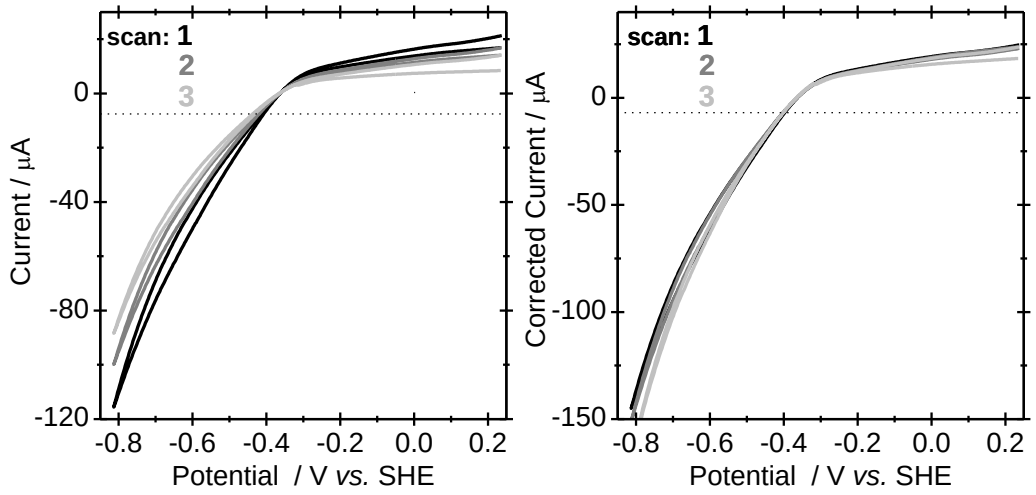

Figure 21: Cyclic voltammograms of *Ca*HydA showing gradual film loss over three successive scans (left) and voltammograms after correction for film loss (right).

2.1.9 Electron Paramagnetic Resonance (EPR)

In electron paramagnetic resonance (EPR) studies the interactions of unpaired electrons in a magnetic field are studied. The energy of an electron with angular momentum, S, in a magnetic field, B_0, is given by the eigenvalues of the spin Hamiltonian according to Equation 1.21:

$$H = g_e \mu_B S B_0 \qquad [1.21]$$

where μ_B is the Bohr magneton (μ_B= 9.274 x 10^{-24} J T^{-1}), and g_e is the proportionality constant for a free electron (g_e= 2.0023).

The interaction of an unpaired electron with a magnetic field is called the Zeeman effect; the magnetic moment (μ) of the unpaired electron acts as a bar magnet when subjected to the magnetic field. The electron can be in one of two orientations with respect to the magnetic field: parallel or anti-parallel. These two states are characterised by the magnetic quantum numbers m_s; for parallel alignment (α state) m_s = +1/2 and for anti-parallel alignment (β state) m_s = -1/2. These two spin states (±1/2) have the same energy in the absence of a magnetic

field, but their energies diverge linearly as the applied magnetic field increases, as shown in Equation 1.22.

$$E = m_s g_e \mu_B B_0 \qquad [1.22]$$

The energy difference (Zeeman splitting) between the two states of an electron in a particular environment is therefore determined by the strength of the magnetic field (Figure 22).

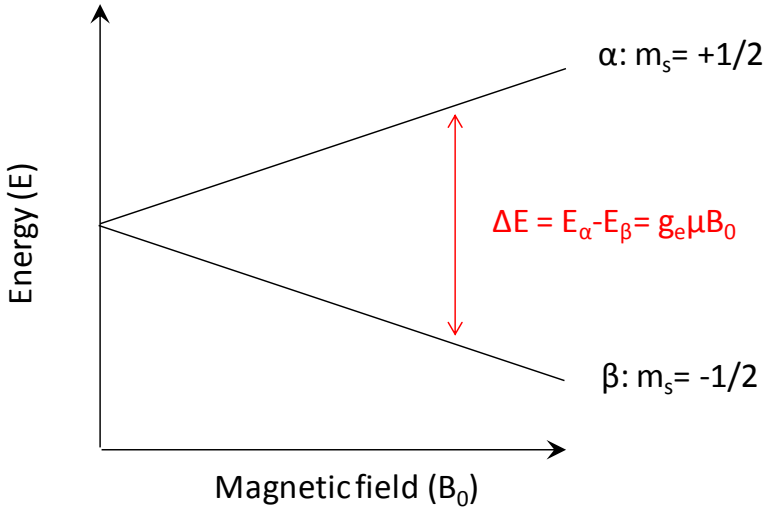

Figure 22: Energies of the spin states of an electron in a magnetic field.

In continuous wave (CW) EPR experiments the allowed transitions between the electron states ($\Delta m_s = \pm 1$) are studied by varying the applied magnetic field (B_0) at a fixed frequency (ν). A peak in the absorption occurs when the magnetic field tunes the two spin states so that their energy difference matches the energy of the radiation, known as the resonance condition. The g value can therefore be determined according to Equation 1.23 where h = Planck's constant:

$$\Delta E = h\nu = g\mu_B B_0 \qquad [1.23]$$

Deviation of g from the free electron value, g_e, in molecular spectroscopy is dictated by the mixing of orbital angular momentum from excited states into the ground state. The g value can therefore give information about the structure around the unpaired electron and the strength of the spin-orbit coupling. When the orientation of the spin changes with respect to the magnetic field, the interaction between the spin and magnetic field is also changes. This anisotropy is best described by defining the g value along each of the three mutually perpendicular axes of the species: g_x, g_y and g_z. For a truly isotropic species the g values would be identical, $g_x = g_y = g_z$ and a single signal observed, whereas a change in symmetry to an axial system causes the signal to split, $g_x = g_y \neq g_z$. When the symmetry of the system is reduced to a rhombic system (no two axes are the same), $g_x \neq g_y \neq g_z$, three signals are seen. In the frozen protein samples studied in this thesis the molecules are randomly oriented with respect to the applied magnetic field. EPR spectra are therefore an average over all possible orientations and are referred to as powder average EPR spectra. Standard EPR spectrometers employ field modulation plus phase sensitive detection to increase sensitivity by filtering out non-resonant noise, a process that results in the first derivative of the absorption being detected as the EPR signal.

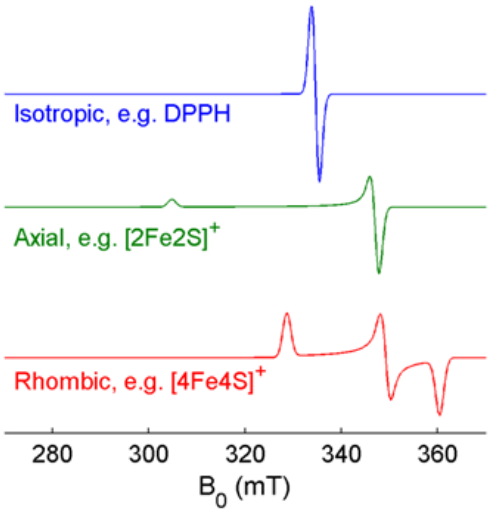

Figure 23: Simulated EPR spectra of examples of 3 systems with different symmetry using $g_{x,y,z} = 2.00$ (DPPH), $g_x = 2.20$, $g_{y,z} = 1.93$ ($[2Fe2S]^+$) and $g_x = 2.04$, $g_y = 1.92$, $g_z = 1.86$ ($[4Fe4S]^+$). (Figure and simulations prepared by Rosalind Davies and reproduced with permission)

2.2 Experimental Methods and Materials

2.2.1 Electrodes

The pyrolytic graphite edge (PGE) working electrodes used in this thesis were constructed in-house as shown in Figure 24.

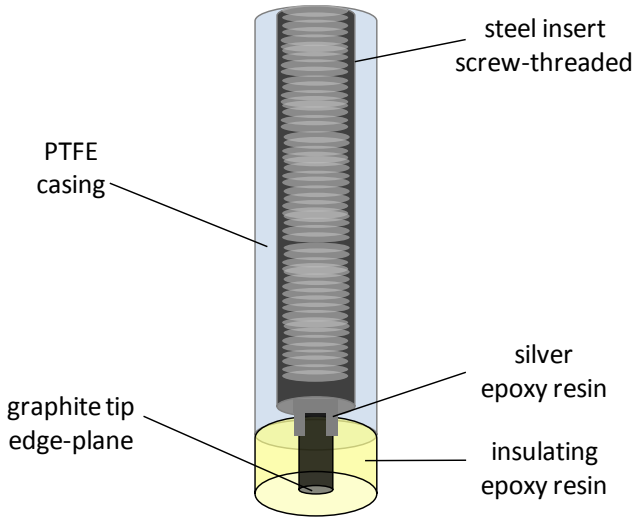

Figure 24: Diagram of the graphite electrodes used in this thesis.

A steel rod is housed within a Teflon (PTFE) casing fitted with a screw thread to allow attachment to a rotator spindle. Pyrolytic graphite was cut into rods and then drilled to form 2 mm diameter (3 mm^2 planar surface area) cylinders with the 'edge' plane as the cross section surface. These graphite cylinders were set into the electrode casing and connected to the steel rod using silver epoxy resin (RS electronics), before being encased in insulating epoxy resin (Robnor Resins). Abrasion of the edge-plane surface, by polishing the electrode with sand paper, damages the exposed graphene rings, creating a polar surface with exposed oxidised functionalities such as -COOH and -CHO, which are thought to enhance the adsorption of enzyme to the surface.[131,132]

2.2.2 Electrode Rotation

The rotating disc electrodes described were used in conjunction with an electrode rotator (EcoChemie Autolab RDE) which fit snugly into the top of the electrochemical cell. In all experiments the electrode was rotated at a constant high rate (> 2500 rpm) to ensure efficient supply of substrate and rapid removal of product from the electrode surface in addition to fast gas-solution equilibration.

2.2.3 Electrochemical Cell

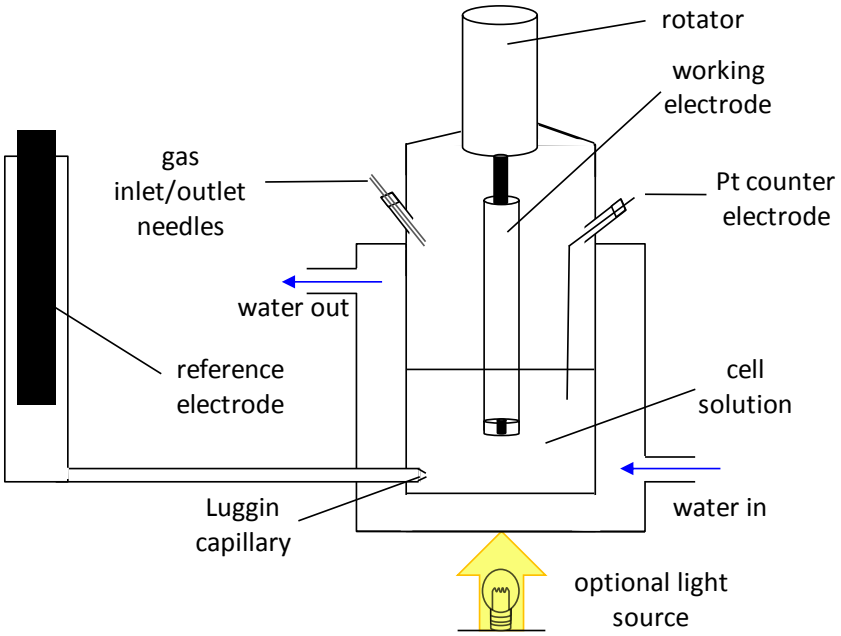

Figure 25: Diagram of the electrochemical cell used in this thesis.

Experiments were carried out using a glass electrochemical cell as shown in Figure 25 (made in-house, Terri Adams). The working electrode compartment contained a platinum wire (counter electrode) and was water jacketed (VWR) to allow temperature control. The sides of the cell were covered in black electrical tape to prevent light-activated processes convoluting catalysis. A saturated calomel reference electrode (SCE) was placed in a side arm containing 100 mM NaCl. The side-arm was connected to the main cell via a Luggin capillary and was not water jacketed, therefore remaining at ambient temperature.

2.2.4 Solution Exchange

In order for the reversibility of aldehyde inhibition to be measured, the buffer solution needed to be exchanged. [Reversibility of inhibition by gaseous molecules was simply measured by flushing the gas out of solution.] A double syringe set up was used, as shown in Figure 24. One syringe was filled with 50 mL of fresh buffer that had been equilibrated to the

experimental temperature and flushed with the experimental gas composition. The two syringes were connected to the electrochemical cell via plastic tubing; the ends of the tubes sat as close to the bottom of the cell as possible, without interfering with electrode rotation.

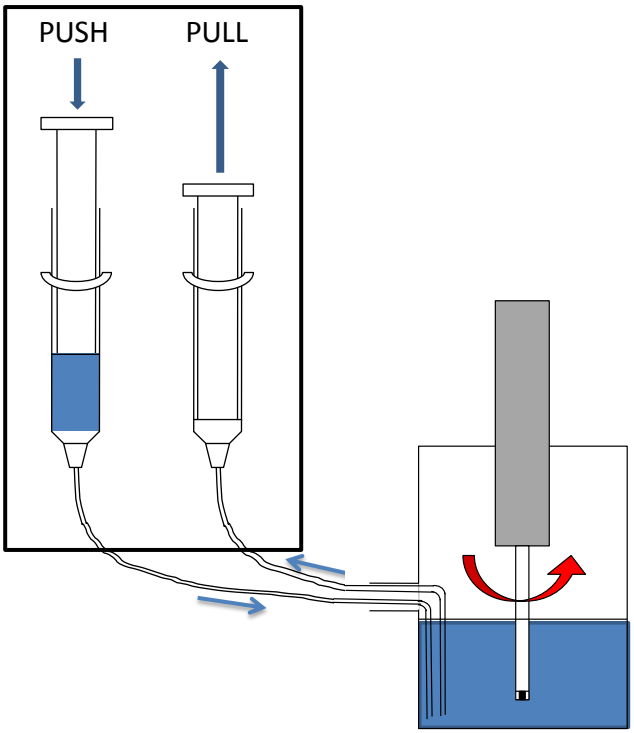

Figure 26: Representation (not to scale) of the pair of syringes used to rinse the electrochemical cell by exchanging the solution with fresh buffer. As fresh buffer was introduced into the electrochemical cell by pushing down on the left-hand syringe, buffer was simultaneously removed from the cell by pulling the right-hand syringe.

To exchange the cell solution (on average 2-5 mL) the full syringe was depressed to push fresh buffer in to the cell, while the empty syringe was pulled to remove the cell solution. Care was taken to keep the solution level above the tip of the electrode at all times to ensure that electrical connection was maintained. A typical cell solution volume of 4 ml was used, and exchanged with 50 ml of fresh buffer.

2.2.5 Light Experiments

A 300 W projector lamp was used in light studies and was situated directly beneath the electrochemical cell to directly illuminate the surface of the electrode. The cell was positioned 2 cm above the lamp, with a UV and IR filter placed in between as shown in Figure 26.

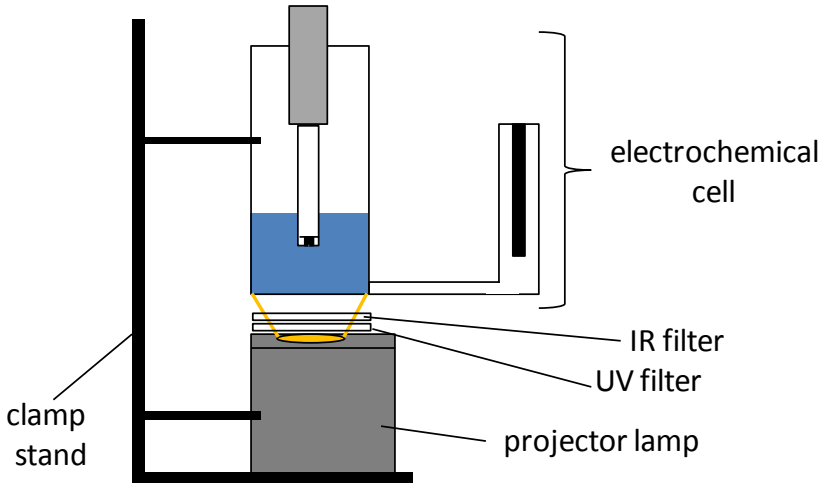

Figure 27: Diagram of the light set up used in illumination experiments.

2.2.6 Glove Box

Due to the high O_2 sensitivity of hydrogenases, all hydrogenase electrochemistry experiments were carried out in an anaerobic glove box (Belle) comprising a N_2 atmosphere ($[O_2]$ = < 3 ppm) unless otherwise stated.

2.2.7 Measurement

Electrochemical experiments were performed using an electrochemical analyser (Autolab PGSTAT20) controlled by NOVA 1.5 software (EcoChemie). Potentials are quoted relative to the standard hydrogen electrode (SHE) using the correction:

$$E_{SHE} = E_{SCE} + E_{CORR} \qquad [1.24]$$

$$E_{CORR} = 0.2412 - 6.61x10^{-4}(T-25) - 1.75x10^{-6}(T-25)^2 - 9.0x10^{-10}(T-25)^3 \quad [1.25]$$

where T = temperature in degrees centigrade.

2.2.8 Solutions

Phosphate buffer solutions consisting of 50 mM phosphate with 100 mM NaCl as additional supporting electrolyte were prepared by titrating solutions of NaH_2PO_4 and Na_2HPO_4 (analytical reagent grade, Sigma) in purified water (Millipore 18 MΩ cm) to the desired pH (Russell 950 from Fisher). Solutions were thoroughly degassed before use; initially flushed with inert gas (N_2) to remove O_2 prior to being taken into the glove box and stirred open to the glove box atmosphere to remove any traces.

2.2.9 Gas Flow

Gas was passed through a water bubbler before being flowed through the cell headspace via inlet/outlet needles. Mass flow controllers (Smart-Trak Series 100, Sierra Instruments) were used to prepare precise gas mixtures (accurate to within 1%) and to provide constant gas flow rates through the electrochemical cell headspace during experiments. The feedstock gases were H_2 (Premier grade, Air Products), N_2 (Oxygen-free, BOC), CO (BOC, CP Grade) and O_2 (Air Products). The high purity of gases used is critical, as very small traces of common contaminants such as O_2, CO and H_2S can inhibit hydrogenases and affect the electrochemistry. For experiments involving injections of saturated solutions of inhibitor gases Henry's Law constants were used to calculate the dissolved gas concentrations.

The Henry's constant (k_H) of a gas is a measure of the solubility of that gas. The solubility of a gas in solution is dependent on the solution temperature; the constant C is a coefficient representing the temperature dependence of k_H. In this thesis the concentration of gases in

solution was calculated using the following equation for the molar concentration of a saturated solution:

$$[gas] = k_H . exp\left\{C\left(\frac{1}{T} - \frac{1}{298}\right)\right\} \quad [1.26]$$

where T is the solution temperature in Kelvin. The Henry's constants (k_H) and temperature coefficients (C) are given in Table 1 for the gases used in this thesis.

Table 1: Values of k_H and C for various gases.

Gas	k_H	C
H_2	0.00078	500
O_2	0.0012	1700
CO	0.00099	1300
N_2	0.00061	1300

2.2.10 Enzyme Samples

Samples of *Dd*HydAB were prepared by Christine Cavazza under the supervision of Juan Fontecilla-Camps at the CNRS Grenoble, France, using a previously published protocol.[42] Samples of the bacterial [FeFe]-hydrogenase *Ca*HydA and the algal hydrogenase *Cr*HydA1 were prepared by Sven Stripp and Camilla Lambertz under the supervision of Thomas Happe at the Ruhr University, Germany, using previously published protocols.[47]

2.2.11 Enzyme Films

To prepare each enzyme film the PGE electrode was first polished with P400 sandpaper to create a fresh surface, and then wiped with cotton wool. 1.5 µL of enzyme solution was

applied to the prepared electrode surface and removed by rinsing with water after approximately 1 minute. The electrode was then placed into enzyme-free buffer in the electrochemical cell ensuring that the experiment was not complicated by the effects of solution enzyme-electrochemistry. Enzyme films were activated before experiments were commenced. The [FeFe]-hydrogenases require very little activation; several cyclic voltammograms in the presence of H_2 is sufficient. For [NiFe]-hydrogenases the electrode was held at a reducing potential (-0.6 V) for several hundred seconds in the presence of H_2 before a cyclic voltammogram was performed to check the activity. These steps were repeated until the activity stopped increasing and successive voltammograms overlaid.

2.2.12 Formaldehyde Solutions

The aldehyde inhibition experiments carried out in this thesis involved injection of solutions of aldehyde in buffer into the electrochemical cell. These aldehyde solutions were gas and temperature equilibrated before use, to avoid any changes in enzyme catalysis relating to differences in temperature of H_2 concentration. Formaldehyde is supplied as a 37% aqueous solution (ACS reagent, 37 wt % in H_2O, containing 10-15% methanol, Sigma-Aldrich), equating to a concentration of 13.4 M. This solution was stored in a fume hood to limit laboratory exposure to this harmful volatile chemical; aliquots were taken into the glove box in vials sealed with a rubber septum. Due to the volatility of formaldehyde degassing was passed through a water bubbler to limit the rate of formaldehyde evaporation from solution and was carried out for the minimum time required to remove all traces of O_2. Typically the experimental gas mixture (often 100% H_2) was bubbled through 10 ml of formaldehyde solution for 10 minutes at a flow fast rate. This formaldehyde solution was then diluted using similarly degassed buffer. A vial of this diluted formaldehyde solution was then placed in a water bath to equilibrate to the experimental temperature, before being injected into the cell.

2.2.13 EPR Experiments

2.2.13.1 Sample Preparation

Samples were prepared in an anaerobic glove box to prevent damage by oxygen. The enzyme was reduced by H_2 in a small glass electrochemical cell comprising a platinum working electrode and an Ag/AgCl reference electrode as shown in Figure 28, allowing the open circuit potential to be measured. Gases were passed through an oxygen scrubber and a water bubbler before entering the cell to ensure gas quality and to avoid sample evaporation.

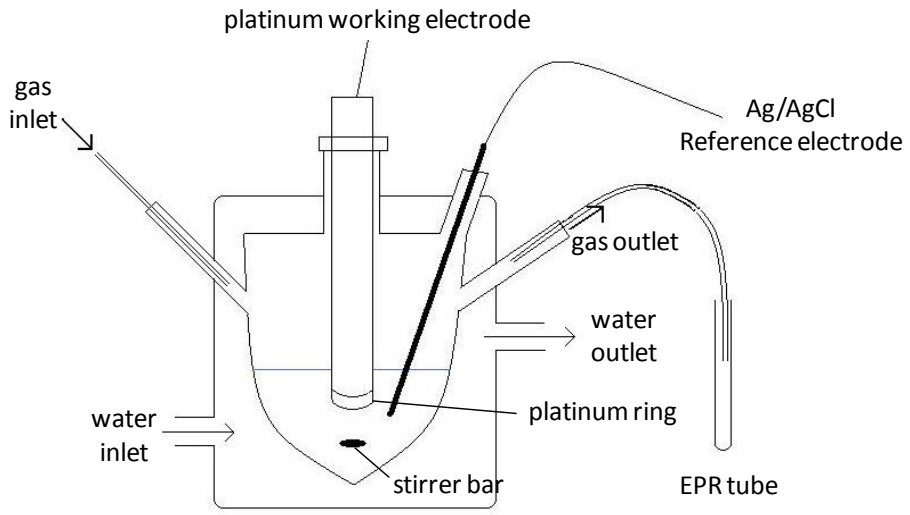

Figure 28: Diagram of the EPR cell used for sample preparation.

The cell was water jacketed for temperature control and stirred using a magnetic stirrer bar and plate. Samples were 'shot' into the EPR tube using a positive gas pressure and thin metal tubing; one end of the gas outlet tube was placed inside the EPR cell while the other was placed below the level of the solution. The EPR tube was then immediately frozen using a cold finger and then stored in liquid nitrogen.

2.2.13.2 Measurements

Continuous wave EPR experiments were performed using an X-band (9-10 GHz) Bruker EMX spectrometer (BrukerBioSpin GmbH, Germany) with an X-band Super High Sensitivity Probehead (Bruker) equipped with a low temperature helium flow cryostat (Oxford Instruments CF935A).

Chapter 3

Carbon Monoxide Inhibition

Abstract

The photolability of the Fe-CO bond formed by CO inhibition of [FeFe]-hydrogenases is well documented. In this chapter the effect of illumination on the recovery of hydrogenase activity after CO inhibition was investigated using protein film electrochemistry. The extent of illumination induced recovery was found to be similar for the hydrogenases from three different organisms, and almost completely potential independent. Illumination of un-inhibited enzyme was shown to be strongly potential dependent; at low potentials the enzyme was irreversibly damaged but at high potentials it appears that illumination stabilises the enzyme film on the electrode, and may induce enzyme activation.

Two active states of the H-cluster are well characterised, H_{ox} and H_{red}, while a third, super-reduced state remains the subject of much scientific debate. In this chapter electrochemistry experiments were utilised to probe the H_2 production activity of [FeFe]-hydrogenase at low potentials (< -0.7 V). It was found that all three remain active and undamaged under these conditions, indicating that the super-reduced state is active at H_2 production, stable and is formed reversibly.

Binding of carbon monoxide (CO) is known to compete with that of H_2, making it a good probe of the catalytic mechanism of H_2 turnover by [FeFe]-hydrogenase. Experiments were performed to probe the CO reaction at very reducing potentials. These experiments revealed the formation of a state at low potential, assigned as the super-reduced state, which rapidly releases the bound CO to regenerate active enzyme. Formation of this state is demonstrated for three different hydrogenases, however the potential of CO release varies between the enzymes. [FeFe]-hydrogenases are known to be extremely sensitive to irreversible oxygen (O_2) damage at oxidising potentials. Electrochemistry experiments revealed that in addition to CO, the super-reduced state of the H-cluster has a very low affinity for O_2. It was found that

[FeFe]-hydrogenases demonstrate a remarkable tolerance to high (100%) O_2 levels at low potential (-0.65 V).

3.1 Introduction

3.1.1 Catalytic States of [FeFe]-Hydrogenases

The various oxidation states experienced by the Fe atoms in the H-cluster of [FeFe]-hydrogenases have been described in section 1.5.2. The catalytically active oxidised state (H_{ox}) and reduced state (H_{red}) have been well characterised using various techniques (such as X-ray crystallography and IR and EPR spectroscopy[59,83]) while the existence and role of a super-reduced state of the H-cluster remains the subject of much scientific discussion and has not yet been well characterised. The super-reduced state (H_{sred}), purported to be formed under strongly reducing conditions,[82,86,87] is thought to result from a one electron reduction of the H_{red} state (or a two electron reduction of H_{ox}). The location of this additional electron has not yet been determined, it is possible that either Fe_p, Fe_d or the $[4Fe4S]_H$ cluster is reduced. Several different resonance structures of the H_{sred} state could exist with different protonation states, as shown below in Scheme 3. To avoid ambiguity super-reduced states are referred to as being at the H_{ox-2} oxidation level.

Despite the importance for understanding how H_2 is produced so efficiently by [FeFe]-hydrogenases, mechanistic detail from experiments is lacking, mainly due to the difficulty of identifying transient, strongly reducing intermediates in a very rapid catalytic cycle (turnover frequency >> 1000 s^{-1})[133,134] involving a sole ubiquitous substrate (H_{aq}^+). In order to be studied, a state must persist for a reasonable amount of time; states that exist only transiently cannot be well characterised. A unique feature of using PFE is the ability to measure catalytic activity (directly as current) as a continuous function of electrode potential:

it can therefore identify potential boundaries between intermediates differing in oxidation level but remaining at steady state during the catalytic cycle.

Scheme 3: Four of the possible states of the H-cluster at the H_{ox-2} oxidation level (H_{sred}), formed by one electron reduction of the H_{red} state. Protonation of the bridgehead N atom is also possible for each of the structures shown.

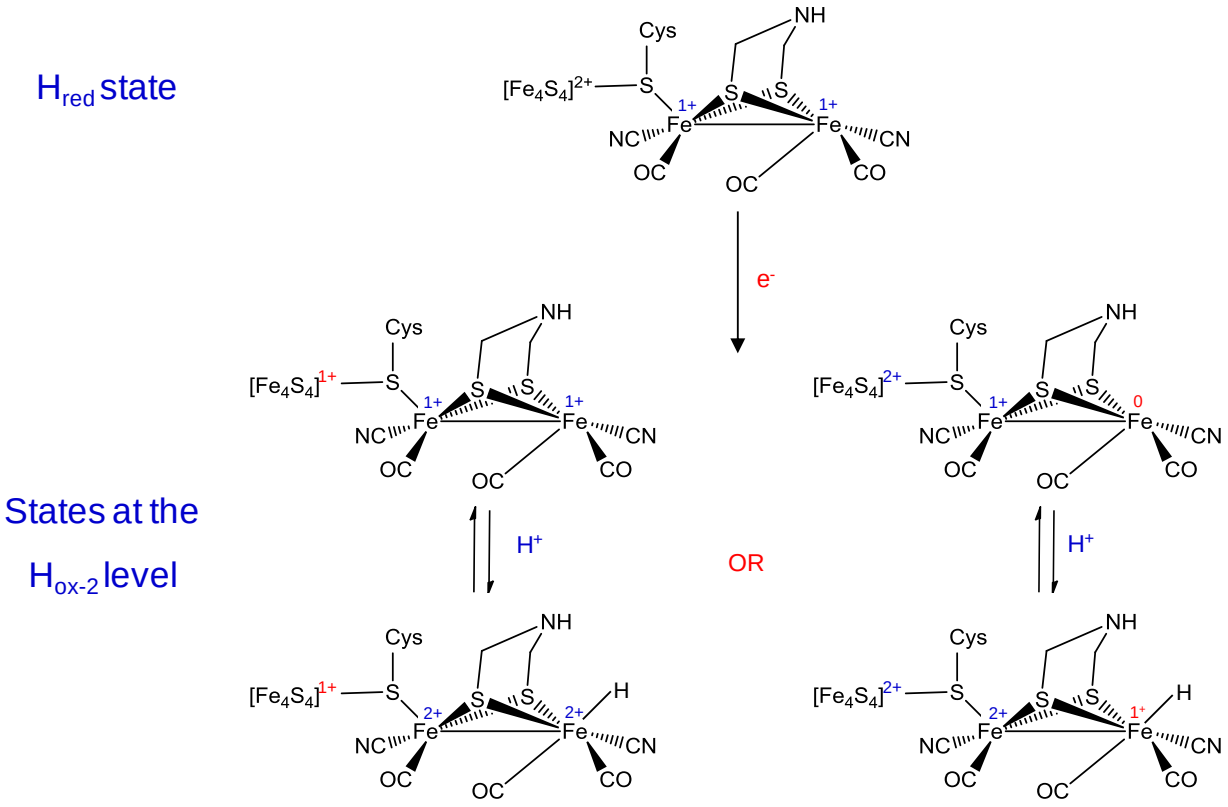

Most studies of [FeFe]-hydrogenase suggest that only the two well characterised active states of the H-cluster, H_{ox} and H_{red}, are stable enough to be intermediates in the catalytic cycle, and in most cases the role of the [4Fe4S] moiety of the H-cluster is not considered.[58,59] It has been suggested that this site plays the role of providing or removing sufficient electrons to the $2Fe_H$ moiety of the H-cluster in order to catalyse the two-electron reaction of either H_2 production or oxidation. The mechanism of proton reduction by [FeFe]-hydrogenases has been investigated extensively using DFT,[88,92,93,135-137] with several studies including the

involvement of a state of the H-cluster at the $H_{ox\text{-}2}$ oxidation level (H_{sred}), however experimental evidence for the role of this state remains lacking. DFT calculations carried out by Greco and co-workers,[93] where the [4Fe4S] cluster domain was included in the model (shown in Figure 29), show that the driving force for H_2 production by a hydride at the $H_{ox\text{-}2}$ oxidation level (H_{sred}) is exothermic, while the corresponding reaction at the $H_{ox\text{-}1}$ level (H_{red}) is an endothermic process. The additional driving force at the $H_{ox\text{-}2}$ level (H_{sred}) relative to the $H_{ox\text{-}1}$ level (H_{red}) is consistent with the anticipated higher electron density on the hydride (greater hydridicity).

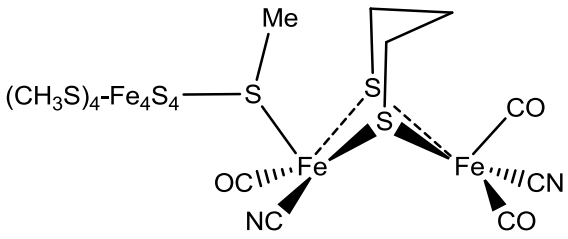

Figure 29: H-cluster model used in calculations by Greco and coworkers.[93] The [4Fe4S] moiety is included, but the bridgehead nitrogen has been omitted from the dithioloate bridge.

3.1.2 Small Molecule Inhibition of [FeFe]-Hydrogenase

The catalytic activity of [FeFe]-hydrogenases is inhibited in the presence of various small molecules. The future of hydrogenases as catalysts in technology requires comprehensive understanding of the chemistry of these enzymes, in particular how and why inactivation occurs. In some instances inhibition is reversible (eg.CO[76,138]), while for others activity is completely lost and is not regained upon removal of the inhibitor (eg.O_2[98]). In many cases the extent and reversibility of the inhibition varies between hydrogenases from different organisms, and is also very dependent on the catalytic state of the H-cluster, as influenced by the applied potential. The presence of these inhibitors, even in very small quantities, must be taken into account when considering the use of these enzymes for practical applications.

Gaining understanding of both the mechanism and conditions under which [FeFe]-hydrogenases interact with inhibitors is of vital importance when considering the use of these enzymes in technical applications such as those described in Chapter 1. For example, sulfide is a common contaminant of H_2 produced commercially by steam reformation;[8] for hydrogenases to be utilised in processes that use H_2 as a fuel (such as enzymatic fuel cells) only those that are resistant to inhibition by sulfide under the conditions used in such a device can be considered. Additionally enzymatic fuel cells couple the activity of a hydrogenase to the reduction of O_2,[112] meaning that the hydrogenase used must be able to catalyse H_2 oxidation in the presence of O_2 without undergoing inactivation. Similarly the hydrogenase used to generate H_2 from protons in the graphite particle system developed to carry out the water-gas shift reaction[120] ($CO + H_2O \leftrightarrow CO_2 + H_2$) described in Chapter 1 must be resistant to inhibition by CO.

Another reason to study small molecule inhibition of [FeFe]-hydrogenases is the understanding that can be gained about the different redox states of the hydrogenase. The mechanism of catalysis of [FeFe]-hydrogenases is not yet fully understood. Many inhibitors bind at the distal iron site, in a similar manner to H_2. Studying the interaction of these inhibitors with the H-cluster provides insight into how [FeFe]-hydrogenases are able to catalyse H_2 cycling.

Greater understanding of the mechanisms of enzyme catalysis and inhibition is also advantageous when designing synthetic analogues. This information can also be used to design complexes that exhibit similar high rates of H_2 cycling to hydrogenases, but avoid the sensitivity to inhibition by other molecules, making them more suited to technical applications.

3.1.2.1 Hydrogen

Although H_2 is the substrate for H_2 oxidation by hydrogenases, it is an inhibitor of H_2 production. The extent of this inhibition varies for [FeFe]-hydrogenases from different organisms[76,139] ranging from < 5% for *Ca*HydA (from *Clostridium acetobutylicum*) to ~20% for *Cr*HydA1 (from *Clamydomonas reinhardtii*) and > 30% for *Dd*HydAB (from *Desulfovibrio desulfuricans*). In all cases product inhibition is much less severe than for most [NiFe]-hydrogenases;[140] [FeFe]-hydrogenases exhibit very high H_2 production activity even in the presence of 100% H_2.[81]

3.1.2.2 Oxygen

Both [FeFe]-hydrogenases[98] and some [NiFe][64] are known to be extremely sensitive to inactivation by O_2, a huge drawback for their utilisation in artificial photosynthesis and other 'biohydrogen' production techniques. The [FeFe]-hydrogenases are particularly sensitive to O_2 and the active oxidised state, H_{ox} (see Figure 6), undergoes irreversible degradation to form a 'dead' state.[98] The initial reaction of O_2 at the H-cluster is thought to be very similar to that of CO; binding is reversible and competitive with H_2, occurring at the distal iron site preferentially to enzyme in the oxidised state of the H-cluster (H_{ox}).[141] The irreversible reaction is attributed to the generation of a reactive oxygen species at the distal iron site, which then damages the [4Fe4S] cluster by either long range oxidation or migration, forming a $[3Fe4S]^+$ cluster,[141] and is followed by complete O_2-induced degradation of the remaining H-cluster.

[FeFe]-hydrogenases can exist in a highly oxidised inactive state, H_{ox}^{inact} (formed electrochemically at potentials greater than 0 V[76,77]), which does not react with O_2 and therefore acts as a 'resting' state that provides protection from this inhibitor.[22] It has been proposed by Bruska *et al.*[142] that this is because formation of a reactive oxygen species is not

energetically feasible for O_2 bound to the H_{ox}^{inact} state. For this reason certain [FeFe]-hydrogenases, such as *Dd*HydAB, can be purified aerobically in the H_{ox}^{inact} state.[42]

Electrochemistry experiments performed by Goldet *et al*.[98] have revealed that the tolerance of [FeFe]-hydrogenases to O_2 is strongly potential dependent; at oxidising potentials (-0.3-0 V), where the hydrogenase catalyses H_2 oxidation, inhibition is rapid, almost complete, and totally irreversible. At a mildly reducing potential (-0.4 V), where the hydrogenase catalyses H_2 production, some activity is retained, and inhibition is partially reversible.[98]

3.1.2.3 Sulfide

Sulfide is a common trace contaminant in H_2 produced by steam reformation and has been shown to reversibly inhibit [FeFe]-hydrogenases.[143] Protein film electrochemistry experiments have shown that the oxidised state of the hydrogenase *Dd*HydAB reacts reversibly with sulfide, but only reactivates at very low potentials.[143] Sulfide can be used to protect the enzyme against irreversible damage by O_2, as enzyme in the sulfide-inhibited state does not react with O_2, indicating that they compete for the same binding site (Fe_d).[143]

3.1.2.4 Carbon Monoxide

Inhibition of [FeFe]-hydrogenase by carbon monoxide (CO) has historically been the subject of extensive study; various techniques, such as EPR[144-146], crystallography[147,148] and infrared spectroscopy[82,83,85] have been utilised, and it has been determined that CO is a reversible inhibitor that competes with H_2 for binding at the H-cluster. There is significant evidence to suggest that exogenous CO binds preferentially to the oxidised form of the H-cluster[86] (yielding the H_{ox}-CO state), at the distal iron site in a position trans to the μ-CO ligand as shown in Figure 30.[147]

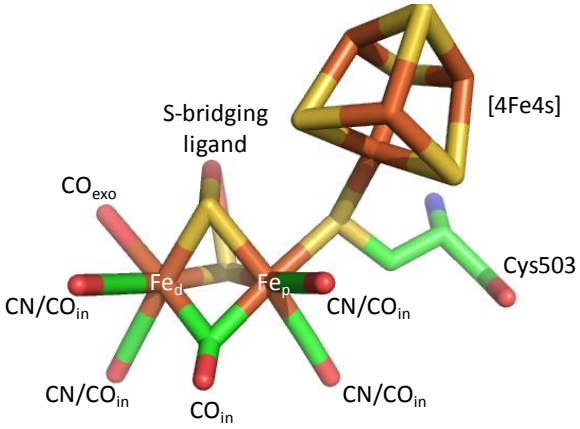

Figure 30: Structure of the CO-inhibited H-cluster of *Cp*I prepared using PyMOL. (PDB code: 1C4C)[147] The intrinsic CO (labelled CO_{in}) and CN ligands have not been assigned in the crystal structure. The exogenous CO ligand is labelled CO_{exo}. The bridging S-ligand was modelled without the $–CH_2-$ groups connecting the bridging S atoms to the bridgehead heteroatom (red).

Further understanding the mechanism of CO inhibition of [FeFe]-hydrogenases is of great interest due to the competitive nature of the binding. Carbon monoxide competes directly with H_2, making it a good probe for investigating the mechanism of catalytic H_2 turnover.

Although formation of the H_{ox}-CO state has been reported for [FeFe]-hydrogenases from various organisms, they do not all show the same change in electron spin density distribution after binding CO.[149,150] Different shifts in the vibrational frequency for the CN^- ligands upon CO binding have been measured for the [FeFe]-hydrogenases *Dd*HydAB[82], *Cr*HydA1[85] and *Cp*I.[151] These variations can be attributed to differences in the protein environment surrounding the conserved H-cluster; there may be differences in H-bonding between the CN^- ligands and surrounding residues.

Both electrochemical techniques and solution assays have been used to study the potential dependence and reversibility of CO inhibition of [FeFe]-hydrogenase.[76,77,138] These studies were performed on [FeFe]-hydrogenases from several different organisms and although the overall protein structures and FeS-cluster electron relay chains vary among the enzymes

(section 1.4.2), the H-cluster is conserved in all. Electrochemical studies have shown that exposure to CO at high potential results in rapid loss of H_2 oxidation activity, and H_2 production activity is also inhibited at low potential (-0.4 V).[76,77] EPR studies have shown that exposure of the reduced state of the enzyme to CO results in formation of the H_{ox}-CO state.[146] It is not clear whether inhibition of H_2 production activity at reducing potentials proceeds via a CO-bound reduced state (H_{red}-CO) or if CO directly traps the oxidised state which is formed transiently during H_2 turnover. Protein film electrochemistry experiments performed by Goldet *et al.*[76] showed that CO inhibition of H_2 oxidation activity is reversible, but inhibition of H_2 production is slower, and only partially reversible. The study involved the three structurally distinct hydrogenases *Ca*HydA, *Dd*HydAB and *Cr*HydA1. The rate and extent of CO inhibition was investigated using chronoamperometry experiments such as those shown in Figure 31 for *Ca*HydA, (this experiment was repeated and verified for this thesis to confirm experimental procedures). Both the rate and extent of inhibition were found to decrease in the order *Dd*HydAB > *Cr*HydA1 > *Ca*HydA for both H_2 oxidation and proton reduction activity, but there was little difference measured for the rate of recovery upon removal of CO.[76]

The potential dependence of CO inhibition of *Ca*HydA is shown clearly in the chronoamperometry experiments in Figure 31. Hydrogen oxidation activity was recorded at +0.15 V and H_2 production activity at -0.55 V, before introduction of 810 μM CO at t = 0 by injection of CO saturated buffer (arrow). The CO concentration then rapidly decreased as it was flushed from solution by the constant flow of 100% H_2 through the cell headspace. Both the rate and extent of inhibition are greater for H_2 oxidation (compare blue and black traces in Figure 31C); at +0.15 V 100% of H_2 oxidation activity is lost in 10 s, with a half life of just 3 s (blue), compared to the loss of 96% of H_2 production activity in 100 s at -0.55 V, with a half life of 15 s (black).

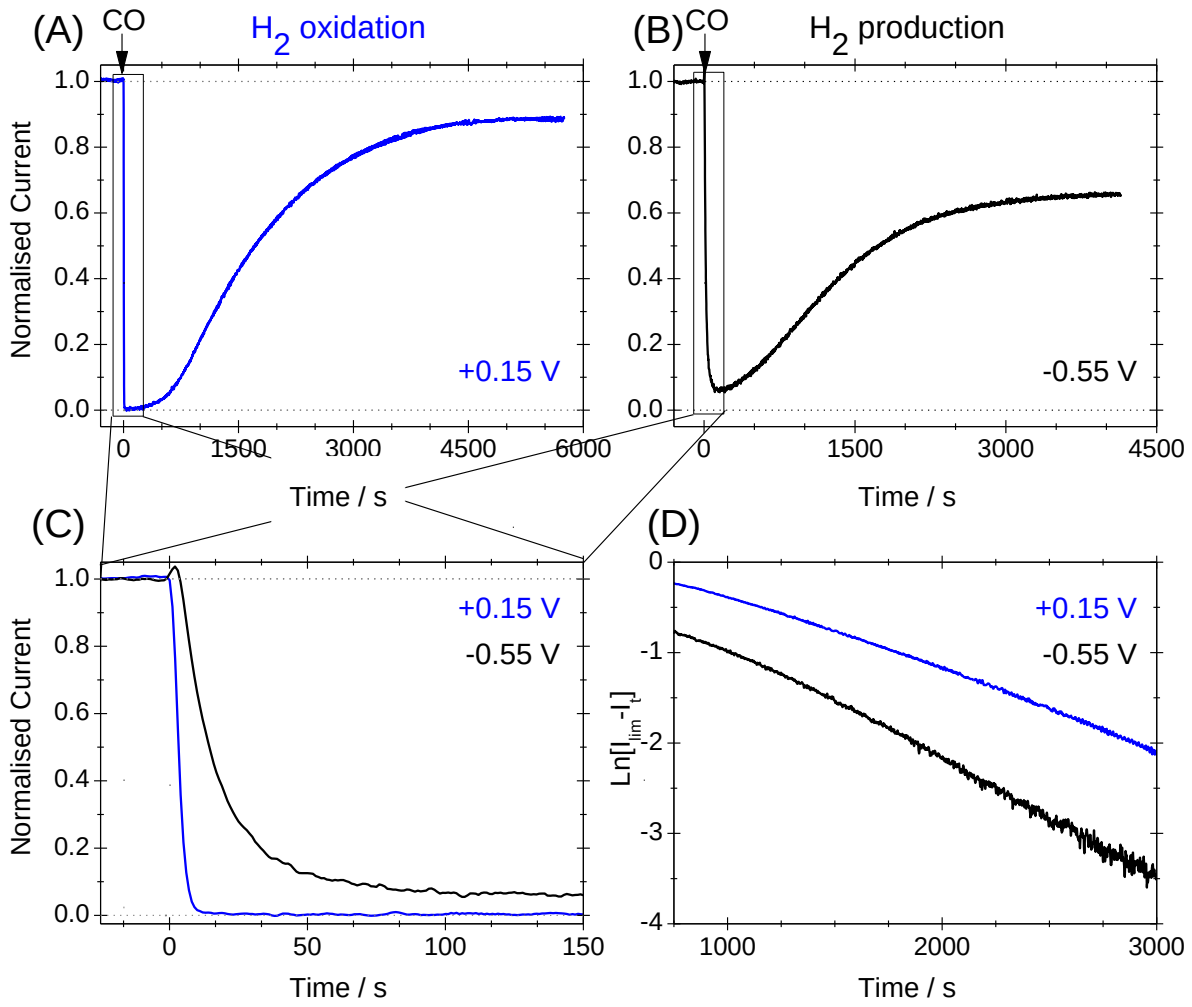

Figure 31: Chronoamperometry experiments showing CO inhibition and subsequent recovery of catalytic activity of *Ca*HydA. Experiments were recorded at +0.15 V to measure H_2 oxidation (A) and at -0.55 V to measure H^+ reduction (B) Panel C shows an expanded section around t = 0, comparing the rate and extent of inhibition at +0.15 V(blue) and -0.55 V (black). Buffer saturated with CO (3 mL) was injected into 2 mL of cell solution at t = 0, giving a total CO concentration of 810 µM. This concentration then immediately decreased as CO was continuously flushed out of solution by the gas flow (1000 mL/min). The cell headspace was flushed with 100% H_2 continuously throughout the experiment. Log plots of the current from experiments A and B are shown in panel D for t > 750 s. Conditions: dark, 5 °C, pH 6 phosphate buffer, ω = 3500 rpm, 100% H_2. Similar experiments were conducted by Goldet *et al.*[76] and were repeated and verified for this thesis to confirm experimental procedures.

The reversibility of inhibition is also strongly potential dependent; the H_2 oxidation activity recorded at +0.15 V is almost completely recovered (90%) after removal of CO (Figure 31A), whereas only ~60% of the H_2 production activity measured at -0.55 V was recovered (Figure 31B). The rate of recovery from CO inhibition was compared by performing log transformations (Figure 31D, Appendix 2) on the latter part of the chronoamperometry

experiment where the activity (current) is recovering after CO has been completely flushed from solution. The first 750 s after CO injection are not considered to ensure the measured rate is not complicated by the flushing of CO from solution and inhibition is not still taking place. The rates are given by the gradient of the plots which are not significantly different for each potential and run almost parallel (gradient = $1x10^{-3}$). In this experiment therefore the rate of recovery from inhibition is not dependent on potential.

The preference for CO binding to the H_{ox} state (Figure 31C) can be rationalised by looking at the valence electron count of the distal iron atom as shown in Scheme 4.

Scheme 4: The reaction of CO with the H-cluster. The oxidation states of Fe_p and Fe_d, as determined by spectroscopy, [59,83] are given above, and the overall 1- charge of the cluster is indicated in the figure. The valence electron count for Fe_p and Fe_d in each state is given below in blue.

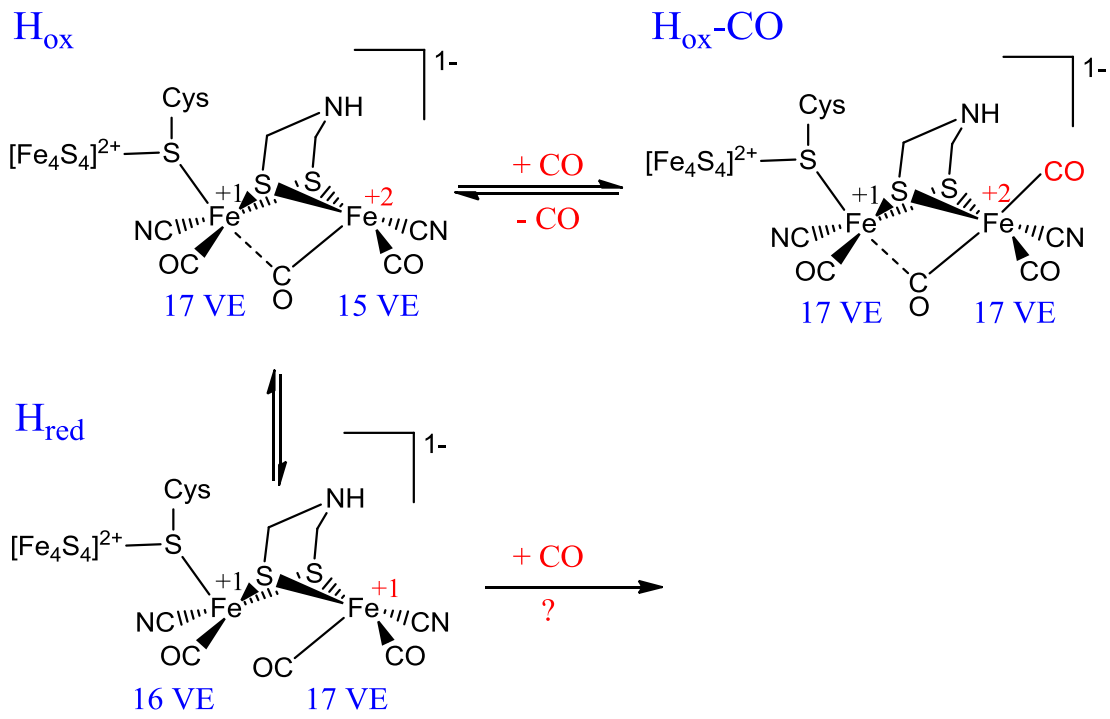

In the H_{ox} state Fe_d is in the +2 oxidation state, and is coordinated to one bridging CO, one terminal CO, one terminal CN, and two bridging sulfur ligands. The electron count of Fe_d is therefore 15 and the binding of exogenous CO is favourable as it brings the electron count to 17. The 18 valence electron rule dictates that metal complexes containing 18 valence

electrons are the most thermodynamically stable, as this maximises the number of electrons in bonding orbitals.[31] More than 18 electrons means electrons are entered into orbitals of non- or anti-bonding character, which results in a less stable complex. In the reduced state (H_{red}), Fe_d is one electron more reduced than in H_{ox}, and the bridging CO ligand moves to a terminal position on Fe_d, giving an electron count of 17. The binding of CO (donates 2 electrons) to Fe_d in this state is therefore disfavoured, as electron density is added to orbitals with anti-bonding character, destabilising the complex.

3.1.2.4.1 Reversibility of CO Inhibition

The small degree of irreversible enzyme damage observed after exposure of [FeFe]-hydrogenases to CO at low potentials[76] (Figure 31B) was investigated by Baffert *et al.* using both electrochemistry and DFT analysis.[152] Their findings are illustrated in Scheme 5; upon binding exogenous CO the valence electron count of Fe_d exceeds 18 and it is suggested that at least one bond will subsequently break.

Scheme 5: The reaction of CO with reduced states of [FeFe]-hydrogenase as calculated by Baffert *et al.*[152] The valence electron count for Fe_p and Fe_d in each state are given below in blue.

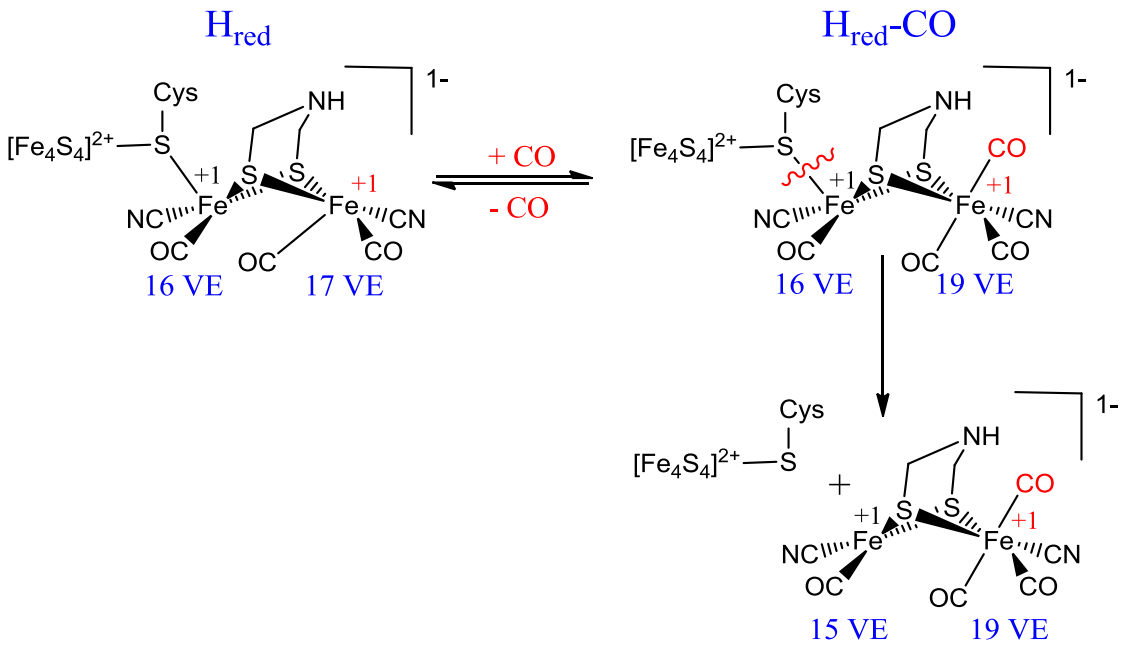

The calculations[152] determined that bonding of CO to the H_{red} state is exothermic (ΔE = -17.3 kcal/mol) and results in lengthening of the Fe_p-S_{cys} bond by more than 0.5 Å, indicating cleavage of this bond. The bond breakage is irreversible, accounting for the observed irreversible loss of enzyme activity. The reaction of H_{red} with CO is favourable (exothermic) because CO is a better ligand for Fe(I) than the S_{cys} ligand, meaning that the Fe-CO bond formed during the reaction is stronger than the Fe-S bond that is broken. EPR experiments however, have shown that inhibition of hydrogenase under reducing conditions results in formation of the H_{ox}-CO state[146] and an H_{red}-CO state has not been isolated experimentally.

Calculations for binding of CO to a super-reduced state[152], with the additional electron residing on the [4Fe4S] cluster ($[4Fe4S]^{+}$Fe(1)Fe(1)), showed that the CO bound H_{sred}-CO complex was stable, although the H_{sred} state has a very low affinity for CO. Chronoamperometry experiments performed by Baffert *et al.*[152] showed that after introduction of a high concentration of CO (385 μM) at a mildly reducing potential (-0.46 V) a step to a more reducing potential (-0.76 V) for 120 s resulted in a slight activation of the enzyme (release of CO), thought to be caused by the formation of a CO bound super-reduced state of the enzyme.

3.1.2.4.2 Photolability of the Fe-CO Bond

The photosensitivity of Fe-carbonyl bonds is a well documented characteristic and the photoactivity of CO ligands bound to hydrogenases is well documented.[82,138,145-147,153,154] The photosensitivity of the [FeFe]-hydrogenase from *Cp*I was first investigated by Lemon *et al.*[148] using X-ray diffraction; crystals of enzyme in the CO inhibited state were irradiated with a He/Ne laser which resulted in a change in the electron density of the H-cluster at the site where exogenous CO is bound. Recent EPR studies have shown that illumination of the

H_{ox}-CO state of *Dd*HydAB at temperatures below 100 K results in the formation of two EPR active states.[155] The first, denoted H_{L1}, is formed by dissociation of the bridging CO ligand (μ-CO) while the second is the active H_{ox} state, generated by loss of the exogenous CO ligand (Scheme 6). The first process is transient and most likely involves light induced recombination of the μ-CO ligand. The second process is "one-way" with no further conversion, although both states revert back to H_{ox}-CO when the sample is warmed (>150 K). Prolonged illumination of the H_{ox} state did not result in any change in the EPR spectrum[155], showing that the H_{ox} state is stable under light (at < 150 K) and cannot be further converted by illumination. It therefore appears that the μ-CO bond is more stable in H_{ox} than in H_{ox}-CO, possibly because of the excess of charge in H_{ox} due to the vacant open coordination site at Fe_d.

Scheme 6: The possible fates of the H_{ox}-CO state of the H-cluster after illumination at cryogenic temperature[155]: Top: dissociation of the exogenous CO ligand to generate the active H_{ox} state. Bottom: dissociation of the bridging CO ligand to generate the H_{L1} state.

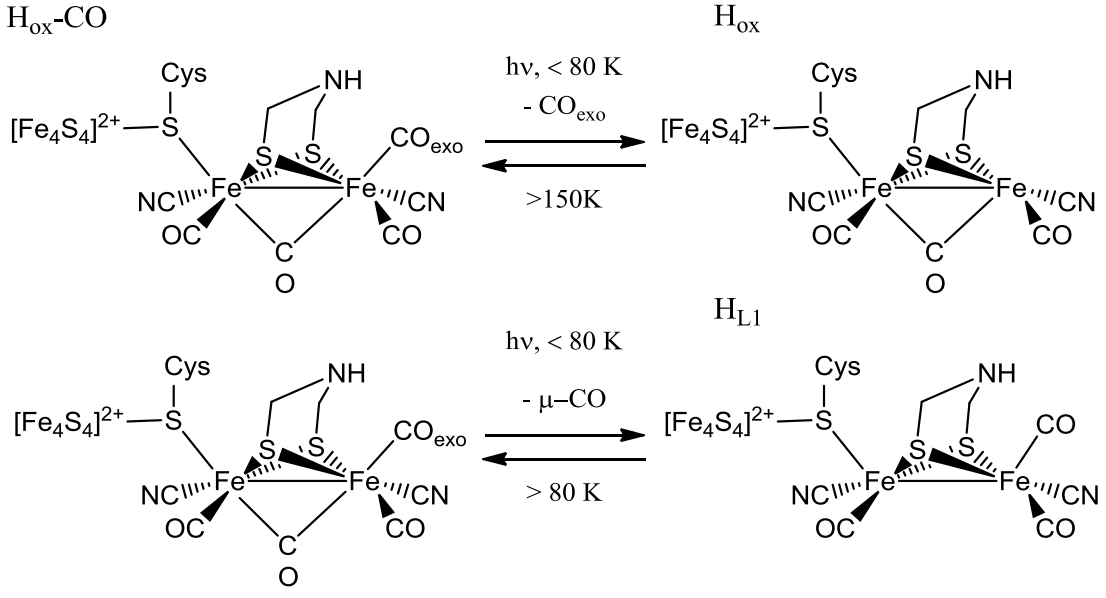

The exogenous CO ligand is terminally bound in a position trans to the μ-CO ligand; the two compete for the back-bonding electrons from Fe_d, making CO_{exo} more chemically labile than the other terminal CO ligands on Fe_d which are positioned trans to sulfur atoms. Dissociation

of the μ-CO ligand in H_{ox}-CO has also been demonstrated in FTIR studies of both *Dd*HydAB[82] and *Cp*I[151] after prolonged illumination, and it was shown that heating the H_{LI} state resulted in regeneration of the H_{ox}-CO state in *Cp*I (Scheme 6, bottom). Although it has been shown that the H_{ox} state is not affected by illumination at cryogenic temperatures[155] EPR experiments[145] have shown that under normal laboratory light (and temperature) conditions, the $[2Fe]_H$ of some enzyme molecules is destroyed. This is attributed to photolysis of the bound CO ligands, and the released CO is able to bind to the H-cluster of active enzyme molecules, explaining the formation of the inhibited H_{ox}-CO state in samples that have never been exposed to CO.[145]

The photosensitivity of the Fe-CO_{exo} bond has also been demonstrated effectively for the [FeFe]-hydrogenases *Ca*HydA and *Cr*HydA1[76] and *Dd*HydAB[77] using the technique of PFE. In both studies chronoamperometry was used to monitor the recovery of H_2 oxidation activity after exposure to CO.

Such an experiment was repeated and the enhancement of H_2 oxidation activity confirmed for *Ca*HydA after exposure to CO (Figure 32). The electrode, with adsorbed enzyme layer, was soaked in CO saturated buffer before the experiment commenced. The potential was held at -0.05 V and the H_2 oxidation current recorded. Yellow boxes denote periods where the electrode was subjected to periods of illumination.

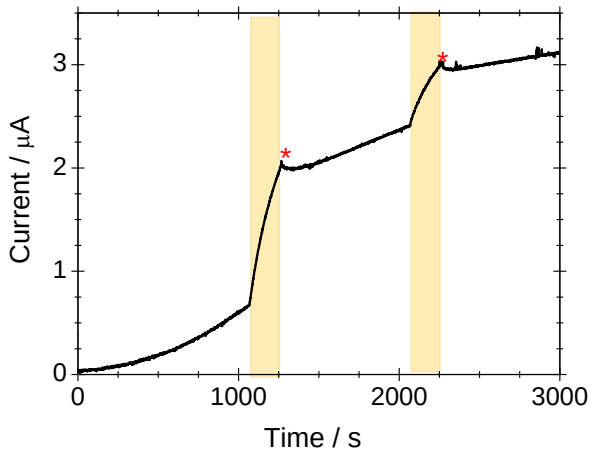

Figure 32: Chronoamperometry experiment showing the effect of illumination on the recovery of H_2 oxidation activity of *Ca*HydA after exposure to CO. Immediately prior to commencing the experiment 450 μM CO was injected into the cell solution. The cell headspace was flushed with 100% H_2 throughout. Conditions: 5 °C, pH 6 phosphate buffer, ω = 3500 rpm, -0.05 V. Yellow shaded regions denote periods of illumination using a 300 W projector lamp, with a UV filter. Red asterisks mark the drop in current upon removal of the light source. Similar experiments were conducted by Goldet *et al.*[76] and were repeated and verified for this thesis to confirm experimental procedures.

Over the course of the experiment shown in Figure 32 CO is flushed out from the electrochemical cell by H_2. This results in an increase in the rate of release of the exogenous CO ligand from the H-cluster due to the shift in the equilibrium caused by removal of CO from solution:

$$H_{ox}\text{—}CO_{exo} \rightleftharpoons H_{ox} + CO_{soln.}$$

This loss of CO from the inhibited H_{ox}-CO state results in the regeneration of the active H_{ox} state, the H_2 oxidation current therefore gradually increases over the course of the experiment. During periods of illumination (yellow boxes) the current dramatically increases as light facilitates the rate of CO_{exo} release (by photolysis of the Fe_d-CO_{exo} bond). Looking at the trace at the point immediately after the light is turned off (Figure 32, asterisk) it can be seen that the current drops sharply, this is thought to result from re-inhibition of the enzyme by CO. The extent of this re-inhibition of *Cr*HydA1 was found to be significantly greater than *Ca*HydA.[76] It is not known whether this re-inhibition is by molecules of CO in the cell solution, or by CO

that remains trapped within the enzyme molecule. A strong potential dependence of Fe_d-CO_{exo} bond photolysis was observed for *Dd*HydAB;[77] an enhancement in the rate of recovery from inhibition was only recorded under illumination at potentials where the enzyme was oxidising H_2, illumination had no effect at potentials where the enzyme was catalysing H_2 production. (The potential dependence has not been studied for *Ca*HydA and *Cr*HydA1).

The enhancement of the rate of recovery from CO inhibition by light strongly suggests that this process is limited by the kinetics of the making or breaking of the Fe_d-CO_{exo} bond rather than transport of CO through the protein molecule. As the H-clusters of *Ca*HydA, *Dd*HydAB and *Cr*HydA1 are all highly conserved, the kinetics of this bond breaking/making are expected to be very similar, explaining the similarity in the rate of recovery from CO inhibition (in the dark) for all three enzymes.[76] The differences in the rate of CO inhibition have been attributed to the existence of a structural barrier/filter for the diffusion of CO into the enzyme, and variations in this barrier between the different hydrogenases.[76]

3.2 Results

3.2.1 Stability in Light

Before further electrochemistry experiments were the carried out to investigate the effect of illumination on the stability of the H_{ox}-CO state of [FeFe]-hydrogenases (photolability of the Fe_d-CO_{exo} bond), control experiments were performed in the absence of CO looking at both the active H_{ox} and H_{red} states. Chronoamperometry experiments were carried out to investigate the effect of illumination (with a powerful (300 W) projector) on the catalytic activity and stability of the enzyme film, shown in Figure 33. The effect of illumination on the H_2 oxidation activity of *Ca*HydA was measured at -0.05 V (Figure 33A) and on the H_2 production activity at -0.55 V (Figure 33B). Experiments were performed in 100% H_2 at 5 °C,

periods of illumination are denoted by yellow shaded boxes. At both potentials studied, the catalytic current steadily decreases throughout the experiment, this current loss is attributed to enzyme 'film loss' (described in section 2.1.8). The phenomenon of 'film loss' can result from one, or a combination of factors including degradation of adsorbed enzyme molecules, reorientation of enzyme molecules on the electrode surface to one less well positioned for efficient electron transfer or the simple desorption of enzyme molecules from the electrode.[126] In Figure 33C and D the current is shown after it has been corrected for initial film loss (before illumination) and normalised. Comparison of the gradient of the current trace in Figure 33C and D during periods of illumination and periods in the dark reveals a significant change. This change in the rate of current loss is not however the same at the two potentials studied.

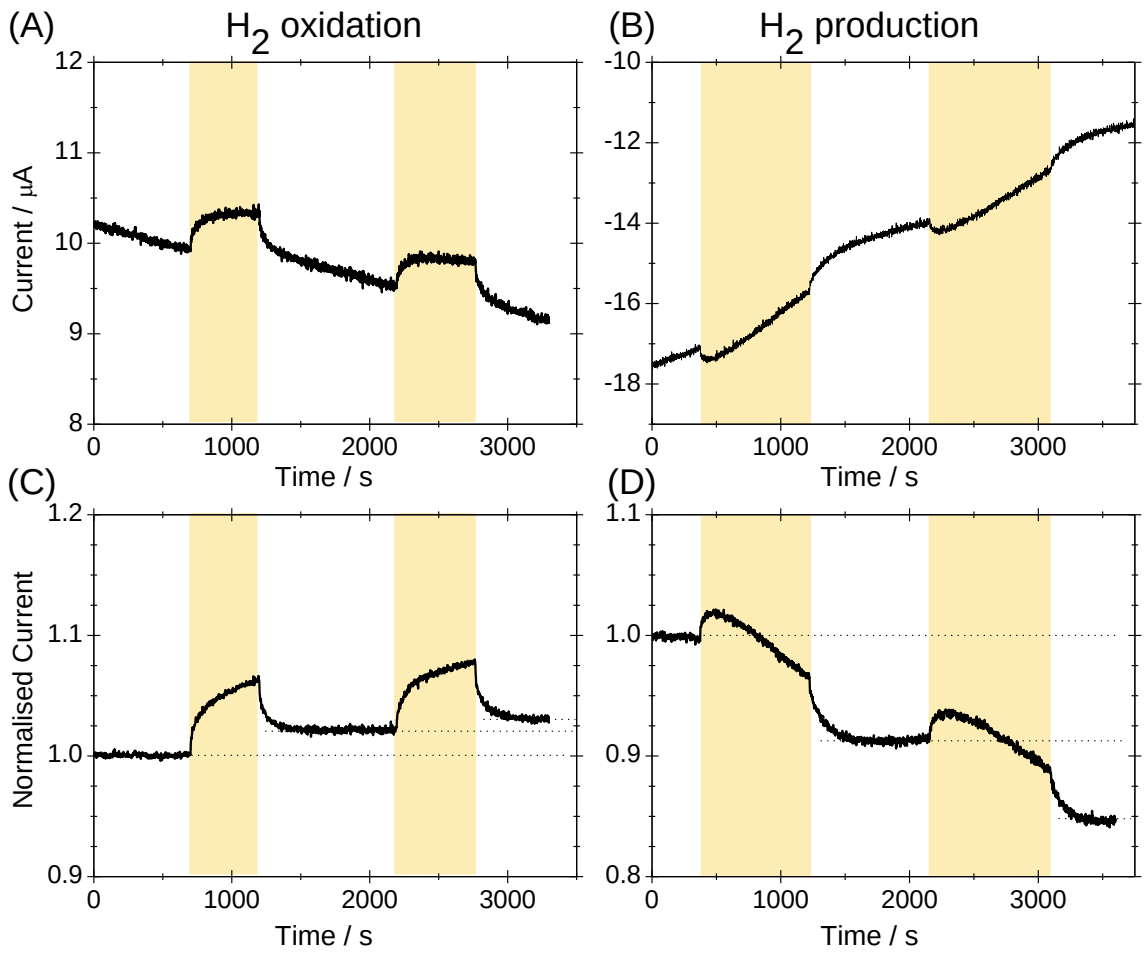

Figure 33: Chronoamperometry experiments comparing the effect of illumination on the activity and stability of *Ca*HydA. Raw data is shown in panels A and B, for H_2 oxidation at -0.05 V (A) and H_2 production at -0.55 V (B). Panels C and D show the data after correction for initial film loss and normalisation. Conditions: 5 °C, pH 6 phosphate buffer, ω = 3500 rpm, 100% H_2, 300 W lamp with UV filter. Dotted lines extrapolate the current during periods in the dark.

During periods of illumination both the H_2 oxidation (positive current, Figure 33A and C) and H_2 production (negative current, Figure 33B and D) activity increase in magnitude; the H_2 turnover reaction is enhanced in the light and by the associated increase in temperature (investigated in section 3.2.2).

Of interest is the effect of illumination on the stability of the enzyme film, most clearly illustrated after the current has been corrected for initial film loss and normalised to 1 at t = 0 (Figure 33C and D). In these two panels the current during periods in the dark is extrapolated

with dotted lines, if the rate of enzyme 'film loss' were to continue at the same rate throughout the experiment the current should return to this same level after each period of illumination (1 or -1).

During H_2 production (Figure 33D) the enzyme film is destabilised during periods of illumination; comparison of the current before the first illumination (t = 0-400 s), to that after (t = 1500-2100 s) reveals a large drop, and the current after illumination is smaller than it was before, dropping from -1 to -0.91. Illumination of the enzyme at this potential (-0.55 V) therefore must damage the enzyme in such a way that when the light source is removed less enzyme molecules remain catalytically active on the electrode surface. This could be due to an increased rate of desorption of the enzyme from the electrode surface or light induced degradation of the enzyme either making it inactive, or less active at H_2 production.

During H_2 oxidation (Figure 33A) the enzyme film is actually stabilised during periods of illumination; comparison of the current before the first illumination (t = 0-700 s), to that after (t = 1500-2100 s) reveals little difference. Similar comparison for the normalised, initial film loss corrected current (Figure 33C) shows that the current is greater after illumination than it was before, increasing from 1 to 1.02. This shows that during illumination at this potential (-0.05 V) the enzyme film is either stabilised in such a way that the rate of 'film loss' decreases, or activated in some way so that the rate of H_2 oxidation is increased, and remains greater even after the light source is removed.

3.2.2 Temperature Effect

The light source used in the PFE experiments described in this chapter is a high powered (300 W) projector lamp which generates a lot of heat when in use. To ensure that the current enhancement observed in Figure 33 is not simply an artefact resulting from the effect of

illumination on the temperature of the cell solution, this was investigated before further electrochemical analysis was carried out. Although the electrochemical cell used had a water jacket to allow the cell solution temperature to be precisely controlled and maintained (Figure 25 and 28Figure 27), it was found that this was not sufficient during illumination (Figure 34). The water jacket temperature was set to 5 °C and the temperature of the cell solution was measured during periods of illumination. After just 60 s of illumination a temperature increase of 0.5 °C was recorded for the cell solution. Figure 34 shows a chronoamperometry experiment demonstrating the effect of a 0.5 °C temperature increase on the H_2 oxidation current of *Ca*HydA compared to the effect of illumination, for which a temperature increase of 0.5 °C was also measured, in the absence of CO.

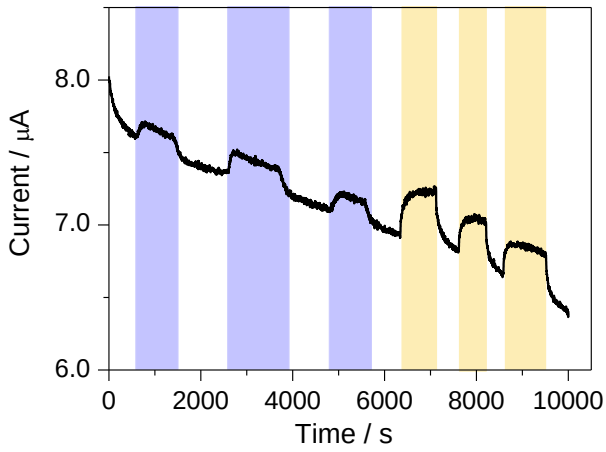

Figure 34: Chronoamperometry experiments comparing the effect of temperature and illumination on the H_2 oxidation activity of *Ca*HydA. Blue boxes denote periods where the water jacket temperature was increased by 0.5 °C. Yellow boxes denote periods of illumination for which a temperature increase of 0.5 °C was also recorded. Conditions: 5 °C, pH 6 phosphate buffer, ω = 3500 rpm, 100% H_2, -0.05 V, 300 W lamp with UV filter.

During periods of illumination longer than 60 s the H_2 oxidation current was found to increase by ~5% (Figure 34, yellow boxes), and during this illumination period a 0.5 °C increase of the cell solution temperature was measured. A temperature increase of 0.5 °C induced only by changing the temperature of the water jacket (Figure 34, blue boxes) however results in a

current enhancement of just ~2 %. This shows that the current enhancement observed under illumination is partially caused by an increase in the solution temperature, but this doesn't account for the entire enhancement. Illumination also inherently increases the rate of H_2 oxidation, most likely due to an increased rate of H-H bond breakage. This experiment demonstrates that for these types of experiments it is vital that the heat generated by the light source is minimised (see Figure 35) and taken into account when results are interpreted.

A heat absorbing infrared (IR) filter was introduced to light experiments to minimise the increase in temperature during periods of illumination (see Figure 34). With the IR filter in place between the light source and the electrochemical cell, the temperature increase was reduced to less than 0.1 °C and only a small enhancement of the H_2 oxidation activity was recorded under illumination (Figure 35). This small enhancement of current observed under illumination with the IR filter in place most likely results from the inherent increase in the rate of catalysis in light, although it is also possible that the small increase in temperature (0.1 °C) during illumination causes this enhancement.

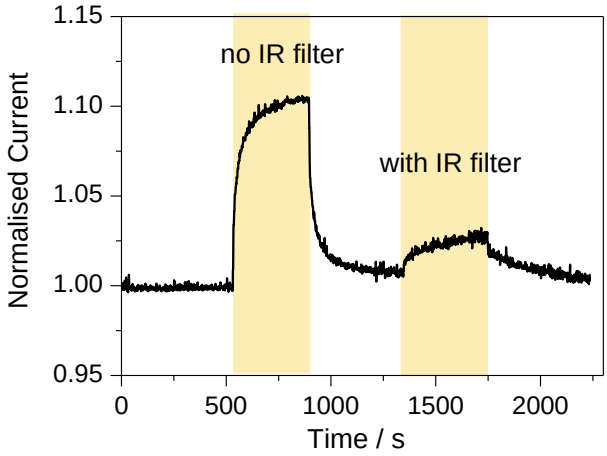

Figure 35: Chronoamperometry experiment comparing the effect a heat absorbing IR filter on the change in H_2 oxidation activity of *Ca*HydA under illumination. Yellow boxes denote periods of illumination, the first (525-900 s) carried out without and the second (1330-1750 s) with an IR filter between the light source and the electrochemical cell. Conditions: 5 °C, pH 6 phosphate buffer, ω = 3500 rpm, 100% H_2, left: -+0.15 V, 300 W lamp with UV filter.

The same IR filter was used to reinvestigate the effect of illumination on the rate of CO release from the H_{ox}-CO state of *Ca*HydA without the results being convoluted by a change in solution temperature during illumination as in Figure 32**.** A chronoamperometry experiment (Figure 36) was performed at +0.15 V to measure the effect of illumination on the rate of recovery of the H_2 oxidation activity of *Ca*HydA after exposure to CO. Buffer saturated with CO was injected into the cell immediately prior to commencing the experiment. This CO was then flushed from the cell by the continuous flow of H_2 (1000 mL/min); the current increases as CO is released from the H-cluster of inhibited enzyme molecules, regenerating the active H_{ox} state. During this recovery of activity the electrode was subjected to periods of illumination. Experiments were recorded both with and without the heat absorbing IR filter in place for comparison purposes.

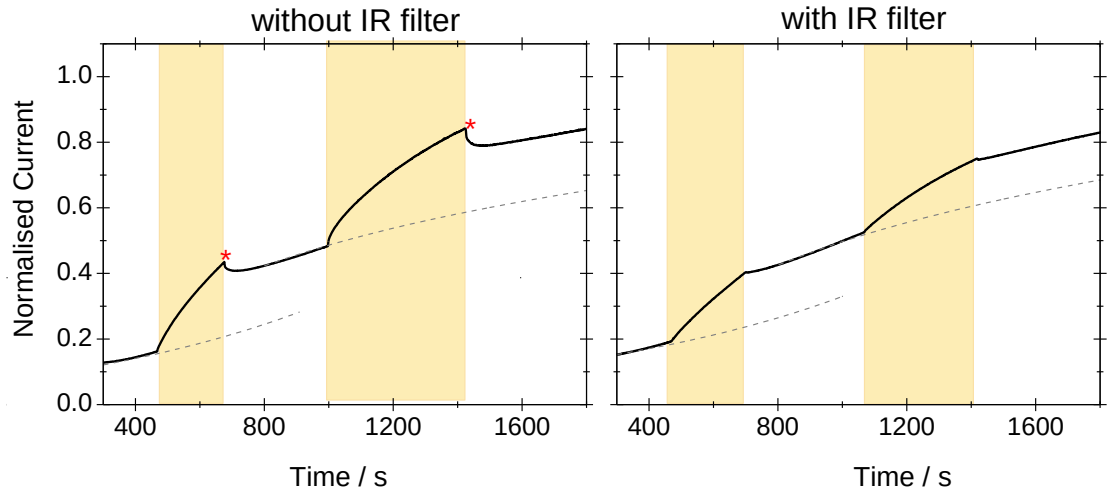

Figure 36: Chronoamperometry experiment comparing the effect of an IR filter on the effect illumination on the rate of recovery of H_2 oxidation activity of *Ca*HydA after exposure to CO. Buffer saturated with CO was injected into the cell immediately prior to commencing the experiment [CO] = 270 µM. The cell headspace was flushed with 100% H_2 throughout. Conditions: 5 °C, pH 6 phosphate buffer, ω = 3500 rpm, 100% H_2, +0.15 V. Yellow shaded regions denote periods of illumination using a 300 W projector lamp, with a UV filter only (left) or with both a UV and IR filter (right). Dotted lines show the extrapolated current in the absence of light. Red asterisks mark the drop in current measured upon removing the light source.

Comparison of the two experiments shown in Figure 36 reveals that even with the effect of temperature minimised (right, using an IR filter) there is still a substantial increase in catalytic current. This increase in current results from both an increase in the the rate of recovery from CO inhibition during periods of illumination (yellow boxes), and the inherent increase in the rate of catalysis during illumination. In both experiments the current increases at a greater rate (steeper gradient) during periods of illumination; light increases the rate of breakage of the Fe_d-CO_{exo} bond, regenerating the active H_{ox} state more rapidly.

The drop in current observed immediately after the light source is removed (Figure 32 andFigure 36, asterisk) has previously been attributed to re-binding of released CO (explained in section 3.1.2.4.2). This drop in current is however not observed in the experiment where an IR filter is used (Figure 36, right). This indicates that the current drop observed without the IR filter in place may simply be an artefact resulting from the decrease in temperature when the light source is removed. The very strong temperature dependence of the rate of both H_2 oxidation and production activity of [FeFe]-hydrogenases was demonstrated and interpreted by Hexter *et al;*[97] temperature changes of just a few degrees have a very large effect on the rate of catalysis.

3.2.3 Potential Dependence of Photolability

The effect of illumination on the rate of recovery of H_2 oxidation and production following inhibition by CO was compared for the three [FeFe]-hydrogenases: *Ca*HydA, *Dd*HydAB and *Cr*HydA1, to determine if the effect is potential dependent. In all cases an IR filter was used to ensure the results were not convoluted by the effect of temperature (as discussed in section 3.2.2). Chronoamperometry experiments were performed at two different potentials for each enzyme, and the effect of illumination on the rate of recovery from CO inhibition was recorded for both H_2 oxidation and H_2 production activity (Figure 37). Carbon monoxide

was introduced to the cell solution by injection of CO saturated buffer, immediately resulting in a drop in the catalytic current (see Figure 37, arrows). The cell was constantly flushed with 100% H_2 (1000 mL/min) and the recovery of catalytic activity was recorded as CO was flushed from the cell solution. During this period of recovery, the cell was illuminated for short periods (yellow boxes).

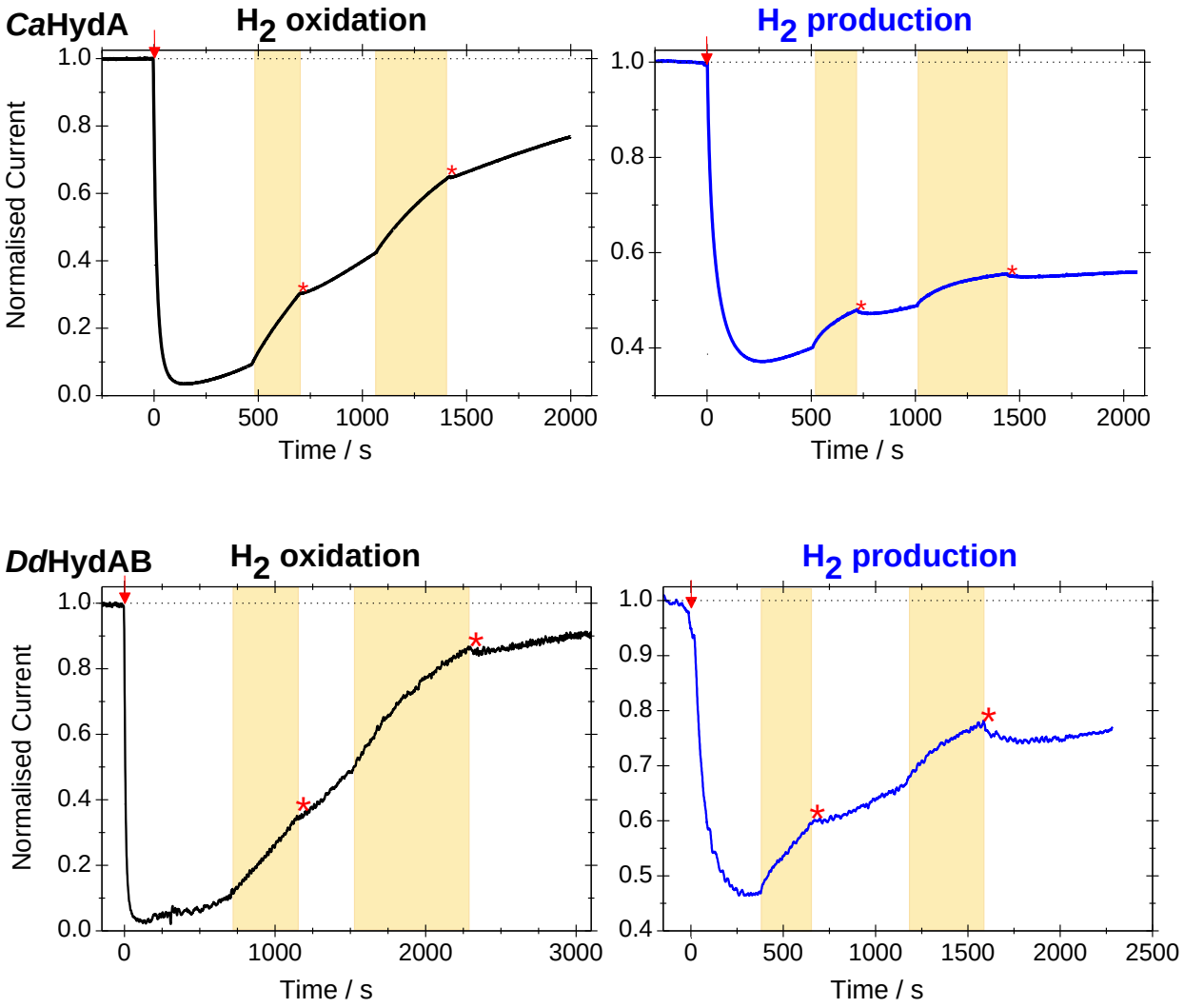

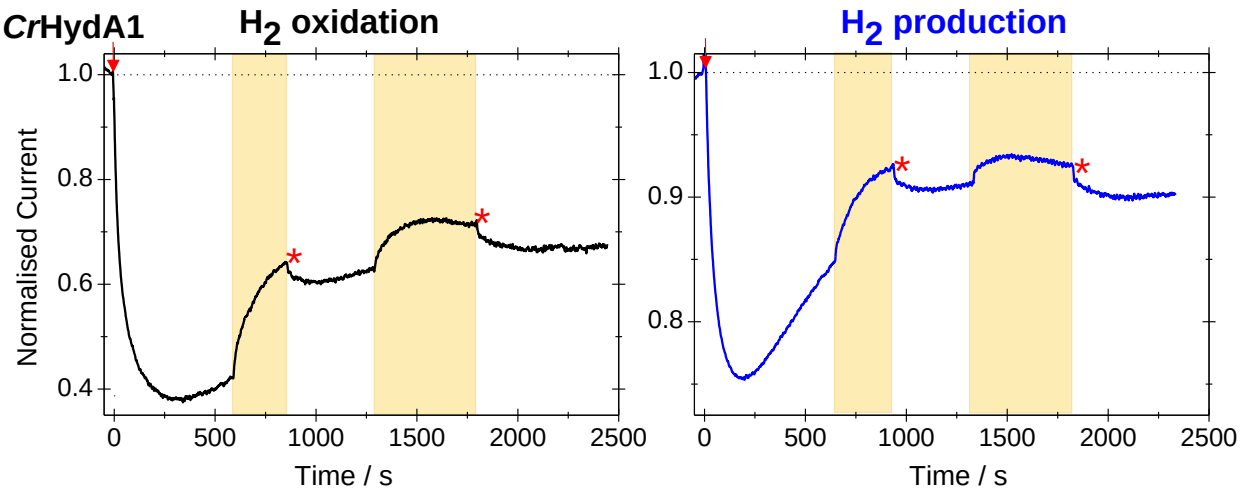

Figure 37: Chronoamperometry experiments comparing the effect of illumination on the rate of recovery of H_2 oxidation (left) and H_2 production (right) activity from CO inhibition for *Ca*HydA (top), *Dd*HydAB(middle) and *Cr*HydA1(bottom). Buffer saturated with CO was injected into the cell at t = 0 s (red arrow) to give a CO concentration of 270 µM (*Ca*HydA), 9.7 µM (*Cr*HydA1) and 5 µM (*Dd*HydAB) in the cell solution. The cell headspace was flushed with 100% H_2 throughout (1000 mL/min). Conditions: 5 °C, pH 6 phosphate buffer, ω = 3500 rpm, 100% H_2, H_2 oxidation at -0.15 V (*Ca*HydA and *Cr*HydA1) and -0.05 V for *Dd*HydAB, H_2 production at -0.55 V. Yellow boxes denote periods of illumination using a 300 W projector lamp, with both a UV and IR filter. A red asterisk marks the drop in current observed when the light source is removed.

The experiments in Figure 37 show that for all three hydrogenases studied, when recovering from inhibition by CO (by flushing CO from solution), illumination results in a significant increase in the rate of recovery, evidenced by the increased gradient of the current trace. This is seen both at high potential (Figure 37, left column) where enzymes catalyse H_2 oxidation and at low potential (Figure 37, right column) where enzymes catalyse H_2 production. As explained in section 3.1.2.4.2 the enhancement of current during illumination results from a combination of both the increase in the inherent rate of catalysis under illumination, and the increased rate of Fe_d-CO_{exo} bond breakage due to photolysis of this bond.

For all three hydrogenases the *extent* of current enhancement does not appear to be potential dependent, being very similar for both H_2 oxidation and H_2 production activity for each enzyme. The rate of recovery is dependent on the rate of Fe_d-CO_{exo} bond breakage, a bond

expected to be stronger for more reduced states of the enzyme. [Carbon monoxide is a π-acceptor ligand, a more reduced metal center is able to donate more electron density into the π* orbital of the CO bond (back-bonding), resulting in a stronger Fe-C bond]. The fact that the increase in the *rate* of recovery during illumination (photolysis of the Fe_d-CO_{exo} bond) appears potential independent (Figure 37) supports the theory that the same inhibited state, H_{ox}-CO, is formed for [FeFe]-hydrogenases in the presence of CO, regardless of potential.[146] These findings contrast with the PFE experiments performed on *Dd*HydAB previously in which illumination was found to have no effect on the rate of recovery of H_2 production activity from inhibition by CO.[77] This difference may be a result of the different light sources used; in the experiments in this thesis a much more powerful source is used.

The recovery profiles differ considerably between the three hydrogenases (Figure 37) due to their different affinities for CO (as reported by Goldet *et al.*[76]), which also meant that different CO concentrations had to be used for each enzyme experiment, making comparison of the extent of light activation difficult. It does appear however in the experiments shown in Figure 37 that illumination increases the rate of recovery from CO inhibition more significantly for *Cr*HydA1 and *Ca*HydA than for *Dd*HydAB. This is noticeable when comparing the change in gradient during illumination (yellow box) to the gradient of the current trace before and after illumination for each hydrogenase in Figure 37. For *Ca*HydA and *Cr*HydA1 (Figure 37 top and bottom) this change is significant, whereas for *Dd*HydAB the change in gradient is more subtle (Figure 37, middle).

The different CO concentrations were used for each hydrogenases in the experiments in Figure 37 also make it complicated to compare the extent of 're-inhibition' (marked by red asterisk) between the enzymes. As described in section 3.1.2.4.2, the drop in current observed immediately upon removing the light source has been attributed to re-binding of CO. The

magnitude of this drop in current appears to be dependent on the potential for both *Ca*HydA and *Dd*HydAB (Figure 37, top and middle). In the experiments monitoring the recovery of H_2 oxidation activity (left) there is very little change in the current when the light is turned off; t = 700 and 1400 s for *Ca*HydA (Figure 37, top left) and t = 1160 and 2300 s for *Dd*HydAB (Figure 37, middle left). In contrast the experiments monitoring the recovery of H_2 production activity (right) for these enzymes show a significant drop in the current when the light source is removed; t = 725 and 1425 s for *Ca*HydA (Figure 37, top right) and t = 650 and 1600 s for *Dd*HydAB (Figure 37, middle right). For *Cr*HydA1 (Figure 37, bottom) there is a significant drop in current immediately after the light is removed at both potentials studied.

The effect of illumination on the kinetics of CO inhibition and reactivation was investigated as shown below in Figure 38. Hydrogen oxidation activity was recorded at +0.15 V and H_2 production activity at -0.55 V, before introduction of 190 μM CO at t = 0 by injection of CO saturated buffer. The CO concentration then rapidly decreased as it was flushed from solution by the constant flow of 100% H_2 through the cell headspace (1000 mL/min) The 'light' experiment was recorded under constant illumination, with both a UV and IIR filter in place between the light source and the electrochemical cell.

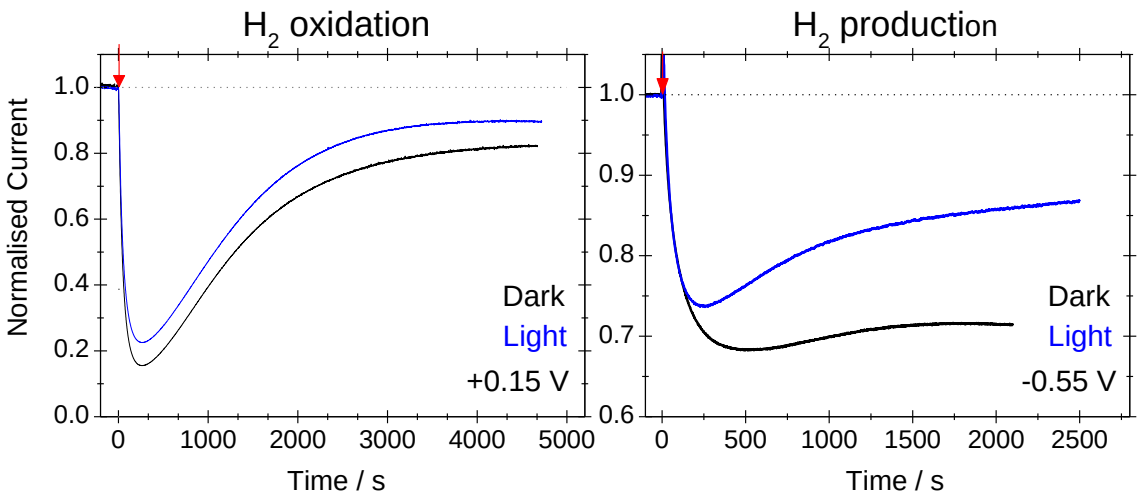

Figure 38: Chronoamperometry experiments showing the effect of illumination on the rate and extent of recovery of H_2 oxidation (left) and H_2 production (right) activity of *Ca*HydA after inhibition by CO. Buffer saturated with CO (0.5 ml) was injected at t = 0 (red arrow) into 3 ml of cell solution, [CO]=194 µM. The cell headspace was flushed with 100% H_2 continuously throughout the experiment (1000 mL/min). Conditions: 5 °C, pH 6 phosphate buffer, ω = 3000 rpm, 100% H_2, left: +0.15 V, right: -0.55 V. 'Light' experiments were performed using a 300 W projector lamp with both a UV and an IR filter.

At both potentials studied the extent of inhibition is slightly greater in the dark (Figure 38, black), than in the light experiment (Figure 38, blue), due to more rapid reactivation of the inhibited H_{ox}-CO state by photolysis of the Fe_d-CO_{exo} bond in the light experiments, irrespective of potential. The irreversibility of the inhibition (the percentage of inhibited activity not recovered after removal of CO) is also slightly greater in the dark experiment. For H_2 oxidation (Figure 38, left) inhibition was 21% irreversible in the dark but 13% irreversible in the light. For H_2 production (Figure 38, right) inhibition was 88% irreversible in the dark but 54% irreversible in the light. The irreversibility of CO inhibition at low potential has been shown to be the result of degradation of the H_{red}-CO state.[152] Formation of this state is not understood and may arise from direct combination of CO with enzyme in the H_{red} state, or by one electron reduction of H_{ox}-CO at reducing potentials. The greater reversibility of CO inhibition measured in the light experiments (Figure 38, blue) can therefore be explained by the more rapid reactivation of inhibited enzyme, leaving less time for the enzyme in the inhibited state to irreversibly degrade. The rate of inhibition, as measured from log plots of the current (Appendix 2), is not significantly affected by illumination. In all experiments the rate of recovery is ~1 $x10^{-3}$ s^{-1} (as previously reported[76]), but at both potentials is slightly faster in the light experiment (+0.3 $x10^{-3}$).

3.3 Summary

The illumination experiments presented in this chapter have shown that for all three [FeFe]-hydrogenases studied, the rate of release of exogenous CO from the inhibited state of the

enzyme to restore catalytic activity is strongly enhanced by light at both potentials where H_2 oxidation and H_2 production occur.

The importance of temperature control during light experiments has been highlighted (Figure 34 and 36); powerful light sources raise the experimental temperature considerably, convoluting the results. The use of a heat absorbing infrared filter effectively minimises this contribution (Figure 35), and illumination without an accompanying temperature change has been shown to increase the rate of catalysis (Figure 35) and the rate of recovery from CO inhibition (Figure 36).

The effect of illumination on the stability of an enzyme film is strongly potential dependent (Figure 33). At both potentials studied (-0.05 and -0.55 V) periods of illumination increase the rate of catalysis, however at potentials where the enzyme catalyses H_2 production (-0.55 V) illumination significantly decreases the stability of the enzyme film (Figure 33B). Upon removing the light source the reduction current is smaller than predicted if enzyme 'film loss' continued at the same rate throughout the experiment (Figure 33D, dotted line). This loss of activity can be explained by light-induced enzyme degradation. Although it has been reported that the H_{ox} state is stable under illumination at cryogenic temperatures,[155] the stability of H_{red} has not been reported, and light induced enzyme degradation has been reported for enzyme samples stored at ambient temperature under normal laboratory light.[82,145] Degradation of the H-cluster under such conditions proceeds via loss of intrinsic CO ligands (Figure 30), and the released CO is able to inhibit undamaged enzyme molecules, generating the H_{ox}-CO state.[82,145] It has been reported that the inhibited H_{ox}-CO state transiently loses the intrinsic bridging CO ligand upon illumination at cryogenic temperatures, forming the inactive H_{L1} state (Scheme 6).[155] Alternatively the observed instability under illumination may result from light-induced desorption of the enzyme from the electrode surface.

Illumination has a very different effect on film stability at high potential (Figure 33C). At potentials where the enzyme catalyses H_2 oxidation (-0.05 V) the activity after illumination is greater than predicted by the initial rate of enzyme 'film loss' (Figure 33A). For clarity the experiment shown in Figure 33A is reproduced and annotated here in Figure 39.

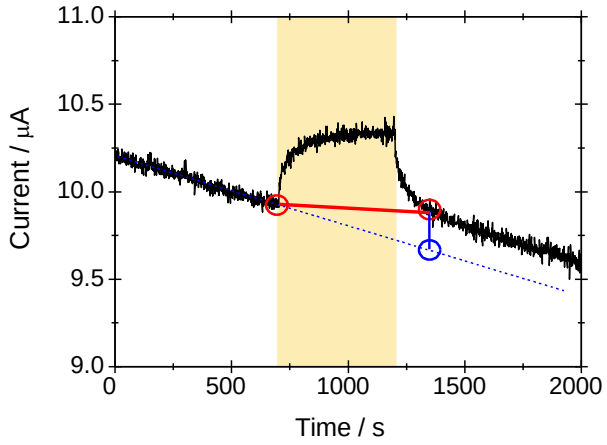

Figure 39: Reproduced from Figure 33A. The effect of illumination on the H_2 oxidation current of *Ca*HydA at -0.05V, 5 °C, pH6, ω = 3500 rpm, 100% H_2, 300 W lamp with UV filter. Red circles show the current immediately before and after illumination. The blue dashed line shows the data extrapolated for a constant rate of film loss and the blue circle denoted the current expected after illumination.

The red circles in Figure 39 show the current immediately before and after illumination, the blue dashed line shows the current extrapolated for a steady rate 'film loss'. Comparison of the current before and after illumination (red circles) reveals very minimal loss of current over this time period (650 s) whereas if the rate of film loss continued at the same rate (blue dashed line) throughout the period of illumination a loss of 0.26 μA is expected (blue circle). It appears that whatever processes are occurring in this experiment that contribute to the observed 'film loss' (desorption, reorientation or degradation of enzyme) these processes stop during illumination, stabilising the enzyme film. Alternatively it is possible that illumination of the enzyme at this potential (-0.05 V) results in activation of the enzyme (unknown process) that compensates for the activity lost due to enzyme 'film loss'. It is possible that during periods of illumination the H-cluster is excited to form an isomer with different activity to the

ground state, possibly involving rotation of the CO and CN ligands around Fe_d. The mechanism of either enzyme activation, or stabilisation must however be a potential dependent process, as this effect is not seen when the enzyme produces H_2 at -0.55 V (Figure 33B).

As stated above, the H_{ox} state is known to release intrinsic CO ligands when exposed to light, inactivating the enzyme.[82,145] It is possible that light induced enzyme degradation is potential dependent, occurring faster for the H_{red} state than the H_{ox} state, explaining the observed decrease in stability of the enzyme during illumination of H_2 production activity. In the H_{red} state the bridging CO ligand moves to a terminal position on Fe_d and the iron is in a more reduced state (Fe^I) as shown in Figure 40.

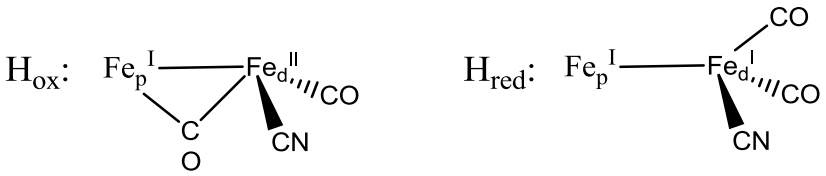

Figure 40: The change at Fe_d of the H-cluster in the H_{ox} and H_{red} states.

For all three hydrogenases, it has been shown that illumination increases the rate of recovery from CO inhibition (Figure 37), both at potentials where the enzyme catalyses H_2 production (-0.55 V) and where it catalyses H_2 oxidation (+0.15 V for *Ca*HydA and *Cr*HydA1, -0.05 V for *Dd*HydAB). [A less oxidising potential was used for *Dd*HydAB due to lower activity of this enzyme sample, to maximise current by limiting high potential inactivation]. The increase in activity during illumination is attributed to the combination of faster reactivation of the inhibited enzyme due to photolysis of the Fe_d-CO bond, and faster catalysis in the light. For each hydrogenase the extent of this current increase is very similar at both potentials studied, indicating that CO is released from the same inhibited state at both potentials, H_{ox}-CO, as

previously reported[76], or that the Fe_d-CO_{exo} bond is of a similar strength for both the inhibited H_{ox}-CO and H_{red}-CO states.

Upon removal of the light source a drop in current is observed, attributed to re-inhibition of the enzyme by CO (Figure 37). This re-inhibition is observed for all three enzymes, and for both *Ca*HydA and *Dd*HydAB the extent of this is dependent on the potential; occurring to a greater extent in the experiment at low potential (Figure 37, right) than at oxidising potentials (Figure 37, left). This is difficult to rationalise, as the amount of CO in the cell solution should be the same at any given time for the experiments at both potentials (same [CO] and flushing time), and CO is known to bind preferentially to the H_{ox} state of the H-cluster.[146] The increase in the extent of re-inhibition of H_2 production activity (at -0.55V) may therefore be attributed to a greater amount of CO remaining trapped within the enzyme molecule at low potential. This could result from a light induced conformational change of the enzyme that takes place only at reducing potential, resulting in slower diffusion of CO out of the enzyme molecule. If this is the case it is more likely that the CO released after photolytic cleavage of the Fe_d-CO bond remains trapped within the enzyme molecule and re-binds more rapidly once the light source is removed.

Alternatively, it is possible that the observed drop in current results not from re-inhibition, but from the lower rate of catalysis in the dark compared to under illumination. The enhancement of current observed during illumination in these experiments (Figure 37) results from both the increased rate of reactivation of the CO inhibited state, but also the increased rate of catalysis in light. Illumination may have a greater effect on the rate of H_2 production (Fe-H bond cleavage) than H_2 oxidation (H-H bond cleavage). A smaller degree of the current enhancement observed during illumination at low potential (Figure 37) would therefore result from photolytic cleavage of the Fe_d-CO bond and a greater degree would result from the

increase in the rate of catalysis in the light. When the light source is removed this component of the current enhancement is lost, appearing as re-inhibition, and occurring to a greater extent at low potential.

3.4 Low Potential Electrochemical Studies

3.4.1 Detection of a Super-Reduced State

The super-reduced state of [FeFe]-hydrogenases is not a well characterised or understood state of the H-cluster. It has been reported, from IR studies that this state is generated at low potentials[82,85], and studies by Baffert *et al.*[152] predict that this state has a very low affinity for CO. Protein film electrochemistry techniques were therefore used to investigate the generation of a super-reduced state of the H-cluster at low potential, and the activity and stability of this state once formed.

Cyclic voltammograms were carried out on three different [FeFe]-hydrogenases, extending the potential range to a very reducing value (-0.8 V, nearing the limit for a PGE electrode), to look for any discontinuity of catalysis in the H_2 production region (Figure 41). The gradient of a voltammogram is directly related to the rate of catalytic turnover.[22] The involvement of a state of the H-cluster one electron more reduced that H_{red} (H_{sred} state or the H_{ox-2} level), predicted to reduce protons at a greater rate than H_{red},[93] would therefore result in an increase in the reduction current upon generation of this state. It is expected that this would be observed as a sharp, positive change in the gradient of the voltammogram at low potential.

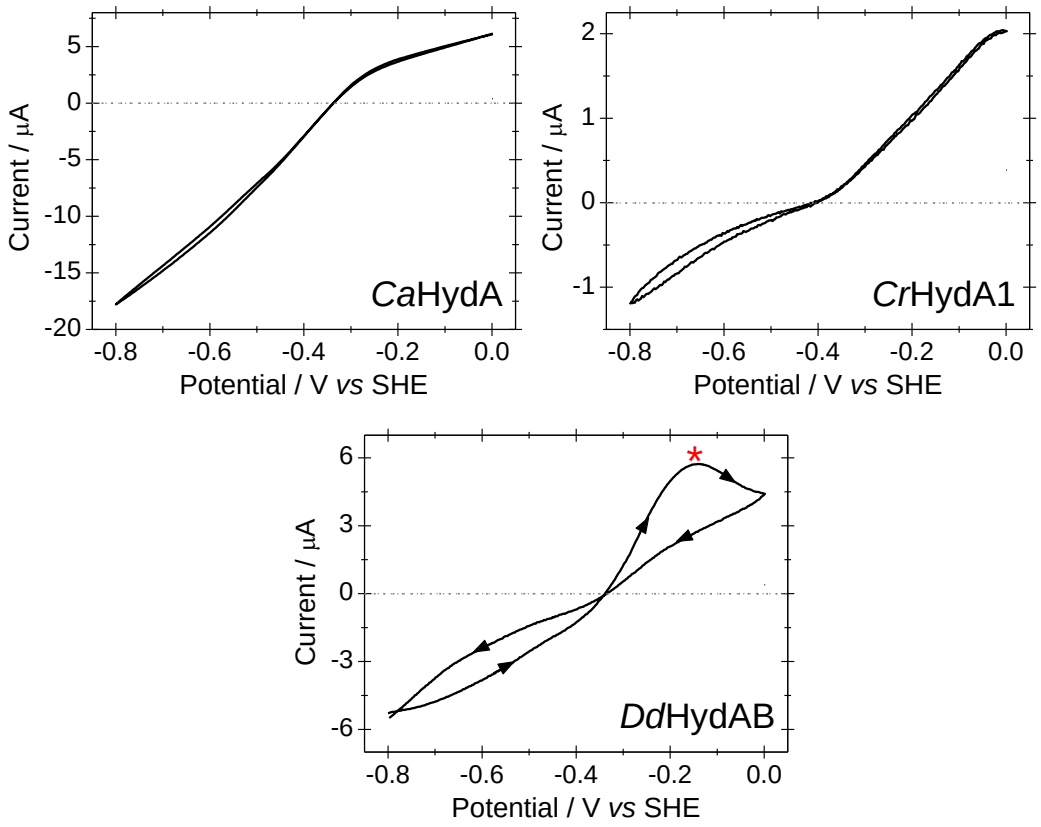

Figure 41: Cyclic voltammograms of three [FeFe]-hydrogenases, *Ca*HydA, *Cr*HydA1 and *Dd*HydAB, showing the effect of a wide potential range on the catalytic current. Conditions: 80% H_2 20% N_2, 0.5 °C, 3 mV/s scan rate, pH 6 phosphate buffer, ω = 3000 rpm, in the dark. An asterisk marks the onset of high potential inactivation of *Dd*HydAB. Arrows denote the scan direction.

The potential was cycled between -0.8 V and 0 V, starting at the low potential limit as shown in Figure 41. Although the general catalytic wave-shape varies between the three enzymes as discussed in section 1.5.2.3, none of the hydrogenases exhibit a clear change in gradient at low potential. For both *Ca*HydA and *Cr*HydA1 the forward and reverse scans almost exactly overlay; exposure to a very reducing potential does not result in any irreversible loss of activity. The voltammogram of *Dd*HydAB is complicated by high potential inactivation (see asterisk on voltammogram) and general instability of the enzyme on the electrode surface as discussed previously,[77] resulting in a greater difference between the forward and reverse scans, however there is no sharp change in the voltammogram gradient in the H_2 production region relating to an increased rate of turnover. Although these voltammograms provide no clear

evidence for the generation of a super-reduced state of the H-cluster, it is possible that a more reduced state is generated under these conditions, but that it does not catalyse the reduction of protons at a significantly greater rate than the H_{red} state.

The activity and stability of the three enzymes at extremely low potential (-0.7 V) was investigated using chronoamperometry (Figure 42). The potential was held at a mildly reducing value (-0.45 V) where the H_{red} state is expected to be the dominant species, and the H_2 production current recorded. The potential was then stepped down to very reducing value (-0.7 V) for several minutes, reported to be sufficient to generate a super-reduced state[82,85] and then returned to -0.45 V to monitor any loss of activity at this potential. The change in H_2 production activity was monitored in addition to any change in the stability (current gradient) of the enzyme film at both potentials. Formation of an inactive state at low potential should result in a positive gradient for the current trace during the low potential step, as activity is lost over time as the enzyme is gradually inactivated. If a super-reduced state is formed irreversibly there would be a loss of activity upon returning the potential to -0.45 V.

For all three hydrogenases, stepping the potential to -0.7 V immediately results in a significant increase in the H_2 production activity (Figure 42), as expected due to the greater driving force for proton reduction. The increase in activity at -0.7 V relative to that at -0.45 V is dependent on the hydrogenase, seen most clearly in the right hand column of Figure 42, where the data has been corrected for initial film loss and normalised to -1 before the potential step. For *Ca*HydA the activity increases by a factor of 4, for *Cr*HydA1 by a factor of 5, but for *Dd*HydAB the activity only increases by a factor of just over 2. This may be due to the lower catalytic bias of this hydrogenase[97] (section 1.5.2.3), or it may be that a super-reduced state is formed under these conditions, and it is either inactive, or less active than the same state for *Ca*HydA and *Cr*HydA1. In all three cases the current at -0.7 V is very stable and

there is no loss of activity at -0.45 V after the low potential step (see dotted line, Figure 42). These experiments show that if a super-reduced state is formed at -0.7 V this state is active, stable, and formed reversibly.

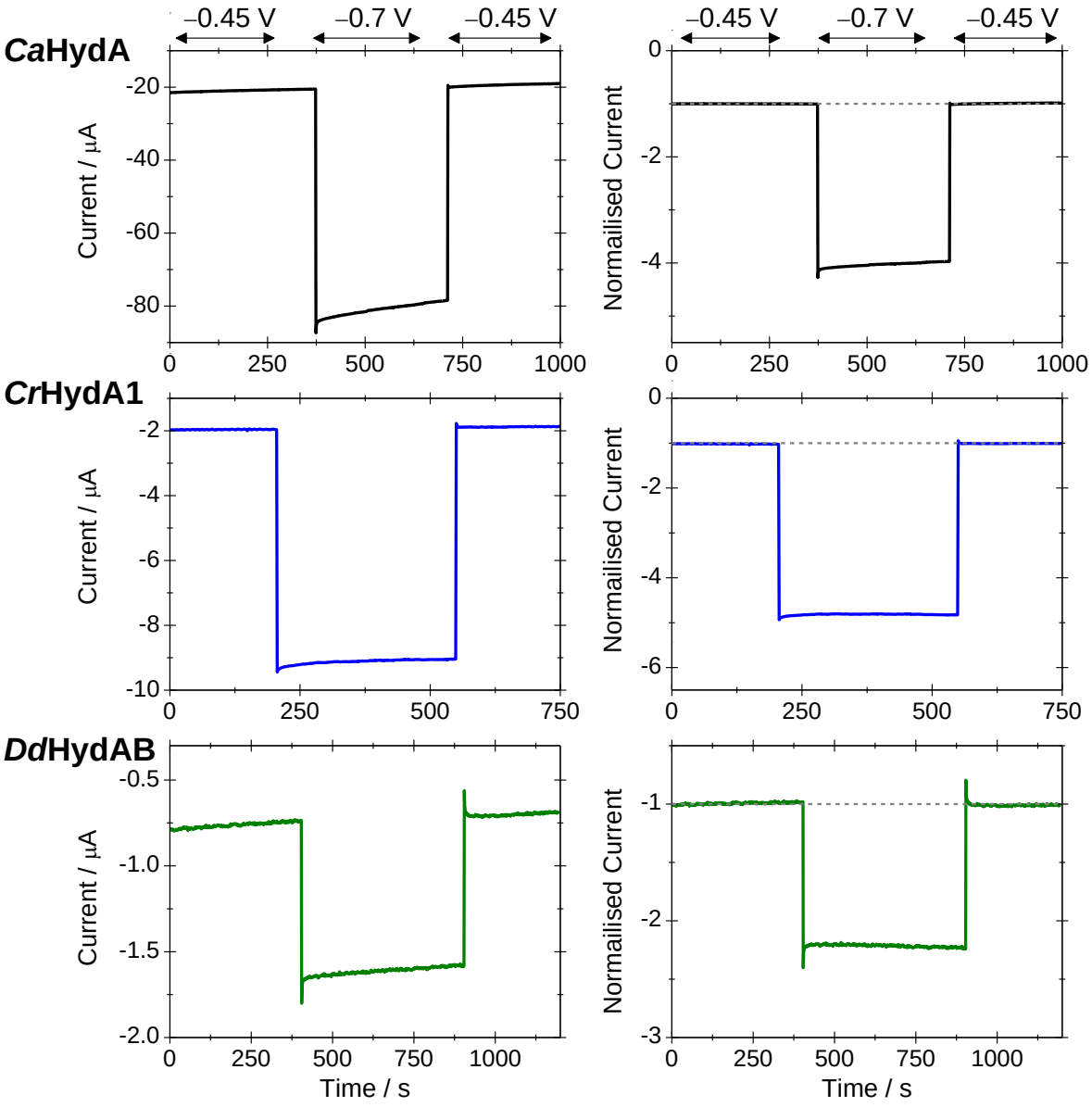

Figure 42: Chronoamperometry experiments investigating the effect of low potential on the stability of a film of [FeFe]-hydrogenase; *Ca*HydA (top), *Cr*HydA1 (middle) and *Dd*HydAB (bottom). The current was recorded while stepping the potential between mildly reducing (-0.45 V) and extremely reducing (-0.7 V) values. The column on the left shows the raw data and the column on the right shows the current after correction for initial film loss and normalisation. Conditions: 100% H_2, pH 6 phosphate buffer, 5 °C, ω = 3000 rpm, dark. A normalised current of -1 is shown by the dotted lines (right panels).

3.4.2 Low Potential Carbon Monoxide Inhibition

Chronoamperometry experiments performed by Baffert *et al.*[152] have shown that exposure of CO inhibited hydrogenase (*Ca*HydA) to a very reducing potential results in activation of the enzyme H_2 production activity, thought to be due to the formation of a CO bound super-reduced state, with a very low affinity for CO. In this thesis the reaction of 3 different [FeFe]-hydrogenases with CO was studied over a very wide potential range using cyclic voltammetry. Voltammograms were recorded in the presence of low levels of CO (Figure 43), sufficient for inhibition to be observed but not to completely inhibit activity, allowing the inhibitory effect to be monitored over a wide potential range, for both H_2 oxidation and H_2 production activity. Figure 43 shows voltammograms recorded in the absence of inhibitor (black scans) immediately prior to addition of CO by a change in gas flow through the cell headspace, controlled by mass flow controllers. One full scan length (530 s, not shown) was allowed for the cell solution to equilibrate with CO before the red scans were recorded. The H_2 concentration was kept constant (80%) throughout the experiment to avoid variations in catalytic current resulting simply from changes in H_2 concentration.

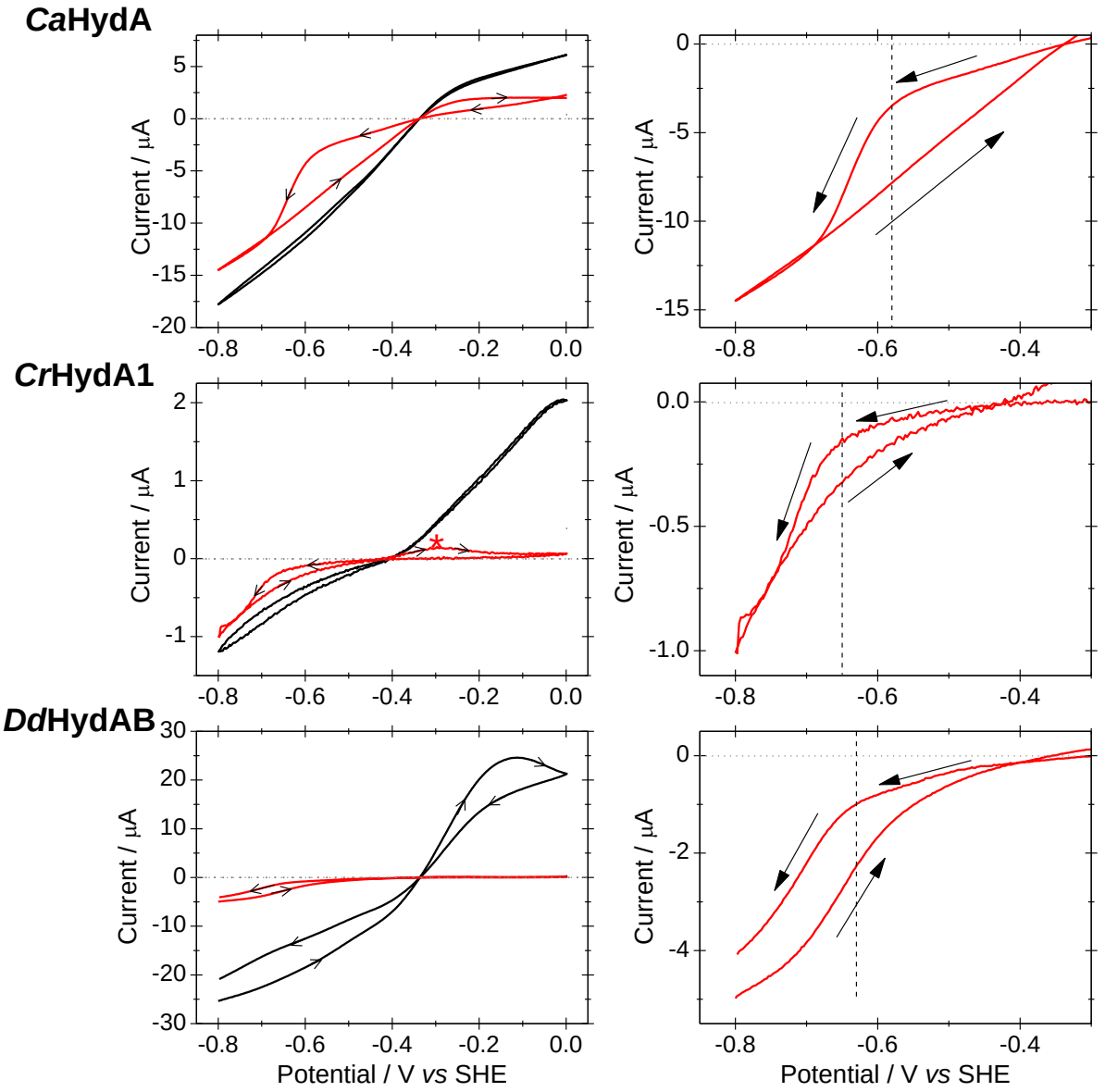

Figure 43: Cyclic voltammograms of three [FeFe]-hydrogenases showing the effect of the presence of CO on the catalytic activity. Black scans were recorded immediately prior to CO addition and red scans after equilibration in CO. The right hand column shows an expanded section of the hydrogen production region, arrows denote the scan direction. Conditions: 80% H_2, 20% (N_2+CO), *Ca*HydA and *Cr*HydA1 in 0.6% CO = 8.1 µM and *Dd*HydAB in 0.2% CO = 2.7 µM, 3 mV/s scan rate, pH 6 phosphate buffer, 5 °C, ω = 3000 rpm, in the dark. Vertical dashed lines show the onset of current activation. An asterisk marks the drop in the H_2 oxidation current of *Cr*HydA1 as the potential is swept to more oxidising values.

The effect of CO on the catalytic activity of three [FeFe]-hydrogenases can be seen by direct comparison of the voltammograms in Figure 43 recorded in the presence (red) and absence (black) of CO. For all three hydrogenases H_2 production activity is inhibited to a much lesser extent than H_2 oxidation; for *Ca*HydA (top) more than 80% of the current measured in the

absence of CO at -0.8 V persists in the presence of 0.6% CO (8.1 μM CO). In comparison, at 0 V, less than 40% of the activity is sustained in the presence of the inhibitor. Similar results are observed for *Cr*HydA1 (middle); almost all H_2 oxidation activity is inhibited at 0 V while there is very little loss of H_2 production activity at -0.8 V. Additionally there is a peak in the H_2 oxidation current in the positive scan direction at -0.25 V (Figure 43, asterisk), after which the current decreases as previously reported;[76] the rate of CO binding rapidly increases as the oxidised states of the enzyme are populated. This peak is not observed in the negative scan direction, showing that the rate of CO release under these conditions is much slower than the rate of CO binding. Although only 20% of H_2 production activity remains at -0.8 V for *Dd*HydAB (bottom) in the presence of 0.2% CO, H_2 oxidation activity is completely inhibited. In all cases the decrease in CO inhibition at highly reducing potentials is observed in the negative scan direction as a sharp increase in current (marked by dashed vertical lines, Figure 43, right), the rationale being that at very negative potentials the enzyme rapidly releases CO, regenerating catalytically active enzyme, most likely due to formation of the inhibited super-reduced state (H_{sred}-CO) which has a very low affinity for CO. This sharp increase occurs at ~ -0.58 V for *Ca*HydA and at ~ -0.64 V for both *Cr*HydA1 and *Dd*HydAB. For both *Ca*HydA and *Cr*HydA1 the voltammogram does not retrace as the electrode potential is raised to more positive values: instead, hysteresis is observed due to the slow rate at which CO re-binds.[76] For *Dd*HydAB this hysteresis is not observed, the wave-shape is very similar in both scan directions, reflecting the greater rate of CO binding for this enzyme.[76] The loss of current observed at -0.8 V (20% for *Ca*HydA and *Cr*HydA1, 80% for *Dd*HydAB) relative to the CO-free experiment (black, Figure 43) reflects both film loss over the course of the experiment and]=the irreversible breakdown of the unstable H_{red}-CO state[76,152] formed during the time of the experiment at less reducing potentials.

3.4.3 Potential of CO Release and Binding

One of the main differences between the voltammograms (Figure 43) in the presence of CO for the three different hydrogenases is the potential at which CO-release occurs. The rate and extent of CO binding has previously been measured for these three hydrogenases,[76] and decreases in the order Dd > Cr > Ca (k_{inact} = 3.9 x10^{-1}, 1.9 x10^{-2} and 1.1 x10^{-3} $s^{-1}\mu M^{-1}$ respectively), whereas the rate of CO release (measured as CO was flushed from solution) did not vary between the three (k_{react} = 2x10^{-3} s^{-1}). The midpoint potential of the enzyme activation at low potential, the steepest point of the voltammogram, where the rate of current increase is greatest, was determined from the position of the maxima in the first derivative of the reductive scan (Figure 44). In these experiments identical CO concentrations (8.1 μM) were used for each hydrogenase, allowing direct comparison of the potentials of activation, unlike the experiments shown in Figure 43.

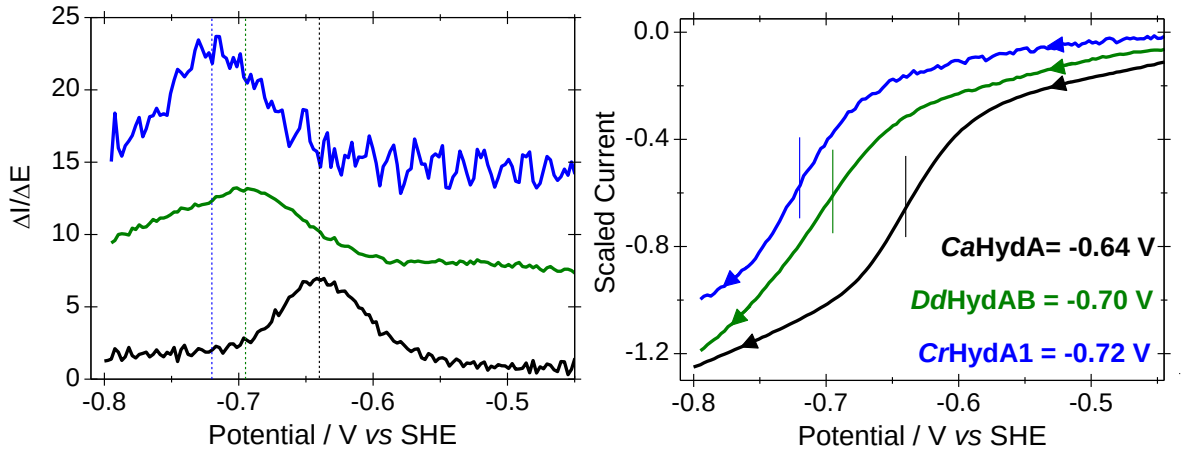

Figure 44: Comparison of the activation potential for H_2 production activity of [FeFe]-hydrogenases in the presence of CO. Left: first derivative of the reductive scan of a cyclic voltammogram recorded in the presence of CO. Right: reductive scan of a cyclic voltammogram recorded in the presence of CO. Data in both panels have been arbitrarily scaled for comparison purposes. Arrows denote scan direction, vertical lines denote the midpoint potential of activation, taken from the peak position in the scan derivative (left). Conditions: 80% H_2, 19.4% N_2, 0.6% CO = 8.1 μM, 3 mV/s scan rate, pH 6 phosphate buffer, 5 °C, ω = 3000 rpm, dark.

The right panel of Figure 44 shows the reductive scan of the voltammograms, with the midpoint potentials marked by vertical lines. The left panel shows the first derivative of the reductive scan of a voltammogram recorded in the presence of 0.6% CO plotted against potential for *Ca*HydA (black), *Dd*HydAB (green) and *Cr*HydA1 (blue). The positions of the maxima in the scan derivatives are marked by the vertical dashed lines (left); -0.64 V for *Ca*HydA, -0.70 V for *Dd*HydAB and -0.72 V for *Cr*HydA1. The driving force (reductive potential) required for activation decreases in the order Dd > Cr > Ca, consistent with the order of the rate and extent of CO binding for these enzymes[76] described in section 3.1.2.4.

The hysteresis observed for *Ca*HydA and *Cr*HydA1, resulting from the difference between the rate of CO release in the reductive scan and the rate of CO re-binding in the oxidative scan, is affected by both the scan rate used to record the voltammogram and on the concentration of CO. The effect of CO concentration is shown in Figure 45A; the H_2 production current was recorded for *Ca*HydA under 100% CO (red) and compared to that under 0.5% CO in N_2 (black). The effect of the presence of H_2 on the onset of CO release, and re-binding was also investigated (Figure 45B). Voltammograms were recorded under 0.6% CO in either 80% H_2 (red) or 0% H_2 (black) in N_2 and are shown normalised at -0.8 V for comparison purposes.

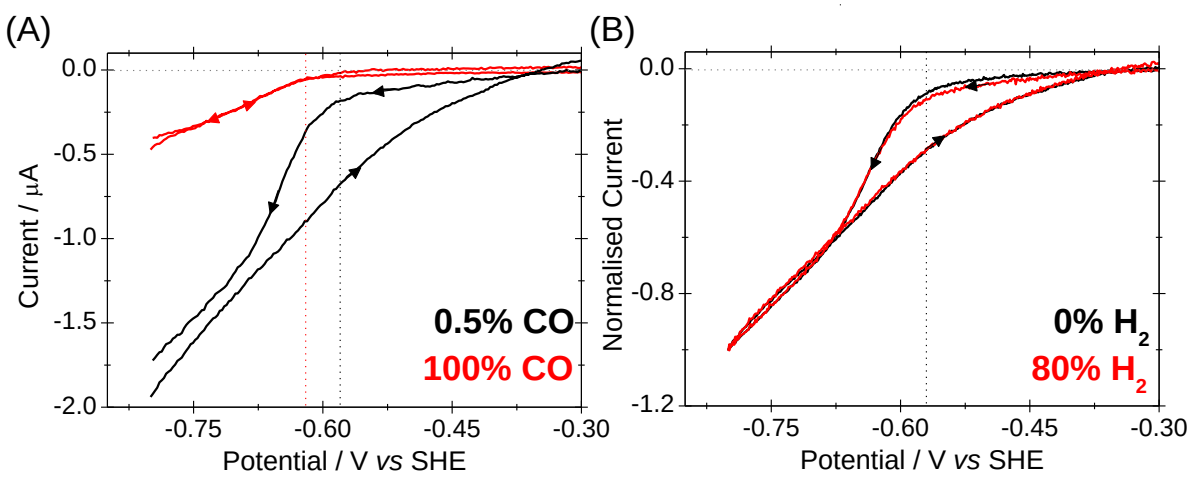

Figure 45: Cyclic voltammograms of *Ca*HydA in the presence of CO. A comparison of the effect of low and high CO concentration is shown on the left, and the effect of the presence of H_2 is shown on the right. Arrows denote the scan direction. Conditions: 3 mV/s scan rate, -0.05 ↔ -0.8 V, pH 6 phosphate buffer, 5 °C, ω = 3000 rpm, dark. (A): 0.5% CO = 6.8 μM in N_2 (black) and 100% CO = 1355 μM (red), (B): 0.6% CO = 8.1 μM in N_2 (black) and 80% H_2, 19.4% N_2 (red). Voltammograms commenced from the low potential limit (A) and the high potential limit (B). Vertical lines show the onset of activation.

The remarkable H_2 production activity of *Ca*HydA in the presence of 100% CO is shown in Figure 45A, 25% of the current recorded at -0.8 V in 0.5% CO (black) remains when the enzyme is exposed to 100% CO (red). The scan recorded under 0.5% CO shows the onset of CO-release (rapid current increase) at -0.58 V in the reductive scan (black dashed line), whereas under 100% CO this current increase does not occur until the potential is swept to a more reducing potential of -0.62 V (red dashed line), reflecting the slower rate of CO release from the enzyme in the presence of higher CO concentrations. In contrast to voltammograms recorded under low CO concentrations (black), in 100% CO the forward and reverse scans overlay (red). Under 0.5% CO binding is not observed in the reductive scan until the potential is swept up to the H_2 oxidation region (not shown), whereas under 100% CO the rate of CO binding is so much faster that it occurs at the same potential as CO release.

Cyclic voltammograms (Figure 45B) demonstrate that the presence of H_2 does not affect the catalytic wave-shape of *Ca*HydA in the presence of 0.6% CO. Although CO is a competitive inhibitor, binding at the same site as H_2,[147] the voltammograms under both conditions, 80%

H_2 (red) and 0% H_2 (black) overlay almost exactly. The onset of CO release occurs at the same potential (-0.58 V, dashed line) and occurs to the same extent regardless of the presence of H_2.

The effect of scan rate on the catalytic wave-shape of H_2 production by *Ca*HydA in the presence of 0.6% CO is shown in Figure 46. The wave-shape for a 3 mV/s scan (black) has been previously described (Figure 43). There is pronounced hysteresis; when scanned in the negative direction CO is released at potentials below -0.6 V (red box), but does not re-bind when the potential is scanned in the positive direction until potentials where H_2 oxidation occurs.

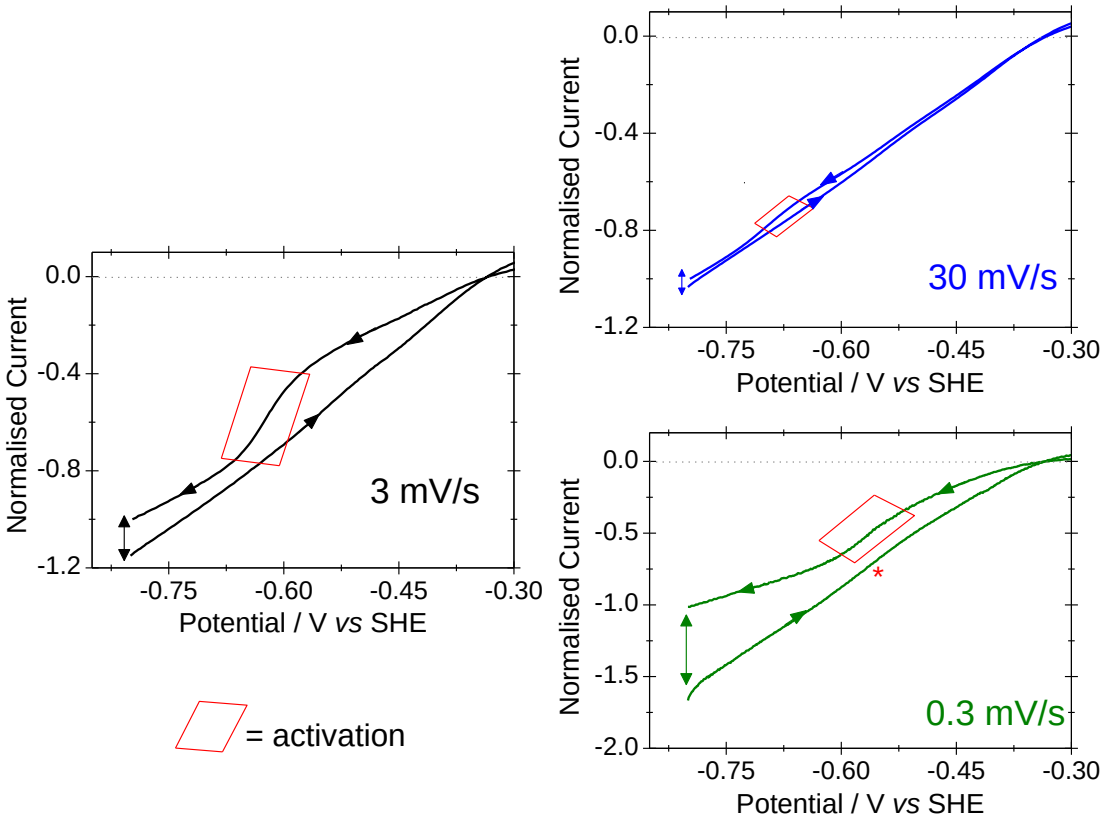

Figure 46: Cyclic voltammograms of *Ca*HydA showing the effect of scan rate on the H_2 production current in the presence of CO. Conditions: 0.6% CO in 80% H_2/19.8% N_2, [CO] = 8.1 µM, pH 6 phosphate buffer, 5 °C, ω = 3000 rpm, in the dark, scan rate given on the figure, potential: -0.8 V↔ 0 V, only the H_2 production region is shown. Red boxes show enzyme activation in the reductive scan and an asterisk marks the point of CO binding in the oxidative scan at 0.3 mV/s.

When the potential is scanned more slowly, at 0.3 mV/s (Figure 46, green), this same hysteresis is observed. The rate of CO release is fast compared to the scan rate and a less reducing activation potential (-0.5 V) is required before the onset of CO release is observed. The scan rate is slow enough for a small degree of CO re-binding to occur when the potential is scanned in the positive direction, seen as a small inflection in the voltammogram around -0.55 V (marked by an asterisk). At this scan rate the potential cycle takes much longer to complete, resulting in a greater degree of film loss over the course of the voltammogram, as seen by the large difference in current at -0.8 V at the beginning and end of the cycle (double headed arrow). When the potential is scanned more rapidly, at 30 mV/s (blue), the forward and reverse scans almost overlay; both the rate of CO release and CO binding are slow compared to the scan rate. Only a very small activation (rapid current increase, red box) due to CO release is observed at low potential and requires approximately 50 mV greater driving force compared to the 3 mV/s experiment.

3.4.4 Rate of CO Release and Rebinding

Chronoamperometry experiments were carried out to investigate the *rate* of CO-release initiated by low potential in the presence of a low level of CO (Figure 47). The cell solution was equilibrated with CO, controlled by mass flow controllers, before commencing the experiment. A low concentration of CO was used, 1% for *Ca*HydA and 0.1% for *Dd*HydAB; the concentration needed to be high enough to ensure a sufficient amount of enzyme molecules bound the CO, but not so high as to completely irreversibly inactivate the enzyme over the timescale of the experiment. The potential was held at -0.5 V before being pulsed to either -0.6 V (Figure 47, blue) or -0.8 V (Figure 47black) for a short period. For *Ca*HydA, a 2 s pulse was long enough to see enzyme activation, whereas for *Dd*HydAB a pulse of at least 20 s was required before any activation was observed.

The experiments shown in Figure 47 demonstrate that for an [FeFe]-hydrogenase to release CO, a sufficiently reducing potential must be applied. When the potential is pulsed to -0.8 V for just 2 s in the presence of 1% CO there is significant activation of the H_2 production activity of *Ca*HydA at -0.5 V (left, black trace); CO is rapidly released and the activity increases by a factor of 4. The activity then slowly decreases as CO re-binds. When the potential is stepped to a less reducing potential, -0.6 V (blue trace), there is no activation; the potential is not sufficiently reducing for release of CO. At the time of a second pulse, 50 s after the first, the enzyme has not been fully re-inhibited and the activity is still more than twice that before the pulse. The second 2 s pulse to -0.8 V activates the enzyme to the same level as the first, indicating that the first 2 s pulse was sufficient to cause all inhibited enzyme molecules to release the bound CO.

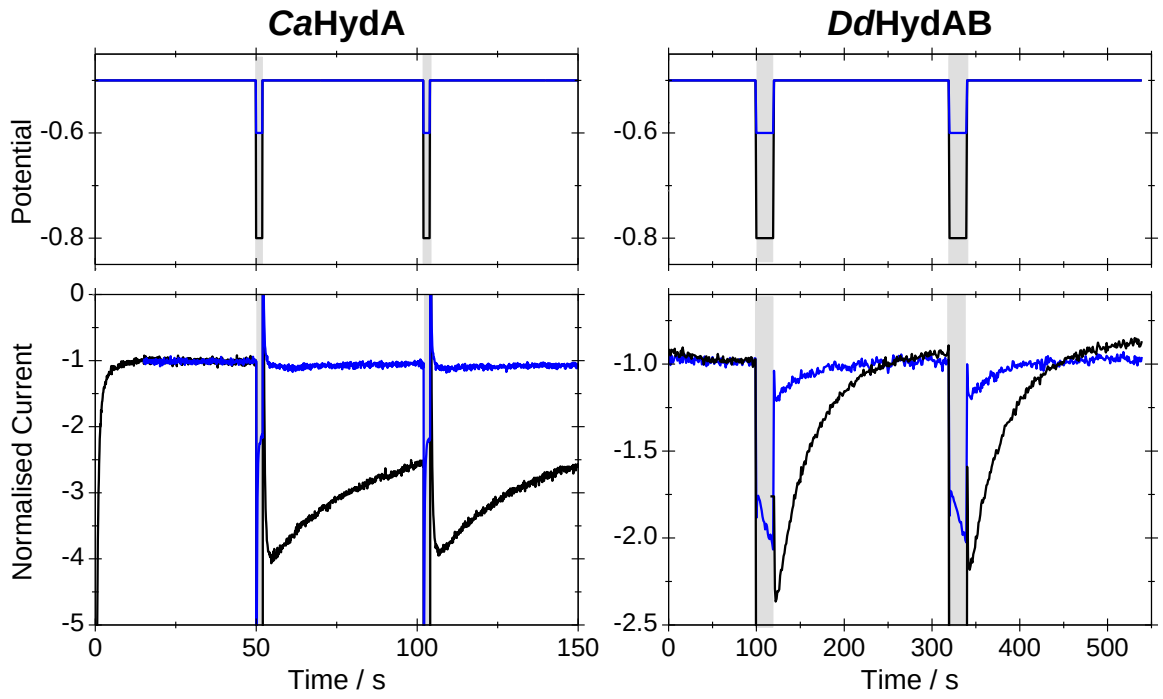

Figure 47: Chronoamperometry experiments showing the effect of short pulses to low potential on the H_2 production current of *Ca*HydA (left) and *Dd*HydAB (right) in the presence of CO. The potential was stepped from -0.5 V to -0.6 V (blue) or -0.8 V (black) for 2 s in 1% CO = 13.6 μM (*Ca*HydA) or for 20 s in 0.1% CO = 1.4 μM (*Dd*HydAB), shown by the grey boxes. Conditions: pH 6 phosphate buffer, 5 °C, ω = 3000 rpm, in the dark, 80% H_2, 20% (N_2 + CO).

Similar results were seen for *Dd*HydAB in the presence of 0.1% CO (Figure 47, right), however longer pulses were required for activation to be observed, reflecting the greater rate of CO binding,[76] and greater driving force required for CO release for this hydrogenase. A small amount of activation is seen for a 20 s pulse to -0.6 V (right, blue trace), but is not significant compared to the activation after a 20 s pulse to -0.8 V (black trace), which causes the activity upon returning to -0.5 V to more than double. This experiment also demonstrates the greater rate of CO binding for *Dd*HydAB compared to *Ca*HydA, observed by the decrease in H_2 production current after the low potential pulse, as CO re-binds. Re-binding occurs with a half life of approximately 25 s for *Dd*HydAB, compared to 50 s for *Ca*HydA.

The requirement of such a strongly reducing potential (-0.8 V) to initiate CO release supports the theory that the most reduced state, H_{sred}-CO is responsible for CO release. Throughout the experiment, at -0.5 V, the enzyme is thought to be predominantly in the reduced state (H_{red}).[82,85] In this state the enzyme rapidly reduces protons and releases H_2, generating the oxidised state (H_{ox}), which is then rapidly reduced by one an electron, supplied by the electrode, to re-generate the H_{red} state. The H_{ox} state has a much greater affinity for CO than the H_{red} state, and it is likely that in this experiment at -0.5 V the inhibited form of the hydrogenase is the H_{ox}-CO state, formed when CO traps the otherwise transiently formed H_{ox} state. It is clear that when a low potential is applied, a state of the H-cluster is generated that does not bind CO, however this potential must be sufficiently reducing, -0.6 V is not sufficient. A potential of -0.6 V however can be reasonably expected to be sufficient to reduce the H_{ox}-CO state by one electron to generate the H_{red}-CO state given that the midpoint potential for the H_{ox}/H_{red} transition at pH 6 has been measured as -0.36 V,[82] although this state (H_{red}-CO) has not been studied spectroscopically. This indicates that it is a super-reduced state of the H-cluster that is generated at -0.8 V and has a very low affinity for CO. Reduction to

form this super-reduced state (H_{sred}-CO) results in rapid release of the bound CO to generate a catalytically active state. A simple scheme is demonstrated below in Scheme 7.

Scheme 7: The proposed binding of CO to the various states of the H-cluster.[76,152]

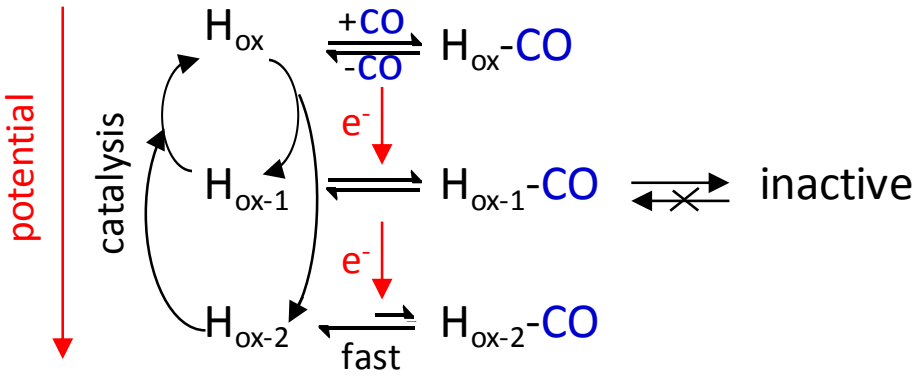

The pulse experiment shown in Figure 47 was repeated for *Ca*HydA, varying the length of the pulse to -0.8 V to investigate the extent of activation and the rate of CO re-binding (Figure 48). It is possible that a very short pulse to -0.8 V causes CO to be released from the H-cluster, reactivating the enzyme, but the CO is not fully released from the enzyme molecule in this short time. If CO is not completely released from the enzyme during a short pulse the rate of CO re-binding is expected to decrease for longer pulses; for a shorter pulse the CO is more likely to remain trapped within the enzyme, and therefore be able to re-bind to the H-cluster more rapidly than external CO.

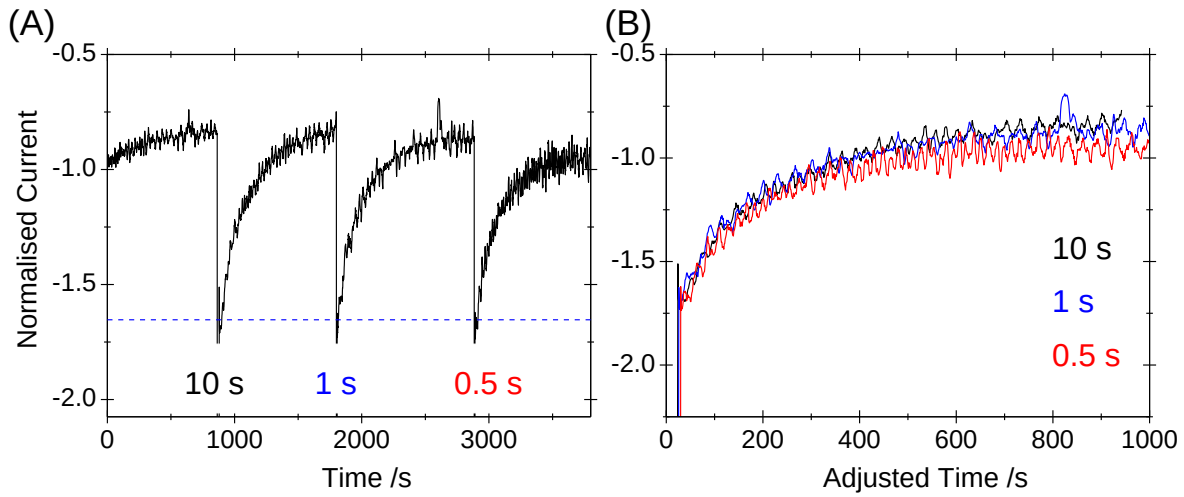

Figure 48: Chronoamperometry experiment showing the effect of the duration of a low potential pulse on the H_2 production current of *Ca*HydA in the presence of CO. The potential was stepped from -0.5 V to -0.8 V for the durations shown on the graph (A). Panel (B) compares the current immediately after each potential pulse. Conditions: pH 6 phosphate buffer, 5 °C, ω = 3000 rpm, in the dark, 80% H_2, 19% N_2 and 1% CO, [CO] = 13.6 μM.

Panel Figure 48A shows the effect of different length pulses to -0.8 V on the extent of CO release from *Ca*HydA. The rate of CO release is too fast for accurate analysis (even at 5 °C); the extent of activation was the same after pulses of 10 s, 1 s and 0.5 s to –0.8 V, consistent with a rate constant of at least 1 s^{-1}. For comparison, in experiments in which the potential is poised at –0.4 V and CO is flushed out of solution,[76] the recovery of activity is very slow with values of $k_{react} = 2 \times 10^{-3}$ s^{-1}. The lack of variation in the extent of activation with pulse length indicates that even the shortest pulse of just 0.5 s is sufficient to release the bound exogenous CO from all inhibited enzyme molecules, fully activating the enzyme film.

Panel Figure 48B compares the current trace after each low potential pulse; the reduction current decreases (gets more positive) as CO re-binds. These traces overlay, showing that the rate of CO re-binding does not vary with pulse length. The external CO concentration remains at 13.6 μM throughout the experiment, but if the released CO remains trapped within the enzyme molecule (after release initiated by the low potential pulse), re-binding of CO is

expected to be faster. We cannot conclude from this experiment whether or not all CO is released from the enzyme molecule for each pulse, but it does show that if any CO remains trapped within the enzyme, the amount does not vary for these different pulse lengths.

The rate of CO re-binding was further investigated using chronoamperometry experiments as shown in Figure 49. The potential was held at -0.5 V and 1% CO was introduced to the cell by concerted injection of CO saturated buffer and a change in gas flow through the cell headspace. The rate of CO binding to uninhibited enzyme after this instantaneous exposure to 1% CO was compared to the rate of CO re-binding after a 2 s pulse to -0.8 V in 1% CO as performed in Figure 47.

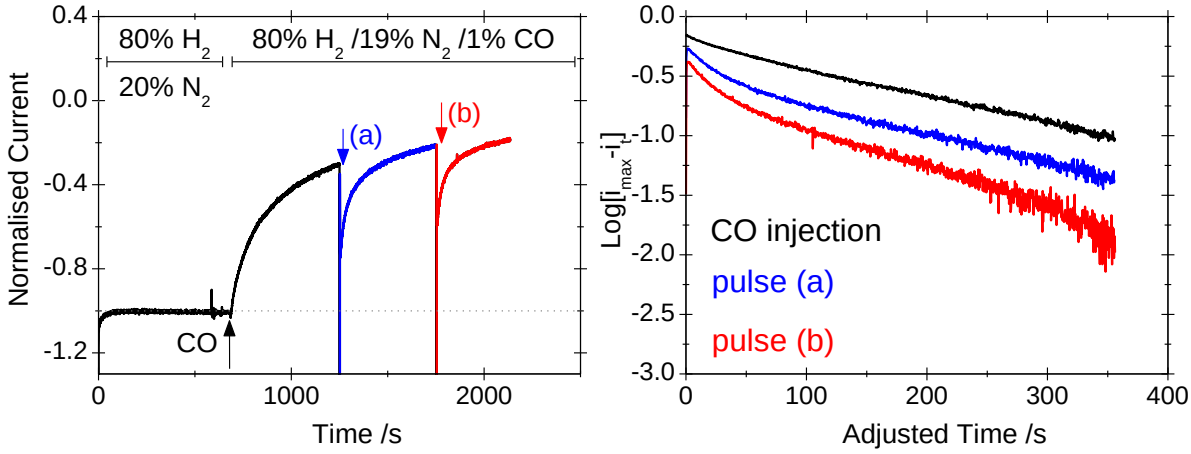

Figure 49: Left: Chronoamperometry experiment comparing the rate of CO binding upon addition of CO to re-binding after a short pulse to low potential. At 650 s (black arrow) 1% CO = 13.6 µM was introduced to the cell by injection of CO saturated buffer and by a change in gas flow through the cell headspace, and the potential was stepped to -0.8 V for 2 s at (a) and (b). Right: Log plots of the current trace after injection of CO (black) and after the two potential pulses (red and blue). Conditions: -0.5 V, pH 6 phosphate buffer, 5 °C, ω = 3000 rpm, dark, 80% H_2, 20% (N_2 + CO).

The left panel of Figure 49 shows the raw data; CO was introduced at 650 s as shown by the black arrow, and the potential was pulsed to -0.8 V for 2 s at 1250 s (blue) and at 1750 s (red). The panel on the right shows the log plots of the current traces after CO injection (black) and potential pulses (red and blue). The rate of CO binding can be taken from the gradient of the log plot. The three log plots are all parallel after the first 50 s; before 50 s the current is

complicated by the charging current upon stepping the electrode potential as shown in Chapter 2, Figure 19. The rate taken from this 50 s period (taken from the initial gradient) is found to be twice as fast after a potential pulse (a and b) compared to the injection, a difference not considered to be significant. This shows that the rate of CO re-binding after a low potential pulse is not significantly different to that of binding exogenous CO, showing that all CO is released from the enzyme molecule during the short potential pulse.

3.4.5 Oxygen Inhibition

The reaction of O_2 with [FeFe]-hydrogenases is known to be very similar to that of CO; binding in a similar manner at the distal iron site, preferentially to a more oxidised state of the H-cluster.[146] Following the discovery that the H-cluster has very little affinity for CO at very reducing potentials (Figure 43 and Figure 47), and CO is rapidly released when a sufficiently reducing potential is applied (Figure 47), the O_2 tolerance of two [FeFe]-hydrogenases was also investigated at a very reducing potential (-0.65 V, Figure 51). Oxygen was introduced to the cell via a change in the flow of gas through the cell headspace, controlled by mass flow controllers. The experiment was carried out in the absence of H_2 to avoid variations in catalytic current resulting simply from changes in H_2 concentration. Measurement of the extent of inhibition of H_2 production activity is complicated by reduction of O_2 at the graphite electrode surface, and is not measured in these experiments. These experiments were carried out to determine the tolerance of [FeFe]-hydrogenase to high O_2 concentrations at low potential. The exact O_2 concentration experienced by the enzyme under these conditions is difficult to calculate, under such reducing conditions O_2 reduction at the electrode surface is extremely rapid and does not reach a limit, as shown below in Figure 50.

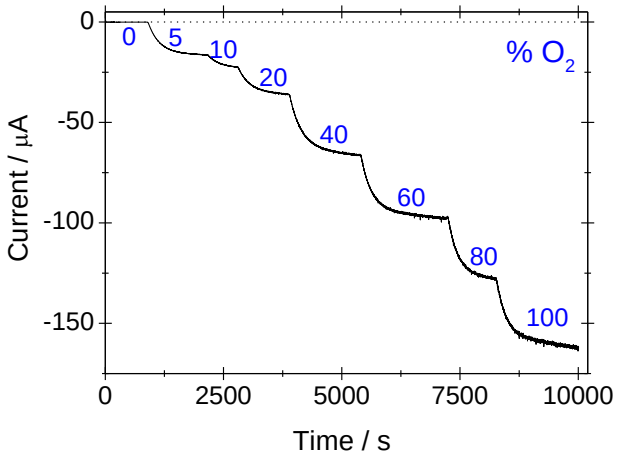

Figure 50: Chronoamperometry experiment showing the increased rate of reduction of O_2 at a bare graphite electrode with increasing O_2 concentration. The O_2 concentration was varied by the gas flow composition, controlled using mass flow controllers (blue). Conditions: -0.65 V, pH 6 phosphate buffer, 20 °C, ω = 3000 rpm, in the dark, 100% (N_2 + O_2).

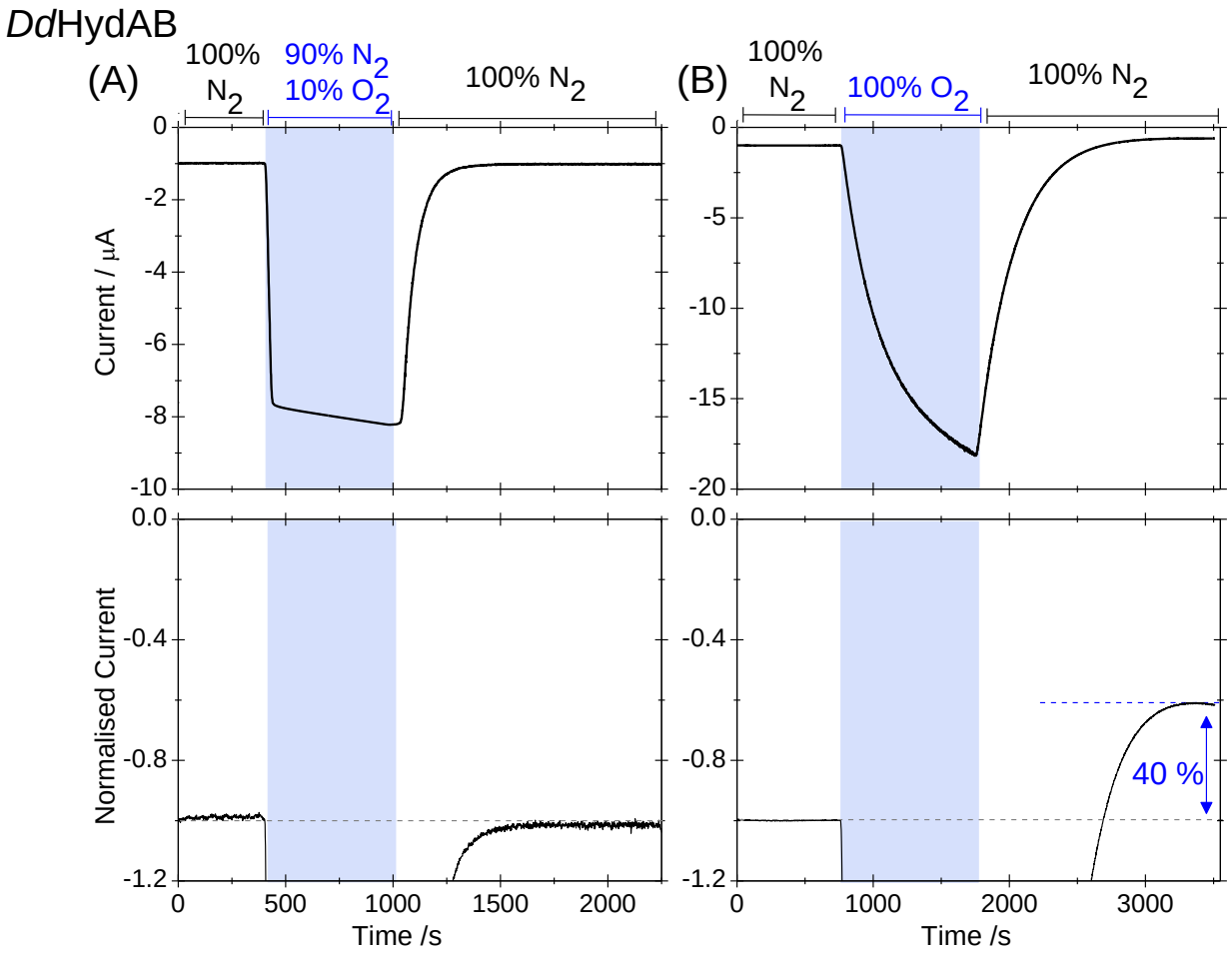

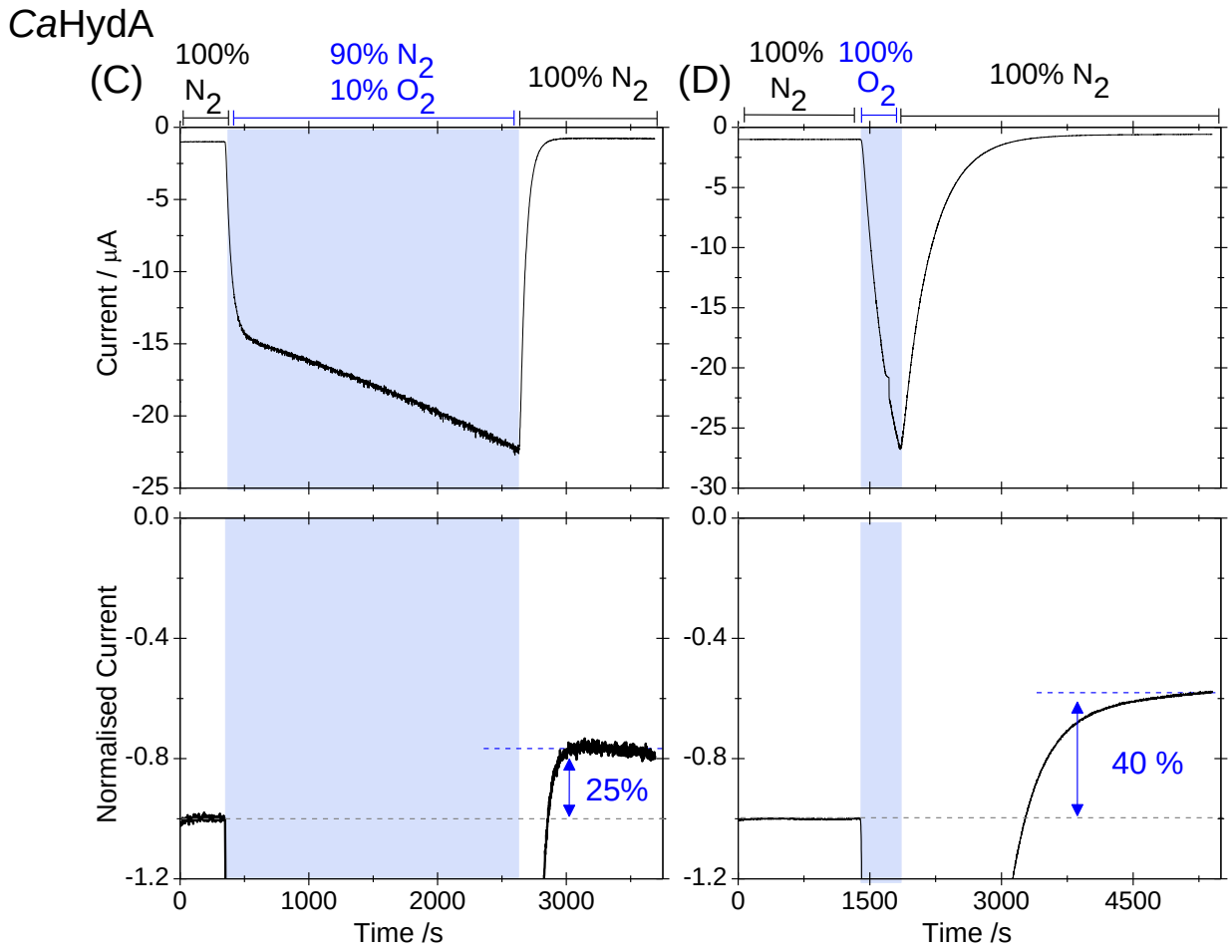

Figure 51: Chronoamperometry experiments showing O_2 inhibition of the H_2 production activity of *Dd*HydAB (A and B) and *Ca*HydA (C and D). Below each experiment the data is shown with the large reduction current in the presence of O_2 (due to O_2 reduction at the graphite electrode) cropped out. Conditions: -0.65 V, pH 6 phosphate buffer, 5 °C, ω = 3000 rpm, in the dark, 10% O_2 in N_2 (A and C) or 100% O_2 (B and D). The percentage of H_2 activity lost after exposure to O_2 is noted on the figure (blue arrows).

The chronoamperometry experiments in Figure 51 demonstrate the high tolerance of the [FeFe]-hydrogenases *Dd*HydAB (A and B) and *Ca*HydA (C and D) to high O_2 concentrations at -0.65 V. It should be noted that although the enzyme was exposed to 10 or 100% O_2 in the cell headspace, the concentration of O_2 experienced by enzyme in the adsorbed film cannot be accurately determined, but will be significantly lower than stated due to rapid consumption (reduction) of O_2 by the graphite electrode (see Figure 50). There is no irreversible damage after exposure of *Dd*HydAB to 10% O_2 for 600 s (Figure 51A) and 60% of the H_2 production activity remains after exposure to 100% O_2 for 1000 s (Figure 51B). Similarly high O_2

tolerance is observed for *Ca*HydA; 75% of activity persists after exposure to 10% O_2 for more than 2000 s (Figure 51C), and almost 60% persists after exposure to 100% O_2 for 800 s (Figure 51D). In the same way that very reduced states of the H-cluster do not bind CO, this experiment shows that the enzyme also has a low affinity for O_2 at low potentials. Additionally, a range of oxygen radicals are expected to be formed at the electrode surface under such reducing conditions, and the hydrogenases are only minimally damaged.

3.4.6 Potential Dependence of CO Inhibition

Chronoamperometry experiments were used to fully investigate the potential dependence of the extent, rate and reversibility of CO inhibition of [FeFe]-hydrogenases over a wide potential range (Figure 52). At t = 0 CO is introduced to the cell solution by concerted injection of CO saturated buffer and a change in composition of the gas flowing through the cell headspace. The grey shaded box represents the time that CO is flowed through the cell, after which the gas composition is returned to 80% H_2, 20% N_2 and CO flushed out of the cell solution. The H_2 concentration is kept constant at 80% throughout the experiment, to avoid variations in catalytic current resulting simply from changes in H_2 concentration; only the percentage of N_2 varies to accommodate the addition of CO.

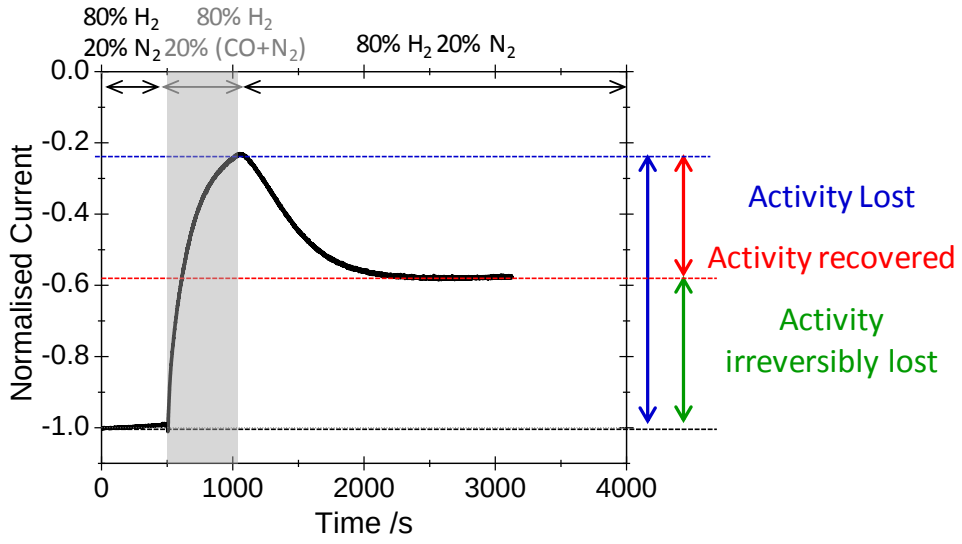

Figure 52: Example chronoamperometry experiment used to study the potential dependence of CO inhibition as in Figure 53. The change in gas composition throughout the experiment is labelled above.

The data is corrected for initial film loss (before introduction of CO) and normalised to -1 for comparison purposes. The extent of inhibition is expressed as a percentage by multiplying the fraction of activity lost after a certain exposure time by 100. The irreversibility of the inhibition can be expressed as a percentage of the total inhibition, defined as:

$$\%\ Irreversibility = 100\ x\ \frac{Fraction\ of\ Activity\ Irreverisbly\ Lost}{Fraction\ of\ Activity\ Lost} \qquad [3.1]$$

The chronoamperometry experiments in Figure 53 show inhibition by CO and subsequent recovery for three [FeFe]-hydrogenases recorded at various potentials over a wide range where the enzyme catalyses H_2 production. Potentials are given on the figure to the right of the data. The table to the right of each figure summarises the change in total percentage of activity lost in CO, and the percentage of activity lost irreversibly in CO at each potential studied.

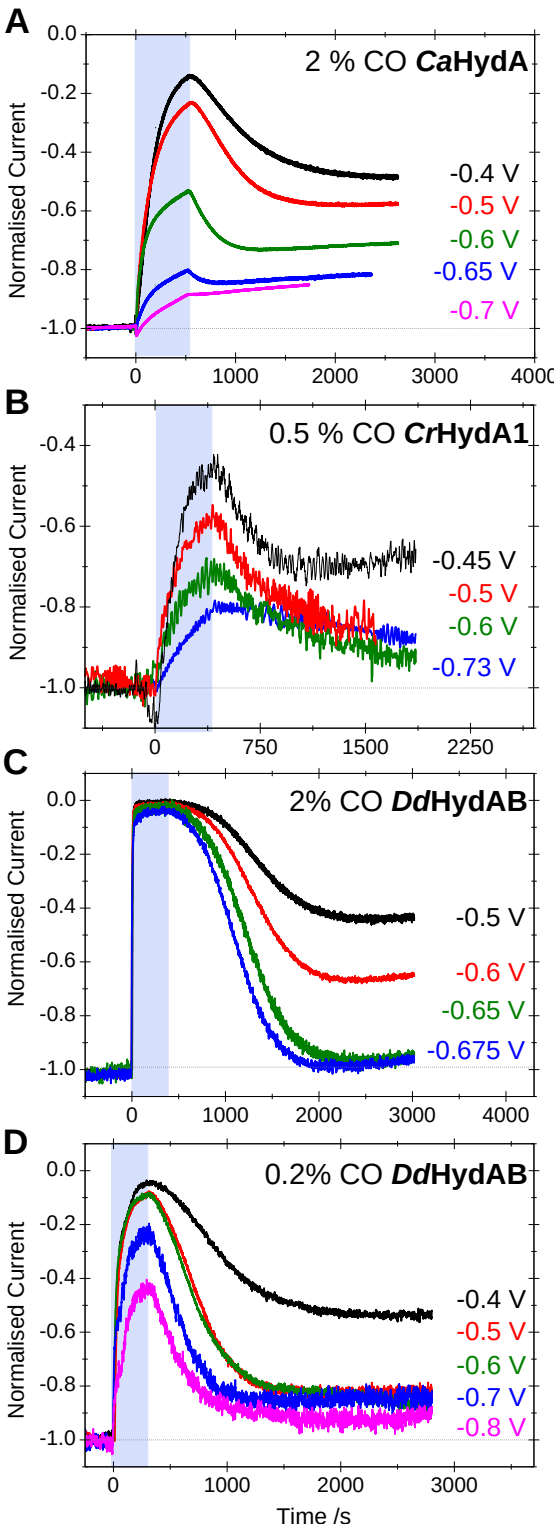

Potential	Inhibited	Irrev. Inhibited
-0.40 V	85%	52%
-0.50 V	75%	42%
-0.60 V	46%	29%
-0.65 V	20%	15%
-0.70 V	12%	12%

Potential	Inhibited	Irrev. Inhibited
-0.45 V	54%	30%
-0.50 V	41%	15%
-0.60 V	28%	8%
-0.73 V	20%	20%

Potential	Inhibited	Irrev. Inhibited
-0.50 V	100%	56%
-0.60 V	98%	35%
-0.65 V	98%	5%
-0.675 V	96%	0%

Potential	Inhibited	Irrev. Inhibited
-0.40 V	95%	47%
-0.50 V	90%	19%
-0.60 V	90%	15%
-0.70 V	75%	15%
-0.80 V	55%	10%

Figure 53: Chronoamperometry experiments showing the potential dependence of CO inhibition of *Ca*HydA (A), *Cr*HydA1 (B) and *Dd*HydAB (C & D). Conditions: pH 6 phosphate buffer, 5 °C, ω = 3000 rpm, in the dark, 80% H_2, 20% (N_2 + CO), *Ca*HydA: 2% CO = 27.1 μM for 500 s, *Cr*HydA1: 0.5% CO = 6.8 μM for 400 s, *Dd*HydAB: 2%, CO for 400 s (C) and 0.2% CO = 2.7 μM (D) for 300 s. The table to the right of each figure summarised the total percentage of activity lost and the percentage of activity lost irreversibly in CO at each potential studied.

Upon introduction of CO at t = 0 (by injection and gas flow) the H_2 production current immediately decreases significantly in all experiments, as the enzyme becomes inhibited (Figure 53). When the flow of CO is replaced by H_2/N_2 (after blue box), the H_2 production current begins to increase (more negative current) as CO is released from inhibited enzyme molecules. For *Cr*HydA1 (Figure 53B) this recovery of activity begins almost immediately after CO is removed from the gas flow mixture, whereas for *Dd*HydAB there is a short 'lag-phase' (Figure 53C and D). This lag-phase is particularly noticeable for the experiment shown in Figure 53C, where the enzyme was exposed to 2% CO and activity is almost completely inhibited. The current remains at almost zero for 100-200 s after removal of CO begins, before the recovery of activity gradually begins, reflecting the greater affinity of this enzyme for CO.[76]

Comparison of the data in Figure 53 for the three different hydrogenases studied reveals a similar potential dependence of the extent of inhibition for all; the extent of inhibition decreases as the potential is lowered, as expected from the cyclic voltammograms in Figure 43, CO appears to bind preferentially to less reduced states of the H-cluster. The potential dependence of the extent of inhibition is discussed in greater detail, in section 3.4.6.2.

The amount of activity irreversibly lost after exposure to CO also decreases as the potential is lowered (Figure 53), however as less of the enzyme becomes inhibited at lower potentials it is more revealing to express the reversibility of CO inhibition as a percentage of the activity lost (Equation 3.1); this is discussed further in Section 3.4.6.1. The irreversible loss of activity after exposure to CO is attributed to degradation of the H_{red}-CO state; the Fe_p-S_{cys} bond is broken, irreversibly forming an inactive state. At all the potentials used in the experiments in Figure 53 the enzyme catalyses H_2 production. The H_{red} state is therefore expected to

dominate, however at more reducing potentials (< -0.6 V) the H_{sred} state may also be formed.[82,85] Binding of CO directly to either of the reduced states is predicted to be extremely slow.[152] During catalysis the H_{ox} state is formed transiently (before being reduced by electrons provided by the electrode) and due to its high affinity for CO it is this state that is trapped by CO to form the inhibited H_{ox}-CO state. The fact that the inhibition shown in Figure 53 is partially irreversible shows that the unstable H_{red}-CO state has been formed, most likely by one electron reduction of the H_{ox}-CO state. At very low potentials the enzyme is expected to be reduced by a further electron, to form the H_{sred}-CO state. This state does not degrade but has a low affinity for CO; upon formation of this state CO is released and active states of the H-cluster are regenerated.

3.4.6.1 Irreversibility of CO Inhibition

The irreversibility of CO inhibition, expressed as a percentage of the activity lost (Equation 3.1), is strongly potential dependent; for both *Ca*HydA (Figure 53A) and *Cr*HydA1 (Figure 53B), the irreversibility of inhibition *increases* as the potential is lowered. For example: removal of CO after inhibition of *Ca*HydA at -0.7 V (Figure 53A, magenta) does not restore any catalytic activity, whereas at - 0.4 V (black) more than 40% of the inhibited activity is recovered upon removal of CO.

In direct contrast the irreversibility of inhibition of *Dd*HydAB shows the opposite trend with potential. This is most clearly demonstrated in (Figure 53C) where exposure to 2% CO almost completely inhibits H_2 production activity across the entire potential range. Upon removal of CO, 100% of activity is restored at -0.675 V (Figure 53C, blue), but less than 50% of activity is recovered at -0.5 V (Figure 53C, black). The variation of irreversibility of CO inhibition with potential, defined as a percentage of the inhibited activity, is summarised in Figure 54 for

all three hydrogenases studied and compared to the potential dependence of the extent of inhibition.

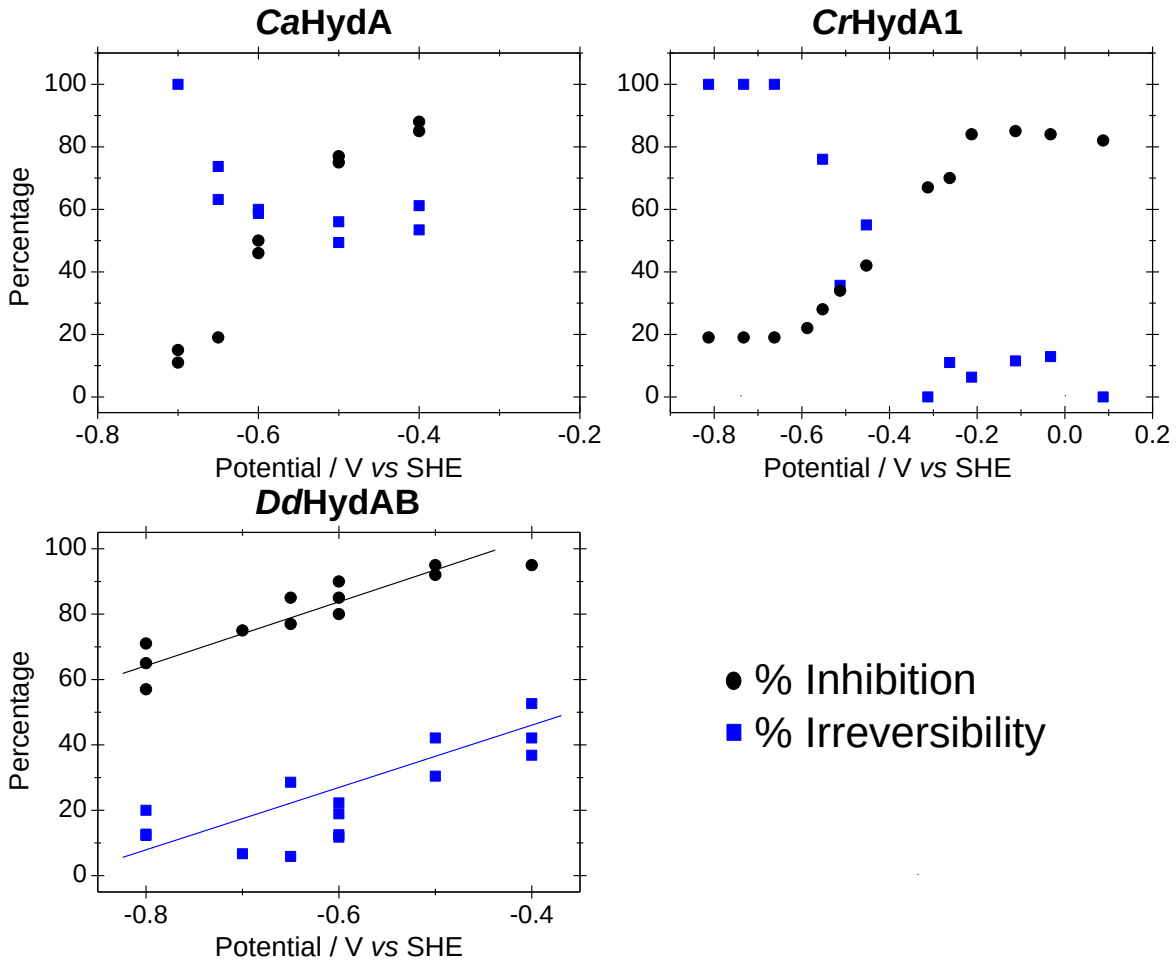

Figure 54: Plots showing the potential dependence of both the extent of CO inhibition (black circles) and the irreversibility of this inhibition (blue squares) for *Ca*HydA, *Cr*HydA1 and *Dd*HydAB. Conditions: pH 6 phosphate buffer, ω = 3000 rpm, in the dark, 80% H_2, 20% (N_2+CO). *Ca*HydA: 5°C, 2% CO = 27.1 µM for 600s, *Cr*HydA1: 20°C, 0.5% CO = 5.4 µM for 400s and *Dd*HydAB: 5 °C, 0.2% CO =2.7 µM for 300s.

For both *Ca*HydA and *Cr*HydA1 the irreversibility of inhibition mirrors the trend of the extent of inhibition (Figure 54, top), and increases as the potential is lowered. This trend is explained by the increased formation of the H_{red}-CO state at lower potentials, which degrades irreversibly. Analysis of the potential dependence of inhibition of *Dd*HydAB is limited by the very small spread and large scatter of the data over the potential range studied (Figure 54, bottom), resulting from the very high sensitivity of this enzyme to CO.[76] It appears however

that for this hydrogenases the irreversibility of CO inhibition decreases as the potential is lowered, the opposite trend to *Ca*HydA and *Cr*HydA1.

The potential dependence of the reversibility of CO inhibition was further investigated using more extreme conditions for both *Ca*HydA and *Dd*HydAB (Figure 55). It can be expected that exposure to CO at very reducing potentials, where the H_{sred}-CO is more likely to be formed, would result in less irreversible loss of activity than inhibition at less reducing potentials where more of the inhibited enzyme is more likely to form the unstable H_{red}-CO state. It has been proposed that the H_{sred}-CO state is stable towards degradation,[152] however this is difficult to verify experimentally, as exposure to CO at a very reducing potential (-0.8 V) will result only in the transient formation of the H_{sred}-CO state; the super-reduced state has a very low affinity for CO, meaning that upon formation of the inhibited state CO is rapidly released, regenerating active states of the H-cluster. To maximise the formation of the inhibited super-reduced state the enzyme was exposed to 100% CO by gas flow for 10 minutes at -0.8 V (Figure 55). The CO was then flushed out of the cell by N_2 and the recovery of activity monitored. The experiment was then repeated at -0.4 V, a potential not expected to be reducing enough to generate the H_{sred}-CO state.[82,85,86]

The variation in both the extent and irreversibility of inhibition is much more potential dependent for *Ca*HydA than *Dd*HydAB, shown by the experiments in both Figure 53 and Figure 55. For *Ca*HydA (Figure 55, top), 98% of the H_2 production activity is inhibited in the presence of 100% CO at -0.4 V (left), but at -0.8 V a limiting current is not reached and 45% of the H_2 production activity still remains after 600 s CO exposure (right). Upon removal of the CO 12% of the initial activity is recovered at -0.4 V (inhibition is 90% irreversible, Equation 3.1) for *Ca*HydA, whereas there is no activity restored at -0.8 V (inhibition is 100% irreversible).

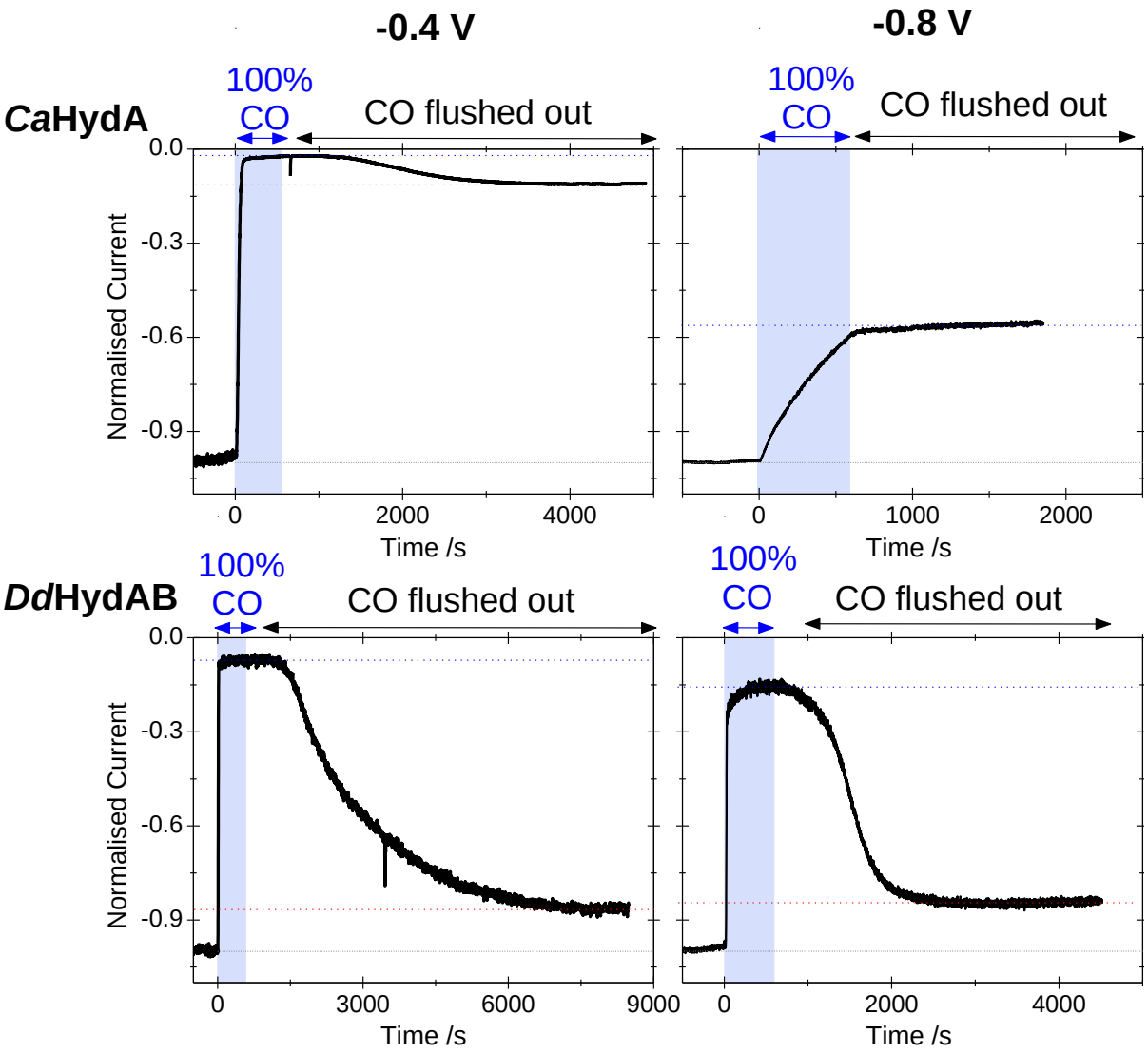

Figure 55: Chronoamperometry experiments comparing the stability of *Ca*HydA (left) and *Dd*HydAB (right) in the presence of high CO concentration at both a mildly (-0.4 V, top) and a strongly reducing potential (-0.8 V, bottom). Conditions: 100% N_2followed by 100% CO for 600 s then returned to 100% N_2, pH 6 phosphate buffer, 5 °C, ω = 3000 rpm, in the dark. Dashed lines mark the initial current (black, normalised to -1), the activity inhibited in CO (blue) and the activity recovered after removal of CO (red).

The potential dependence is much less pronounced for *Dd*HydAB (Figure 55, bottom) under such a high CO concentration. At -0.4 V (left) 93% of activity is inhibited, and 87% of the initial activity is recovered when CO is removed (inhibition is 14% irreversible). At -0.8 V (right) 84% of activity is lost, and 85 % of the initial activity is recovered (inhibition is 18% irreversible).

These differences are surprising given that *Dd*HydAB has been reported to have a greater affinity for CO than *Ca*HydA;[76] yet *Ca*HydA is inhibited to a greater extent at -0.4 V (98%) than *Dd*HydAB (93%), although this difference is small. The opposite trend is seen at -0.8 V, where inhibition of *Dd*HydAB is much greater (84%) and more rapid than for *Ca*HydA (45% after 600 s). At both potentials studied inhibition by CO is more irreversible for *Ca*HydA; 90% and 100% at -0.4 V and -0.8 V respectively for *Ca*HydA compared to 14% and 18% at -0.4 V and -0.8 V respectively for *Dd*HydAB. For each hydrogenase the difference in irreversibility at both potentials studied is very small; irreversibility of inhibition is not very potential dependent at these high CO concentrations. It is therefore not possible confirm the relative stability of the H_{red}-CO and H_{sred}-CO states.

3.4.6.2 Extent of CO Inhibition

The smaller extent of CO inhibition observed at more reducing potentials in the experiments shown in Figure 53 is explained by the preference of CO for binding to more oxidised states of the H-cluster, as indicated from the voltammograms in Figure 43. At potentials were the enzyme catalyses H_2 production, inhibition occurs by trapping of the H_{ox} state formed transiently during catalysis. As the potential is lowered, the rate of reduction of this state (H_{ox} to H_{red}) by electrons supplied by the electrode is more rapid, resulting in a shorter lifetime of this state, and therefore a lesser degree of inhibition. For experiments performed on *Dd*HydAB, even in the presence of just 0.2% CO, there is only a small spread in the extent of inhibition over this potential range, due to the very high sensitivity of the enzyme to CO.[76] The potential dependence of the extent of CO inhibition for *Ca*HydA and *Cr*HydA1 determined from chronoamperometry experiments such as those in Figure 53 is shown in Figure 56, fitted to a Nernstian sigmoid using Microsoft Excel Solver.

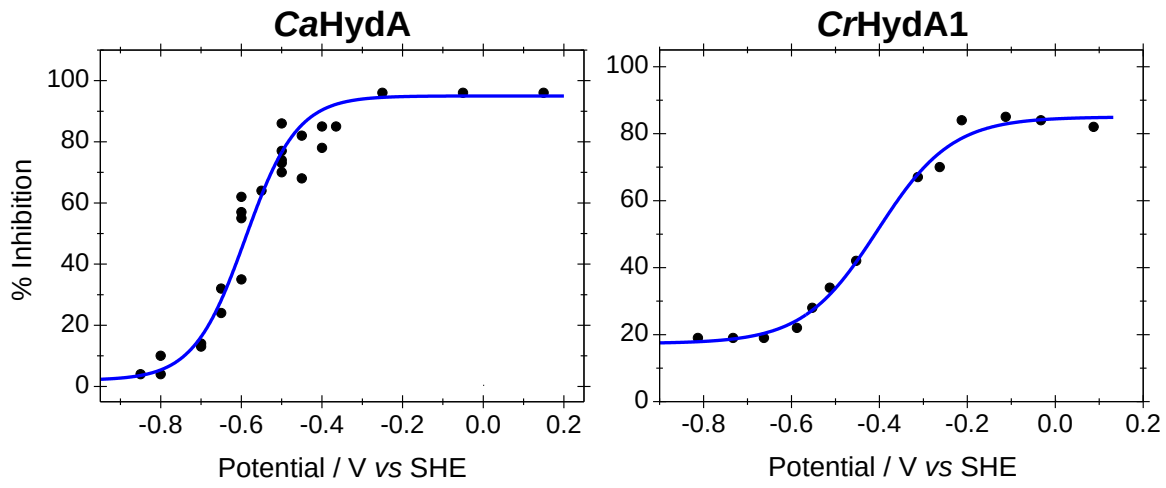

Figure 56: Plots showing the potential dependence of the extent of CO inhibition of *Ca*HydA (left) and *Cr*HydA1 (right). The extent of inhibition was measured after 100 s exposure to 10% CO (107 µM) for *Ca*HydA and after 200 s exposure to 2% CO (21.4 µM) for *Cr*HydA1. The data is shown fitted to a single nernstian sigmoid (blue) (fitted using Microsoft Excel Solver) Conditions: pH 6 phosphate buffer, ω = 3000 rpm, 20 °C, in the dark, 80% H_2, 20% (N_2+CO). [A lower concentration of CO was used for *Cr*HydA1, due to the greater CO affinity of this enzyme, to ensure good data spread] Data was acquired using chronoamperometry experiments such as those shown in Figure 53.

There are less data points in the region -0.35 to -0.45 V for *Cr*HydA1 (Figure 56, right) than *Ca*HydA (left) due to the lower activity of this enzyme sample; there is very little driving force for H_2 production in this potential region, and the H_2 production activity of *Cr*HydA1 was not sufficient for a chronoamperometry experiment to be performed at these potentials. Although the sigmoids shown in Figure 56 (blue) fit well to both the data sets, for both hydrogenases the value of n was less than one (0.4). The n value represents the number of electrons involved in the reaction,[156] so a value of less than one is not physically possible. The data was therefore fitted to two n = 1 sigmoids as described below, to model a reaction with two sequential one electron steps.

The values of F (Faraday's constant, the magnitude of electric charge per mole of electrons) and R (ideal gas constant) are known constants, and T (in K) and E (in V *vs.* SHE) are experimental parameters. Microsoft Excel Solver was used to vary the parameters E_1^0, E_2^0, ΦH_{ox}, $\Phi H_{ox\text{-}1}$ and $\Phi H_{ox\text{-}2}$ to find the best fit of the experimental data to the equation:

$$\%\ \boldsymbol{inhibition} = \mathbf{100} - (\%\boldsymbol{H_{ox}}.\boldsymbol{\phi H_{ox}} + \%\boldsymbol{H_{ox-1}}.\boldsymbol{\phi H_{ox-1}} + \%\boldsymbol{H_{ox-2}}.\boldsymbol{\phi H_{ox-2}})$$

This equation was derived as shown below.

Consider 3 oxidation levels:

$$H_{ox} \underset{}{\overset{E_1}{\rightleftharpoons}} H_{ox-1} \overset{E_2}{\rightleftharpoons} H_{ox-2}$$

The H_{red} state is at the H_{ox-1} oxidation level, and the H_{sred} state at H_{ox-2}.

From the Nernst equation the equilibrium potentials can be expressed:

$$E_1 = E_1^0 - \frac{RT}{n_1 F} ln\left[\frac{H_{ox-1}}{H_{ox}}\right] \quad \textbf{and} \quad E_2 = E_2^0 - \frac{RT}{n_2 F} ln\left[\frac{H_{ox-2}}{H_{ox-1}}\right]$$

The total hydrogenase concentration ($[H]_0$) is the sum of the concentrations of hydrogenase in each of the three oxidation levels:

$$[H]_0 = [H_{ox}] + [H_{ox-1}] + [H_{ox-2}]$$

The percentage of hydrogenase in each oxidation level can be expressed as a function of potential:

$$\%H_{ox} = \frac{[H_{ox}]}{[H]_0} \times 100 = \frac{100}{1 + exp\left(\frac{n_1 F}{RT}\Delta E_1\right) + exp\left(\frac{n_2 F}{RT}\Delta E_2\right)}$$

$$\%H_{ox-1} = 100 - \%H_{ox} - \%H_{ox-2}$$

$$\%H_{ox-2} = \frac{[H_{ox-2}]}{[H]_0} \times 100 = \frac{(100 - \%H_{ox}).exp\left(\frac{n_2 F}{RT}.\Delta E_2\right)}{1 + exp\left(\frac{n_2 F}{RT}.\Delta E_2\right)}$$

Where $\Delta E_i = E_i^0 - E$

For hydrogenase in each oxidation level there are two possibilities; it is either active or inhibited.

$$H_i^{active} \underset{}{\overset{CO}{\rightleftharpoons}} H_i^{inhib}$$

$$[H_i] = [H_i^{active}] + [H_i^{inhib}]$$

The fraction of active enzyme (ϕ_i) for each oxidation level is:

$$\phi_i = \frac{[H_i^{active}]}{[H_i]}$$

The percentage of inhibited enzyme can then be expressed:

$$\%\ \boldsymbol{inhibition} = \mathbf{100} - (\%\boldsymbol{H_{ox}}.\boldsymbol{\phi H_{ox}} + \%\boldsymbol{H_{ox-1}}.\boldsymbol{\phi H_{ox-1}} + \%\boldsymbol{H_{ox-2}}.\boldsymbol{\phi H_{ox-2}})$$

The model is however limited;

- the potentials calculated (E_1 and E_2) are equilibrium potentials for the transitions between enzyme at each oxidation level, in both the active and inhibited states.

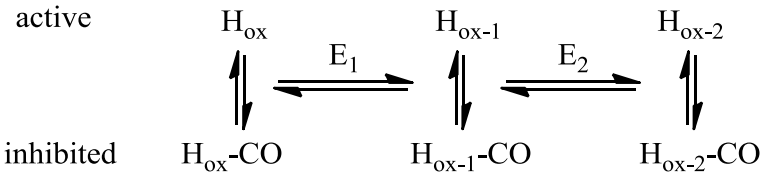

– the proportion of enzyme (Φ_i) at each oxidation level that is in the active (uninhibited) state is fitted as a potential independent parameter, which is not likely to be the case.

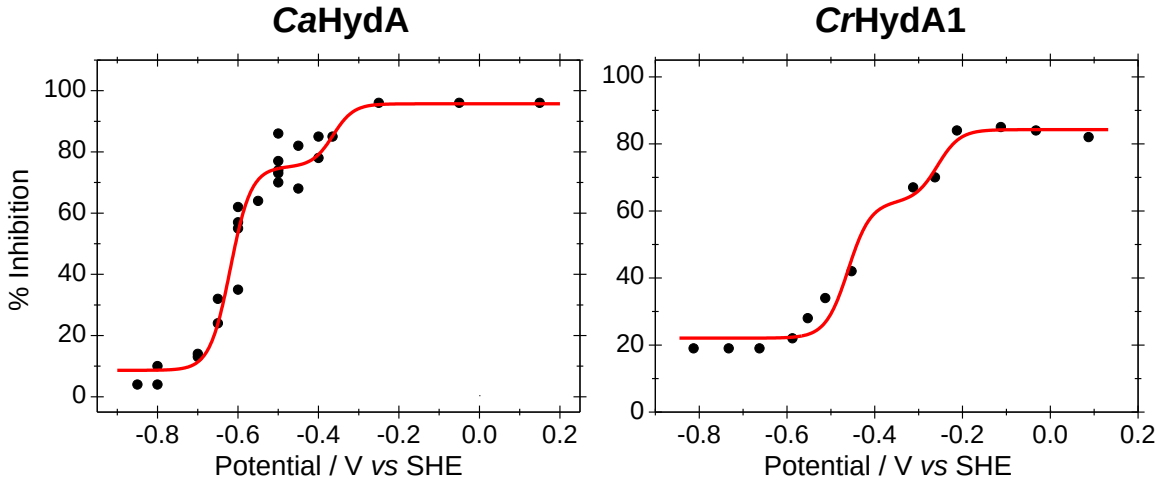

Figure 57: Plots showing the potential dependence of the extent of CO inhibition of *Ca*HydA (left) and *Cr*HydA1 (right). The extent of inhibition was measured after 100 s exposure to 10% CO (107 µM) for *Ca*HydA and after 200 s exposure to 2% CO (21.4 µM) for *Cr*HydA1. The data is shown fitted to two n=1 sigmoids (fitted using Microsoft Excel Solver). Conditions: pH 6 phosphate buffer, ω = 3000 rpm, 20 °C, dark, 80% H_2, 20% (N_2+CO).

Table 2: The equilibrium potentials (E_1 and E_2) and proportions of enzyme at each oxidation level that is in the active state (Φ_i) calculated for both *Ca*HydA and *Cr*HydA1.

	E_1	E_2	ΦH_{ox}	ΦH_{ox-1}	ΦH_{ox-2}
***Ca*HydA**	-0.36 V	-0.62 V	0.04	0.25	0.91
***Cr*HydA1**	-0.26 V	-0.48 V	0.16	0.33	0.80

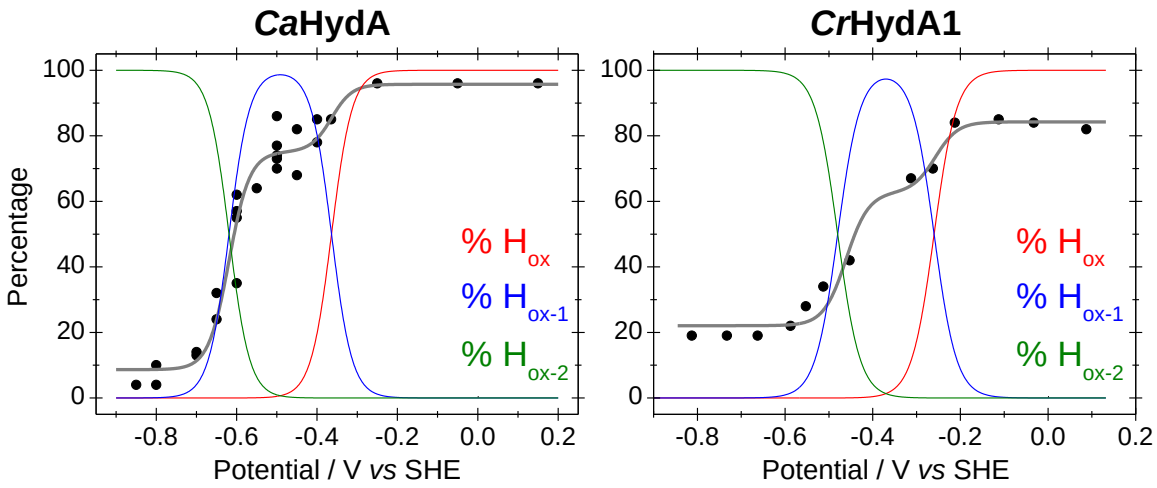

Figure 58: Plots showing the potential dependence of the extent of CO inhibition (black circles) of *Ca*HydA and *Cr*HydA1 as above (Figure 26). The grey line shows the double sigmoid fit. The overlaid coloured lines show the change in proportion of active enzyme with potential for each of the 3 oxidation levels considered to be involved over this potential range.

The data in Figure 57 and Figure 58 is shown fitted to a double sigmoid, which fits well for both *Ca*HydA (left) and *Cr*HydA1 (right). The parameters for the double sigmoidal fit are summarised for *Ca*HydA and *Cr*HydA1 in Table 2. In Figure 58 the proportions of the enzyme at each oxidation level (H_{ox}, H_{ox-1} and H_{ox-2}) is also plotted (coloured lines). Carbon monoxide binds most strongly at high potentials, where H_{ox} is the dominant species, less strongly to a state one electron more reduced, at the H_{ox-1} level (H_{red} state) and only binds very weakly at the H_{ox-2} oxidation level (H_{sred}). This double sigmoidal fit, corresponding to two one electron Nernstian processes, confirms that it is the super-reduced state H_{sred}-CO (H_{ox-2}-CO) that releases CO to reactivate the enzyme; a two electron reduction reaction is required to reactivate the inhibited H_{ox}-CO state.

3.5 Summary

The work presented in this chapter provides insight into the very strong potential dependence of inhibition of [FeFe]-hydrogenases by CO, and provides strong experimental evidence for the formation of a super-reduced state of the H-cluster. This state is two electrons more

reduced than the H_{ox} state, is active, stable and has a very low affinity for CO. This information is useful when considering the use of [FeFe]-hydrogenases in technological application involving CO contamination such as those described in Chapter 1; if the potential in such a system is low (< -0.5 V) inhibition by CO is therefore minimal. This potential dependence of the extent of CO inhibition is observed for all three [FeFe]-hydrogenases studied, despite their differing structures and topologies away from the active site (Chapter 1, Figure 3). This suggests that the potential dependence of the rate and extent of reaction [FeFe]-hydrogenases with CO results predominantly from electronic changes at or close to the active site with potential, and not from a structural change in the protein structure limiting CO transport.

The strong potential dependence of CO inhibition is demonstrated by cyclic voltammograms performed in the presence of CO (Figure 43); inhibition of H_2 oxidation activity is much greater than that of H_2 production activity. Enzyme activation is observed as a steep change in the gradient as the potential is lowered, corresponding to the release of CO from an inhibited state to regenerate active enzyme. Data in Figure 58 shows that this reduced inhibited state is H_{sred}-CO. The voltammetry experiments in Figure 43 therefore prove that the H_{sred} state of [FeFe]-hydrogenase is active for all three hydrogenases studied; the release of CO from this state is observed as a rapid increase in the H_2 production current. The H_{sred} state generated by CO release is therefore active; if the H_{sred} state were inactive, as suggested from IR studies of *Dd*HydAB[82] and *Cp*I,[86] the voltammetry experiments would not reveal any activation at low potential.

Inhibition of [FeFe]-hydrogenase is therefore very small at very reducing potentials (Figure 57), as the H_{sred} state, formed electrochemically, has a very low affinity for CO. Chronoamperometry experiments (Figure 42) show that this super-reduced state is stable for

all three hydrogenases studied; none of the H_2 production activity at -0.45 V is lost after exposure to -0.7 V for several minutes (to generate H_{sred}). This supports the observed stability of a super-reduced state of *Cr*HydA1 measured by FTIR experiments[85] but contradicts the findings of similar FTIR studies on *Dd*HydAB[82] where formation of the super-reduced state was found to be largely irreversible.

The release of CO from the inhibited H_{sred}-CO state is extremely rapid (Figure 47), and much faster than the rate of CO binding for *Ca*HydA and *Cr*HydA1, as evidenced by the hysteresis in the voltammograms of these hydrogenases in the presence of CO (Figure 43). This hysteresis is not seen for *Dd*HydAB, as the rate of CO re-binding is faster for this enzyme.[76] Although the rate of recovery from CO inhibition has previously been found to be both potential and hydrogenase independent,[76] the potential of activation (CO release from the H_{sred}-CO state) is different for the three hydrogenases studied, decreasing in the order Ca > Cr > Dd (Figure 44). A significantly stronger driving force (reducing potential) is required to initiate CO release for *Cr*HydA1 and *Dd*HydAB than for *Ca*HydA. This corresponds with the order for the rate and extent of CO binding, which increases in the order Ca < Cr < Dd;[76] the greater activation potential for CO release reflects the great affinity of the oxidised state of these enzymes for trapping the released CO.

The chronoamperometry experiments shown in Figure 47 reveal that release of CO from inhibited states of *Ca*HydA at -0.5 V can be initiated by a short (2 s) pulse to -0.8 V; reduction of the H_{ox}-CO inhibited state to form the H_{sred}-CO state is rapid at this potential. This reduction is complete; all inhibited molecules are reduced and release CO. A second pulse (before all the enzyme can be re-inhibited) does not activate the enzyme to a greater level than the first (Figure 47). The rate of CO re-binding after a low potential pulse is no greater than for exogenous CO (Figure 48), suggesting that the released CO completely exits

the enzyme during this short potential pulse. For *Dd*HydAB a longer pulse length (20 s) is required for CO release to occur, there is no activation observed after 2 s. This reflects the higher affinity of this enzyme for CO and the lower potential required to fully reduced inhibited enzyme to the H_{sred}-CO state, as measured in Figure 44.

The high sensitivity of [FeFe]-hydrogenases to irreversible damage by O_2 is a well documented limitation, O_2 binds rapidly to oxidised states of the H-cluster, and results in irreversible enzyme degradation.[98,141] A remarkable tolerance of enzyme activity in the presence of high O_2 concentrations has now been demonstrated at low potentials (Figure 51). The binding of O_2 to the H-cluster is very similar to that of CO, both bind directly at the distal iron.[141,147] The most reduced states of the H-cluster have a very low affinity towards both inhibitors and activity is retained even under high inhibitor concentrations (Figure 51). The low affinity of reduced states of the H-cluster towards both CO and O_2 is also observed for sulfide.[143] Sulfide inhibition only occurs at oxidising potentials (> 0 V) while reactivation of the inhibited state only occurs when the enzyme is exposed to sufficiently reducing potentials (< -0.4 V). The reaction of [FeFe]-hydrogenases with O_2 differs from reaction with CO (Figure 47) or sulfide[143] in that exposure to the inhibitor at high potential cannot be reactivated by exposure to low potential, as high potential irreversible degradation of the O_2 inhibited state is so rapid.[139]

A strong potential dependence of the reversibility of reaction of [FeFe]-hydrogenase with CO was discovered, complementary to that of the extent of inhibition (Figure 54). The fraction of activity inhibited by CO that is not recovered upon removal of CO is attributed to formation of the unstable H_{red}-CO state. This state degrades irreversibly, via loss of the Fe_p-S_{cys} bond (Scheme 5), forming an inactive state.[152] At higher potentials, the extent of inhibition is very high, reflecting the preference of CO for binding to the H_{ox} state, and the reaction is almost

completely reversible. At higher potentials the enzyme remains in the H_{ox}-CO state, and is not reduced to form the unstable H_{red}-CO state. At more reducing potentials where the extent of inhibition is lower, the reversibility of inhibition also decreases. At these potentials more of the inhibited enzyme is reduced to the H_{red}-CO state, resulting in irreversible degradation. The different reactions of CO with [FeFe]-hydrogenase are summarised in Scheme 8 as the potential is varied.

Scheme 8: The different reaction of [FeFe]-hydrogenase with CO at different potentials.

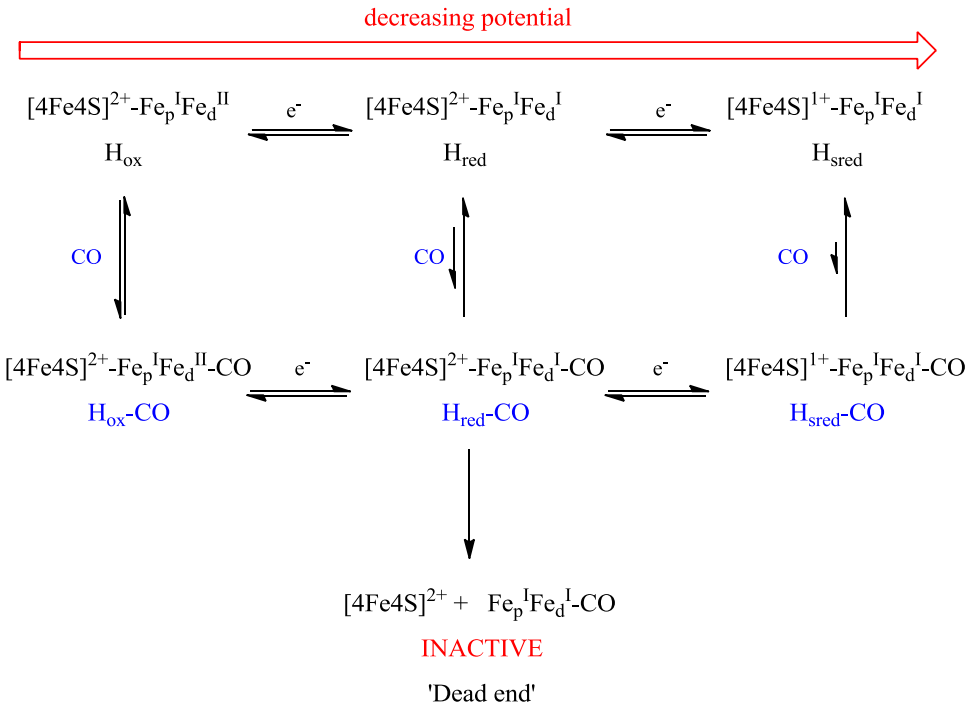

It might be expected that at very reducing potentials inhibition of CO may become more reversible, as inhibited enzyme can be fully reduced to the H_{sred}-CO state, a state not believed to degrade.[152] This trend however is not seen (Figure 54); inhibition is less reversible for *Ca*HydA and *Cr*HydA1 at very low potentials (-0.6 to -0.8V, Figure 54) than at more mildly reducing potentials (-0.4 to -0.6 V). This shows that while at more mildly reducing potentials only some of the inhibited enzyme is reduced to form the unstable H_{red}-CO state, at more reducing potentials almost all inhibited enzyme molecules form this state. If any inhibited

enzyme is fully reduced to the H_{sred}-CO state, it rapidly releases CO, re-entering the catalytic cycle, and thus this inhibition is not observed electrochemically.

The large difference in the reversibility of CO inhibition of *Ca*HydA and *Dd*HydAB recorded in 100% CO (Figure 55) is not fully understood; reaction of *Ca*HydA is almost completely irreversible while very little activity of *Dd*HydAB is irreversibly lost in CO. Given that irreversible inhibition results from degradation of the H_{red}-CO state the significantly smaller extent of irreversible loss observed for *Dd*HydAB could be related to several factors:

(1) **A more reducing midpoint potential for the H_{ox}-CO/H_{red}-CO transition.** The H_{ox}-CO does not degrade;[152] if reduction of this state to form the unstable H_{red}-CO state is more difficult there will be less irreversible degradation observed.

(2) **Greater stability of the H_{red}-CO state.** The Fe_p-S_{cys} bond is broken to irreversibly form an inactive state,[152] however if this state is more stable towards degradation, less of the inhibition will be irreversible.

(3) **A less reducing midpoint potential for the H_{red}-CO/H_{sred}-CO transition.** If this transition occurs more readily the enzyme will spend less time in the unstable H_{red}-CO state, resulting in less irreversible degradation.

It is not possible to determine which, if any of these factors explain the high reversibility of CO inhibition observed for *Dd*HydAB (Figure 55), however option (3) is highly unlikely. The voltammograms recorded in Figure 44 indicate that the H_{red}-CO/H_{sred}-CO transition occurs at a more reducing potential for *Dd*HydAB (-0.70 V) than for *Ca*HydA (-0.64 V). Additionally option (2) is unlikely as the H-cluster is highly conserved in [FeFe]-hydrogenases. This leaves

option (1), the H_{ox}-CO/H_{red}-CO potential, the investigation of which would be an excellent continuation of these studies.

Chapter 4

Formaldehyde Inhibition

Abstract

The electrochemical studies outlined in this chapter investigate the potential dependence of aldehyde inhibition of [FeFe]-hydrogenases. It was found that formaldehyde binds preferentially to the most reduced state of the H-cluster, assigned as the super-reduced state (H_{sred}). This directly contrasts with the potential dependence of CO binding outlined in Chapter 4. The ability of aldehydes to trap and stabilise this redox state of the H-cluster may be exploited to allow spectroscopic characterisation of this state (Chapter 6). The potential and rate at which formaldehyde binds and is released from the H-cluster was investigated. It was found that activation can be rapidly induced by modulation of the potential in a similar manner to CO; inhibition at low potential is reversed by exposure to more oxidising potentials. In contrast to CO however, re-binding of formaldehyde after the change in potential is too rapid to be observed; activity is inhibited immediately upon returning to reducing potentials.

Binding of formaldehyde is shown to protect the enzyme against irreversible O_2 damage, suggesting that formaldehyde competes for binding at the distal iron site (Fe_d) of the H-cluster, supported by DFT studies performed by Tobias Kraemer. It is proposed that Fe_d in the H_{sred} state donates a hydride to the aldehyde, leading to formation of a formaldehyde bound state involving an Fe_d-O bond. It is also suggested that the super-reduced state of the H-cluster is involved in the mechanism of catalytic H_2 production by [FeFe]-hydrogenase.

Formaldehyde is shown to bind to the H-cluster at very oxidising potentials (> 0 V). The rate and nature of this binding was investigated and experiments suggest that reversible formaldehyde binding occurs more readily than oxidation to generate the inactive H_{ox}^{inact} state. Additionally formaldehyde is shown to limit the extent of high potential inactivation, attributed to the presence of formaldehyde preventing formation of the H_{ox}^{inact} state.

4.1 Introduction

4.1.1 Reactions of Formaldehyde

Formaldehyde, or methanal, is the simplest form of aldehyde, with the molecular formula CH_2O. Aldehydes are organic molecules with the general formula RCHO, and in formaldehyde the -R group is simply a proton (HCHO). Formaldehyde is a small molecule, similar in size to water, but has a very low boiling point (19 °C) and exists as a colourless, pungent gas at room temperature[157], as the hydrogen bonds formed between water molecules do not exist to the same extent for formaldehyde. Aldehydes are highly vulnerable to nucleophilic attack at the electrophilic carbonyl site (C=O) and formaldehyde is particularly reactive as the carbonyl bond is sterically unhindered. Formaldehyde can be dissolved in water to form the commercial solution formalin, consisting of 30-50% formaldehyde by mass. In solution formaldehyde exists in equilibrium with the hydrated form (methanediol), generated by nucleophilic attack of an –OH group from a water molecule on the carbonyl bond of the aldehyde, as shown in Scheme 9.

Scheme 9: The reaction of formaldehyde with water to form the hydrate methandiol.

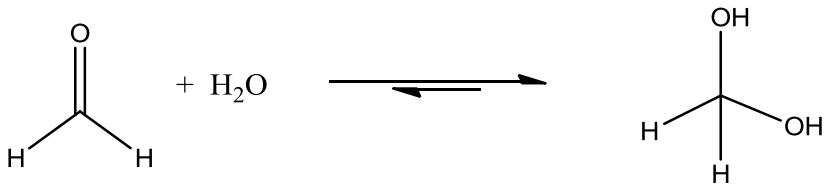

The equilibrium constant of this reaction, K_{eqm}(hydration), is large (~2000 at 25 °C[158]) as there are no bulky electron donating alkyl groups to lower the electrophilicity of the carbonyl bond. The nucleophilic -OH groups of the hydrated aldehyde can attack the carbonyl bonds of non-hydrated aldehyde molecules, resulting in polymerisation to form paraformaldehyde, as shown in Scheme 10.[157]

Scheme 10: The reaction of formaldehyde with methanediol leading to polymerisation.

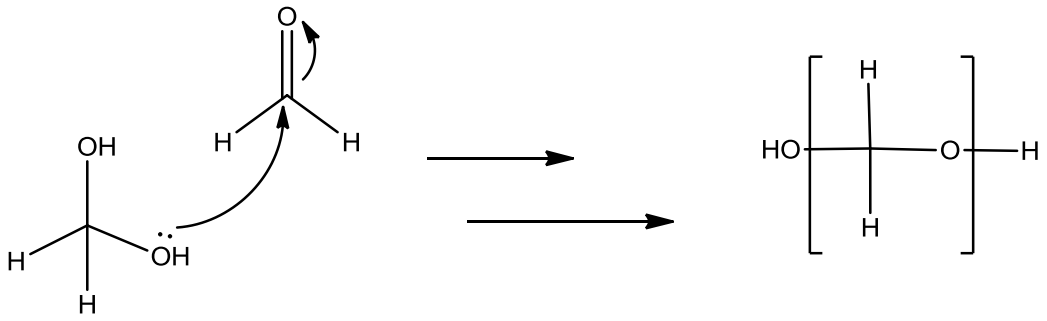

To avoid excessive polymerisation a small amount of stabiliser, such as methanol, is usually added; typically a formalin solution will contain 10–12% methanol.

In addition to being a useful building block for synthesis of more complex organic compounds, formaldehyde is also used as a disinfectant and biocide; it kills most bacteria and fungi and can inactivate bacterial products. Additionally formaldehyde solutions are used as preservation agents for biological specimens. Tissue and cells are 'fixed' by a combination of reversible and irreversible cross-linking of amine groups in proteins with other nitrogen atoms in protein or DNA via a $-CH_2-$ linkage.[159] Initial stages are rapid and reversible; nucleophilic N atoms of an amine group (lysine residues) attack the aldehyde carbonyl bond in a Schiff base reaction (Scheme 11). This reaction can be used to methylate lysine residues if the Schiff base adduct is reduced with an agent such as borohydride.[160]

Scheme 11: The reaction of formaldehyde with a primary amine, resulting in the formation of a Schiff base.

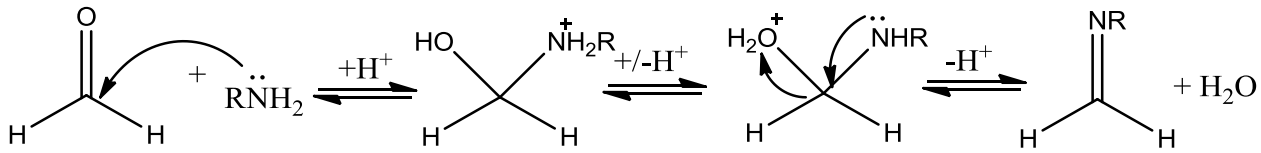

Cross-linking occurs when the nucleophilic side chain of a neighbouring amino acid attacks a protonated Schiff base adduct (Scheme 12).

Scheme 12: Example of a cross linking reaction of a protonated Schiff base adduct with a secondary amine.

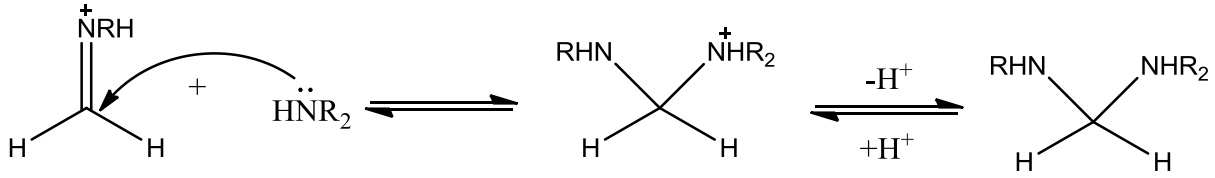

Formaldehyde can also react with nucleophilic sulfur groups, such as a cysteine residue –SH, resulting in the formation of a thioacetal.

Scheme 13: The reaction of formaldehyde with a thiol group, resulting in formation of a thioacetal.

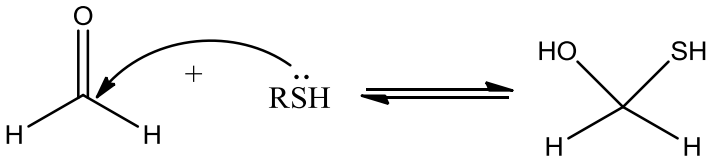

The biocide applications of formaldehyde lead to the speculation that it is likely to irreversibly inhibit enzyme catalysis by causing irreversible enzyme degradation. Electrochemical studies performed by Wait *et al.* have however shown that formaldehyde is in fact a rapid and reversible inhibitor of [FeFe]-hydrogenases.[161]

4.1.2 Formaldehyde as a Hydrogenase Inhibitor

In the early 1980s studies by Slatyer *et al.*[162] showed that the H_2 oxidation activity of the hydrogenase from *Anabaena cylindrica* is inhibited by acetaldehyde (ethanal, R = CH_3). There was no recovery of catalytic activity after the cells were washed with fresh medium, leading to the conclusion that aldehyde inhibition is irreversible. In contrast, solution assays and EPR studies by Rao *et al.*[163] found that the hydrogenases from both *Clostridium pasteurianum* and *Desulfovibrio desulfuricans* were unaffected by the presence of either acetaldehyde or glutaraldehyde.

More recently protein film electrochemistry studies carried out in the group of Prof. Fraser Armstrong by Annemarie Wait have shown that formaldehyde is a potent inhibitor of three [FeFe]-hydrogenases, *Ca*HydA, *Cr*HydA1 and *Dd*HydAB despite their differing structures and topologies away from the active site.[161,164] Aldehyde is thought to enter the enzyme in the non-hydrated form. Corresponding studies carried out on [NiFe]-hydrogenases revealed only a very slight degree of inhibition. Formaldehyde inhibition of [FeFe]-hydrogenase is rapid and reversible, the extent of inhibition increasing in the order *Ca*HydA << *Cr*HydA1 ~ *Dd*HydAB. This is not consistent with the trend observed for inhibition by CO which increases in the order *Ca*HydA < *Cr*HydA1 < *Dd*HydAB.[76] For CO inhibition the rates of reaction increase in the same order, while the rates of reactivation vary very little.[76] For formaldehyde inhibition the rates of inhibition and reactivation both increase in the order *Dd*HydAB < *Cr*HydA1 < *Ca*HydA.

A strong potential dependence of inhibition was established; H_2 production activity is inhibited to a far greater degree than H_2 oxidation activity. This indicates that a reduced state of the enzyme is the target of formaldehyde binding, with the target site of reaction being at, or in close proximity to, the H-cluster.

Formaldehyde inhibition was found to consist of two phases; a fast phase and a slow phase, indicating the involvement of two different reaction pathways. The proportion of reaction proceeding via each phase is potential dependent, with a greater extent of the fast phase reaction at low potential and more of the slow phase reaction at high potential. Although inhibition is reversible, the irreversibility of the reaction is also strongly potential dependent and correlates with the extent of slow phase, leading to the conclusion that the fast phase reaction is completely reversible while the slow reaction is at least partially irreversible.

Inhibition of [FeFe]-hydrogenases by longer chain aldehydes was also studied and a similar dependenceon potential was obserbed for acetaldheyde; inhibition is greater at more reducing potentials.[164] The extent of inhibition decreases with increasing chain-length for straight chain aldehydes, possibly due to more restricted access to the active site. More bulky, branched chain aldehydes only inhibit activity very weakly, and do not display the same potential dependence, indicating that these aldehydes are unable to access the buried active site.

The work carried out in this chapter is a continuation of the above studies by Annemarie Wait.

4.1.2.1 Binding Sites of Formaldehyde

The surface of [FeFe]-hydrogenases is populated with exposed cysteine, lysine and histidine residues, all of which are possible targets for reaction with formaldehyde. Reaction at the protein surface however does not correspond with the observed inhibition, which is extremely potential dependent. The strong potential dependence of formaldehyde inhibition, and the lesser degree of inhibition by branched chain aldehydes, indicate that the target site of formaldehyde binding is at, or in close proximity to, the H-cluster. There are several possible binding sites, as illustrated in Figure 59.

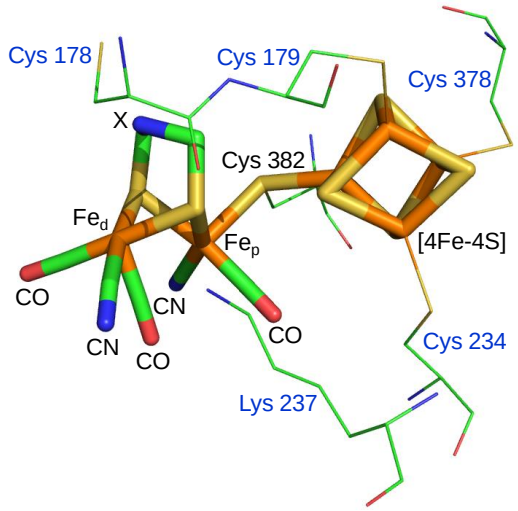

Figure 59: Structure of the H-cluster of *Dd*HydAB in the reduced state H_{red}. Reactive amino acid residues in close proximity (< 5 Å) are also shown. [57]

Figure 59 shows a representation of the H-cluster of *Dd*HydAB, showing the position of the nucleophilic amino acid residues in close proximity (< 5 Å) to the H-cluster, that are conserved in the three [FeFe]-hydrogenases studied in this chapter.[57] The observed aldehyde inhibition may be explained by reaction at either:

(1) **The bridgehead atom**. As explained in Chapter 1, there is still some scientific debate as to the identity of this atom, but it is widely believed to be a N atom, and in this thesis it is assumed to be so. Schiff base reaction could occur at this site, and block proton transfer from this site to Fe_d, the site of H_2 binding. Binding at this site may also sterically hinder catalysis.

(2) **The nucleophilc residues**. The amine and thiol side chains of the conserved surrounding amine acids (Lys237 and Cys178 in *Dd*HydAB[57]) are nucleophilic centres that could attack the carbonyl bond of formaldehyde. Crystal structures and modelling studies suggest that these sites are directly involved in proton transfer,[165] thus reaction at this site will disturb catalytic H_2 turnover.

(3) **The distal iron (Fe_d).** In reduced states of the enzyme, Fe_d might directly react with formaldehyde, blocking the site of proton binding, and inhibiting H_2 turnover.

4.2 Results

4.2.1 Potential Dependence of Formaldehyde Inhibition

Initial experiments carried out by Annemarie Wait to investigate the potential dependence of formaldehyde inhibition focussed only on *Ca*HydA and *Dd*HydAB. In this chapter the potential dependence of formaldehyde inhibition is investigated in greater detail, and includes a third [FeFe]-hydrogenase, *Cr*HydA1, to ensure the same behaviour is observed for a hydrogenase lacking the FeS-cluster relay chain. As the structures of the three

[FeFe]-hydrogenases vary (section 1.4.2), but the H-cluster is conserved in all, similarities in the reactions of these enzymes indicate that the reaction occurs at the H-cluster. Cyclic voltammograms of *Ca*HydA and *Dd*HydAB performed in the presence of formaldehyde display a characteristic wave-shape in the H_2 production region,[164,166] as described below, reflecting the greater affinity of formaldehyde for reduced states of the H-cluster. Figure 60 shows cyclic voltammograms of *Cr*HydA1 in the presence of formaldehyde, compared to voltammograms of *Ca*HydA (repeated and verified for this thesis). Voltammograms were recorded in the absence of inhibitor (black traces) and immediately after equilibration with formaldehyde (red). A diluted formaldehyde solution was prepared from a 37% by mass formalin solution using the experimental buffer. This solution was prepared in the glove box, and degassed with the experimental gas composition, and temperature equilibrated before injection in to the cell solution. The formaldehyde concentration quoted in the experiments in this chapter refers to the total aldehyde concentration; the concentration of non-hydrated formaldehyde in solution is 2000 times less (K_{eqm}(hydrate) = 2000).

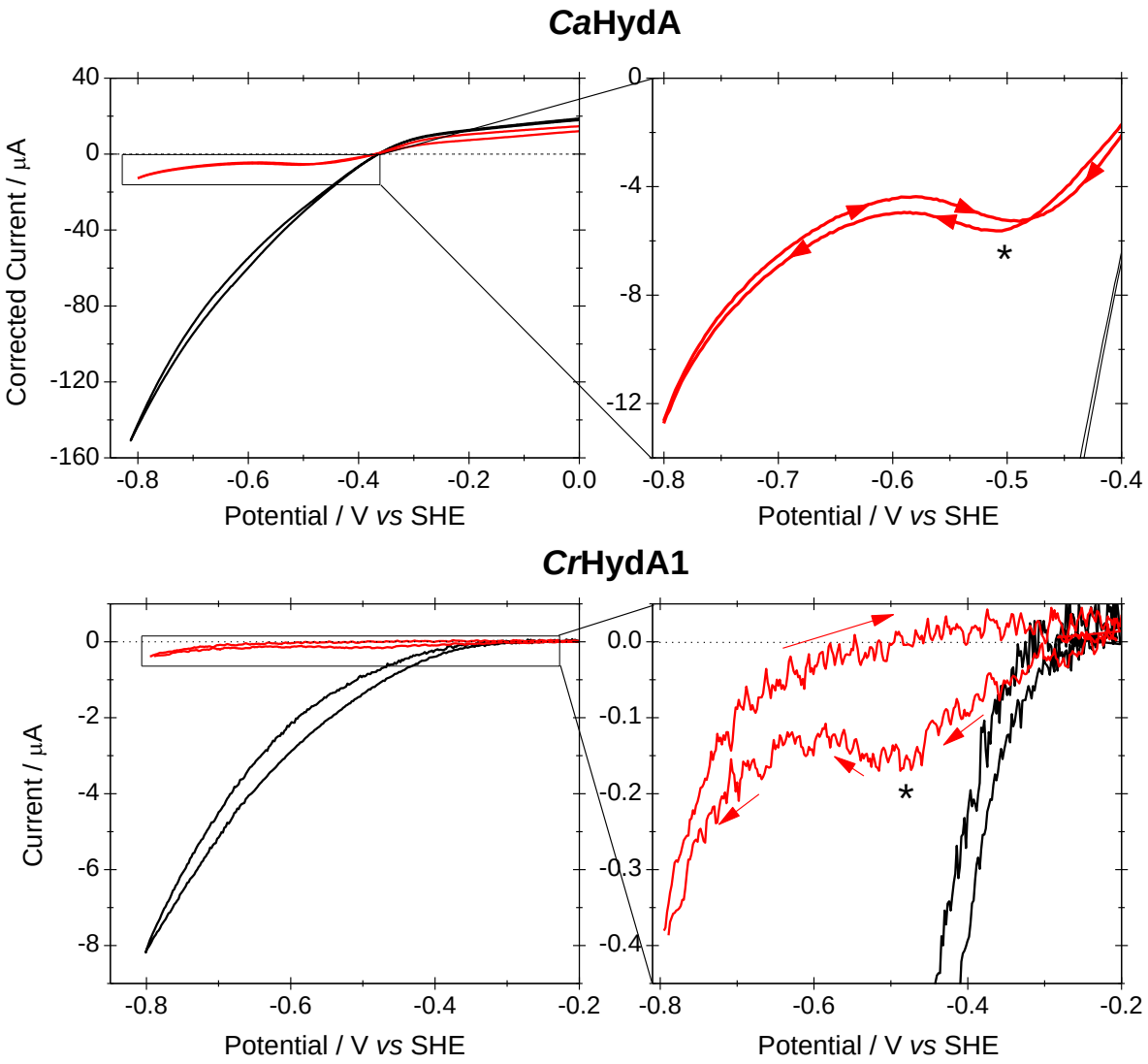

Figure 60: Cyclic voltammograms showing the effect of formaldehyde on *Ca*HydA (top) and *Cr*HydA1 (bottom). All scans commenced from the high potential limit. The black traces were recorded prior to addition of HCHO, and the red scans were performed in the presence of formaldehyde. Conditions: pH 6, ω = 3000 rpm *Ca*HydA: 33 mM HCHO, 3 mV/s, 20 °C, 100% H_2, *Cr*HydA1: 38 mM HCHO, 10 mV/s scan rate, 5 °C, 100% N_2. "Corrected current" denotes that data has been corrected for a linear loss of current over time (see Supporting Information). An asterisk marks the onset of rapid current loss at low potential.

The voltammograms of both hydrogenases shown in Figure 60 display the same characteristic wave-shape in the H_2 production region in the presence of formaldehyde. Inhibition of proton reduction activity is far greater than that of H_2 oxidation activity. For *Ca*HydA (Figure 60, top), a total concentration of 33 mM HCHO (corresponding to approximately 15 µM anhydride) results in the loss of approximately 90% of the proton reduction current at –0.8 V,

whereas 70% of the H_2 oxidation activity remains at 0 V. For *Cr*HydA1 (Figure 60, bottom), a total concentration of 38 mM HCHO (corresponding to approximately 19 μM anhydride) results in the loss of 95% of the proton reduction current at −0.8 V. Importantly both the voltammograms obtained in the presence of formaldehyde reveal a sharp transition between −0.5 and −0.6 V (asterisk on figure), superimposed on the general slope of the voltammogram. This sharp decrease in current is attributed to the increased rate of binding of formaldehyde to a reduced state of the H-cluster formed at low potential. The potential for the onset of this transition varies between the two enzymes: -0.5 V for *Ca*HydA and -0.58 V for *Cr*HydA1, partly an effect of the faster scan rate used for the *Cr*HydA1 voltammogram, but also in agreement with the faster rate of formaldehyde inhibition for *Ca*HydA.[161] The forward and reverse scans almost overlay for *Ca*HydA (Figure 60, top); the rate of reactivation is similar to the rate of inhibition, but for *Cr*HydA1 (Figure 60, bottom) reactivation is not observed in the oxidative scan. This shows that the rate of reactivation (formaldehyde release) is greater than the rate of formaldehyde re-binding for this enzyme under these conditions.

4.2.1.1 Potential of Formaldehyde Release

The variation in the extent of formaldehyde inhibition with potential was further investigated for *Ca*HydA using chronoamperometry experiments (Figure 61). The potential was stepped between values where the enzyme catalyses H_2 oxidation (-0.1 V) and H_2 production (-0.55 V). The initial current at each of these potentials was recorded before 200 mM formaldehyde was injected into the cell as shown by the red arrow in Figure 61. The potential was then stepped repeatedly between these two values in experiment (A) and gradually stepped up from -0.55 V to -0.1 V in experiment (B).

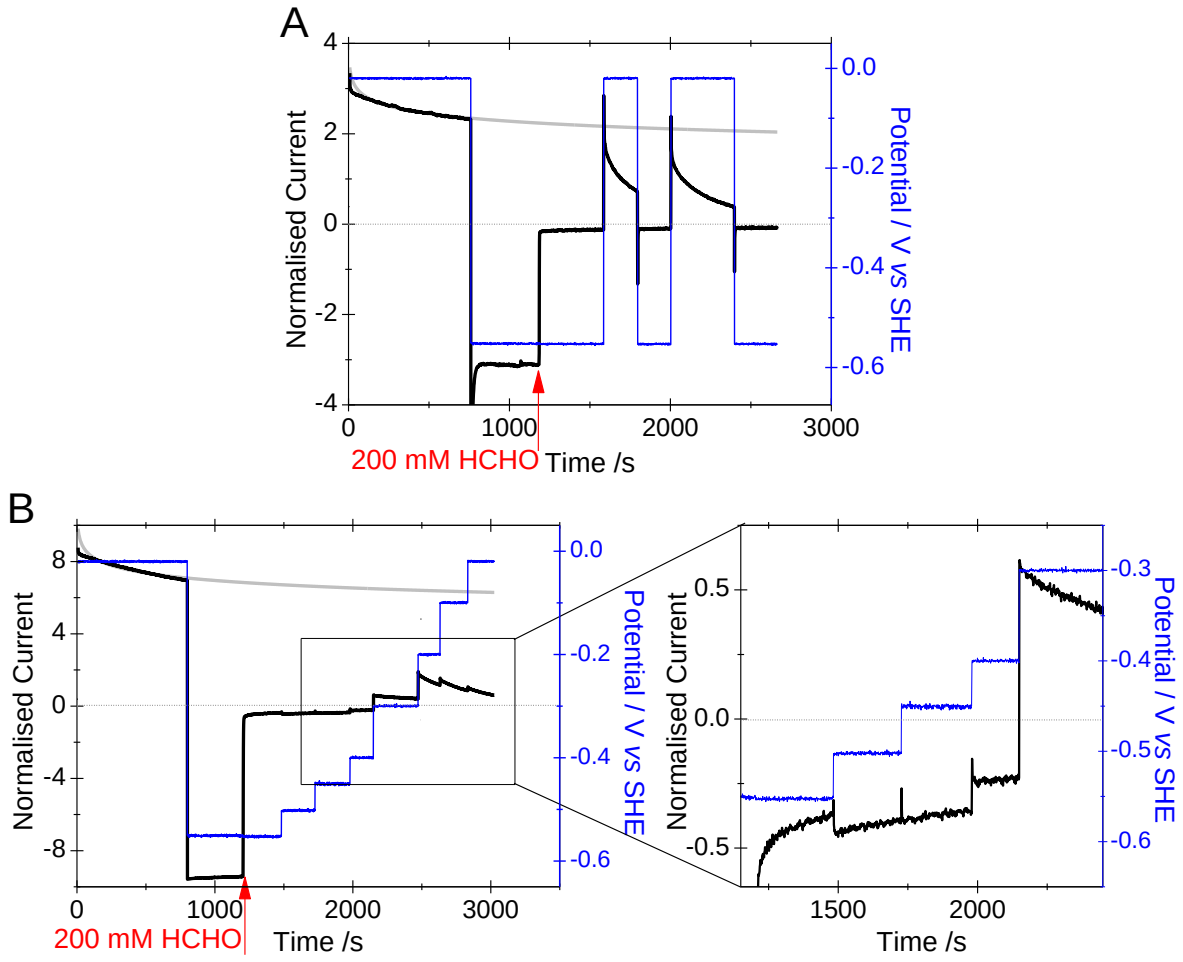

Figure 61: Chronoamperometry experiments measuring the potential dependence of the extent of formaldehyde inhibition for *Ca*HydA. The grey trace shows the exponential film loss, the blue trace shows the modulation in potential throughout the experiment. A cropped section of experiment B is shown on the right. Conditions: 10 °C, pH 6, ω= 3000 rpm, 100% H_2, 200 mM HCHO.

Stepping the potential between -0.55 V and -0.1 V in the presence of 200 mM formaldehyde (Figure 61A) reveals the great preference of formaldehyde for binding to reduced states of the H-cluster. Almost zero activity is recorded at -0.55 V, while a significant amount of the H_2 oxidation activity is retained at -0.1 V. After the step to high potential, the current rapidly peaks and then begins to exponentially decrease; exposure to high potential reactivates the formaldehyde-bound reduced state, by release of formaldehyde, and the enzyme re-enters the catalytic cycle. The gradual decrease of H_2 oxidation activity at this potential (-0.1 V) shows slow re-binding of formaldehyde; although at -0.1 V the H_{ox} state is expected to be the

dominant species, during catalysis (H_2 oxidation) reduced states of the enzyme are generated transiently, and can be trapped by formaldehyde. Figure 61B shows the reactivation of the formaldehyde-bound state as the potential is gradually increased. Although as the potential is increased, the driving force for proton reduction decreases, when the potential is stepped from -0.55 V to -0.5 V (at 1500 s) the H_2 production current increases. This step in potential is sufficient to partially activate the enzyme, forming the active H_{red} state, which re-enters the catalytic cycle. This suggests that it is not the H_{red} state that is the target of formaldehyde binding, but a more reduced (super-reduced) state.

4.2.1.2 Rate of Formaldehyde Release

Chronoamperometry experiments such as those shown in section 3.5.2 with CO, were carried out on *Ca*HydA in the presence of formaldehyde, to investigate the rate of formaldehyde release from the active site (Figure 62). In Figure 62A the potential was held at -0.55 V and the solution equilibrated with 27 mM formaldehyde before stepping the potential up to -0.02 V for short periods (5 or 20 s). If formaldehyde is released from the enzyme by a pulse to high potential, upon returning to -0.55 V the H_2 activity is expected to have increased. The current is then expected to gradually decrease as formaldehyde re-bind. In Figure 62C the converse experiment was conducted; the potential was held at -0.02 V and pulsed to -0.55 V. The H_2 oxidation activity was expected to decrease immediately after the low potential pulse, due to increased formaldehyde binding at low potential, and then increase as the formaldehyde is released at high potential.

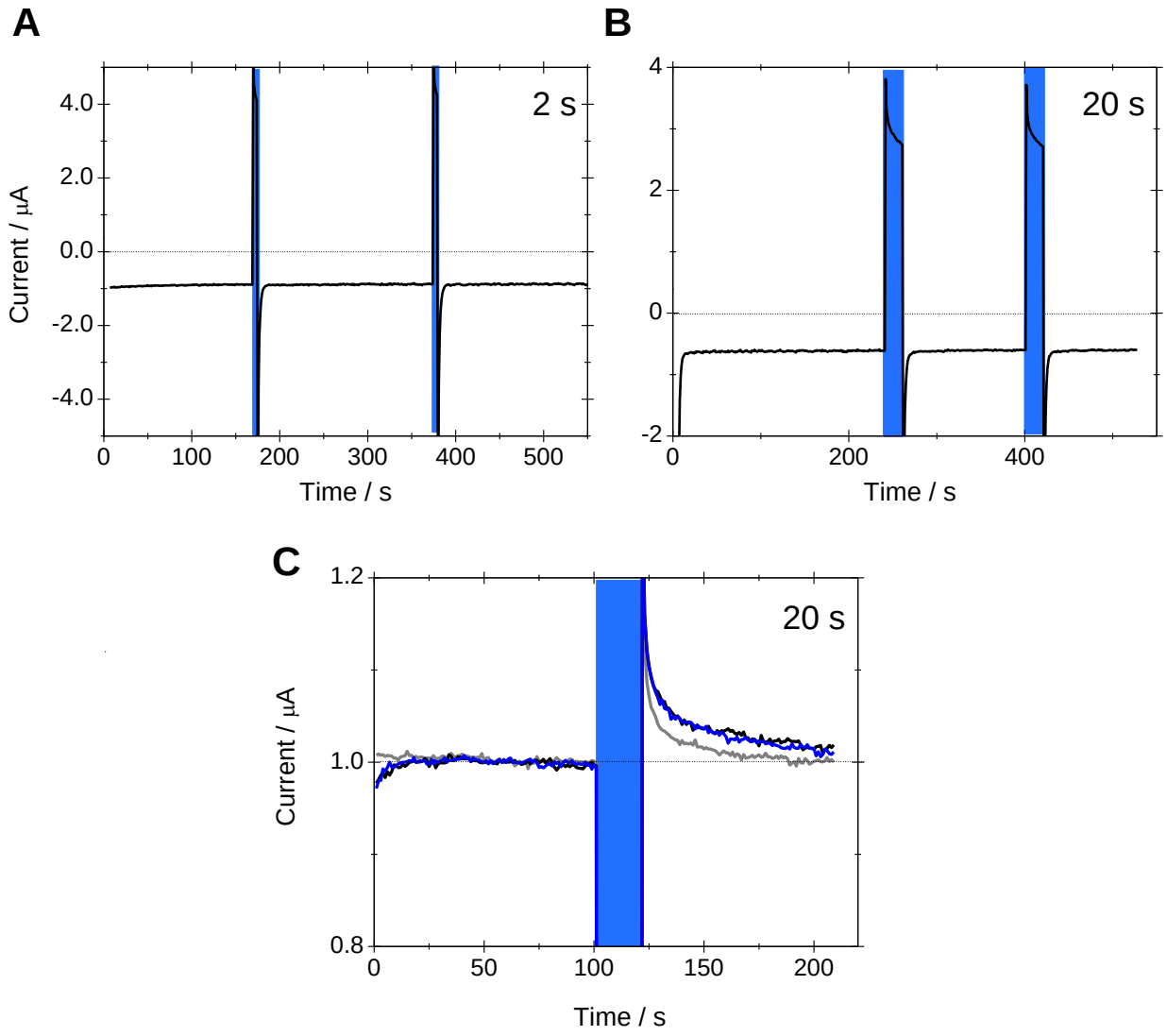

Figure 62: Chronoamperometry experiments on *Ca*HydA to investigate the rate of formaldehyde release at high potential (-0.02 V) and binding at low potential (-0.55 V) Blue boxes indicate potential pulses, from -0.55 V to -0.02 V for 2 s (A) and 20 s (B) and down from -0.02 V to -0.55 V for 20 s (C). The black and blue traces in (C) are experiments recorded in the presence of formaldehyde and the grey trace is a control experiment recorded in the absence of inhibitor. Conditions: 5 °C, pH 6, ω = 3000 rpm, 100% H_2, 27 mM (A and B) or 10 mM (C) HCHO.

As can be seen by comparing the current traces in Figure 62A and B, the H_2 production activity of *Ca*HydA at -0.55 V in 10 mM formaldehyde is not affected by either a 2 or 20 s pulse to -0.02 V. The H_2 production activity was expected to be greater after the pulse, as the enzyme activates at high potential (Figure 61A) assumed to be the result of formaldehyde release. This indicates that re-binding of formaldehyde is extremely rapid under these

conditions; alternatively it is possible that the formaldehyde is not fully released from the enzyme molecule at high potential. The loss of H_2 oxidation activity at -0.02 V predicted after a low potential pulse (20 s at -0.55 V) is also not observed; in Figure 62C the current after the low potential pulse is not significantly greater than before the pulse. The pulses in the presence of formaldehyde (Figure 62C black and blue) result in an almost identical change in activity as the formaldehyde free experiment (grey). There is a peak in the oxidative current immediately after the potential is stepped back to -0.02 V, which then decays. This profile is not affected by the presence of formaldehyde, meaning that this current change is simply a charging current related to changes at the electrode surface. These experiments suggest that both release of formaldehyde from the enzyme, initiated at high potential, and re-binding at low potential are extremely rapid under these conditions.

4.2.2 Protection Against Oxygen

As explained in section 3.1.2.2, [FeFe]-hydrogenases are very sensitive to irreversible damage by O_2. Initial binding of O_2 occurs at the distal iron site of the H-cluster, the same site as H_2 binding.[141] The effect of the presence of formaldehyde on the extent of irreversible damage by O_2 was investigated using chronoamperometry (Figure 63). The potential was held at -0.45 V throughout the experiment in the presence of 100% N_2 before 25% O_2 was introduced to the cell for 1000 s, controlled using mass flow controllers. The effect of formaldehyde was investigated by injection of 1 ml of 134 mM formaldehyde solution into 3 ml of cell solution (total concentration = 33.5 mM) prior to introduction of O_2. After the O_2 was removed by flushing the cell with N_2 the cell solution was exchanged with fresh buffer (using the setup shown in section 2.2.4) to remove the formaldehyde. This step was also performed in the control experiment in the absence of formaldehyde.

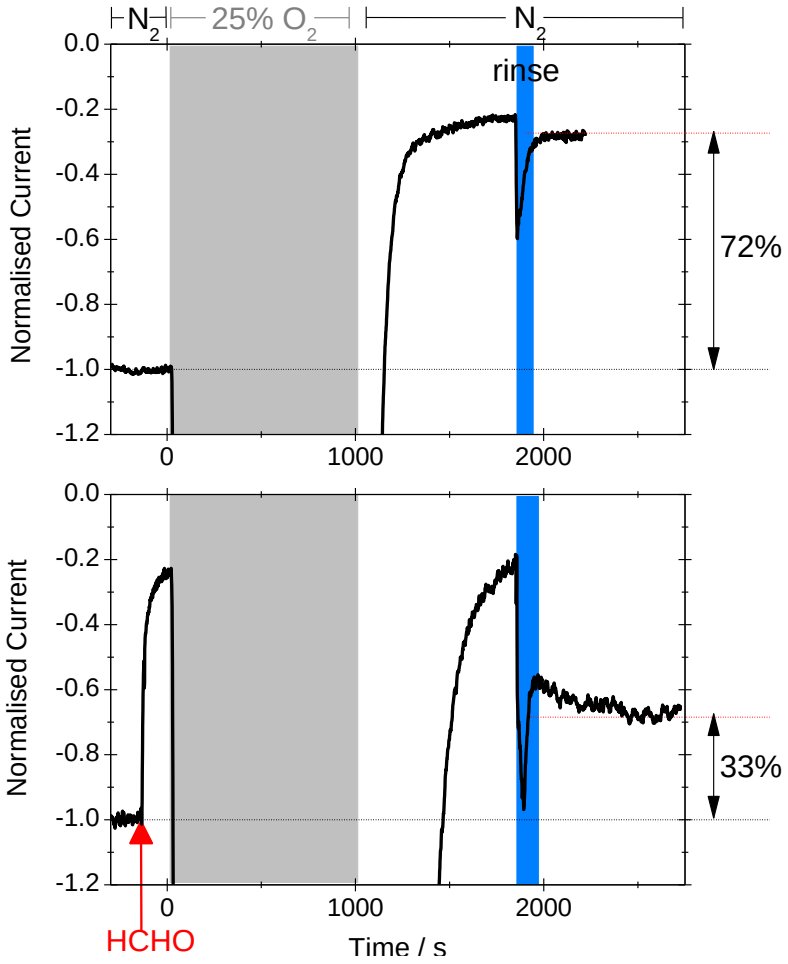

Figure 63: Chronoamperommetry experiments showing the partial protection afforded by formaldehdye for *Ca*HydA against irreversible damage by O_2. In both experiments 25 % O_2 was introduced for 1000 s (shown by grey box) by a change in the gas composition from 100 % N_2 to 25 % O_2 in N_2. In the bottom panel the red arrow indicates injection of 1 ml of 134 mM HCHO solution into 3 ml of cell solution (final [HCHO] = 33.5 mM) prior to introduction of O_2. In both experiments the cell was rinsed with 50 ml of buffer at 1850 s (blue box). Conditions: -0.45 V, 20 °C, ω = 3000 rpm, pH 6. [Under these conditions, in the presence of 25% O_2 there is a very large reduction current, this has been cropped out of view in the figures.]

The control experiment (Figure 63, top) shows that at -0.45 V exposure to 25% O_2 for 1000 s results in loss of 72% of the proton reduction activity of *Ca*HydA. The bottom panel shows that inhibition by 33.5 mM formaldehyde prior to exposure to O_2 partially protects the hydrogenase against irreversible damage; almost 70% of H_2 production activity is retained after removal of both inhibitors. This shows that formaldehyde somehow restricts access of

O_2 to the H-cluster either by physically blocking access, or by competitively binding at the same site (Fe_d).

4.2.3 Effect of Light

As demonstrated in Chapter 3 the Fe_d-CO_{exo} bond is extremely photolabile; illumination increases the rate of recovery from CO inhibition as this bond is broken. If formaldehyde binds directly to the H-cluster illumination could also be expected to increase the rate of bond (Fe_d-HCHO) breakage and the catalytic activity in the presence of formaldehyde would increase during illumination. The effect of illumination was investigated for formaldehyde inhibited [FeFe]-hydrogenase using chronoamperometry experiments (Figure 64).

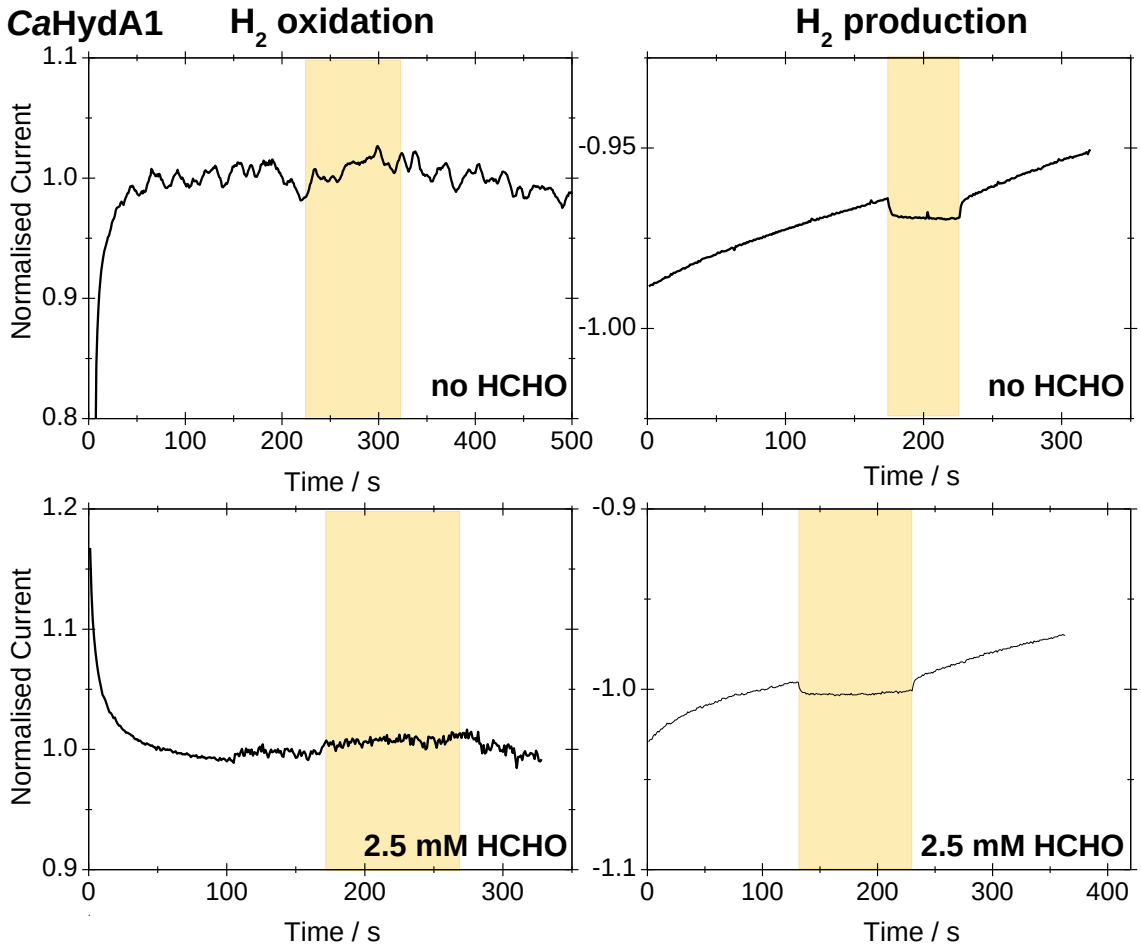

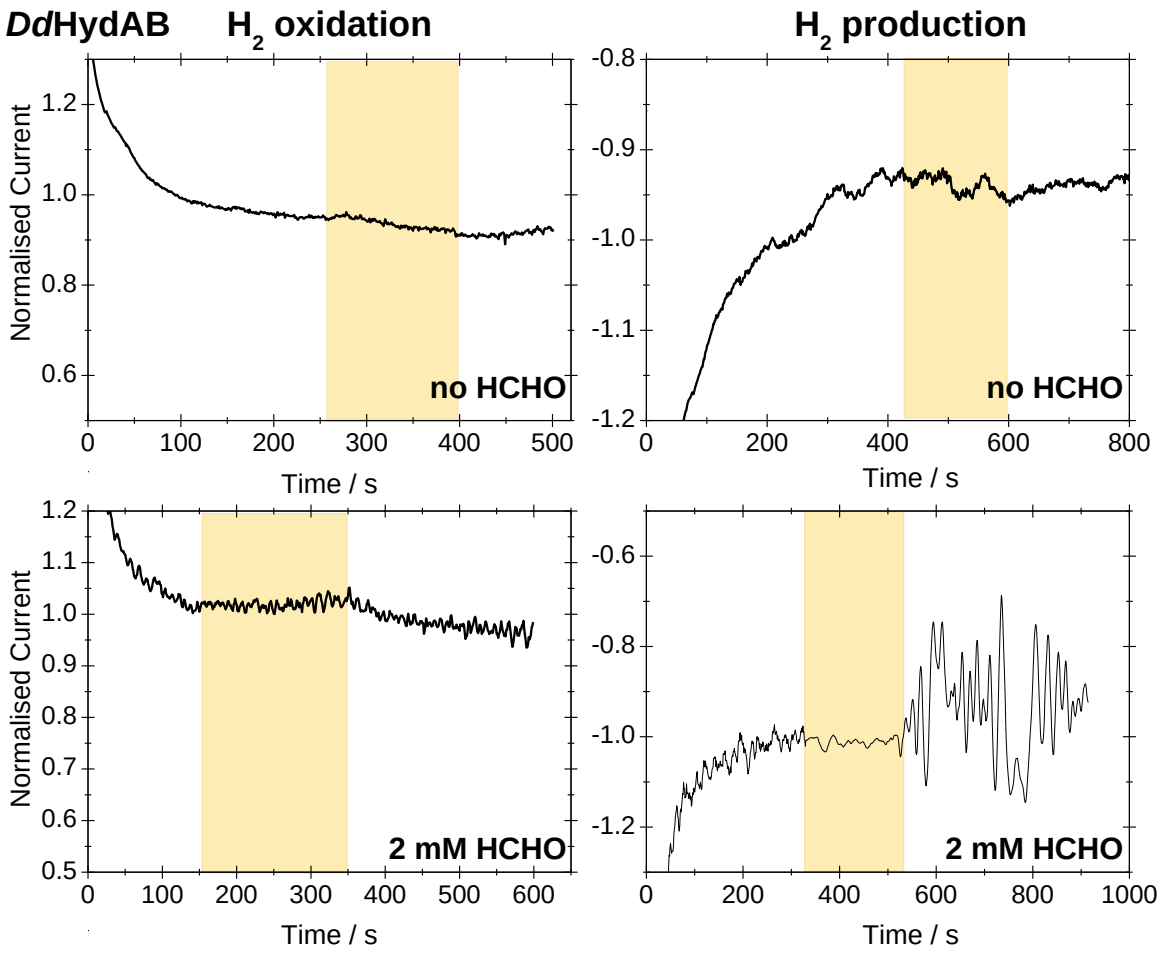

Figure 64: Chronamperometry experiments investigating the effect of illumination on the H_2 oxidation activity at -0.1 V (left) and H_2 production activity at -0.8 V (right) in the presence of formaldehyde, performed on *Ca*HydA (top) and *Dd*HydAB (bottom). Conditions: 5 °C, ω = 3000 rpm, pH 6, 100% H_2, 300 W lamp with IR and UV filters.

The potential was held either at -0.1 V (Figure 64, left), to study H_2 oxidation activity, or at -0.8 V (Figure 64,right), to study H_2 production activity, and the electrode was illuminated to measure the effect of light on the catalytic activity in the absence of inhibitor. The experiment was then repeated in the presence of 2 mM formaldehyde.

In the experiments shown in Figure 64 illumination of both *Ca*HydA (top) and *Dd*HydAB (bottom) has only a minimal positive effect on the catalytic activity; observed as a small increase in the catalytic current, and this effect is no greater in the presence of formaldehyde.

This suggests that the bond formed upon binding of formaldehyde to the H-cluster is strong, and not weakened by illumination with visible light.

4.2.4 Potential Dependence of the Extent of Inhibition

The potential dependence of the extent of formaldehyde inhibition was monitored using chronoamperometry experiments, such as those in section 3.7 with CO, and were repeated over a wide range of potentials (Figure 65). Experiments were performed on both *Ca*HydA and *Cr*HydA1 under identical conditions to allow direct comparison.

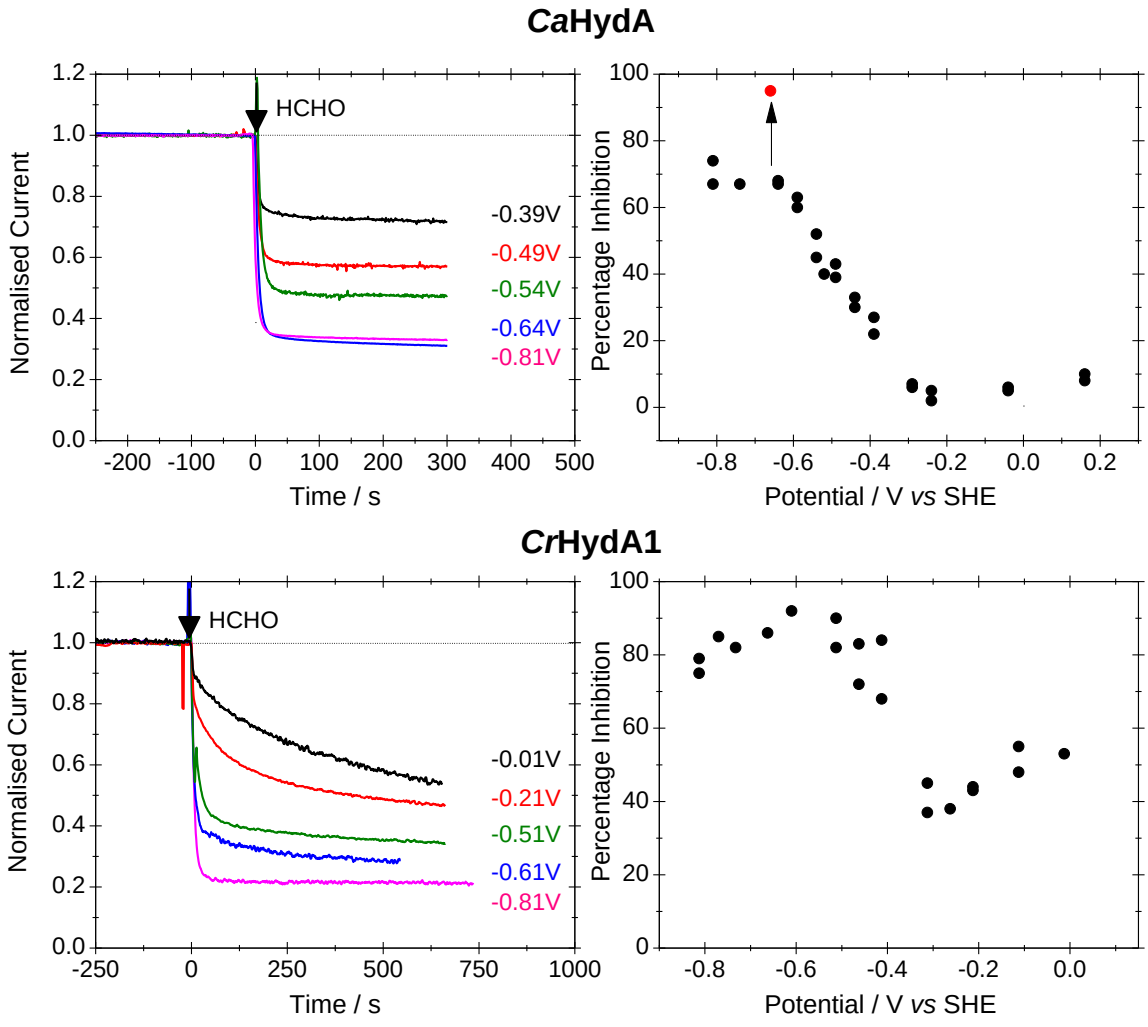

Figure 65: Chronoamperometry experiments performed on *Ca*HydA (top) and *Cr*HydA1 (bottom) to probe the potential dependence of the extent of inhibition with 4.5 mM formaldehyde. The percentage inhibition (right) was measured after 100 s for *Ca*HydA and 200 s for *Cr*HydA1. Conditions: 20 °C, pH 6, ω = 3000 rpm, 100% H_2, 4.5 mM HCHO, potentials are given next to each plot.

For each experiment the potential was held constant throughout, and 4.5 mM formaldehyde was injected at t = 0. The extent of inhibition was recorded at a fixed time after injection, and recorded as a percentage of activity lost. The aldehyde concentration used was chosen to ensure a good spread in the extent of inhibition for both enzymes across the potential range. A greater formaldehyde concentration results in a greater extent of inhibition, as shown by the red data point (Figure 65, top) recorded for inhibition of *Ca*HydA with 45 mM formaldehyde.

As can be seen in Figure 65, at all potentials measured the catalytic current immediately drops upon introduction of formaldehyde to the cell solution (black arrow). Both *Ca*HydA and *Cr*HydA1 show very similar profiles for the potential dependence of the extent of formaldehyde inhibition. This is clearly displayed in Figure 65 (right panels) by the plot of the percentage of inhibition after a certain exposure time (100 s for *Ca*HydA or 200 s for *Cr*HydA1) against the applied potential. Inhibition occurs to a far greater extent in the H_2 production region than the H_2 oxidation region, as expected from the cyclic voltammograms in Figure 60. The behaviour of *Cr*HydA1 at high potential does however differ to that of *Ca*HydA; rather than reaching a limiting value at high potential the extent of inhibition increases with potential in the region –0.2 to +0.1 V. This high potential behaviour is similar to that observed for *Dd*HydAB.[164] The experiments performed in this region may be convoluted by anaerobic inactivation (formation of H_{ox}^{inact}) observed electrochemically at high potential for *Cr*HydA1 and *Dd*HydAB (not seen for *Ca*HydA), which is partially irreversible for *Cr*HydA1.[76,139] These results suggest that the rate of formation of the H_{ox}^{inact} state is increased in the presence of formaldehyde, resulting in greater inhibition of H_2 oxidation activity than expected by the observed preference for binding of formaldehyde to reduced states of the H-cluster. This effect is investigated in section 4.2.6.1.

As previously explained (section 4.1.2), formaldehyde inhibition is biphasic, consisting of a fast phase and a slow phase reaction. The variation in the proportion of inhibition proceeding by each of these phases with potential is shown for *Ca*HydA and *Cr*HydA1 in Figure 66. It has previously been shown that the reversibility of formaldehyde inhibition correlates with the proportion of inhibition proceeding via the fast phase reaction.[164] The proportion of fast phase reaction increases at more reducing potentials for both *Ca*HydA and *Dd*HydAB,[164] while the proportion of the slow phase reaction increases at higher potentials.

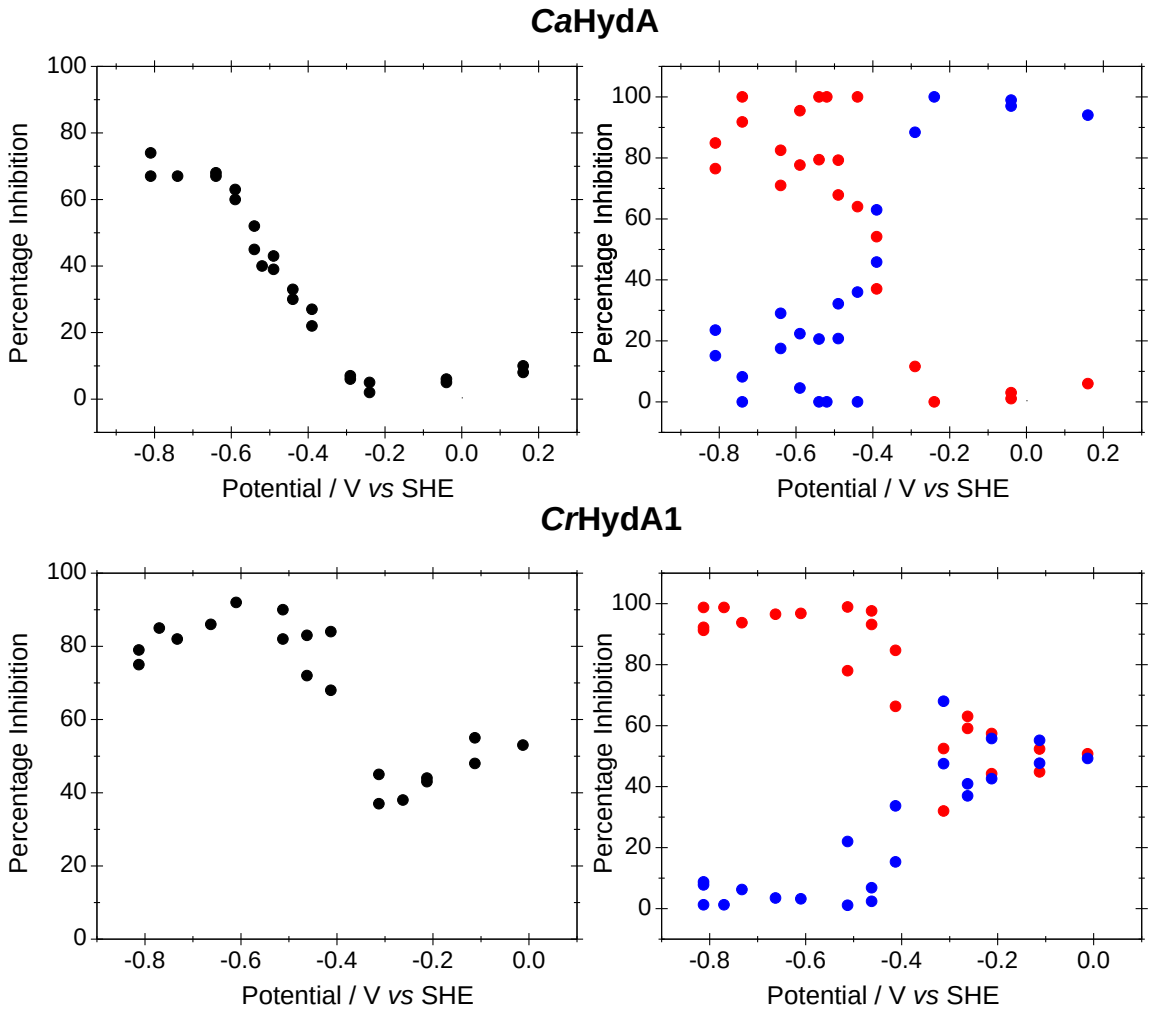

Figure 66: Left: plots showing the variation in the extent of formaldehyde inhibition with potential for *Ca*HydA (top) and *Cr*HydA1 (bottom), measured from chronoamperometry experiments in. Right: plots showing the variation in the percentage of the inhibition that is due to the fast phase reaction (red) and slow the phase reaction (blue) with potential for both hydrogenases.

In the H_2 production region the proportion of formaldehyde inhibition proceeding via the fast phase reaction is very high, and the proportion via the slow phase reaction is very low for both hydrogenases (Figure 66, right). At high potentials (> -0.3 V) inhibition of the H_2 oxidation activity of *Ca*HydA is almost completely due to the slow phase reaction, however for *Cr*HydA1 inhibition proceeds equally by both processes.

The rates of the fast and slow phases of reaction are shown in Figure 67 plotted as a function of potential for both *Ca*HydA and *Cr*HydA1.

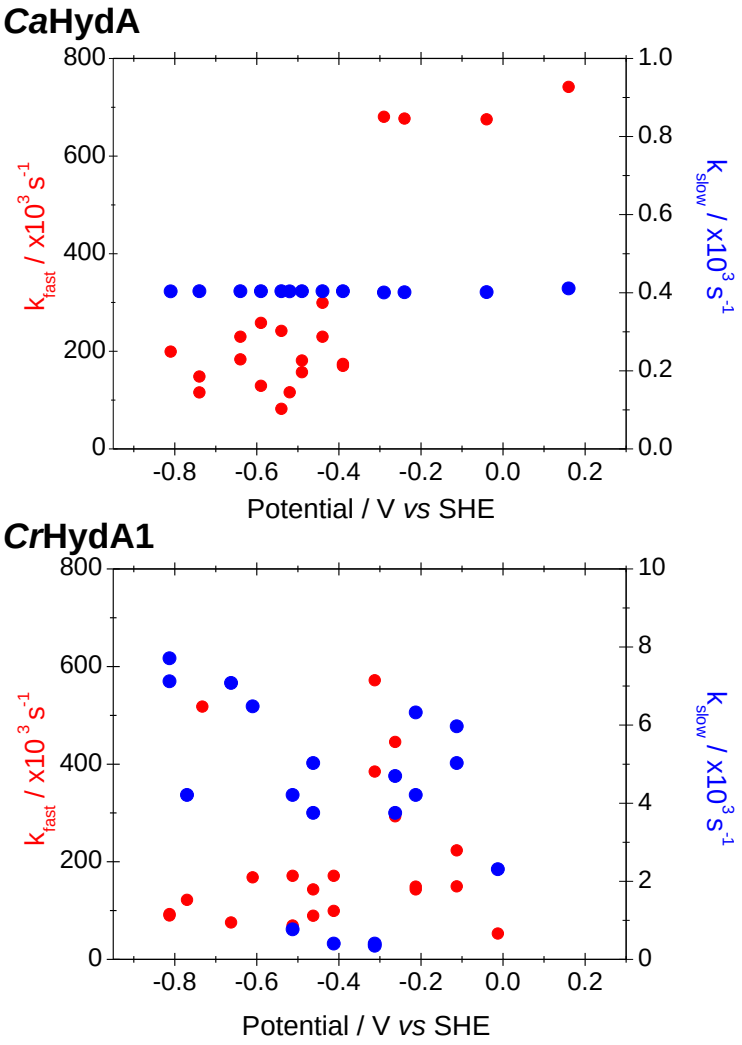

Figure 67: Plots showing the potential dependence of the rates of the fast and slow phases of the biphasic formaldehyde reaction *Ca*HydA (top) and *Cr*HydA1 (bottom), measured from chronoamperometry experiments in Figure 65. The fast phase is shown in red and the slow phase in blue.

Comparison of the top and bottom panels of Figure 67 reveals that the difference between the rate of the fast and slow phase reactions differs between the two hydrogenases studied. For *Ca*HydA (top) the rate of the fast phase reaction is approximately 10^3 times greater than the rate of the slow reaction, while for *Cr*HydA1 (bottom) the difference is only a factor of approximately 10^2. Additionally, for *Ca*HydA the rate of the slow phase reaction does not change with potential, but the rate of the fast phase reaction increases (more than doubles) at potentials where the enzyme catalyses H_2 oxidation (> -0.35 V). For *Cr*HydA1 there is a large spread in the rates of both processes, and a potential dependence cannot be determined.

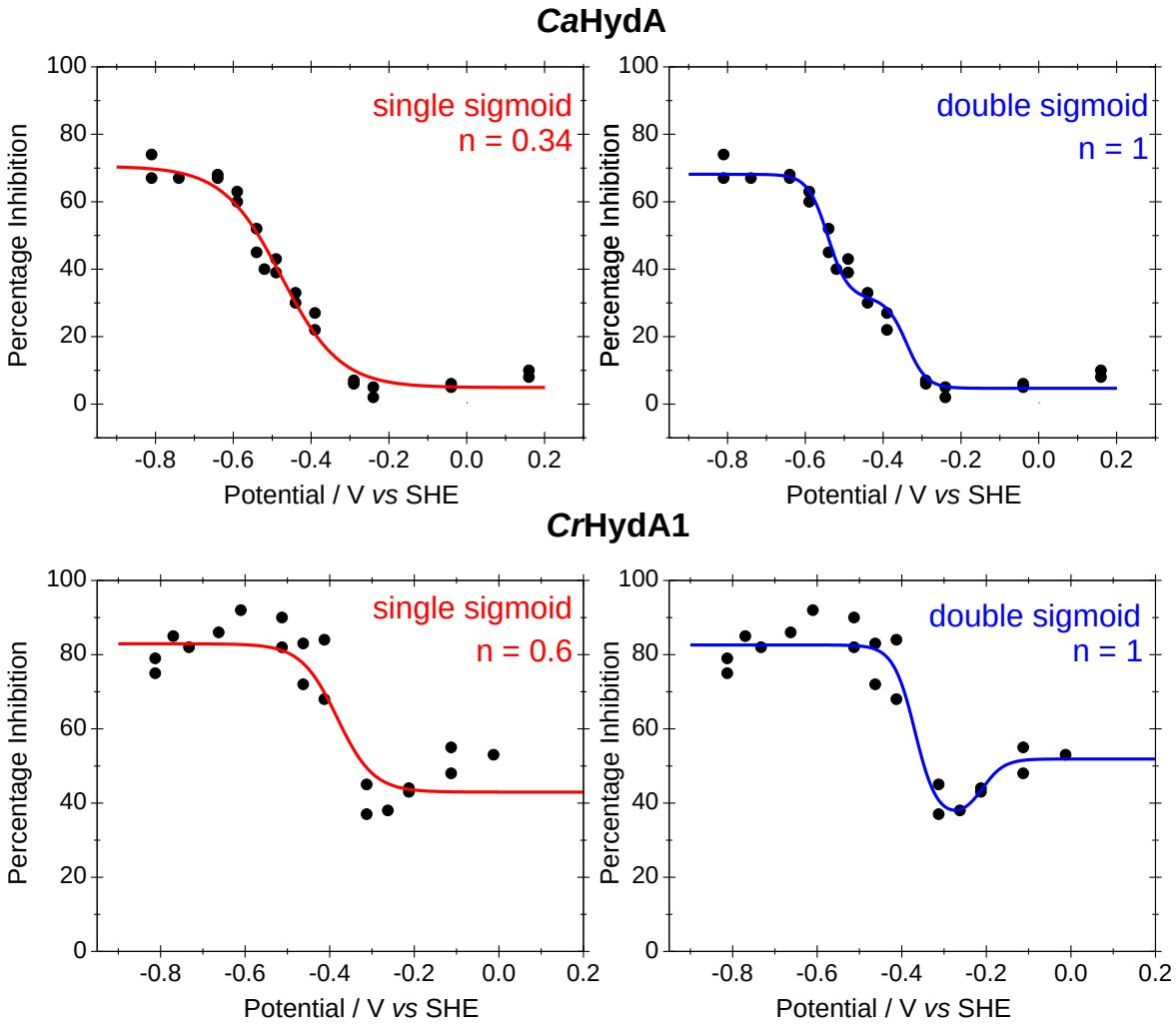

Figure 68: The extent of formaldehyde inhibition of *Ca*HydA (top) and *Cr*HydA1 (bottom), measured from chronoamperometry experiments in Figure 65, overlaid with sigmoidal fits involving a single

electron transfer step (left, red) or two sequential one electron transfer steps (right, blue). Both sigmoids were fitted using Microsoft Excel Solver.

The plots in Figure 68 show attempts to fit the variation in the extent of formaldehyde inhibition to a Nernstian process. Both the data for *Ca*HydA (top) and *Cr*HydA1 (bottom) fit relatively well to a single Nernstian electron transfer process (single sigmoid, red). For both hydrogeases however the value of n for this sigmoid is less than 1, which is unphysical; n = 0.34 for *Ca*HydA and 0.6 for *Cr*HydA1. The data was therefore fitted to two sequential Nerstian electron transfer steps (double sigmoid, blue), as in section 3.7.2 for CO inhibition, and the data fits well for both enzymes. This shows that three oxidation states of the H-cluster, each separated by one electron, are involved in the reaction across this potential range, and formaldehyde binds most strongly at the H_{ox-2} oxidation level (H_{sred}), and least strongly to the H_{ox} oxidation level.

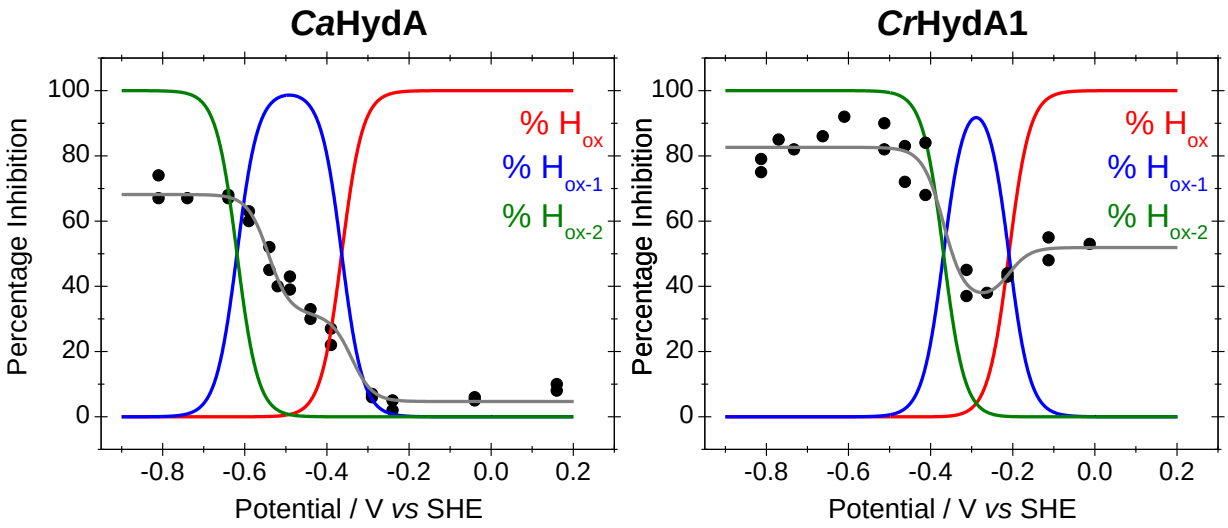

Figure 69: The extent of formaldehyde inhibition of *Ca*HydA (left) and *Cr*HydA1 (right), measured from chronoamperometry experiments in Figure 65, with double sigmoid fit overlaid (grey), and the percentages of enzyme at each oxidation level overlaid (red, blue and green).

Table 3: Summary of the parameters determined by fitting the data to a double sigmoid. E_1 is the midpoint potential for the H_{ox}/H_{ox-1} transition and E_2 is the midpoint potential for the H_{ox-1}/H_{ox-2} transition. Φ_i is the proportion of active enzyme at each oxidation level.

	E_1	E_2	ΦH_{ox}	ΦH_{ox-1}	ΦH_{ox-2}
***Ca*HydA**	-0.38 V	-0.55 V	0.94	0.64	0.31
***Cr*HydA1**	-0.21 V	-0.37 V	0.48	0.64	0.17

Both the midpoint potentials E_1 and E_2 are ~ 180 mV more negative for *Ca*HydA than for *Cr*HydA1 (

Table 3), reflecting the greater extent of reaction of *Cr*HydA1 with formaldehyde.[161] Formaldehyde binds preferentially to a state of the H-cluster at the H_{ox-2} oxidation level (H_{sred} state), shifting the potential of the H_{ox-1}/H_{ox-2} transition to a less reducing value. This potential shift is smaller for *Ca*HydA, as the extent of formaldehyde binding is smaller for this enzyme. This difference in formaldehyde affinity is also illustrated by the different Φ_i values (proportion of enzyme at each oxidation level that is in the active form,

Table 3); at the H_{ox-2} level 31% of the enzyme is active in the presence of 4.5 mM formaldehyde for *Ca*HydA, compared to just 17% for *Cr*HydA1. The strong preference of formaldehyde binding for a certain oxidation level of the H-cluster (H_{ox-2} or H_{sred} state) strongly suggests that binding occurs directly at the H-cluster.

4.2.5 Reaction with [NiFe]-Hydrogenase

[NiFe]-hydrogenases have been shown to be far less extensively inhibited by formaldehyde than [FeFe]-hydrogenases.[161] The potential dependence of the reaction of the [NiFe]-hydrogenase *E. coli* Hyd-2 was investigated (Figure 70). Cyclic voltammograms were recorded in the presence of a high formaldehyde concentration, in both 100% H_2 (black) and 100% N_2 (blue) to allow the effect of formaldehyde on catalytic activity to be studied for both H_2 oxidation and H_2 production.

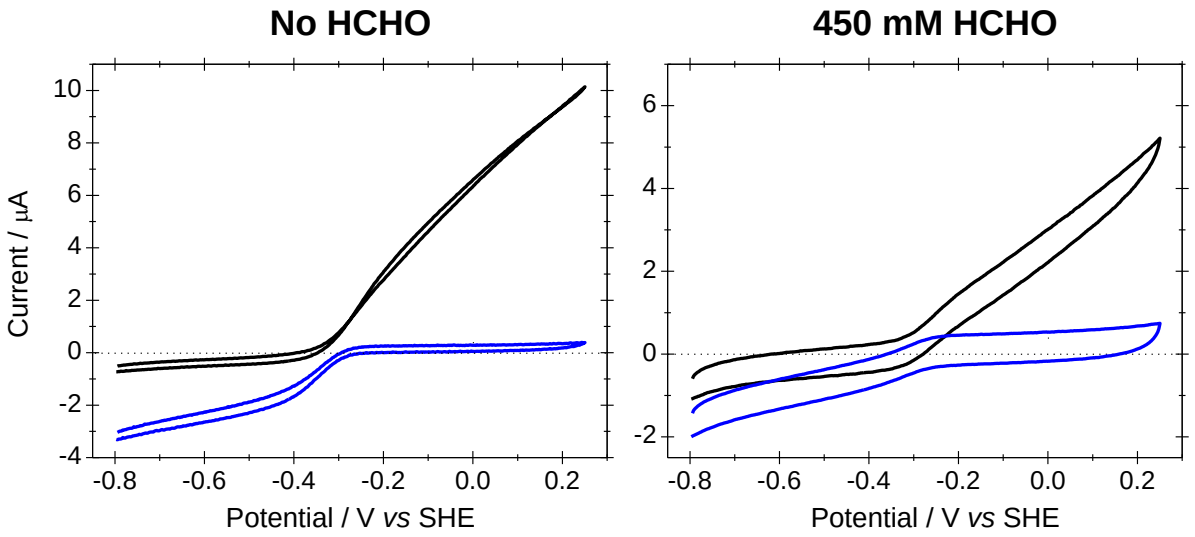

Figure 70: Cyclic voltammograms of *E. coli* Hyd-2 recorded in the absence (left) and presence (right) of 450 mM formaldehyde. Voltammograms were recorded in 100% H_2 (black) and 100% N_2 (blue) to allow the effect of formaldehyde on both the H_2 oxidation and production activity to be monitored. Conditions: 20 °C, 20 mV/s scan rate, ω = 3000 rpm, pH 6.

Voltammograms of the [NiFe]-hydrogenase *E. coli* Hyd-2 performed in the presence of formaldehyde (Figure 70, right) display very little inhibition, and do not exhibit the characteristic change in catalytic wave-shape at low potential observed for the [FeFe]-hydrogenases (Figure 60). The extent and potential dependence of the formaldehyde inhibition of *E. coli* Hyd-2 was investigated further (Figure 71) using chronoamperometry experiments such as those in Figure 65.

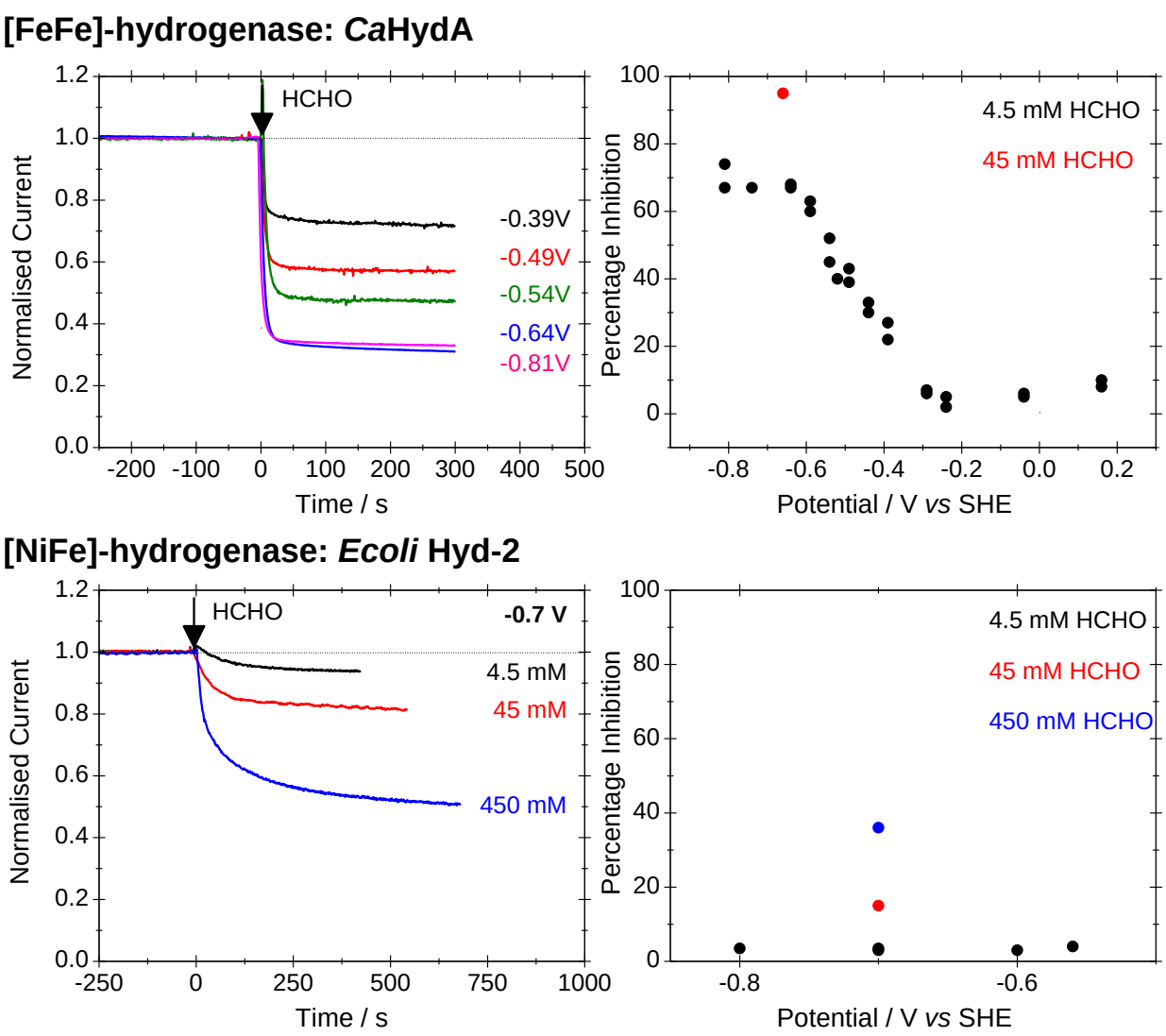

Figure 71: Chronoamperometry experiments performed on *Ca*HydA (top) and *Ecoli* Hyd-2 (bottom) to probe the potential dependence of the extent of inhibition with 4.5 mM formaldehyde. The percentage inhibition (right) was measured after 100 s exposure to the aldehyde. The experiments were repeated in 45 mM and 450 mM formaldehyde. Conditions: 20 °C, pH 6, ω = 3000 rpm, 100% N_2 (*Ecoli* Hyd-2), 100% H_2 (*Ca*HydA).

Comparison of the chronoamperometry experiments of *Ca*HydA and *E. coli* Hyd-2 in Figure 71 reveals a large difference in the extent of reaction of an [FeFe]-hydrogenase (top) and a [NiFe]-hydrogenase (bottom) with formaldehyde. In both cases the catalytic current drops immediately upon injection of formaldehyde (black arrow), however the percentage of activity lost is much greater for the [FeFe]-hydrogenase; < 5% of H_2 activity is inhibited at -0.7 V for *E. coli* Hyd-2 compared to > 65% at the same potential for *Ca*HydA.

Additionally inhibition of the H_2 production activity of *E. coli* Hyd-2 by 4.5 mM formaldehyde is completely potential independent across the range studied (Figure 71, bottom right).

4.2.6 High Potential Inactivation

As described in section 1.5.2 [FeFe]-hydrogenases can form a highly oxidised inactive state called H_{ox}^{inact}. The enzymes *Dd*HydAB and *Cr*HydA1 form this state when exposed to high potential (> 0 V) as seen in the cyclic voltammograms in Chapter 1, Figure 7, whereas *Ca*HydA forms very little of this state electrochemically. The rate of formation of this state increases as the potential is swept to more oxidising values (> 0 V), and the enzyme is reactivated to form the active H_{ox} state when the potential is scanned back to more reducing values. As previously described, the wave-shape of *Dd*HydAB (section 1.5.2.3) consists of two peaks in the oxidative region, and the exact nature of both peaks is not well understood.[77] It is possible that there are two different inactive oxidised states formed for this enzyme, one requiring a greater driving force for formation/reactivation, or that there are two different mechanisms for formation of the H_{ox}^{inact} state.

4.2.6.1 Effect of Formaldehyde on Inactivation Potential

The chronoamperometry experiments performed on *Cr*HydA1 to investigate the potential dependence of the extent of formaldehyde inhibition (Figure 65) were complicated at high potential, attributed to formation of the H_{ox}^{inact} state. Cyclic voltammograms of *Dd*HydAB and *Cr*HydA1 (recorded by Annemarie Wait[164]) performed in the presence of formaldehyde revealed a shift in the potential at which high potential inactivation and reactivation occurred, compared to the formaldehyde free voltammogram. This effect was further investigated as

shown in Figure 72 for *Dd*HydAB (as high potential inactivation is completely reversible for this hydrogenase[139]) at a slower scan rate (1 mV/s), for more accurate analysis.

At the beginning of the experiments shown in Figure 72 (top) the potential was held at +0.25 V for 20 s to inactivate the enzyme film (H_{ox}^{inact}) before the voltammogram commenced. The voltammogram then commenced by slowly sweeping the potential (1 mV/s) in the reductive direction. The potential of reactivation, in the reductive sweep, and potential of inactivation, in the oxidative sweep, were calculated from the peak positions in the first derivative of the scans (Figure 72, inset). The potentials of inactivation and reactivation (marked on the figure) were not affected by the length of the inactivation step at +0.25 V (5000 s *vs* 20 s), showing that an initial 20 s poise is sufficient to convert all enzyme to the inactive H_{ox}^{inact} state. The experiment was then repeated in the presence of 8.9 mM formaldehyde in the cell solution (Figure 72, bottom) to determine the effect of formaldehyde on the potential of formation and reactivation of the H_{ox}^{inact} state.

There are two clear peaks in the reductive scans in both of the voltammograms in Figure 72; (inhibitor free, top and formaldehyde, bottom). The first peak appears at +125 mV in the absence of formaldehyde (top, left) and at +45 mV in the presence of formaldehyde (bottom, left). This peak is thought to correspond to reactivation of the H_{ox}^{inact} state (to form H_{ox}) and a potential 80 mV more reducing is required for this reactivation in the presence of formaldehyde. The second peak, of which the origin is not understood, appears at the same potential (-80 mV) in both experiments, meaning that the process to which this activation relates is not affected by formaldehyde.

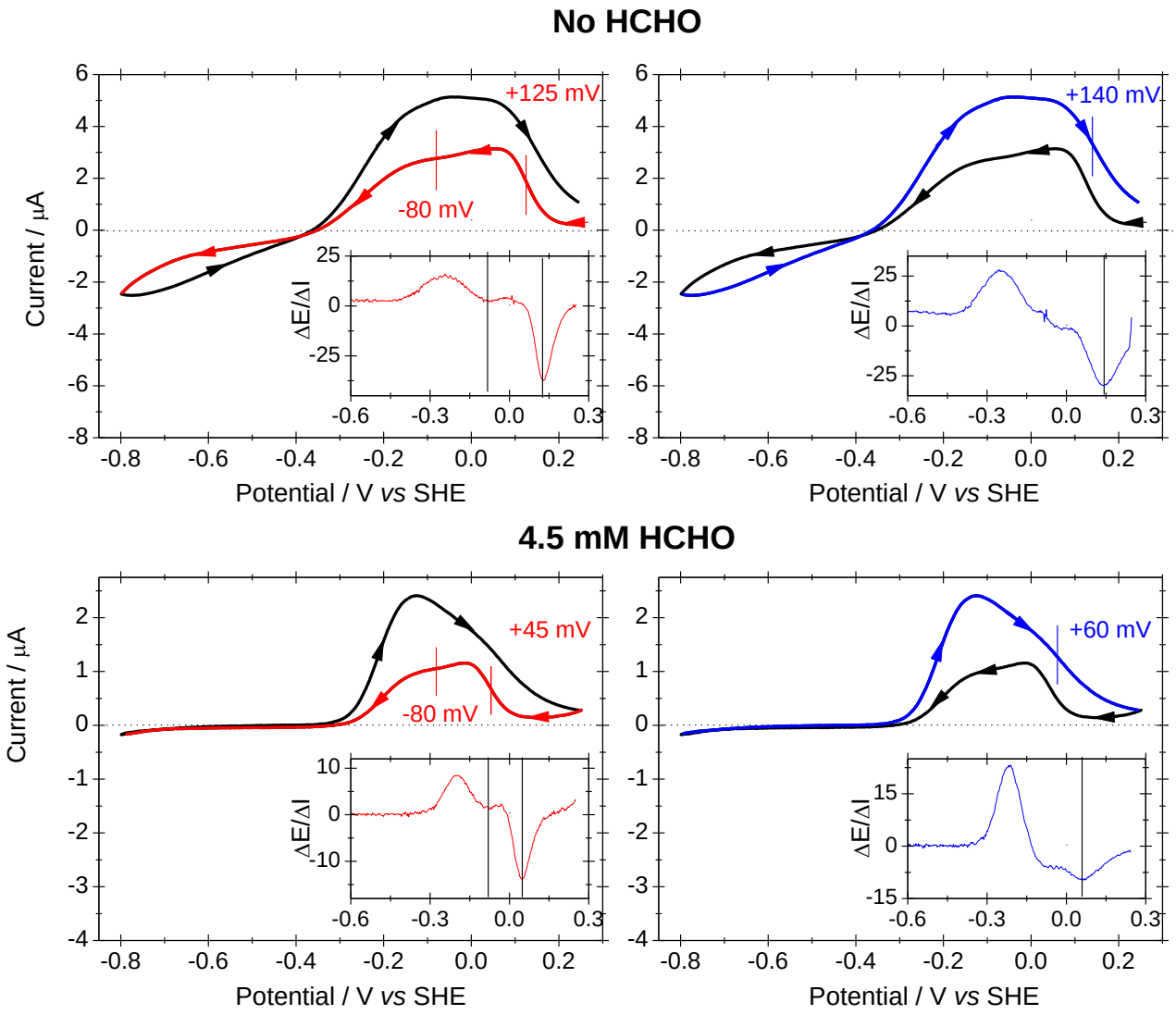

Figure 72: Cyclic voltammograms of *Dd*HydAB showing high potential inactivation and reactivation in the absence (top) and presence (bottom) of formaldehyde. The potential was poised at +0.25 V for 20 s before the voltammograms commenced. Reductive scans are shown in red and the positive scans in blue. The first derivative of the negative (left) and positive (blue) scans are inset and the potential minima in these plots are marked on the voltammogram. Conditions: 15 °C, 1 mV/s scan rate, pH 6, ω = 3000 rpm, 100% H_2, 4.5 mM formaldehyde.

There are also two peaks in the oxidative scan of both voltammograms, although only the position of the peak at higher potential can be determined from the scan derivative. This peak occurs at +140 mV in the formaldehyde free experiment (top, right) and at +60 mV in the formaldehyde experiment (bottom, right), again a difference of 80 mV. The additional 80 mV driving force required for inactivation and reactivation in the presence of formaldehyde leads to the conclusion that either:

(1) Formaldehyde reacts with the H-cluster at high potential in such a way as to stabilise the formation of the H_{ox}^{inact} state

(2) An oxidised formaldehyde-bound state exists, distinct from and more stable than H_{ox}^{inact}, possibly H_{ox}^{inact}-HCHO or even H_{ox}-HCHO

Three possible inactivation reactions are shown in Scheme 14.

Scheme 14: Possible high potential inactivated states in the presence of formaldehyde. Top: simple oxidation to form H_{ox}^{inact}, middle: oxidation to form H_{ox}^{inact} facilitated by interaction with formaldehyde and bottom: oxidation to form a formaldehyde bound state H_{ox}^{inact}-HCHO.

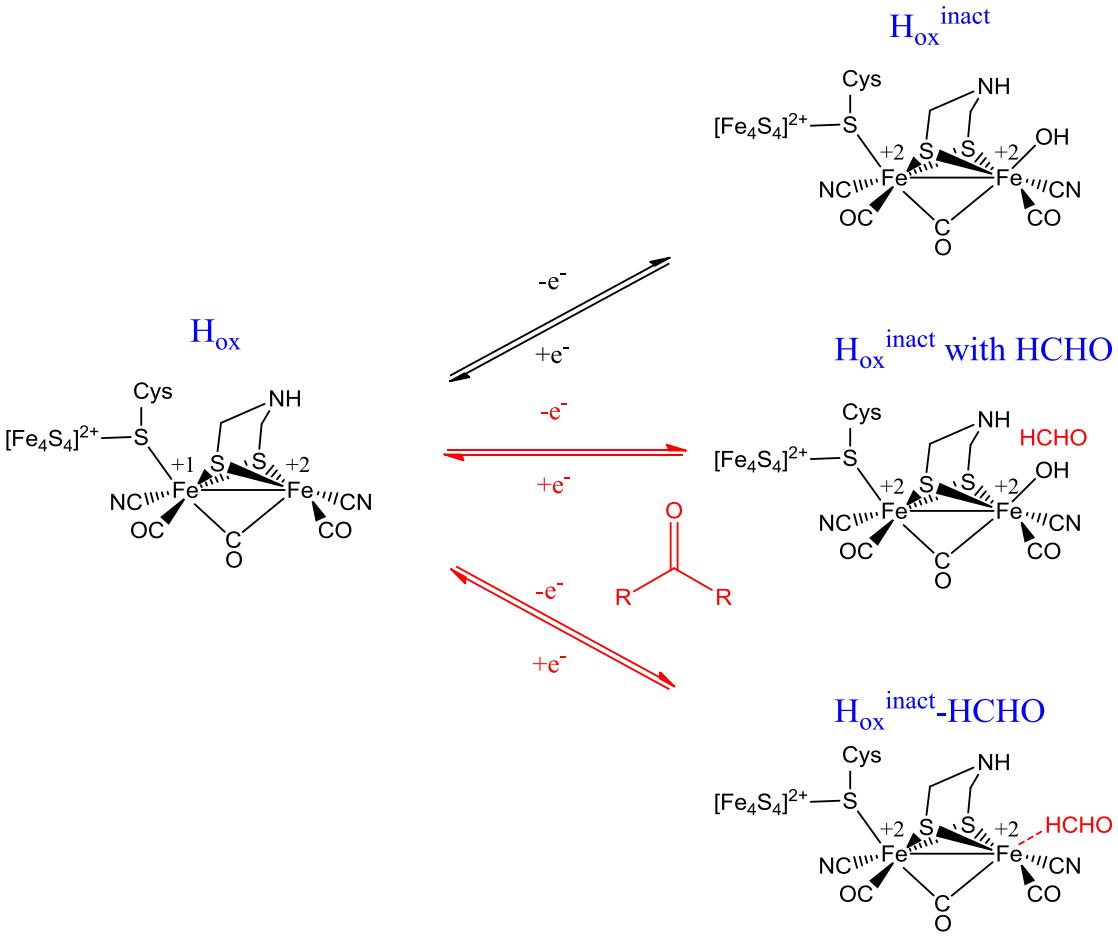

4.2.6.2 Effect of Formaldehyde on the Rate and Extent of High Potential Inactivation

The apparent stabilisation of the H_{ox}^{inact} state of *Dd*HydAB in the presence of formaldehyde determined by cyclic voltammetry (Figure 72) was further investigated using

chronoamperometry analysis (Figure 73). The effect of formaldehyde on the rate and extent of high potential inactivation and reactivation was investigated by monitoring the effect of a step to high potential (+0.25 V) on the H_2 oxidation activity of *Dd*HydAB.

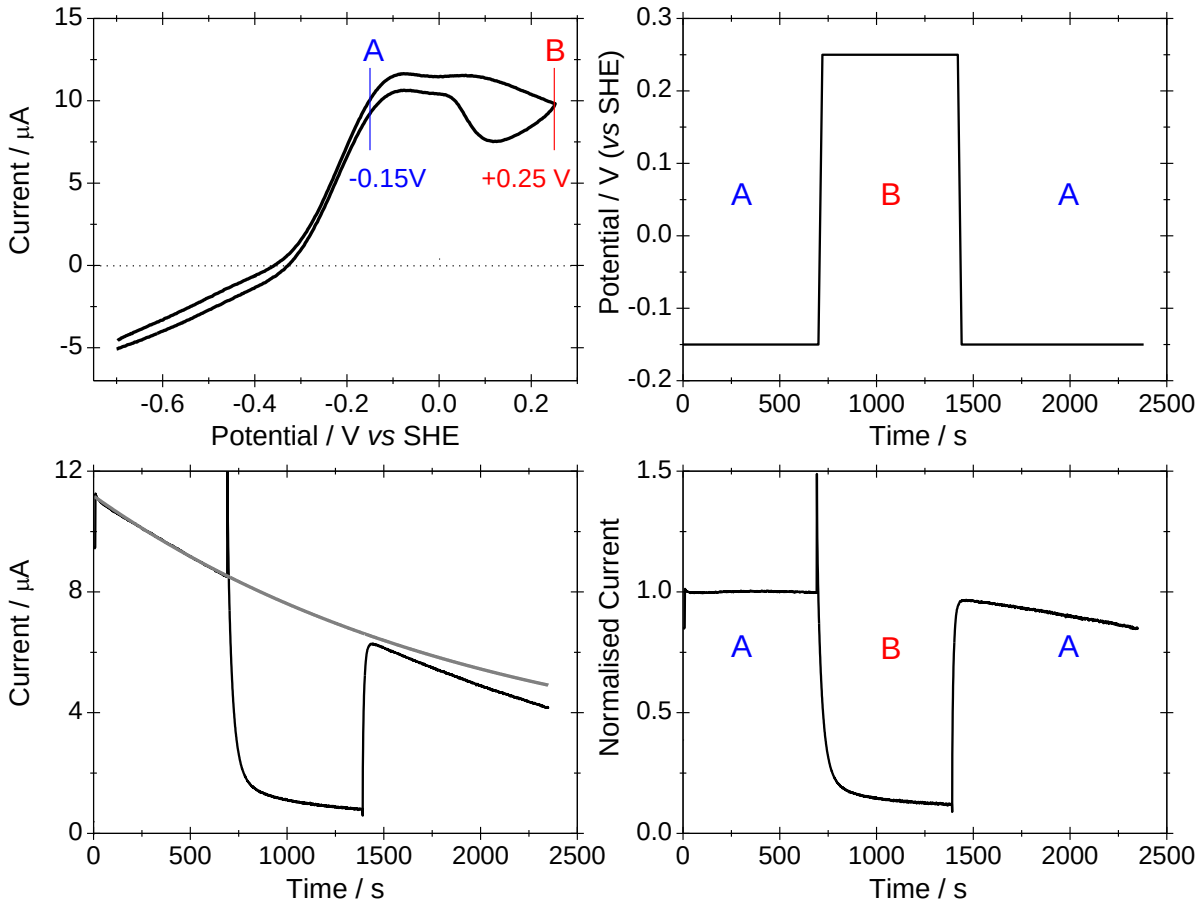

Figure 73: Example chronoamperometry experiment performed to determine the effect of formaldehyde on the extent of high potential inactivation, and rate of inactivation and reactivation. Top left: voltammogram of *Dd*HydAB recorded at 20 mV/s scan rate, with potentials A (-0.15 V) and B (-0.15 V) used in the chronoamperometry experiment marked. Top right: Profile of the variation in potential with time in the chronoamperometry trace. Bottom left: Chronoamperometry experiment, raw data. The exponential fit used to correct for film loss is overlaid in grey. Bottom right: Experiment after correction for initial film loss. Experiments were carried out both in the presence (8.9 mM) and absence of formaldehyde. Conditions: 10 °C, pH 6, ω = 3000 rpm, 100% H_2.

The chronoamperometry experiment shown in Figure 73 commenced at -0.15 V, a potential at which the enzyme catalyses H_2 oxidation, but not in the region where high potential inactivation (H_{ox}^{inact}) occurs (this potential is marked in Figure 73 (top, left) as 'A' on the

voltammogram). After the current had stabilised the potential was stepped up to +0.25 V to induce formation of the H_{ox}^{inact} state, thus inactivating the enzyme; the rate and extent of inactivation was studied. After 700 s the potential was returned to -0.15 V and reactivation, the recovery of oxidation current, was monitored. A profile of the change in potential with time during the experiment is shown in the top, right panel of Figure 73, while an example experiment is shown in the bottom panel. The bottom, left panel (Figure 73) shows the raw data and the bottom right panel shows the current after correction for film loss and normalization. The data was corrected for film loss and normalised to allow the extent of inactivation and reversibility to be compared between different experiments, performed in the absence of inhibitor, or in the presence of 8.9 mM formaldehyde.

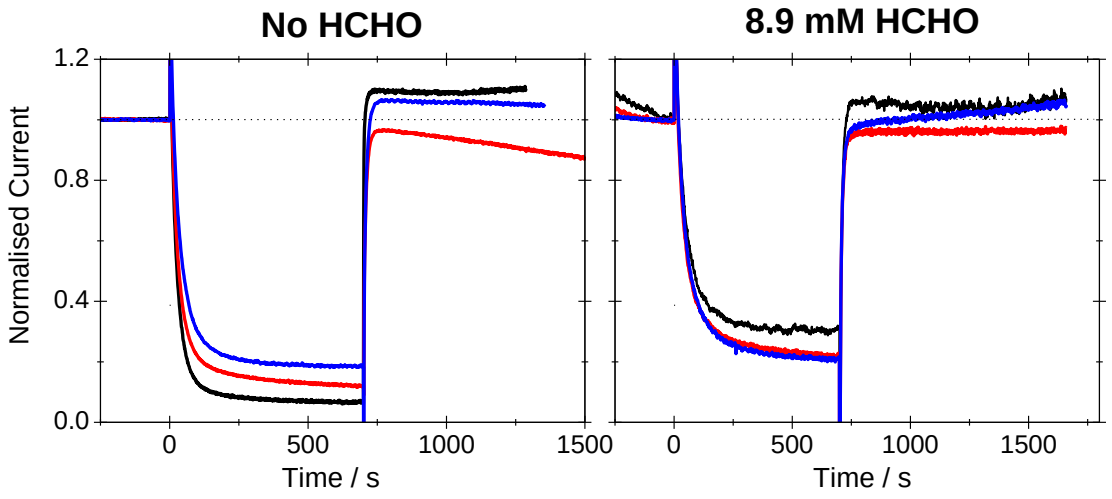

Figure 74: Comparison of chronoamperometry experiments performed on *Dd*HydAB as described in Figure 73. Conditions: -0.15 V stepped up to +0.25 V from 700-1400 s, 10 °C, pH 6, ω = 3000 rpm, 100% H_2.

Three different repeats of the chronoamperometry experiments performed are shown in Figure 74, compared in the presence (right) and absence (left) of formaldehyde. The average proportion of inactivation during the high potential step is 87% in the absence of formaldehyde and 76% in the presence of 8.9 mM formaldehyde. The lesser extent of inactivation in the presence of formaldehyde does not correspond with the decrease in driving

force required for inactivation observed in the cyclic voltammograms in Figure 72, however the accuracy of this data, with just three repeats, is limited.

As can be seen by comparison of the experiments in Figure 74, inactivation under these conditions is almost completely reversible, independent of whether formaldehyde is present or not. This shows that if a formaldehyde-bound high potential state is formed, it is stable and formed reversibly. In approximately half of the experiments the H_2 oxidation activity (current) at -0.15 V after the 700 s step to +0.25 V is actually greater than the current before the step. This is not considered to be an artefact as the exponential corrections used film loss fitted the data before the high potential step with high accuracy and the same effect has been observed in other experiments (data not shown). This implies that although the enzyme forms an inactive state under these conditions (H_{ox}^{inact}), during this high potential step the enzyme also undergoes some sort of activation process.

The rates of high potential inactivation and reactivation were calculated using log plots as shown in Figure 75, and the results are summarised in Table 4. The rate is taken from the initial gradient of the log plot.

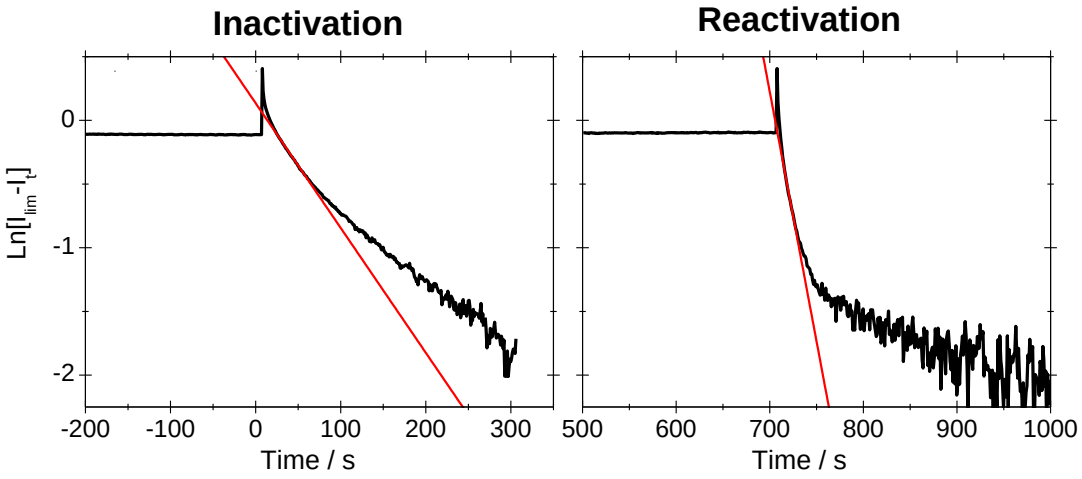

Figure 75: Log plots of one of the chronoamperometry experiments in Figure 73. The rate of inactivation initiated by the step to +0.25 V at t = 0 is shown in the left panel, and the rate of reactivation by the step to -0.15 V at t= 700 s is shown on the right. The initial gradient is marked by the red line.

Table 4: Summary of the effect of the presence of 8.9 mM formaldehyde on the rate of high potential inactivation of *Dd*HydAB, and the rate of reactivation after exposure to +0.25 V for 700 s. Rates were determined using log plots such as those shown in Figure 75.

	Repeat	Rate Inactivation / $x10^{-3}$ s^{-1}	Rate Reactivation / $x10^{-3}$ s^{-1}
No HCHO	1	15.4	46.9
	2	14.7	55.3
	3	14.3	48.2
	4	11.44	43.9
	Average	14.0	48.6
8.9 mM HCHO	1	9.9	46.6
	2	10.6	41.5
	3	9.8	39.2
	Average	10.1	42.4

Comparison of the data in Table 4 reveals that the rate of inactivation is slightly greater in the presence of formaldehyde, corresponding to the predicted stabilisation of the H_{ox}^{inact} state, however the rate of reactivation is also slightly greater, which does not support this theory. This inconsistency may be a limitation of the experiment; the rate of inactivation and reactivation are both very rapid under the conditions used, and the differences between the rates in the formaldehyde and inhibitor free experiments are minimal.

The effect of formaldehyde on the high potential inactivation of *Ca*HydA, an enzyme that does not form much of the H_{ox}^{inact} state electrochemically, was also investigated (Figure 76). Voltammograms were commenced after poising the potential at +0.25 V for 5000 s to inactivate the enzyme; however after this period more than 50% of the H_2 oxidation activity remained (data not shown) reflecting the very minimal formation of the H_{ox}^{inact} state for this hydrogenase. A slow (1 mV/s) voltammogram was recorded (Figure 76), but only minimal reactivation/inactivation was observed.

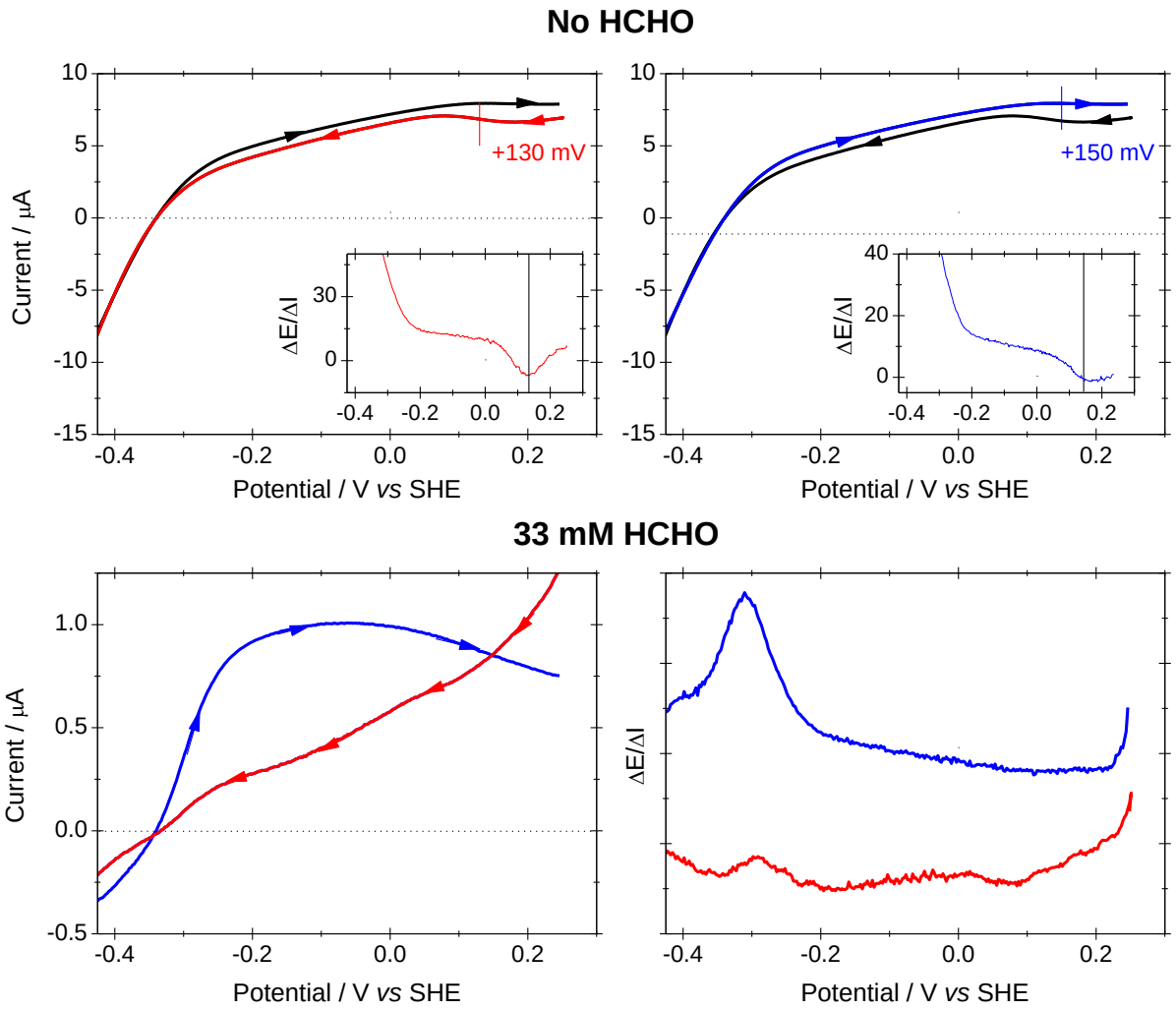

Figure 76: Cyclic voltammograms of *Ca*HydA showing high potential inactivation and reactivation in the absence (top) and presence (bottom) of formaldehyde. Voltammograms commenced from high potential limit, reductive scans are shown in red and the positive scans in blue. The first derivative of the negative and positive scans are inset (left and right respectively) and the potential minima in these plots are marked on the voltammograms. Conditions: +0.25 V↔ -0.8 V, 1 mV/s scan rate, 15 °C, pH 6, ω = 3000 rpm, 100% H_2, 33 mM HCHO.

In the absence of formaldehyde (Figure 76, top left) the voltammogram has one small peak at +130 mV, corresponding to reactivation of the H_{ox}^{inact} state during the reductive scan. This is 5 mV higher than *Dd*HydAB, while the potential of inactivation of *Ca*HydA (Figure 76, top right) is 10 mV higher than *Dd*HydAB at +150 mV. A greater formaldehyde concentration (33 mM) was used in these experiments than for the corresponding experiments on *Dd*HydAB (Figure 72) due to the lesser extent of reaction of *Ca*HydA with formaldehyde. The reductive

voltammogram recorded in the presence of formaldehyde (Figure 76, bottom) varies greatly from the aldehyde free voltammogram (Figure 76, top). The low potential behaviour (not shown) has previously been described (Figure 60), but there are also more than three peaks visible in the reductive scan in the oxidative region -0.3 ↔ +0.25 V. The nature of each of these peaks is not understood.

4.3 Density Functional Theory

To explore the nature of the interactions between the H-cluster and formaldehyde, density functional theory (DFT) was used to calculate the potential energy surfaces. Calculations were performed in collaboration with the group of Prof. John McGrady, by DPhil student Tobias Kraemer and are summarised in

Scheme 15. The strong potential dependence of formaldehyde inhibition observed in electrochemistry experiments presented in this chapter suggests that binding of formaldehyde occurs at, or very close to, the H-cluster, and targets a reduced state at the $H_{ox\text{-}2}$ level (H_{sred}). We sought to establish how formaldehyde might intercept intermediates in H_2 evolution corresponding to oxidation levels $H_{ox\text{-}1}$ and $H_{ox\text{-}2.}$ Proton reduction by [FeFe]-hydrogenases has been studied extensively by DFT,[88,93,137,167-171] most recently by de Gioia and coworkers[93] who incorporated the [4Fe-4S] cluster domain into their model. The computational methodology developed in reference 93 was followed, full details are given in Appendix 1. Electronic energies were calculated using the Born-Oppenheimer approximation, with the molecules modelled in the gas phase with a polarisable continuum (dielectric constant $\varepsilon = 4$).

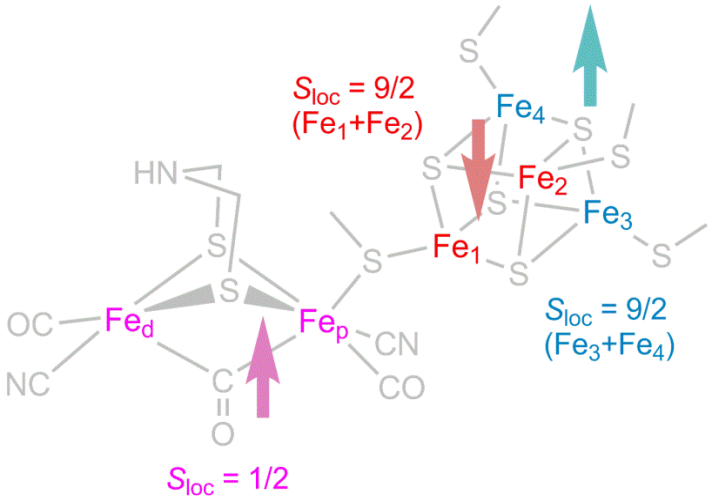

Figure 77: Diagrammatic representation of the 3-spin model according to Greco and co-workers. The state shown corresponds to a H_{ox-2} state with antiferromagnetic coupling between the $[2Fe]_H$ domain and the Fe_1Fe_2 unit in the [4Fe4S] domain (referred to as BS1).

The pathways for H_2 evolution by enzyme at both the H_{ox-1} and H_{ox-2} oxidation levels (H_{red} and H_{sred}) are shown in

Scheme 15 in grey – where the structures of the various intermediates are essentially identical to those reported by de Gioia and co-workers. At this level of theory, formation of H_2 from the intermediate hydride IV (H_{ox-2} level) is exothermic (-3 kcal/mol) whereas the corresponding reaction from II (H_{ox-1} level) is endothermic, ΔE = +4 kcal/mol. This supports the theory that a state at the H_{ox-2} level is involved in the catalytic cycle. The 7 kcal/mol additional driving force at the H_{ox-2} level is consistent with the anticipated higher electron density on the hydride (greater hydridicity). Of interest is the fact that when the [4Fe4S]-cluster is omitted from the model and the structure simplified by replacement with a methyl group, spontaneous release of H_2 is thermodynamically favoured. When the FeS-cluster is included H_2 release is not spontaneous although release of H_2 is energetically favoured overall. This is because the FeS cluster appears to generate a second minimum in the potential energy surface, most likely by providing a site for electron delocalisation.

Scheme 15: How formaldehyde may intercept intermediates in the catalytic cycle of [FeFe]-hydrogenases, according to their oxidation level. Formaldehyde products are shown in green (hydride attack) and blue (Schiff base attack). Species in grey are intermediates proposed on the basis of DFT calculations by de Gioia and colleagues[93]. Figure adapted with permission from reference 166 (Foster, C. E. *et al. J. Am. Chem. Soc.* 2012, *134*, 7553-7557). Copyright (2012) American Chemical Society.

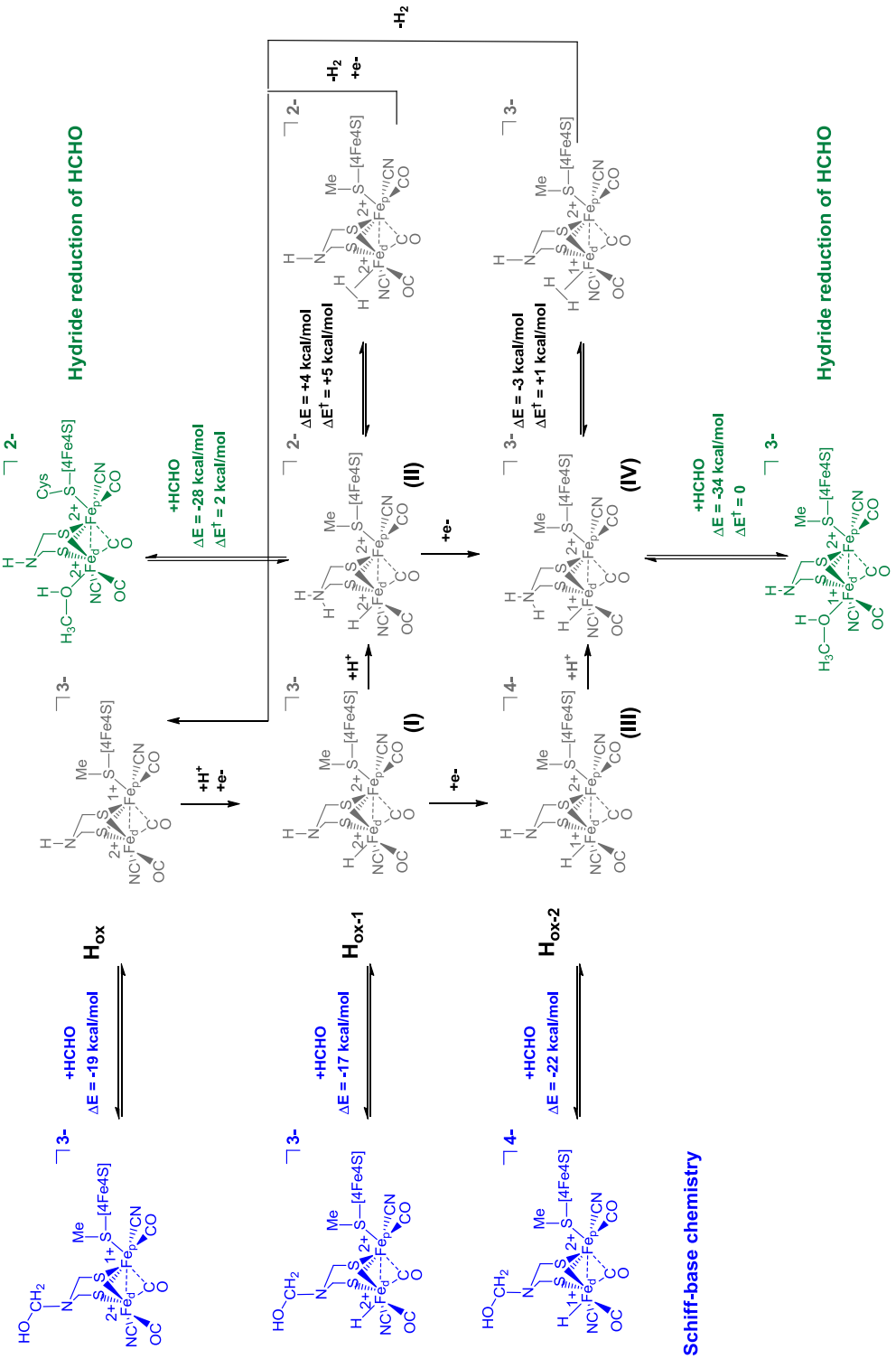

The established chemistry of aldehydes offers two distinct possibilities for interaction with the H-cluster:

(1) **Green**: nucleophilic attack at the carbonyl-C by a Fe_d hydride species leading to methanol-like derivatives (analogous to metal hydride reductions)

(2) **Blue**: Schiff base chemistry at the bridgehead-N.

Considering first the hydridic attack on formaldehyde: at the H_{ox-1} level (H_{red}), the approach of formaldehyde to Intermediate II is repulsive, and optimisations where the initial position of the formaldehyde is far from the cluster (> 3 Å) lead only to a weakly bound adduct. Closer approach leads to a rather asynchronous transition state (ΔE = +2 kcal/mol) where hydride transfer is well developed but the proton remains bound strongly to the bridgehead-N. This transition state then collapses to a minimum where methanol is coordinated to Fe_d via the oxygen donor. The overall reaction is strongly exothermic (ΔE = -28 kcal/mol relative to free reactants), indicating that the H_{ox-1} level of the H-cluster (H_{red}) is thermodynamically competent to bind formaldehyde, albeit with a small barrier. Significantly, the reaction with formaldehyde is also > 30 kcal/mol more favourable than the proton reduction step at the same oxidation level. Upon adding a further electron to achieve the H_{ox-2} level (H_{sred}), the corresponding surface for formaldehyde binding appears to be barrierless: we have been unable to locate either a minimum corresponding to the weak precursor complex or a transition state connecting it to the methanol product. The overall reaction is again strongly exothermic (ΔE = -34 kcal/mol) and the difference of 6 kcal/mol between the H_{ox-1} and H_{ox-2} levels mirrors that noted for the competing proton reduction step ($\Delta\Delta E$ = 7 kcal/mol).

Schiff-base chemistry with the bridgehead-N produces aminol intermediates (ΔE = -18, -17 and -22 kcal/mol for reactions at levels H_{ox}, H_{ox-1} and H_{ox-2}, respectively). In the presence of protons these would, in turn, decompose exothermically to form irreversible products via

dehydrated imine intermediates, regardless of the oxidation level. We do not, however, consider these subsequent steps explicitly, as the energetics are dominated by the large and unphysical electrostatic components in this model arising from the high negative charge on the isolated clusters. In the actual enzyme the surrounding protein environment will play large a role in modulating this high charge, so the energetic of these reactions will differ greatly to the calculated values. DFT studies, such as those by Bruschi *et al.*[93] have demonstrated the importance of the surrounding protein environment on the energetics and structural orientation of the ligands in the H-cluster.

4.4 Perspectives

This chapter has presented detailed studies of aldehyde inhibition of catalysis by [FeFe]-hydrogenases and the strong potential dependence of this inhibition. These studies provide compelling evidence that formaldehyde binds directly at the active site, most likely at the distal iron.

Cyclic voltammograms (Figure 60) performed in the presence of formaldehyde show that formaldehyde binds preferentially to a reduced state of the H-cluster. The current at low potential (H_2 production activity) is inhibited to a greater extent than the current at high potential (H_2 oxidation) in the presence of formaldehyde, measured by comparison with an inhibitor free voltammogram. As the potential is swept below -0.5 V a characteristic wave-shape is observed; the current dramatically decreases as the rate of formaldehyde inhibition increases. The fact that this same potential dependent behaviour is observed for all three structurally distinct hydrogenases (*Ca*HydA, *Cr*HydA1 (Figure 60) and *Dd*HydAB[164]) suggests that formaldehyde reaction occurs at the conserved H-cluster. Detailed chronoamperometry studies of the potential dependence of the extent of formaldehyde

inhibition of both *Ca*HydA and *Cr*HydA1 show the same preference for reduced states of the enzyme (Figure 65). The variation in the extent of formaldehyde inhibition over the potential range -0.8 to +0.15 V does not fit to a single Nernstian process (Figure 68) showing that three oxidation levels are involved in the potential range, and formaldehyde binds preferentially to the most reduced state, the $H_{ox\text{-}2}$ level, formed at potentials below -0.5 V. This corresponds to a super-reduced state of the H-cluster, a state that has not yet been well characterised and has previously been reported to be inactive and only formed irreversibly.[82,86] The observed decrease in current at potentials below -0.5 V in voltammograms performed in formaldehyde, corresponding to inhibition of the super-reduced state, shows that this state is formed electrochemically during the voltammogram. The high activity recorded at these potentials in the absence of inhibitor therefore indicates that the super-reduced state is active, and formed reversibly during enzyme catalysis.

The strong preference for a specific oxidation level of the H-cluster is a strong indication that formaldehyde binds directly at the H-cluster; a binding site further away from the H-cluster (surface or surrounding residues) would be largely unaffected by variations in the electronic state of the enzyme, and thus the extent of formaldehyde binding would be potential independent.

Formaldehyde has been shown to partially protect [FeFe]-hydrogenases against damage by oxygen (Figure 63). Only 28% of the H_2 production activity at -0.45 V is retained after exposure to 25% O_2 for 1000 s, whereas introduction of 4.5 mM formaldehyde prior to O_2 exposure brings this to almost 70%. Binding of O_2 is known to occur at the distal iron of the H-cluster and formaldehyde blocks access to this site, suggesting that formaldehyde also attacks at this position.

Illumination of formaldehyde inhibited hydrogenase has no effect on the catalytic activity (Figure 64), whereas a large activation is observed for CO inhibited enzyme (Chapter 3). The Fe-CO bond is known to be extremely photolabile (section 3.1.2.4.2), but the bond formed upon formaldehyde binding is not, showing that this is a stronger covalent bond.

Density functional theory calculations, using a model that includes the [4Fe4S]-cluster, show that H_2 reduction is actually an endothermic process for H_{red} (H_{ox-1}) and is 7 kcal/mol more favourable for the H_{sred} state (H_{ox-2} level), for which the process is exothermic (

Scheme 15, grey). The involvement of the H_{sred} state in catalysis by [FeFe]-hydrogenases is therefore highly likely and challenges the notion that only the well characterised active states H_{ox} and H_{red} can be stable intermediates of catalysis. This is supported by the electrochemistry experiments, as described above, which also indicate that this state is formed during enzyme catalysis. States at the H_{ox-2} level do not have a long lifetime, as protons, the substrate of H_2 production are always in supply, and proton reduction by this state is extremely rapid, explaining the difficulty encountered when trying to characterise this state spectroscopically.[82]

The calculations involving formaldehyde show that there are two possible modes of binding, both of which are exothermic and favoured over H_2 production, and both modes are more favourable for more reduced states of the H-cluster. The first method of binding is Schiff base reaction at the bridgehead-N atom (

Scheme 15, blue), resulting in aminol formation (R_2N-CH_2OH); this state will then decompose exothermically. The second binding mode is hydridic attack of the Fe_d-H^- bond on the carbonyl bond (

Scheme 15, green), followed by proton abstraction and rearrangement to form the methanol bound state (Fe_d-OCH_3). Hydridic attack is more exothermic than Schiff base reaction, and can only occur for H_{red} and H_{sred}, while Schiff base reaction is also possible for the H_{ox} state (with greater driving force than H_{red}). Both Schiff base modification of the H-cluster and formation of a strongly bound methanol are consistent with the enhanced inhibition observed when H_2 production is monitored at a more negative potential, but neither option is consistent with the observed reversibility of the inhibition.[161] The protein environment around the H-cluster must therefore play an important role in destabilising or hindering formation of the

exothermic final products, thus moderating the actual potency of the aldehyde as an enzyme inhibitor. Unlike Schiff base chemistry, hydridic attack on formaldehyde does not result in strong covalent modification of the enzyme itself, leading us to favour the latter reaction pathway.

It is possible that both modes of binding occur in [FeFe]-hydrogenases; formaldehyde inhibition is biphasic, consisting of a fast and a slow phase. The more energetically favoured hydridic attack by Fe_d may be the fast phase reaction, and the less energetically favoured Schiff base chemistry the slow phase. The variation in the percentage of inhibition resulting from each phase as the potential is varied (Figure 66) reveals that for both *Ca*HydA and *Cr*HydA1 inhibition of H_2 production activity is almost completely due to the fast phase reaction. This reflects the greater driving force for the hydridic attack reaction for the H_{red} and H_{sred} states. For *Ca*HydA inhibition of H_2 oxidation activity is almost completely due to the slow phase reaction; reflecting the dominance of the H_{ox} state at high potential, which is unable to react with formaldehyde by hydridic attack, meaning that reaction proceeds via the slower Schiff base reaction. The proportion of inhibition due to the slow phase reaction also increases at high potentials for *Cr*HydA1, but an equal proportion of the reaction also proceeds via the fast phase reaction. For *Ca*HydA the fast phase reaction is 1000 times faster than the slow phase, whereas for *Cr*HydA1 this difference is just a factor of 100 (Figure 67). Additionally the rates of these two phases do not vary with potential for *Cr*HydA1, but for *Ca*HydA the rate of the fast reaction phase increases at oxidising potentials, difficult to rationalise with this reaction phase being hydridic attack. It is possible that a different, fast reaction occurs for formaldehyde binding to the H_{ox} state of *Ca*HydA.

[NiFe]-hydrogenases are far less sensitive to formaldehyde inhibition than [FeFe]-hydrogenases (Figure 71); a formaldehyde concentration 100 times greater is required

for the extent of inhibition of *E.coli* Hyd-2 to approach that of *Ca*HydA at -0.7 V. Inhibition of the H_2 production activity of *E.coli* Hyd-2 is completely potential independent; however formaldehyde does inhibit catalysis of [NiFe]-hydrogenases to some extent. This may be either by physically blocking H_2 access to the active site, or by direct binding to the active site, but is not affected by the oxidation state of the active site. This adds further weight to the suggestion that formaldehyde binds directly to the H-cluster of [FeFe]-hydrogenases; if reaction occurs at a position away from active site, inhibition would be expected to be more similar for both [NiFe] and [FeFe]-hydrogenases.

Interesting high potential inhibition is observed for both *Cr*HydA1 and *Dd*HydAB, thought to be related to formation of the H_{ox}^{inact} state, as this behaviour is not seen for *Ca*HydA, an [FeFe]-hydrogenase that forms very little of this state electrochemically. The extent of formaldehyde inhibition increases at high potentials (> -0.25 V) for *Cr*HydA1 (Figure 61) and cyclic voltammograms of *Dd*HydAB (Figure 72) indicate that formaldehyde stabilises the H_{ox}^{inact} state, as a smaller driving force is required for inactivation, and a greater driving force for reactivation. It is also possible that formaldehyde binds to the H-cluster at high potentials, generating an inhibited state more rapidly than formation of the H_{ox}^{inact} state can occur. Chronoamperometry experiments (Figure 75) however revealed that high potential inactivation and reactivation of *Dd*HydAB are too rapid for a difference to be accurately measured in the presence of formaldehyde using this method.

The extent of high potential inactivation of *Dd*HydAB is actually slightly greater in the absence of formaldehyde (Figure 74), suggesting that although it appears from voltammetry (Figure 72) that formaldehyde stabilises the inactive H_{ox}^{inact} state, it actually partially protects the enzyme against high potential inactivation. One possible explanation for the observed behaviour is proposed here, illustrated in Figure 78.

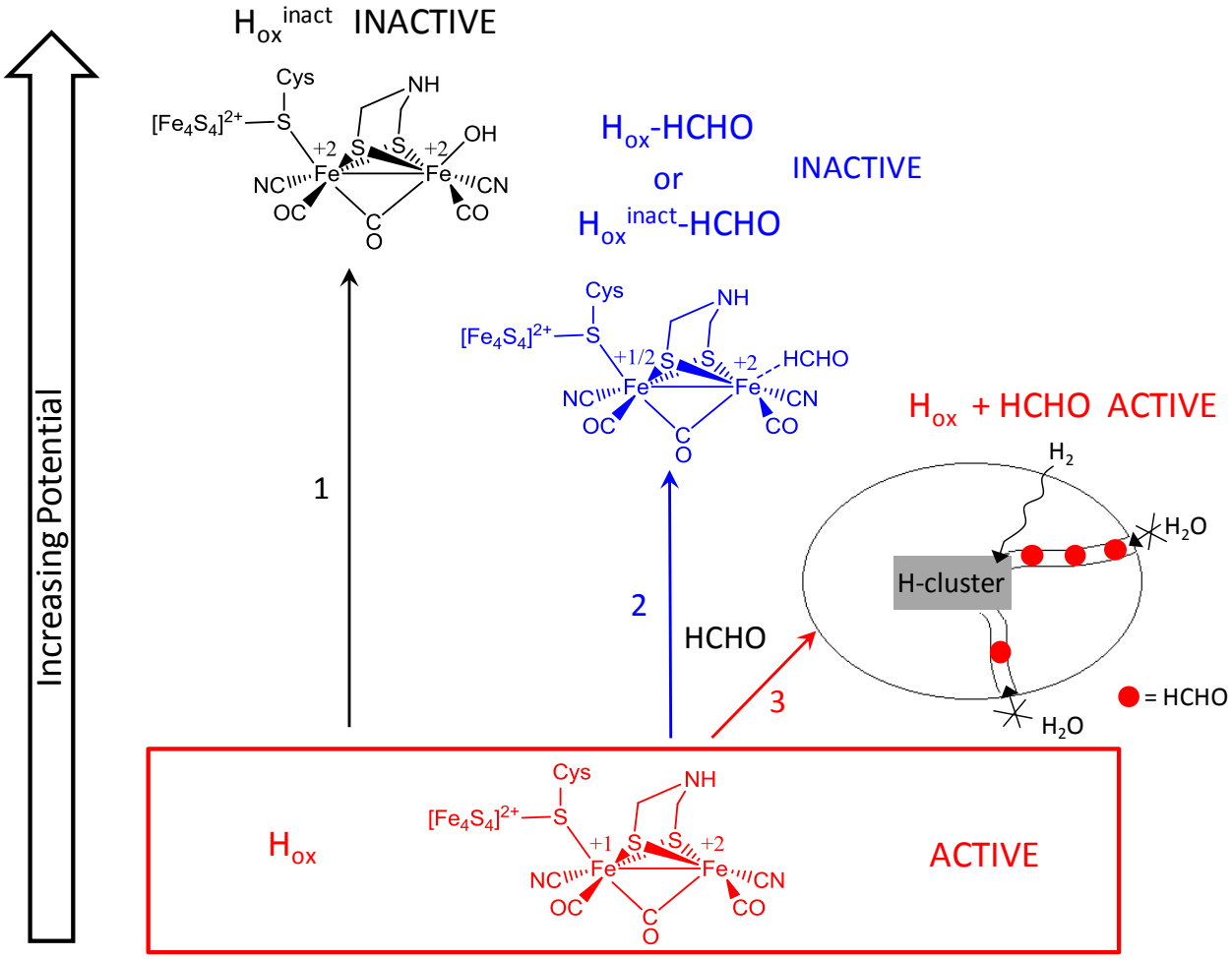

Figure 78: Cartoon showing the various possible fates of the H_{ox} state of the H-cluster at high potential. Reaction 1 shows one electron oxidation to form the H_{ox}^{inact} state. Reaction 2 shows the formation of an oxidised formaldehyde inhibited state, this could be at the same oxidation level as H_{ox}, or H_{ox}^{inact} but occurs at a less oxidising potential than formation of the H_{ox}^{inact} state. Reaction 3 shows the possible interaction of the enzyme with formaldehyde, where aldehyde does not bind to the H-cluster, but rather blocks access of water to the active site, while H_2 is still able to diffuse through the protein.

At oxidising potentials formaldehyde preferentially inhibits the enzyme before high potential inactivation to form the H_{ox}^{inact} state can occur. It therefore appears in voltammograms (Figure 72) that inactivation occurs at a less oxidising potential in the presence of formaldehyde, and reactivation at a more reducing potential. Formaldehyde inhibition however is not 100%, and some enzyme molecules remain active. The active molecules do not however form the H_{ox}^{inact} state, as formaldehyde is present in the gas channels of these molecules. The exact nature of gas transport through [FeFe]-hydrogenases is not yet fully understood (section 1.6.2), and it is

possible that H_2 is able to diffuse through the protein and access the active site, while other molecules, such as water, are blocked by the presence of formaldehyde. In this case catalysis can continue, but the H_{ox}^{inact} state cannot be formed as this state requires an oxygenic ligand (OH/H_2O) to be bound at Fe_d, and the access of water is restricted. This would explain the greater extent of inactivation observed in the absence of formaldehyde (Figure 74).

Experiments were conducted by Andreas Bachmeier (under my supervision) to characterise the potential dependence of inhibition with longer chain aldehydes to help gain further understanding of the mechanism of aldehyde inhibition. The possible reactions of formaldehyde (HCHO) and acetaldehyde (CH_3CHO) at both Fe_d-H and the bridgehead-N are compared in Scheme 16.

The reactions shown in black (Scheme 16) correspond to hydride reduction of the aldehyde by a reduced state of the H-cluster. This reaction is expected to extremely potential dependent; the hydricity of the H-cluster will increase as the potential is lowered. The reactions shown in blue correspond to Schiff base chemistry by attack of the bridgehead-N on the aldehyde. Although this pathway involves several reversible steps to generate an iminium ion ($H_2C=N^+R_2$), the final hydride reduction step to generate the alkylated amine (blue boxes) is expected to be completely irreversible.

Scheme 16: Two possible reaction pathways of formaldehyde and acetaldehyde with the H-cluster; transfer of a hydride from Fe_d to form an alkylate is shown in black, while Schiff base chemistry by attack from the bridgehead nitrogen is shown in blue. The hydride transferred in the final step may be supplied by Fe_d-H.

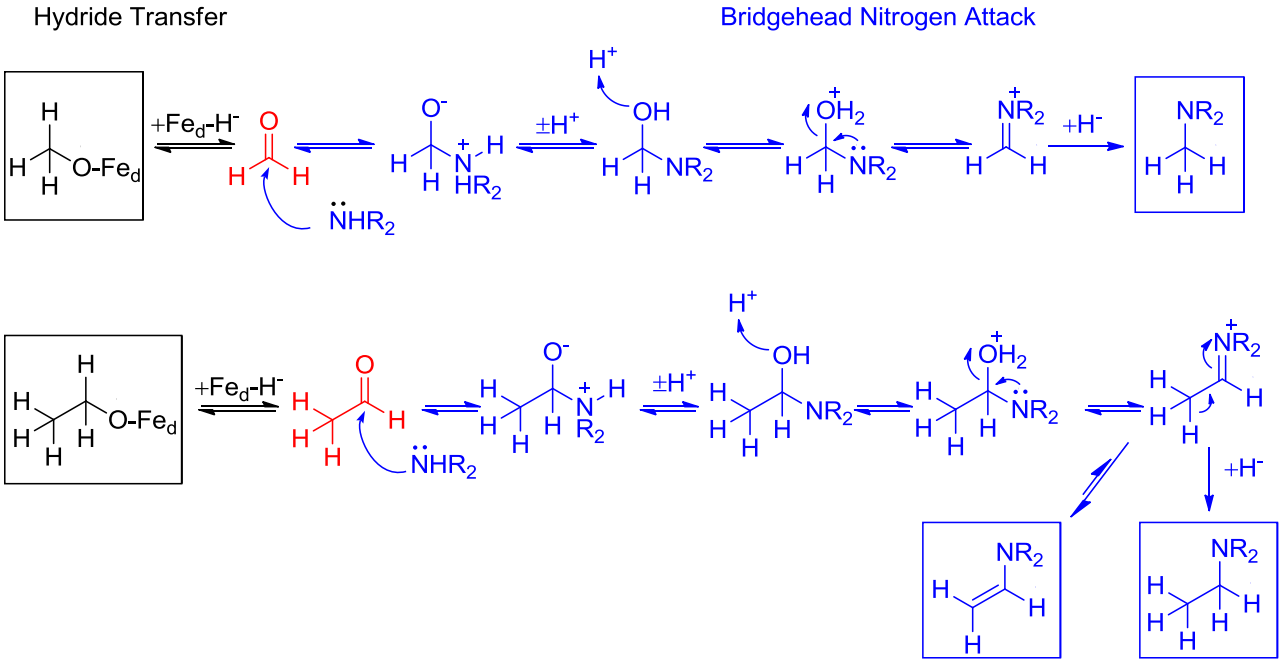

In longer chain aldehydes where there is a proton in the alpha position to the carbonyl bond there are two possible fates of the iminium ion: (1) hydride reduction to irreversibly form the alkylated amine or (2) loss of the alpha proton to reversibly form the corresponding enamine. (Although this reaction *is* reversible, the enamine is a rather stable product).

Chronoamperometry experiments were performed to characterise the potential dependence of acetaldehyde inhibition of *Ca*HydA (Figure 79), using the same method as in Figure 65 for formaldehyde inhibition. One difficulty of using acetaldehyde is the high volatility of this aldehyde in solution. For this reason experiments were performed at low temperature (5 °C) and the flow of gas was turned off immediately prior to aldehyde injection. Additionally a greater concentration of acetaldehyde was required for significant inhibition to be observed (336 μM CH_3CHO compared to 4.5 mM HCHO) due to the slower reaction of hydrogenase with this more sterically bulky, less electrophilic aldehyde. [The equilibrium constant of

acetaldehyde is 1, so 336 µM CH_3CHO corresponds to 168 µM of the non-hydrated aldehyde, while 4.5 mM HCHO correspond to 2.25 µM (K_{eqm}=2000) of the non-hydrated aldehyde, and it is the non-hydrated molecule that is believed to enter and inhibit the enzyme.[161]]

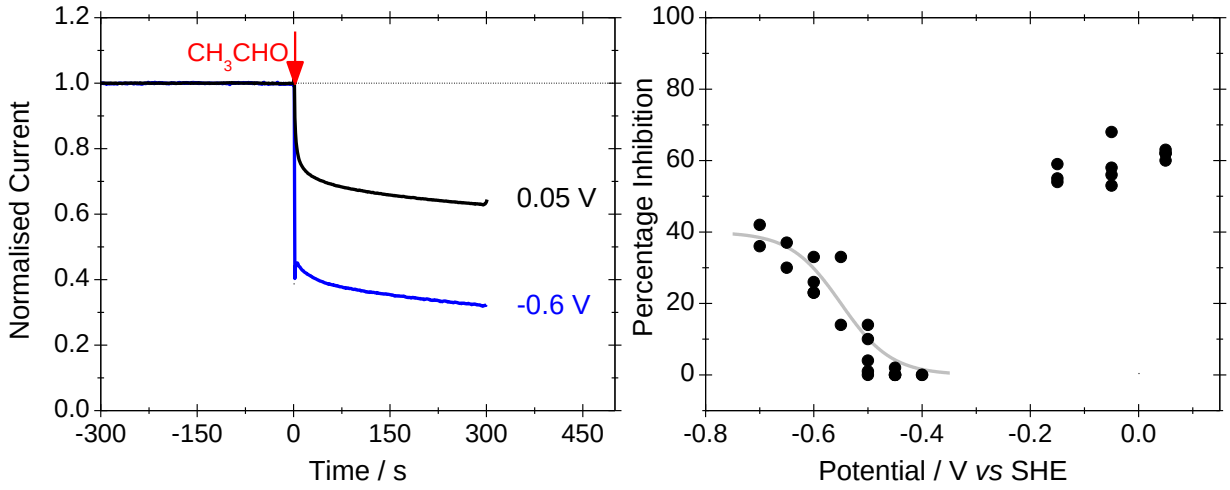

Figure 79: Representative chronoamperometry experiments performed on *Ca*HydA to probe the potential dependence of the extent of inhibition by 336 µM acetaldehyde (left) and the percentage inhibition after 100 s (right). The red arrow indicates injection of acetaldehyde at t = 0, immediately prior to which the gas flow was turned off. Conditions: *Ca*HydA, 336 µM CH_3CHO, 5 °C, ω = 3000 rpm, pH 6, 100% H_2. [The effect H_2 consumption at high potential (because there is no gas flow after aldehyde injection) was determined in a control experiment where buffer was injected in place of aldehyde, and the loss of activity monitored. Less than 5% of the activity was lost in these experiments.]

Example chronoamperometry experiments are shown in Figure 79 on the left, and the extent of acetaldehyde inhibition after 100 s is shown on the right across a potential range -0.7 to +0.05 V. Inhibition of H_2 production activity (-0.7 to -0.4 V) by acetaldehyde (Figure 79) shows the same potential dependence as formaldehyde inhibition (Figure 65); the extent of inhibition increases as the potential is lowered, reflecting the increased hydricity of the H-cluster. This supports the theory that aldehyde inhibition proceeds via direct reaction at the H-cluster by hydride reduction. Acetaldehyde inhibition at potentials where the enzyme catalyses H_2 oxidation (> -0.3 V) does not however show the same potential dependence as formaldehyde. There is very little formaldehyde inhibition (< 15%) at all oxidising potentials for *Ca*HydA (Figure 65), whereas ~60% of the H_2 oxidation activity is inhibited by

acetaldehyde (Figure 79). The ratio of the extent of inhibition at -0.7 V to 0.05 V is 14:1 for formaldehyde but just 0.7:1 for acetaldehyde; although the extent of acetaldehyde inhibition of H_2 production activity increases as the potential is lowered, acetaldehyde inhibits H_2 oxidation activity to an even greater extent. The reasons for this difference can be rationalised by looking at the reactions in Scheme 16. Inhibition of H_2 oxidation activity is unlikely to proceed via hydride reduction (Scheme 16, black) as reduced hydride-bound states of the H-cluster are unlikely to persist under such oxidising conditions. Reaction at high potentials is therefore more likely to proceed via nucleophilic attack by the bridgehead-N (Scheme 16, blue), resulting in formation of an iminium ion which can then be irreversibly reduced to methylamine. The greater extent of acetaldehyde inhibition at high potential, compared to formaldehyde indicates that nucleophilic attack by the bridgehead-N is more favoured for acetaldehyde. This may be related to the greater steric bulk of acetaldehyde favouring this reaction over binding at Fe_d. It is hard to rationalise why the high potential reaction occurs to such a great extent (Figure 79, right), although it is possible that acetaldehyde facilitates formation of H_{ox}^{inact} for *Ca*HydA as seen for *Dd*HydAB (Figure 72) in a way that formaldehyde does not.

Experiments were also conducted using trifluoroacetaldehyde, a more electrophilic analogue of acetaldehyde (Figure 80). The possible reactions of this aldehyde at the H-cluster are shown in Scheme 17. The possible reactions of CF_3CHO (Scheme 17) are very similar to CH_3CHO (Scheme 16), except that there are no alpha protons, meaning that the only possible fate of the iminium ion (other than the reverse reaction) is irreversible reduction to form the fluorinated alkylamine.

Scheme 17: The possible reactions of trifluoroacetaldehyde with the H-cluster; transfer of a hydride from Fe_d to form an oxalate shown in black, while Schiff base chemistry by attack from the bridgehead nitrogen is shown in blue.

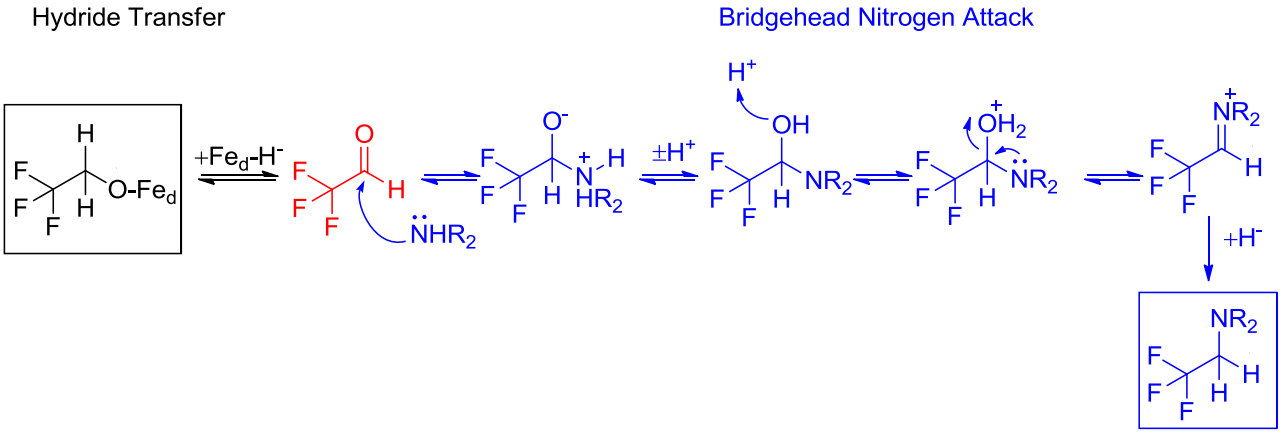

Chronoamperometry experiments were performed (Figure 80), as in Figure 79, to characterise the potential dependence of inhibition of *Ca*HydA. A maximum concentration of 182 mM CF_3CHO (corresponding to just 6.3 µM non-hydrate) was possible due to the high equilibrium constant of this aldehyde with the hydrate in aqueous solution (K_{eqm} = ~2.9 x10^4).

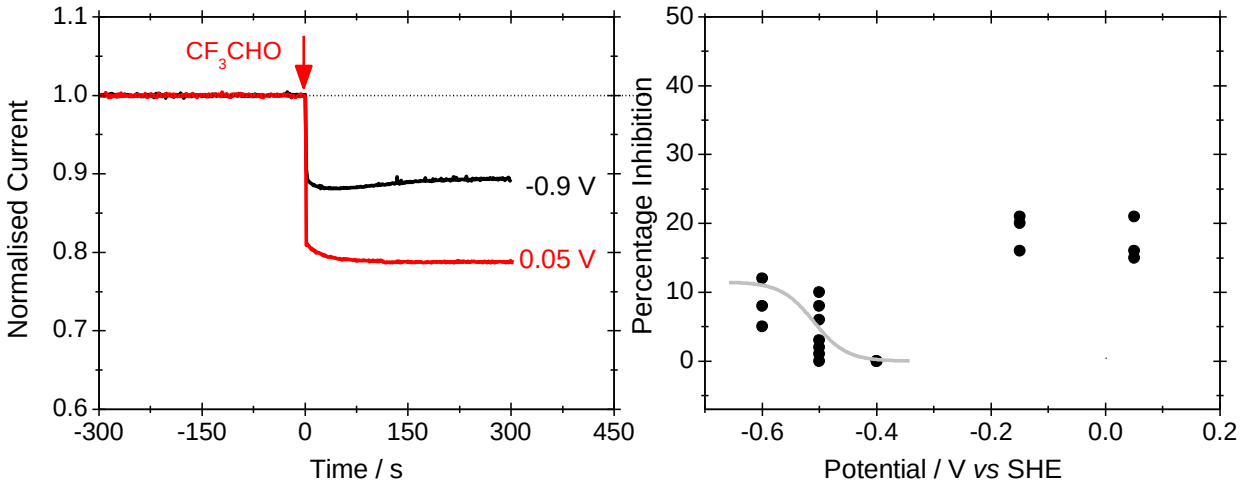

Figure 80: Representative chronoamperometry experiments performed on *Ca*HydA to probe the potential dependence of the extent of inhibition by 336 µM acetaldehyde (left) and the percentage inhibition after 100 s (right). The red arrow indicates injection of acetaldehyde at t = 0 Conditions: *Ca*HydA, 6.2 µM CF_3CHO, 20 °C, ω = 3000 rpm, pH 6, 100% H_2.

The extent of trifluoroacetaldehyde inhibition follows a very similar potential dependence profile to that of acetaldehyde inhibition. The differences include:

(1) The extent of inhibition. The extent of inhibition cannot be directly compared, as different aldehyde concentrations were used, however the concentration of acetaldehyde was more than 50 times greater than that of trifluoroacetaldehyde while the extent of inhibition is only approximately twice as great. This indicates that trifluoroacetaldehyde reacts to a greater extent, explained by the greater electrophilicity of the carbonyl bond in this aldehyde due to the electron withdrawing CF_3 group.

(2) **The ratio of high to low potential inhibition.** The extent of inhibition is 30% greater at +0.05 V than at -0.7 V for acetaldehyde, compared to an increase of 50% for trifluoroacetaldehyde. If high potential inhibition is considered to proceed via Schiff base chemistry at the bridgehead-N this suggests that attack by the bridgehead-N is more limited by the electrophilicity of the carbonyl bond than direct hydride reduction at Fe_d.

Comparison of the potential dependence of the rate of inhibition, proportions of fast and slow phase, and reversibility of inhibition for these two aldehydes is expected to shed more light on the reactions of aldehydes at the H-cluster, and experiments are ongoing.

Chapter 5

Comparative Analysis of Carbon Monoxide and Formaldehyde Inhibition

Abstract

The inhibition of [FeFe]-hydrogenases by carbon monoxide and formaldehyde was investigated in Chapters 3 and 4 and found to be strongly potential dependent. In this chapter these reactions are compared and contrasted, and a mechanism for H_2 production by [FeFe]-hydrogenase involving the H_{sred} state of the H-cluster is proposed.

5.1 Direct Experimental Comparisons

Cyclic voltammograms of [FeFe]-hydrogenase performed in the presence of either CO or formaldehyde reveal the preference of these inhibitors for binding to certain redox states of the H-cluster. The voltammograms of *Ca*HydA are compared in Figure 81, in the presence of CO (A) or formaldehyde (HCHO) (B).

These voltammograms reveal the complementary behaviour of CO and formaldehyde inhibition of [FeFe]-hydrogenase. Comparison of the non-inhibited (black) and CO inhibited (red) voltammograms in Figure 81A shows that CO targets an oxidised state of the hydrogenase; the H_2 oxidation activity (positive current) is inhibited to a greater extent than H_2 production activity (negative current). The opposite trend is seen for formaldehyde (Figure 81B), which binds preferentially to a reduced state of the H-cluster.

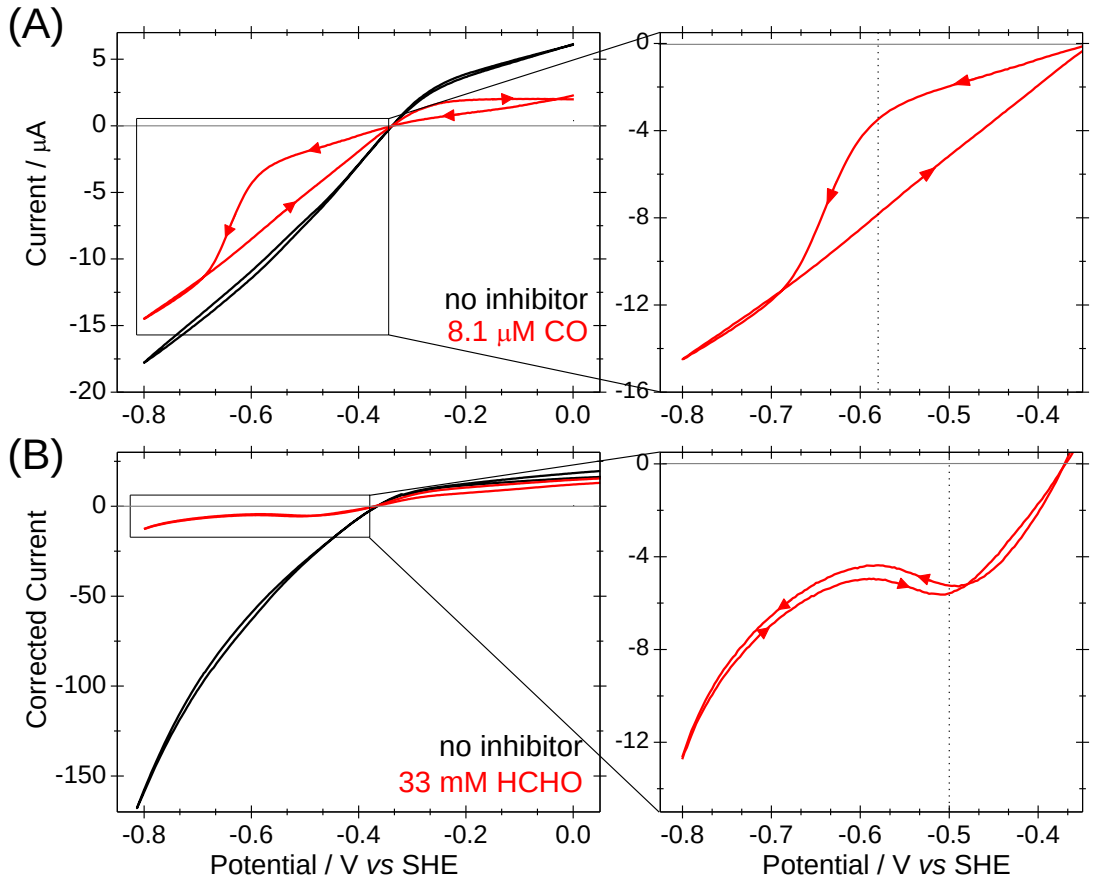

Figure 81: Cyclic voltammograms showing the complementary effects of CO and HCHO on *Ca*HydA. All scans were started from the high-potential limit. Black traces were recorded before addition of inhibitor and red scans were performed in the presence of: (A) 0.6% CO (8.1 μM), 80% H_2, 20% (N_2 + CO) or (B) 33 mM HCHO, 100% H_2. "Corrected current" denotes that data have been corrected for a linear loss of current over time (see section 2.1.8). Conditions: pH 6 phosphate buffer, ω = 3000 rpm, 3 mV/s scan rate, dark, 5 °C (A), 20 °C (B). The right hand panels show expanded sections of each voltammogram.

For both inhibitors the wave-shape of the inhibited scan (red) deviates greatly from the non-inhibited scan (black) at low potential. In the CO scan (Figure 81A, red) there is a sharp activation (increase in current) as the potential is swept below -0.58 V (dashed line). This corresponds to the formation of a state at low potential that rapidly releases CO, and has been identified as the super-reduced H_{sred}-CO state (section 3.7.2). This wave-shape is only seen in the reductive scan; re-binding of CO in the oxidative scan does not occur until the potential is swept above -0.35 V. In the formaldehyde voltammogram (Figure 81B, red) there is a decrease in the reduction current when the potential is swept below -0.5 V (dashed line). This

corresponds to the increased rate of formaldehyde binding to a state of the H-cluster formed at low potential, also identified as the super-reduced state (section 4.2.4). The oxidative scan shows the same wave-shape, revealing that in contrast to CO the rate of formaldehyde release is similar to the rate of formaldehyde binding under these conditions.

The rate of inhibitor release and re-binding was investigated using potential pulse chronoamperometry experiments (Figure 47 (CO) and Figure 62 (HCHO)). The experiments for CO and formaldehyde inhibition of *Ca*HydA are compared in Figure 82. In the CO experiment (Figure 82A, 13.6 μM CO) the H_2 production current was monitored at -0.5 V and the potential was stepped down to -0.8 V for 2 s. This potential step was intended to reduce inhibited enzyme molecules and generate the super-reduced inhibited state (H_{sred}-CO). This state is expected to release bound CO, reactivating the enzyme, resulting in an increase in the H_2 production current immediately after the potential step. The current is then expected to gradually decrease as CO rebinds.

In the formaldehyde experiment (Figure 82B, 27 mM HCHO) the H_2 production current was monitored at -0.55 V and the potential was stepped up to -0.02 V for 20 s. This step was intended to generate the oxidised state of the H-cluster that has a low affinity for formaldehyde (Figure 61A), to reactivate the enzyme by releasing the bound formaldehyde. It is therefore expected that immediately after this potential step the H_2 production current at -0.55 V will increase, and then gradually decrease as formaldehyde re-inhibits reduced states of the H-cluster.

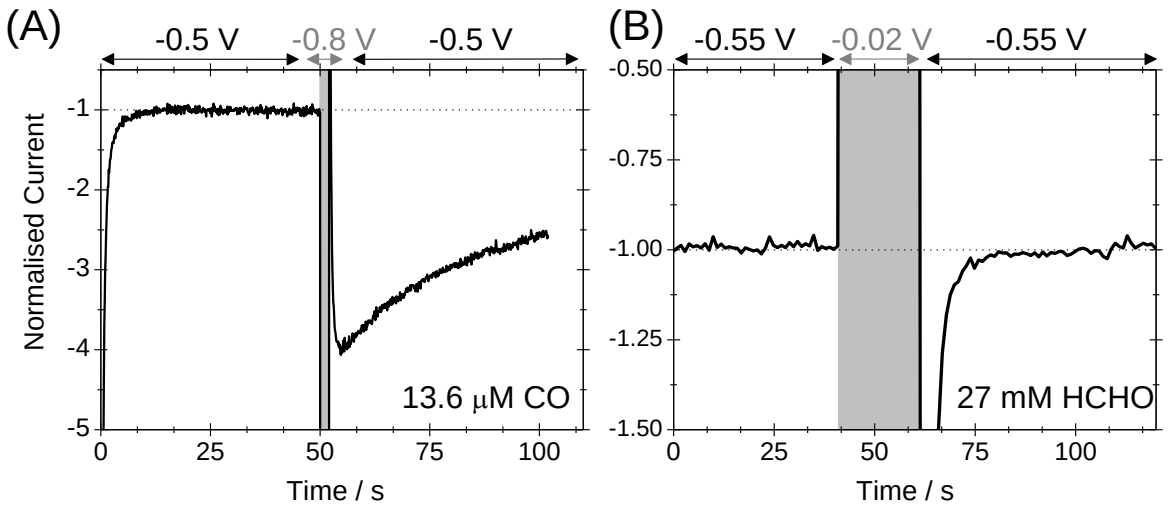

Figure 82: Chronoamperometry experiments showing the effect of short potential pulses on the H_2 production current of *Ca*HydA in the presence of either 13.6 μM CO (left) or 27 mM HCHO (right). For the CO experiment (A) the potential was stepped from -0.5 V to -0.8 V for 2 s and for the HCHO experiment (B) the potential was stepped from -0.55 V to -0.02 V for 20 s. Grey boxes denote potential pulses. Current has been corrected for 'film loss' and normalised to -1 before the potential step, dotted lines extrapolate the normalised current. Conditions: pH 6 phosphate buffer, 5 °C, ω = 3000 rpm, in the dark, 80% H_2/20% (N_2 + CO) or 100% H_2 (B).

The CO experiment (Figure 82A) shows the expected behaviour; a short (2 s) pulse to low potential is sufficient to reactivate the enzyme by generating the super-reduced inhibited state, which rapidly releases the bound CO. The H_2 production current at -0.5 V increases by a factor of 4, and then slowly decreases as CO re-binds.

The formaldehyde experiment (Figure 82B) shows no activation after the potential pulse even though a longer pulse length was used (20 s). This shows that either the rate of formaldehyde re-binding at -0.55 V is too fast for activation to be observed, or formaldehyde is not actually released from the H-cluster at high potential, even though activity at high potential is observed (Figure 61A). The latter case would mean that formaldehyde binds to the H-cluster in such a way that it inhibits H_2 production activity, but leaves the enzyme able to catalyse H_2 oxidation. The mechanism of H_2 cycling by [FeFe]-hydrogenase is not completely understood (section 1.5.2.2) and it is possible that H_2 oxidation is not a simple reversal of the steps involved in H_2 production.

Chronoamperometry experiments were performed in Chapters 3 and 4 (Figure 53 andFigure 65) to fully characterise the potential dependence of CO and formaldehyde inhibition. The variation in the extent of inhibition with potential was fitted to a Nernstian sigmoid (Figure 56 and Figure 68), however in both cases a value of n < 1 was found. The data however did fit to a double sigmoid reflecting two n = 1 Nernstian processes, as shown in Figure 83. This confirmed the involvement of three active states of the H-cluster: H_{ox}, H_{red} (H_{ox-1}) and H_{sred} (H_{ox-2}) in catalysis over the potential range studied.

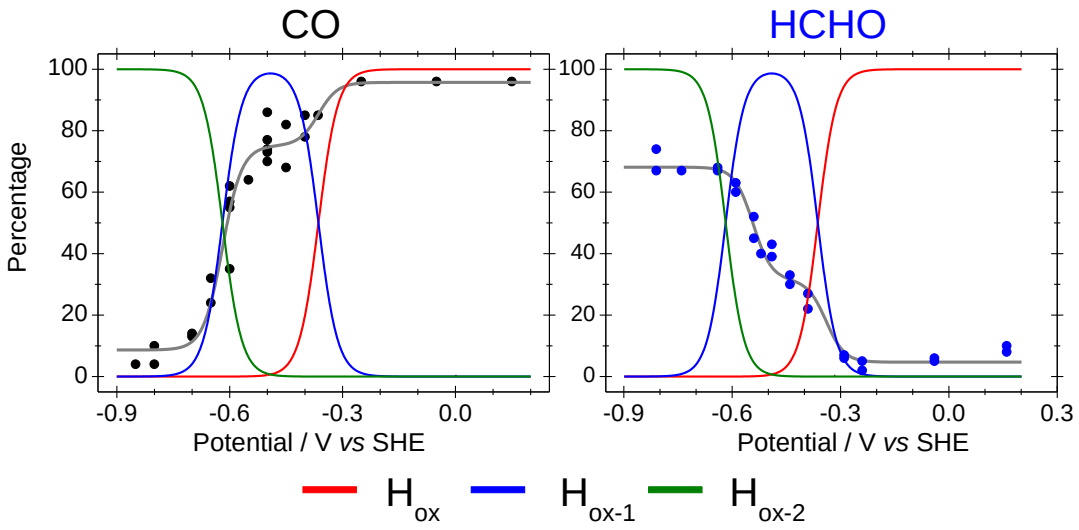

Figure 83: Plots showing the potential dependence of the extent of CO (left) and HCHO (right) inhibition of *Ca*HydA. The extent of inhibition (blue or black circles) was measured after exposure to inhibitor for 100 s; 107 µM CO in 80% H_2/20% (CO + N_2) or 4.5 mM HCHO in 100% H_2. Data was fitted to two n = 1 Nernstian sigmoids using Microsoft Excel Solver (grey lines, see section 3.7.2). The percentage of enzyme in each redox state is shown by the coloured lines, H_{ox} (red), H_{red} (blue) and H_{sred} (green). Conditions: pH 6 phosphate buffer, ω = 3000 rpm, 20 °C, in the dark.

Table 5: Summary of the potentials (E_1 and E_2) and proportions of active enzyme (Φ_i) for each redox level calculated from the double Nernstian fits shown in Figure 83 for *Ca*HydA.

Parameter	E_1	E_2	ΦH_{ox}	ΦH_{ox-1}	ΦH_{ox-2}
CO	-0.36 V	-0.62	0.04	0.25	0.91
HCHO	-0.38 V	-0.55	0.94	0.64	0.31

The plots in Figure 83 show the opposing potential dependence of the extent of CO inhibition of *Ca*HydA to that of HCHO. In both cases three redox levels of the hydrogenase are involved: H_{ox}, H_{ox-1} (H_{red}) and H_{ox-2} (H_{sred}). Binding of CO under the conditions used in the chronoamperometry experiments is very weak for the H_{sred} state (10-30%) and very strong for the H_{ox} state (> 90%) while binding of HCHO is very strong for the H_{sred} state (65-75%) but only weak for the H_{ox} state (5-15%). The coloured lines reflect the change in proportion of enzyme at each redox level as the potential is varied. The midpoint potentials (E_1 and E_2) of the transitions between redox states are compared in Table 5 in addition to the proportion of active enzyme at each redox level (Φ_i) as determined from the fit described in section 3.7.2.

There is only a small difference between the potential of the H_{ox}/H_{ox-1} couple (E_1) in CO and HCHO (-0.36 *vs.* -0.38 V) whereas the potential of the H_{ox-1}/H_{ox-2} couple (E_2) differs greatly for the two inhibitors (-0.62 V in CO *vs.*-0.55 V in HCHO). The higher E_2 potential measured in HCHO reflects the affinity of the H_{ox-2} level (H_{sred} state) for binding HCHO. This state (H_{ox-2}-HCHO) is stabilised relative to uninhibited states at the H_{ox-2} level (H_{sred}) meaning that a less reducing potential is required to generate it.

The Φ_i values shown in Table 5 reflect the proportion of enzyme at each redox level that is active (eg. for CO: $\Phi H_{ox} = \frac{[H_{ox}]}{[H_{ox}]+[H_{ox}-CO]}$). These values show that in CO only ~4% of enzyme at the H_{ox} level is in the active (un-inhibited) state, whereas in HCHO ~94% is in the active state. The opposite trend is shown for enzyme at the H_{ox-2} level; in CO ~91% of enzyme at the H_{ox-2} level (H_{sred} state) is in the active, un-inhibited state, whereas in HCHO only ~31% is in the active state.

Both CO[76] and HCHO (Figure 63) have been shown to protect [FeFe]-hydrogenase against damage by O_2, strongly suggesting that all three inhibitors bind to the same site; the distal iron of the H-cluster.

5.2 Implications

The different known redox states of [FeFe]-hydrogenases shown in Figure 6 can now be updated to include the states resulting from reaction with CO and HCHO (Figure 84).

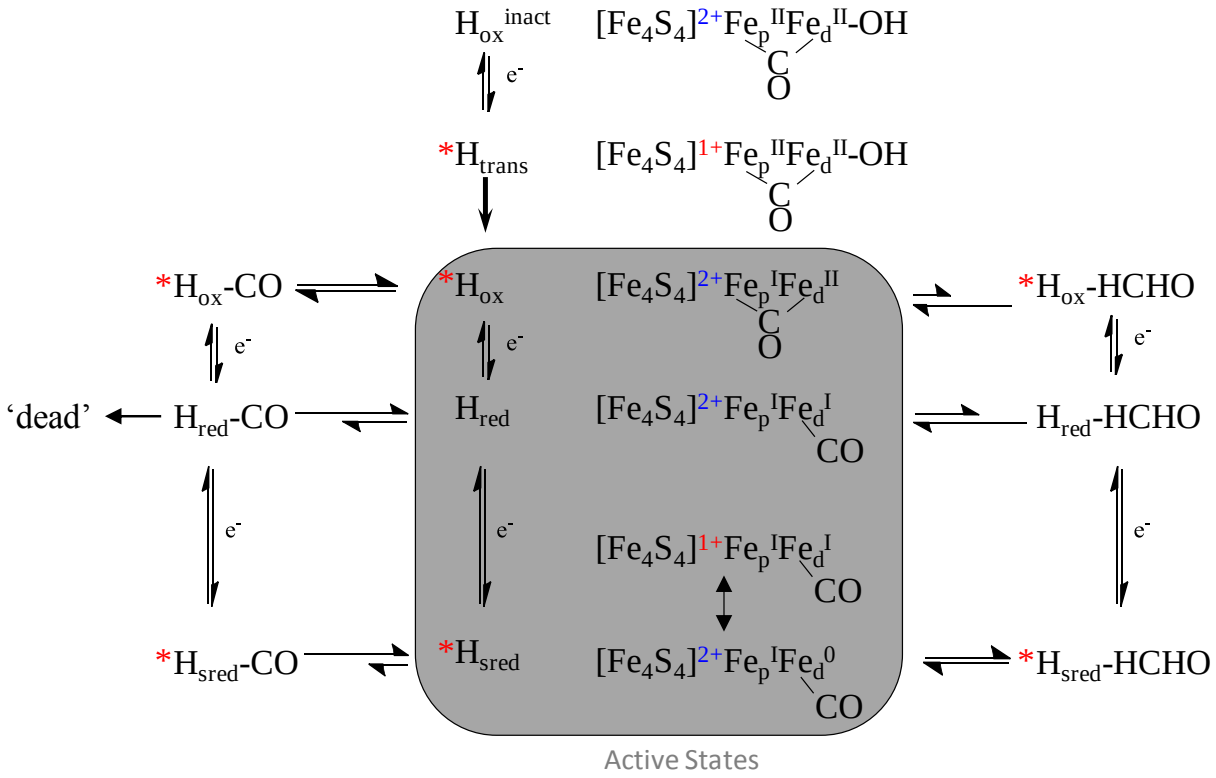

Figure 84: Summary of the redox states of [FeFe]-hydrogenase including the reaction of these states with CO and HCHO. The grey box denotes active states. Paramagnetic species (EPR active) are marked with an asterisk.

As discussed in Chapters 3 and 4 the experiments shown in Figure 81 toFigure 83 demonstrate that a super-reduced state of the H-cluster is generated at low potentials (< ~ -0.55 V), and that this state is able to catalyse H_2 production. The grey box in Figure 84 shows the active states of the H-cluster and has been updated to include the super-reduced

state. The states formed by reaction with CO are shown to the left, and with HCHO to the right. The H_{ox} state is shown to strongly bind CO but only weakly bind HCHO while the converse is true of the H_{sred} state, which is shown to bind CO only very weakly, but HCHO strongly. The H_{red}-CO state is shown to irreversibly degrade to form an inactive state.

Both the electrochemistry experiments in Chapters 3 and 4, and the DFT calculations summarised in Scheme 15 (Chapter 4) indicate that the super-reduced state of the H-cluster is involved in catalysis. The reaction of this state with formaldehyde indicates that a terminal hydride species (Fe_d-H^-) is involved. A possible cycle for H_2 production by [FeFe]-hydrogenase involving the super-reduced state of the H-cluster is shown in Scheme 18.

Scheme 18: Possible mechanism for H_2 production by [FeFe]-hydrogenase involving the super-reduced state.

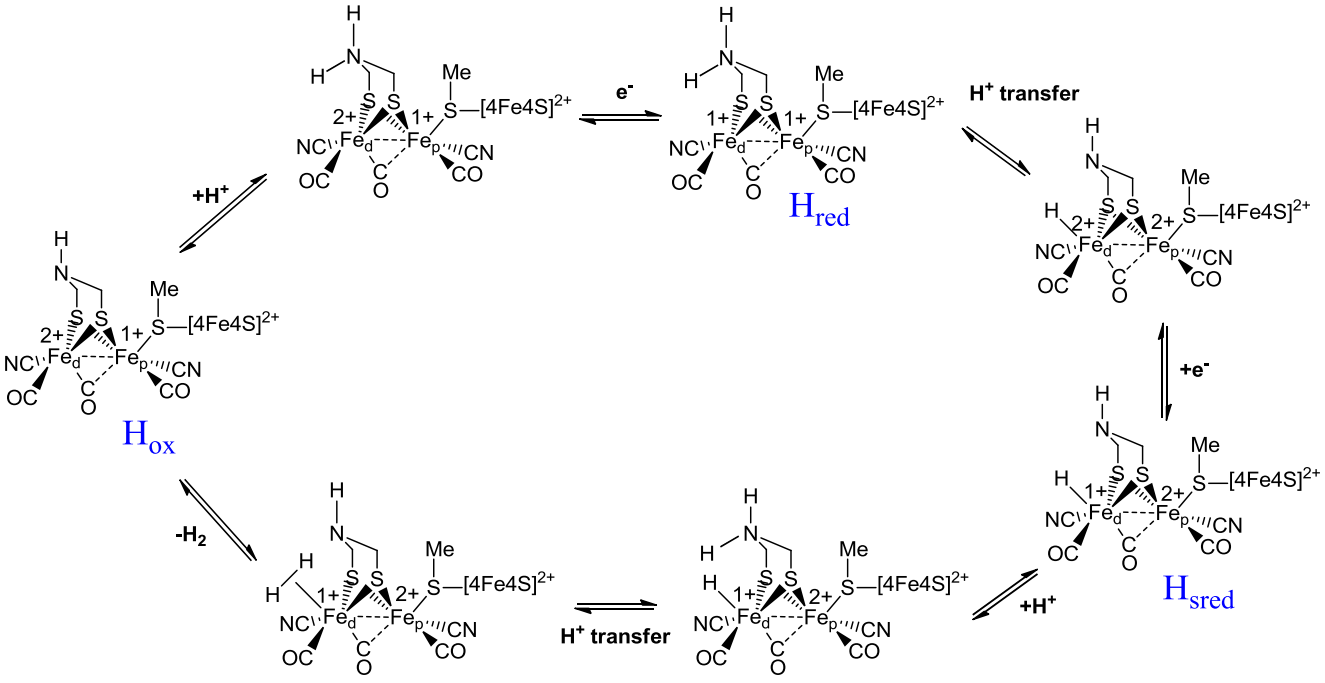

The cycle is initiated by protonation of the H_{ox} state (at the bridgehead N) followed by one electron reduction to form the H_{red} state, with the electron residing on Fe_d. This state is not expected to persist,[166] the proton is rapidly abstracted by Fe_d, binding as a hydride to form an $Fe^{II}Fe^{II}$-H^- state. The DFT calculations presented in

Scheme 15 show that although this state can be protonated and go on to release H_2 it is more energetically favourable for H_2 to be released from the H_{sred} state generated by a further one electron reduction. After reduction to form the H_{sred} state ($Fe^{II}Fe^{I}$-H^-) the bridgehead-N is protonated. This proton combines with the bound hydride to form H_2, the release of which regenerates the H_{ox} state. Alternatively it is possible that the cycle is initiated by one electron reduction rather than protonation, and the H^+/e^- steps are inverted. It is also possible that the H_{red} state ($Fe_p^{I}Fe_d^{II}$) is reduced to form the H_{sred} state ($Fe_p^{I}Fe_d^{I}$) before hydride abstraction occurs.

The position of the additional electron in the super-reduced state is not known; it could be localised on Fe_p, Fe_d or the [4Fe4S] cluster. In this cycle the electron is shown on Fe_d due to the greater affinity of this state for binding of HCHO. The DFT calculations in

Scheme 15 indicate that HCHO binds via hydridic attack on the carbonyl bond, as shown in Scheme 19.

Scheme 19: The mechanism of HCHO binding to reduced states of the H-cluster as shown in Scheme 15.

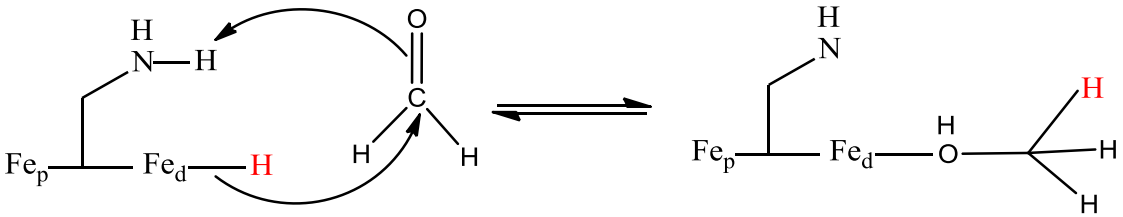

The increased rate of binding of HCHO to the H_{sred} state of the H-cluster (relative to the H_{red} state) results from the greater hydricity of this state, and this difference is most significant if the electron resides on Fe_d.

Hydridic reduction of HCHO by the H-cluster as shown in

Scheme 15 presents a striking parallel with the hydrogenation catalysts developed by Noyori[172,173] The essence of this analogy, depicted in Scheme 20, is that in both cases HCHO targets a state in which a reactive metal hydride is generated at an optimal position relative to an acidic amine. Nucleophilic attack by the hydride at the carbon with concomitant proton transfer to the oxygen leads to substrate reduction. Significantly, for the naked H-cluster, reaction with HCHO competes very favourably with catalytic formation of the H^--H^+ bond. If this mechanism is correct, it could open up interesting new possibilities for [FeFe]-hydrogenases to be engineered to perform other reactions.

Scheme 20: Simplified scheme showing the similarity between the proposed reaction of an [FeFe]-hydrogenase with formaldehyde and the known reaction of the Noyori catalyst.

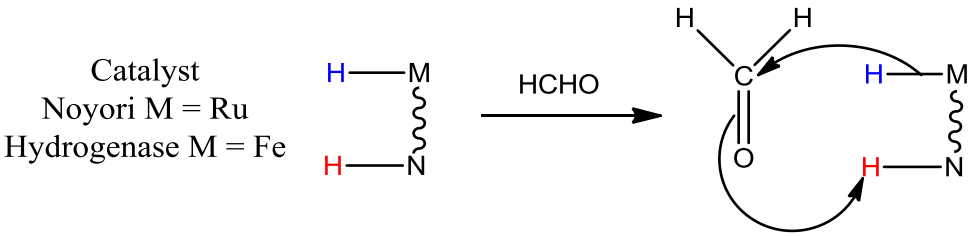

The involvement of reactive metal hydrides in biological systems is not isolated to hydrogenases. It has been suggested from computational studies that the mechanism of CO_2 reduction ($CO_2 + H_2 \rightarrow CO + H_2O$) by Ni-containing carbon monoxide dehydrogenase (CODH) involves a state containing a terminally bound Ni^{2+} hydride.[174] Reaction involves insertion of CO_2 into the Ni-H bond, and is unusual in that this results in formation of the metallocarboxylate (M-CO(OH)) rather than the more common metal formate (M-O-C(O)H). This unusual mode of insertion has been explained by the steric hinderance induced by the amino acid side chains surrounding the active site which prevents approach of CO_2 in the orientation leading to the transition state of metal formate formation.

Reduction of N_2 to ammonia by the Mo-dependent nitrogenase requires the action of two component proteins; the Fe-protein and the MoFe-protein.[175] The MoFe-protein contains the multimetallic FeMo-cofactor catalytic cluster [7Fe-9S-Mo-X-R-homocitrate], where substrates bind, and the auxiliary P-cluster [8Fe-7S], proposed to mediate electron transfer from the Fe-protein.[176] There are several different possible modes for H^+/H^- binding in the FeMo-cofactor including Fe and Mo hydrides.[177] It has been suggested from ENDOR spectroscopy studies[177] that H_2 production by the FeMo-cofactor involves a state containing two chemically equivalent iron hydrides, either two in a terminal position on one Fe atom (H-Fe-H) or two in a bridging position between two Fe atoms 2x(Fe-H-Fe).

Chapter 6

Development of Spectroscopic Techniques

Abstract

In this chapter several different spectroscopic techniques are presented, they were all used to characterise the reactions of [FeFe]-hydrogenases at low potential. Infrared spectroscopy (IR) was used in an attempt to characterise the super-reduced state of the H-cluster. The development and use of both a silicon based transmission cell and an attenuated total reflectance cell are described. The reaction of reduced states of [FeFe]-hydrogenase with formaldehyde was used as a way to trap the super-reduced state of the H-cluster for characterisation using electron paramagnetic spectroscopy (EPR). The mechanism of reaction of formaldehyde with [FeFe]-hydrogenase was investigated using nuclear magnetic resonance (NMR). This technique was employed to allow the detection of the products of reaction based on the hydridic attack mechanism proposed in Scheme 15 (Chapter 4) using H/D exchange. The super-reduced state of the H-cluster of [FeFe]-hydrogenases however remains elusive and this state was not successfully characterised in the experiments described in this chapter.

6.1 Introduction

It has been shown, from the electrochemistry experiments described in Chapter 4, that formaldehyde binds preferentially to the super-reduced (H_{sred}) state of the H-cluster of [FeFe]-hydrogenases. Binding at the H-cluster is thought to be via an Fe-O bond created by hydridic attack as shown in Scheme 21. Spectroscopic techniques, including FTIR and EPR, have allowed the different oxidation states of the H-cluster to be extensively characterised.[20,59,82,84,85] The super-reduced H_{sred} state however remains only poorly characterised. This is largely due to the great difficulty of isolating and capturing such a reactive species. With protons as the only substrate, immediately upon reduction of the H-

cluster to reach the super-reduced state the enzyme will rapidly reduce protons to form H_2, regenerating the more oxidised state of the enzyme, and thus eluding capture.

Scheme 21: The proposed process of hydridic reduction of formaldehyde by the H-cluster to generate the methanol bound species, taken from

Scheme 15.

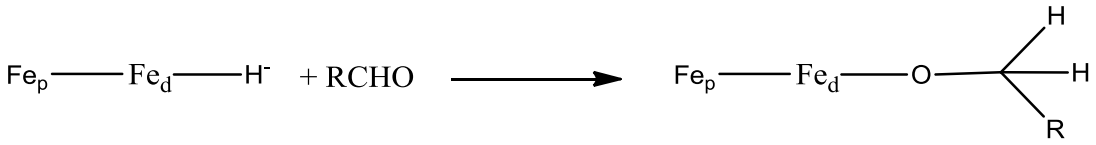

The preference of formaldehyde for binding to the H_{sred} state means that it can be used as a probe to trap the hydrogenase in this state. With formaldehyde bound, the enzyme becomes inactive, incapable of reducing protons, and the inhibited "H_{sred}-HCHO" state should be relatively stable (inhibition is only reversed when the potential is raised, Figure 61, or formaldehyde is removed from solution[161]). It should therefore be possible to 'trap' this state and carry out both IR and EPR studies.

If the alcohol generated by aldehyde binding is released from the enzyme, [FeFe]-hydrogenases could be regarded as reductases, catalysing the reduction of aldehydes to alcohols. If this is the case, the release process must be slow, since inhibition of activity is observed in PFE experiments, and formaldehyde binding followed by methanol production would still result in considerable negative current.

6.1.1 Infrared Spectroscopy

6.1.1.1Infrared Spectroscopy Techniques

Infrared (IR) spectroscopy exploits the fact that molecules absorb specific frequencies of radiation that are characteristic of their structure, these absorptions are thus resonant frequencies. The frequency of the absorbed radiation matches the frequency of the bond or group that vibrates. In this way the different functional groups or bonds present in a molecule

can be identified from the characteristic frequencies that the sample absorbs. Infrared spectroscopy is commonly used to characterise the structure of the active site of enzymes.[82,178,179]

Spectroelectrochemistry (SEC) techniques involve coupling the spectroscopic study of a protein sample with a system that allows potential control, allowing the different redox states of enzymes to be studied. Potential control may be achieved by either chemical or electrical means.[180] The various redox states of an enzyme can be reached chemically by reaction with different redox partners, substrates or inhibitors. Electrochemical methods allow more precise potential control, but the rate of oxidation/reduction of the enzyme sample is often slow. There are several different types of IR cell that can be used for spectroscopy including: (1) optically transparent cells (2) perforated electrodes and (3) reflective electrodes.

Transmission cells, made using an optically transparent electrode, are the simplest SEC systems. The electrode material must be both electrically conductive and allow the transmission of radiation over the energy range studied. Materials such as doped tin oxide and B-doped diamond have been shown to be effective materials.[180-182] Perforated electrodes can also be used; a thin gauze of a conductive material acts as the working electrode. Moss *et al.*[183] have developed a cell that incorporates a 6 μm thick, 70% transparent gold mini-grid as the working electrode. A platinum foil acts as the counter electrode and an Ag/AgCl reference electrode is incorporated into the cell to complete the three electrode system. The enzyme solution fills the cavity between two CaF_2 plates, while the outer cavity of the cell is filled with buffer solution.

One advantage of this cell design is the very small enzyme sample requirement, just 3-5 μL of enzyme solution is sufficient to fill the cell cavity. Additionally, the working electrode surface area to cell volume ratio is high, meaning that potential equilibration of the enzyme sample is

relatively rapid (1-2 min). The rate of electron transfer can be enhanced by adding redox mediators to the sample solution. One disadvantage of this cell design is the use of gold as the working electrode; gold is only chemically inert over a small potential window and H_2 is produced at potentials below ~ -0.65 V.

Absorption/reflection cells are systems more complicated than traditional transmission cells. They incorporate a thin layer of sample solution trapped between a working electrode and a barrier; light passes through the barrier, but reflects off the electrode. The barrier must be made from a material that is transparent to radiation over the energy range studied but also sufficiently reflective. The working electrode is a small disc of a conductive material, such as vitreous carbon or platinum, and is positioned so that the probe beam is focused on it. The reflected beam is refocused using a spherical or off-axis parabolic mirror and directed to the detector.

The advantages of this approach include an effective doubling of the optical path length, a reduced average distance between enzyme molecules in the solution and the electrode surface, leading to faster potential equilibration, and a more flexible range of cell geometries. The sample volume requirement however is larger than the Moss transmission cell, at approximately 70 μL per sample.[184]

6.1.1.2 Infrared Spectroscopy of [FeFe]-Hydrogenase

Infrared spectroscopy has played a crucial role in the characterisation of the H-cluster of [FeFe]-hydrogenases. In most studies a transmission cell (Moss cell) as described above, has been used, comprising a gold mesh working electrode.[82,85,183] The change in position of the IR bands relating to the intrinsic CO and CN ligands of the H-cluster as a result of potential

modulation provides information about the changes in both the oxidation state of the $[2Fe]_H$ sub-cluster, and the mode of binding of these ligands (eg. terminal*: t*-CO or bridging: μ-CO).

Studies of *Dd*HydAB[82] have revealed that the aerobically purified hydrogenase (H_{ox}^{inact} state) can be activated electrochemically to transiently form the inactive H_{trans} state by application of a reducing potential. [The different redox states accessible to the H-cluster of [FeFe]-hydrogenase are summarised in Chapetr 5, Figure 84.] Application of a more reducing potential results in the irreversible formation of the active H_{ox} state, and this state can be further reduced to form the H_{red} state.[82] These transitions are monitored by the gradual change in intensity of the ligand bands as the potential is modulated. For example: the stretching frequency of the terminally bound CO ligand on Fe_d decreases as the potential is lowered; the strength of the CO bond depends on the extent of back-bonding from the metal center. On reduction of the H_{ox} to the H_{red} state Fe_d changes from Fe(II) to Fe(I) and is therefore able to donate more electron density into the anti-bonding (π^*) orbital of the CO bond. This weakens the CO bond thus decreasing the vibrational frequency. For *Dd*HydAB in the H_{ox} state this *t*-CO stretching band is seen at 1940 cm^{-1} while in the H_{red} state it shifts down to 1916 cm^{-1}.[82] Additionally, the transition of the bridging CO ligand in all oxidised states of *Dd*HydAB, to a terminal position on Fe_d in H_{red} is easily monitored as the vibrational frequency increases dramatically. The midpoint potential of the H_{ox}/H_{red} couple of *Dd*HydAB was measured as -395 mV (at pH 8).[82] Application of a potential lower than -487 mV led to the disappearance of the most prominent H_{red} peak (the *t*-CO at 1894 cm^{-1}) which was replaced by a variety of new (much weaker) signals.[82] These new signals were attributed to the generation of a super-reduced state, H_{sred}. Formation of this state appeared to be largely irreversible; application of a more oxidising potential did not lead to the re-appearance of H_{red} or H_{ox} bands, leading to the conclusion that application of very low potential results in the destruction of the

H-cluster. The mid-point potential of the H_{red}/H_{sred} couple of *Dd*HydAB was measured as -540 mV (at pH 8). It should be noted however, that at such a reducing potential the enzyme rapidly reduces protons, releasing H_2 and re-generating the oxidised H_{ox} state, meaning that spectra recorded under these conditions correspond to enzyme in a mixture of redox states.

Similar studies were carried out on the algal hydrogenase *Cr*HydA1, with similar observations.[85] Notable differences include:

(1) The bridging CO ligand does not move to a terminal position in the H_{red} state, but does so in the H_{sred} state.

(2) The mid-point potential of the H_{red}/H_{sred} couple was measured as -460 mV (at pH 8), much higher than for *Dd*HydAB (-540 mV).

(3) Generation of the H_{sred} state is reversible, and the state appears to be stable; peaks relating to this state do not decay over time.

6.1.2 Electron Paramagnetic Resonance

Electron paramagnetic resonance (EPR) spectroscopy is a powerful method for obtaining structural information about molecular centres with unpaired electrons. Details of this technique were given in Chapter 2. EPR spectroscopy is commonly utilised for the characterisation of redox proteins in different oxidation states, however the study of [FeFe]-hydrogenases is limited by the fact that not all of the H-cluster states are paramagnetic (Chapter 5, Figure 84). Nevertheless EPR spectroscopy of [FeFe]-hydrogenases has been instrumental in determining the spin density distribution over the $[4Fe4S]_H$ and $[2Fe]_H$ subclusters of the active site,[145,185] the oxidation states of the individual iron atoms in the

$[2Fe]_H$ subcluster[59,84] and in determining the identity of the bridgehead atom of the dithiolate ligand.[185]

The [FeFe]-hydrogenases from both *Desulfovibrio desulfuricans* and *Desulfovibrio vulgaris* can be purified aerobically[42,75] and are isolated in an inactive form (H_{ox}^{air} or H_{ox}^{inact}). The inactive state can be reductively activated using either H_2 or artificial reductants, and was investigated by Patil *et al*. using continuous wave (CW) EPR.[79] Typical EPR spectra of [FeFe]-hydrogenase at different potentials are shown in Figure 85. The EPR spectrum of the as-isolated state (Figure 85A) has an almost isotropic signal at g = 2.02 (Figure 91a). This signal is attributed to trace amounts of an oxidised ferredoxin-type [4Fe4S] cluster (F-cluster) that has lost an Fe atom, and this is thus assigned to a $[3Fe4S]^+$ cluster, while the H-cluster itself is not in an EPR active state. As the potential is lowered a rhombic signal appears with *g* values of 2.06, 1.96 and 1.89 (Figure 91b), attributed to the transient formation of a state with the $[4Fe4S]_H$ cluster reduced, denoted H_{trans}.

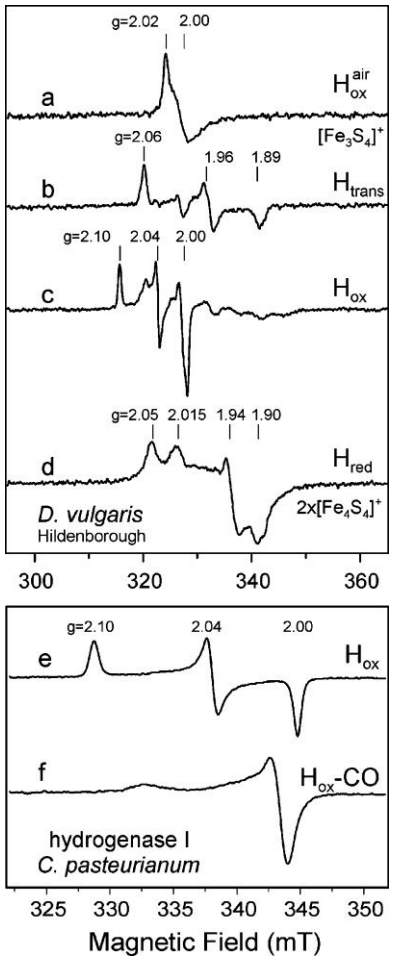

$[4Fe4S]^{2+}$— Fe_p^{2+}— Fe_d^{2+}

$[4Fe4S]^{1+}$— Fe_p^{2+}— Fe_d^{2+}

$[4Fe4S]^{2+}$— Fe_p^{1+}— Fe_d^{2+}

$[4Fe4S]^{2+}$— Fe_p^{1+}— Fe_d^{1+}

$[4Fe4S]^{2+}$— Fe_p^{1+}— Fe_d^{2+}

$[4Fe4S]^{2+}$— Fe_p^{1+}— Fe_d^{2+} — CO

Figure 85: EPR spectra of the [FeFe]-hydrogenase from *D. vulgaris* Hildenborough (a-d) under different redox conditions. (a) as isolated protein (b) rhombic signal at -160mV (H_{trans}) (c) rhombic signal at -255 mV (H_{ox}) and (d) fully reduced enzyme under H_2 (H_{red}). The bottom panel shows EPR spectra of *Cp*I (e) oxidised and (f) CO inhibited. Figure reproduced with permission from reference 59 (Lubitz, W *et al. Chem. Rev. (Washington, DC, U. S.)* 2007, *107*, 4331-4365). Copyright (2007) American Chemical Society. The oxidation state of the $[2Fe]_H$ and [4Fe4S] sub-clusters of the H-cluster are shown to the right of the spectra for each state.

Upon further reduction this signal is replaced by another rhombic signal with *g* values of 2.10, 2.04 and 2.00 (Figure 91c). This is a characteristic signal observed for all [FeFe]-hydrogenases and is assigned to the active oxidised form of the H-cluster, H_{ox}.[54,79,145,150,186] At more reducing potentials this signal is lost and the reduced active form of the H-cluster, H_{red} is formed. Although the H_{red} state is EPR-silent a complicated EPR signal is obtained (Figure 91d), resulting from dipolar coupling of the two reduced F-clusters. The CO inhibited state (H_{ox}-CO) is also paramagnetic and is characterised by an axial signal with g values of 2.006

and 2.065 (Figure 91e). This signal has also been observed for enzyme samples that have *not* been exposed to exogenous CO[145] explained by light induced 'cannibalisation'. Even under low-light laboratory conditions the H-cluster of some enzyme molecules becomes damaged and breaks down, the released CO is then able to bind to the H-cluster of undamaged enzyme molecules to form the H_{ox}-CO state.[82,145]

6.1.3 Nuclear Magnetic Resonance

Nuclear magnetic resonance (NMR) is a technique very commonly used to determine the structure of organic compounds. Electromagnetic energy is absorbed and re-emitted from the nuclei of atoms placed in a strong magnetic field. The nuclei of different atoms absorb unique frequencies of radiation depending on their magnetic properties and the surrounding chemical environment, thus by observing which frequencies are absorbed by a sample placed in a strong magnetic field, it is possible to learn much about the samples identity and structure.

The chemical shift of a nuclear environment (measured in ppm) depends on the magnetic field experienced by the nucleus. This is affected by the chemical environment; proximity to an electron withdrawing group (eg. Cl) deshields the nucleus, and results in a greater chemical shift. The relative intensities of the different NMR signals from a compound are proportional to the number of nuclei in each environment in the compound studied. The signals are often split into multiplets, dependent on the interaction (or coupling) with the spin of other nuclei in close proximity. The NMR signal from a particular nuclear environment is split into η lines by coupling to n (chemically equivalent) nuclei: $\eta = 2n\mathrm{I} + 1$, where I is the nuclear spin quantum number (H: I = ½, D: I = 1).

Products of the reaction of formaldehyde with [FeFe]-hydrogenases (Scheme 21) were studied using NMR spectroscopy. The proposed hydridic reduction of aldehyde by [FeFe]-

hydrogenase indicates that after binding of aldehyde (eg. formaldehyde) to the H-cluster the corresponding alcohol (methanol) will be generated. The NMR spectrum of methanol is different to that of formaldehyde, making its detection possible.

6.2 Experimental Methods

6.2.1 Infrared Spectroscopy

Silicon Transmission Infrared Cell

In this section the development of a transmission cell for IR spectroelectrochemistry investigation of hydrogenases is described. Developments were carried out together with Dr Alison Parkin. This cell was developed to allow in-house IR characterisation of [FeFe]-hydrogenase with particular interest in isolating and characterising the super-reduced state. The cell was designed utilising a thin silicon plate as the working electrode, rather than the more common gold mesh, believed to induce faster potential equilibration of the enzyme sample due to the larger electrode surface area. The cell design is shown in Figure 86. Initial experiments were conducted using the [NiFe]-hydrogenase from *Escherichia coli* (*E. Coli* Hyd-1) of which samples were more readily available than [FeFe]-hydrogenase, as this enzyme is purified in-house.

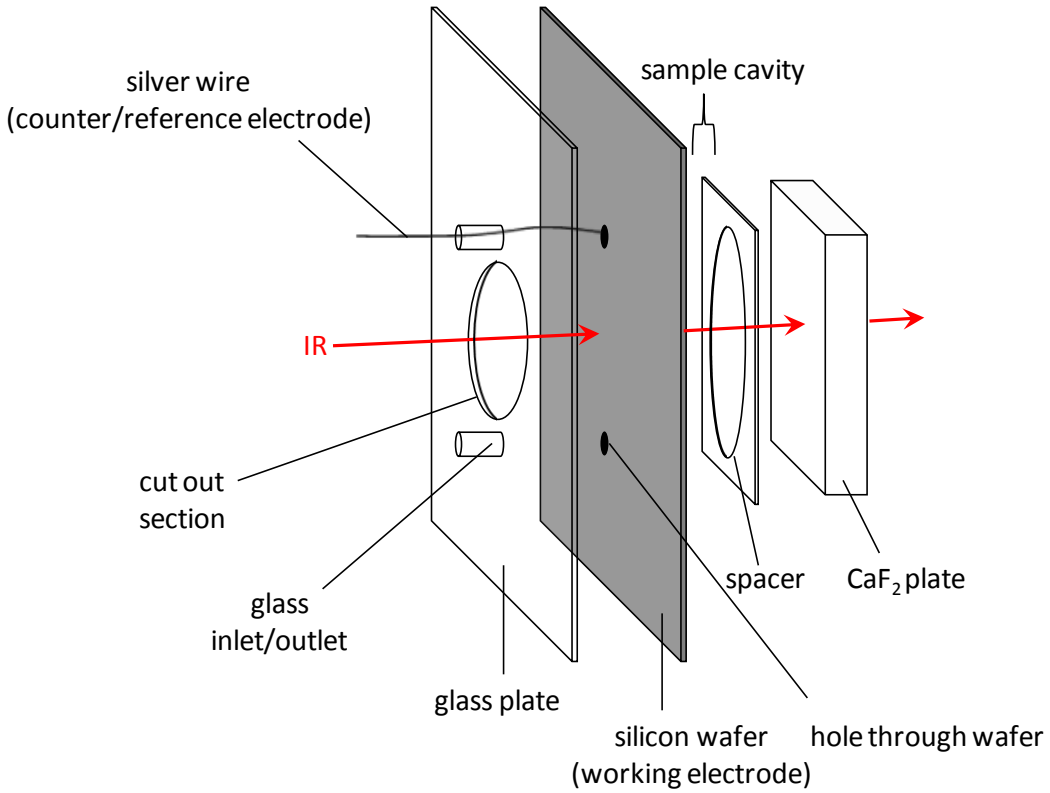

Figure 86: Lift out diagram of the silicon transmission IR cell developed.

The silicon wafer (280 µm thick, <100> surface, phosphorous doped, 0.01-0.02 Ω/cm resistance, one polished face, supplied by Compart Technology), was cut into small (~6 x 3 cm) rectangles using a diamond cutter. The wafer was strengthened by attaching a glass plate to the back (Araldite rapid epoxy was used to attach all cell components). A circular hole was cut out of the middle of the glass plate so that the IR beam does not have to pass through the glass. A spacer was made from a thin sheet of plastic (50 µm thick) glued around the edges of a CaF_2 plate, again with a hole cut out as shown in Figure 86. Once dry, glue was applied to the other side of plastic spacer and attached to the polished side of the silicon wafer. The thin space remaining between the silicon wafer and the CaF_2 plate, created by the thin plastic sheet (spacer) comprises the cell cavity. Two holes were made in the glass/silicon side of the cell, one at each end of the cavity, to allow solution to be injected. Glass inlets were glued over these holes, and sealed with rubber septa. After injection of sample (~30-50 µL) a silver wire

was inserted in one of the septa; the wire was in contact with the sample solution, but not with the silicon wafer. The Ag wire acted as a combined reference/counter electrode, while the silicon wafer acts as the working electrode, connected simply via a crocodile clip. Samples of *E. coli* Hyd-1 were prepared (0.3-0.5 mM) and injected into the cell in an anaerobic glove box. The rubber septa were sealed using a silicon rubber compound (RS Components) before the cell was removed from the glove box and transferred to the IR spectrometer.

Attenuated Total Reflectance IR Cell

An attenuated total reflectance (ATR) infrared spectroelectrochemical cell[187] was used with the aim of characterising the super-reduced state of [FeFe]-hydrogenase, in collaboration with the group of Dr Kylie Vincent. The cell comprised a silicon parallelogram ATR prism as described in reference 187.

A high surface area electrode is prepared by adsorbing enzyme on the surface of pyrolytic graphite particles. These particles are mixed with a neutral solution of Nafion in phosphate and are then coated on to the surface of the ATR prism.[187] The solution is left to dry, resulting in a hydrated polymer network of Nafion, through which proton transfer is efficient, with the enzyme coated graphite particles distributed through the network. The evanescent wave from the internally reflected IR beam penetrates ~5 μm beyond the prism into the film (**Error! Reference source not found.**a). An electrochemical cell is arranged on top of the prism and includes a silver wire counter electrode and Ag/AgCl reference electrode housed in buffer (**Error! Reference source not found.**b). The working electrode consists of the graphite particles in the Nafion network which are in contact with a small piece of carbon paper, and connected electrically via a gold wire. One advantage of this system over traditional IR cells is that the enzyme is in the partially dry Nafion network, so there is a reduction in the intensity of vibrational bands from solvent water. Only small solution volumes are required

(< 20 μL) but the enzyme solution must be of a high concentration (~100 μM) as approximately 2-2.5 nmol of enzyme is required in the film for signals to be significantly intense.

The ATR IR cell was employed for experiments on both the [FeFe]-hydrogenases *Dd*HydAB and *Cr*HydA1. The goal was to expose the enzyme sample to low potentials in order to record a spectrum of the super-reduced state of the H-cluster. Since the H_2 production activity of these hydrogenases at reducing potentials is so great, isolation of this state is difficult, For this reason enzyme was exposed to formaldehyde prior to the experiment; upon application of a reducing potential the enzyme is then expected (from PFE experiments in Chapter 4) to form the inhibited H_{sred}-HCHO state. The cell was assembled in an anaerobic glove box. Approximately 10 μL of 200 μM hydrogenase (in phosphate buffer) was mixed with 1.5 μL of a suspension of graphite particles (1mg/ml), 2 μL of Nafion phosphate solution and 5 μL of formaldehyde (13.4 mM). After mixing, this solution was spotted onto the surface of the ATR prism and left to dry for 10-15 mins. A small piece of carbon paper was placed on top of the enzyme film, and the rest of the cell assembled, forming a gas tight seal around the enzyme film. The cell was then removed from the glove box and transferred to the spectrometer. After the spectrometer chamber was purged, to remove atmospheric water, a spectrum could be recorded

6.2.2 Electron Paramagnetic Resonance

EPR samples were prepared by first activating 420 μL of *Dd*HydAB (41 μM in pH 6 phosphate buffer) under a flow of H_2 at 30 °C for 4hours[188] in an EPR cell (Figure 28). After activation a sample (140 μL) was then flash frozen in an EPR tube (‘*activated’).* Another 140 μL was removed from the cell and reserved for the ‘*control*’ sample. The formaldehyde sample (‘*HCHO’*) was prepared by injection of 2 μL of formaldehyde (13.4 M) to 140 μL of

the activated enzyme, immediately followed by injection of 7.5 μL of 20 mM electrochemically-reduced methyl viologen solution (in pH 6 phosphate buffer). The formaldehyde was introduced prior to the addition of mediator to encourage binding of formaldehyde immediately upon reduction of the enzyme to form the super-reduced state, before proton reduction could occur. The '*control*' sample was prepared in the same way, but with buffer injected in place of the formaldehyde. For each sample the final enzyme concentration was ~38 μM (measured using a Bradford assay[189]). For both the '*HCHO'* and '*control'* samples the methyl viologen concentration was 1 mM, and for the '*HCHO*' sample the overall formaldehyde concentration was 0.19 M, equating to approximately 100 μM of the non-hydrated form (Scheme 9, Chapter 4). EPR spectra were recorded at both 15 and 45 K (Figure 91).

6.2.3 Nuclear Magnetic Resonance

Experiments were designed to test whether alcohol is produced and released from the enzyme during the reaction of an [FeFe]-hydrogenase with an aldehyde (formaldehyde or acetaldehyde). Both ^{1}H and ^{13}C-NMR was used in conjunction with deuterated aldehyde and buffers to allow the putative alcohol product of the reaction to be detected, which would validate the proposed mechanism (Scheme 21).

A chronoamperometry experiment (Figure 87) was used to prepare an NMR sample. A 3-electrode set up was used, comprising a large surface area (~ 1cm^2) graphite working electrode, an Ag/AgCl reference electrode and a platinum wire counter electrode. The cell was water-jacketed and cooled to 5 °C before addition of 650 μL deuterated phosphate buffer (pH 6), 20 μL methyl viologen solution (50 mM) and 30 μL enzyme solution (*Ca*HydA, 0.17 mM).

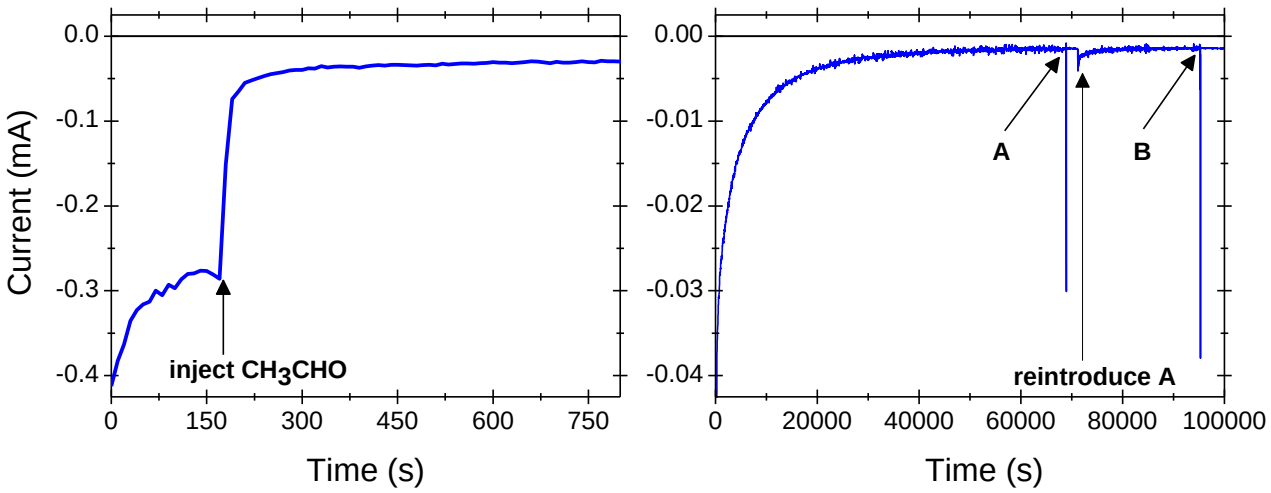

Figure 87: Chronoamperometry experiment monitoring the effect of acetaldehyde on the H_2 production activity of *Ca*HydA in solution with a large carbon electrode. The left panel shows the first 800 s of the experiment, acetaldehyde was injected at 170 s and left overnight. The right panel is an expanded section, showing the H_2 production current over the 27 hours after introduction of acetaldehyde. Conditions: -0.7 V, 5 °C, pH 6 deuterated phosphate buffer, 5.1 µM *Ca*HydA, 1 mM methyl viologen, 5.34 M acetaldehyde, sealed cell, no gas flow, stirred solution. The labels A and B represent the times at which the respective samples were taken, sample A was reintroduced to the cell at 71500 s. (The experiment in Figure 96 shows that exposure to aldehyde for such extended time periods does not irreversibly damage the enzyme).

A potential of -0.7 V (SHE) was applied (Figure 87), and after 150 s 300 µL of acetaldehyde was injected into the cell (left, arrow), the solution was then left stirring overnight. After 19 hours a sample of the cell solution was taken for NMR analysis (right, sample A). After NMR analysis the sample was reintroduced to the cell (indicated on Figure 87) and left for a further 6.5 hours to react before further analysis (sample B). Finally the potential was raised to -0.25 V for 300 s (not shown) and another sample (C) taken. The high potential step was performed to aid the release of aldehyde bound at the H-cluster, as observed using PFE (Figure 61A); aldehyde binds more tightly at low potential and is released when the potential is stepped to more oxidising values. A proton NMR spectrum of acetaldehyde in deuterated buffer is shown in Figure 93 and a spectrum of the experimental sample A is shown in Figure 94.

Another method of NMR product detection involved the use of deuterated, carbon 13 labelled formaldehyde ($D^{13}CDO$) in deuterated buffer in a H_2 atmosphere. The carbon label makes it possible to study the reaction with ^{13}C-NMR spectroscopy, eliminating the problem of the

water signal in ^{1}H-NMR, and therefore meaning that formaldehyde, supplied in an aqueous solution, can be used.

The experiment was carried out in an NMR tube inside an anaerobic glove box. A control experiment without enzyme was first run over 48 hours to ensure that no H/D exchange or alcohol production occurs simply for formaldehyde in H_2 saturated deuterated buffer. A solution of 4.4 mM D^{13}CDO was prepared using H_2 saturated pH 6 deuterated phosphate buffer, and added to the NMR tube. The tube was placed in a water bath at 5 °C and left under a gentle flow of H_2. The experiment with enzyme was carried out in the same way but with hydrogenase also in solution (8.5 μM, *Ca*HydA). In both cases a NMR spectrum was obtained after 24 and 48 hours (Figure 95).

6.3 Results

6.3.1 Infrared Spectroscopy

Silicon Transmission Cell

The silicon cell (Figure 86) was used to study one the [NiFe]-hydrogenases *E. coli* Hyd-1. As can be seen in Figure 88(a), very little light is detected in the cyanide region (red box, 2050-2100 cm^{-1}) when using this cell, while substantially more light is transmitted in the CO region (blue box, 1930-1960 cm^{-1}). A CO band is very clearly observed (the band consists of two overlapping peaks because the enzyme sample includes enzyme in a mixture of redox states), centred at 1940 cm^{-1} (Figure 88b), but the signals in the cyanide region are lost in the noise and cannot be identified. A spectrum of the same enzyme sample in a simple commercially available CaF_2 cell (without potential control) shows a cyanide band centred at 2090 cm^{-1} (Figure 88c).

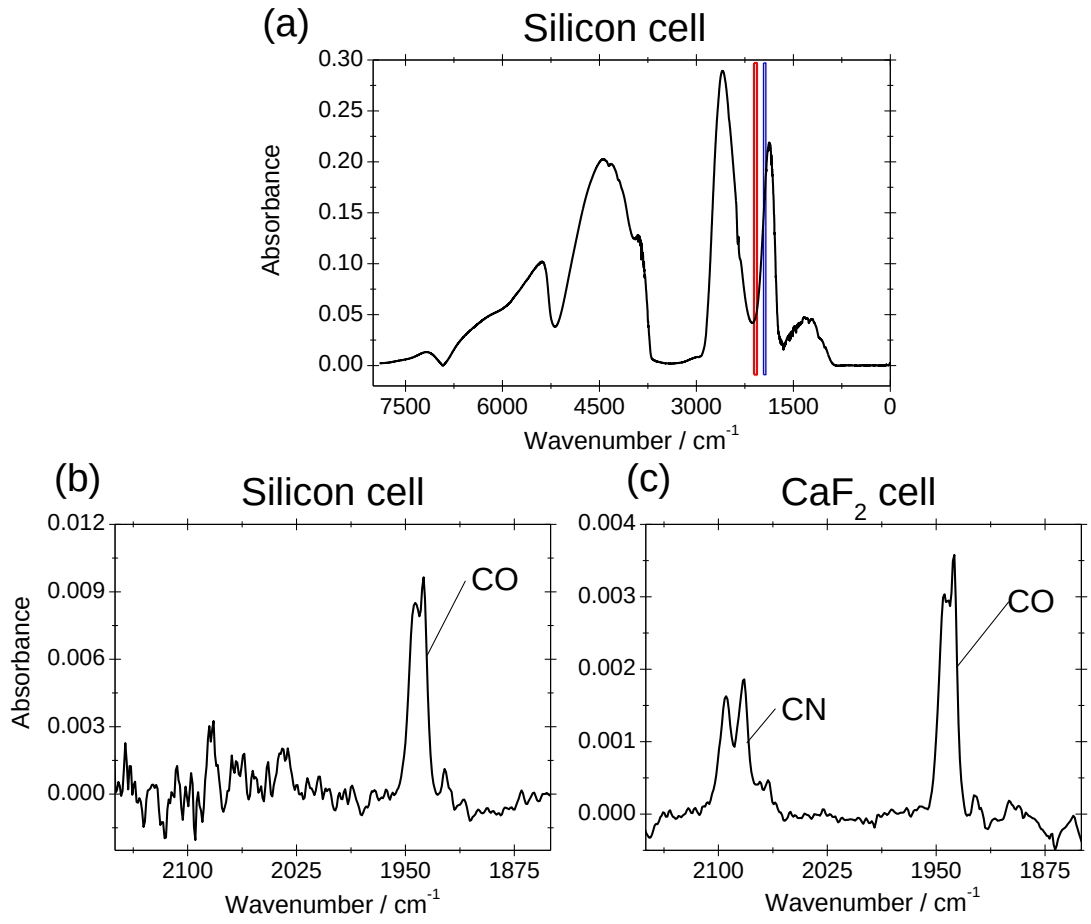

Figure 88: IR spectrum of as isolated *E. coli* Hyd-1 [NiFe]-hydrogenase in the silicon spectroelectrochemical cell (a and b) compared to a conventional CaF_2 transmission cell (c). The position of CO and CN bands are marked on the figure.

Potential control of the hydrogenase sample was possible as shown by the difference spectra in Figure 89. The different redox states of [NiFe]-hydrogenases are summarised in Chapter 1, Figure 5. A CO peak at 1944 cm^{-1} is attributed to enzyme in the Ni-B state,[27] and a peak at 1914 cm^{-1} to the Ni-SI state.[27] The black trace shows the change in absorption after application of 0 V for 1000 s; the peak at 1944 cm^{-1} grows, while a peak at 1915 cm^{-1} disappears, due to oxidation of the Ni-SI state to the oxidised Ni-B state. Application of a reducing potential (-0.7 V) shows the opposite effect; in the red trace (after 3000 s) the peak at 1944 cm^{-1} disappears while the peak at 1915 cm^{-1} grows.

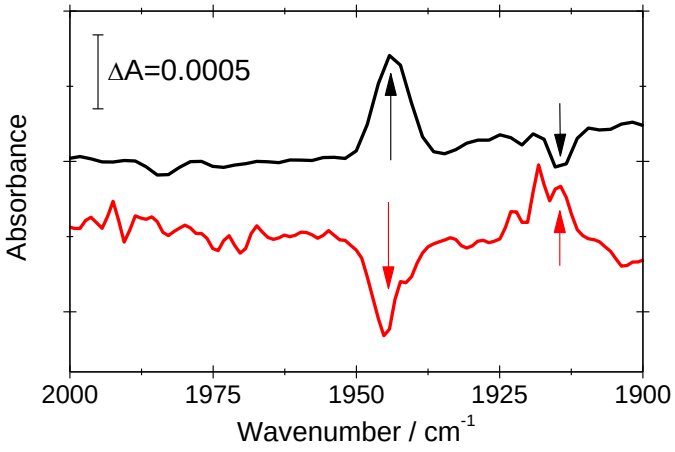

Figure 89: Difference spectrum of *E. coli* Hyd-1 recorded using the silicon IR cell. Black: 1000 s oxidation at 0 V (vs Ag wire) Red: 3000 s reduction at -0.7 V (vs Ag wire). 0.3 mM *E. coli* Hyd-1 in pH 6 buffer containing 100 mM Tris and 100 mM NaCl. Arrows indicate growth or loss of intenstity.

Although the sample is clearly under potential control, the equilibration time (time for peaks to stop changing in intensity) is very long (> 1000 s) and was considerably longer for the reduction process than the oxidation process.

Thicker spacers were placed between the CaF_2 plate and silicon (Figure 86) to help enhance the strength of the CN signals by allowing more protein to be interrogated by the IR beam; however peaks were still not resolved. In order to increase the amount of light able to pass through, the silicon the wafers were etched, both chemically and physically. Chemical etching[190] involved soaking in a 30% potassium hydroxide solution at 37 °C while physical etching involved using a sand bead blaster on the wafer surface. The physical method was more abrasive and did generate several holes in the wafer. The effect of these etching techniques on the transmission of light through the wafer was measured (Figure 90).

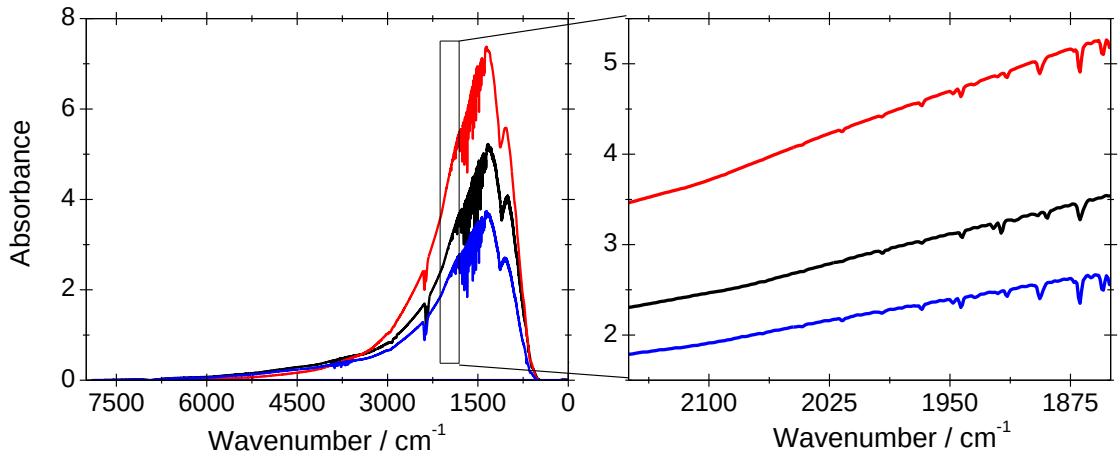

Figure 90: IR spectra of a 280 µm thick silicon wafer (not in an IR cell) after no treatment (black), chemical etching in 30% KOH solution for 120 mins (red) and after one surface was bead blasted (blue). A close up of the region of interest is shown on the right.

Comparison of the spectra of the wafer before etching (Figure 90, black) and after two hours of chemical etching (Figure 90, red) shows that slightly more light passes through in the region of interest (2100-1930 cm^{-1}). Physical etching (blue) however actually damaged the surface in such a way that less light was able to pass through the wafer, most likely due to increased scatter of the IR beam. Spectra of *E. coli* Hyd-1 recorded in a cell made with the chemically etched silicon wafer (not shown) however still did not exhibit a visible cyanide band.

Attenuated Total Reflectance IR Cell

Spectra recorded using the ATR IR cell (Figure 93) both in the presence and absence of formaldehyde, showed characteristic protein amide bands around 1500 cm^{-1} for both *Dd*HydAB and *Cr*HydA1. Bands relating to the CO and CN ligands of the H-cluster however were not seen, even after application of an oxidising potential to ensure that all enzyme molecules were in the same redox state (H_{ox}), or a reducing potential (to form H_{red} or H_{sred}). It is possible that H_2 production by the [FeFe]-hydrogenase in the film is so rapid that bubbles of H_2 gas are produced on the prism surface, explaining the lack of observed signals. The

samples prepared with formaldehyde, although expected to be inhibited, may still have been able to produce H_2, as the formaldehyde may have evaporated during formation of the film on the prism and formaldehyde inhibition of H_2 production is known to be reversible (Chapter 4). These [FeFe]-hydrogenases may also be simply incompatible with the partially dry Nafion network used, leading to enzyme degradation during film preparation.

6.3.2 Electron Paramagnetic Resonance

The CW EPR spectra of the samples described in section 6.2.2 are shown in Figure 91. At 45 K the F-cluster signals broaden significantly, due to more rapid spin relaxation, so only signals arising from H-cluster species are visible.

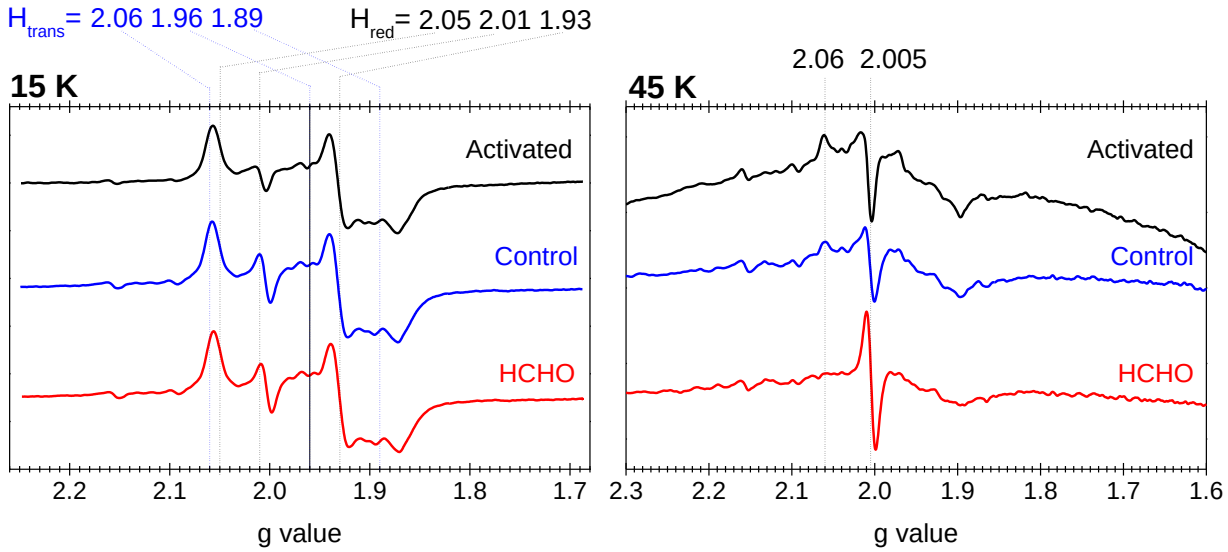

Figure 91: CW EPR spectra of *Dd*HydAB recorded at 15 K (left) and 45 K (right). Spectra were measured at 9.38 GHz with 0.126 mW (15 K) or 2 mW (45 K) icrowave power and a modulation amplitude/frequency of 1 mT/ 100 kHz. All enzyme samples were activated for several hours in a H_2 atmosphere at 30 °C (see methods). The top trace in both panels shows the enzyme after H_2 activation. [HCHO] = 0.19 M, [MV] = 1 mM in '*HCHO*' and [HCHO] = 0, [MV] = 1 mM in '*Control*'.

Figure 91 compares the EPR spectra of the three different samples prepared (section 6.2.2); there are no significant differences between the samples and no indication that a new state has been formed in the presence of formaldehyde. The spectra at 15 K are fairly complicated, but resemble those reported for the H_{red} state of *Dd*HydAB[79] (Figure 85), and are thought to

comprise of signals from two states of the enzyme. Most of the enzyme has been reduced to the H_{red} state, evidenced by the dominant complex rhombic signal with *g* values of 2.05, 2.01 and 1.93 which is attributed to the two dipolar coupled, reduced ferredoxin-type [4Fe4S] clusters.[79] A second rhombic signal with *g* values of 2.06, 1.96 and 1.89 is attributed to a small quantity of enzyme in the H_{trans} state,[79] showing that activation was incomplete. There is a small peak at g = 2.10 which may be due to traces of enzyme in the H_{ox} state. Methyl viologen radicals have an EPR signal at g = 2.0, which may explain the increased intensity of the signal around this value for the '*HCHO'* and '*control'* samples compared to the '*activated'* sample which did not contain any mediator. At 45 K the signals are much broader and less intense than at 15 K, but there is still a very prominent signal at g = 2.01, the origin of which is not fully understood. This signal is likely to relate to mediator (methyl viologen), however the 'activated' sample was not exposed to any methyl viologen.

The experiment was repeated with a much greater formaldehyde concentration (6.3 M), equating to 3.2 mM of the non-hydrated form, giving a ratio of almost 200:1 of the non-hydrated aldehyde to the enzyme. Once again there was no difference between the EPR spectrum of the '*HCHO'* and '*control*' samples, indicating that it is not a lack of formaldehyde that limits formation of the inhibited "H_{sred}-HCHO" state.

The lack of detection of a new reduced state of the H-cluster at low potentials in the presence of formaldehyde is attributed to insufficient accumulation of the H_{sred}-HCHO state. It is possible that under the conditions used to generate the EPR samples the rate of H_2 production by the enzyme in the H_{sred} state is so rapid that the formaldehyde simply cannot trap it. It is however most likely that methyl viologen ($E°(MV^{2+}/MV^{+})$ = -460 mV at pH 7)[191] simply does not lower the potential sufficiently to generate this state; the use of other, lower potential mediators such as europium may rectify this.

Further experiments were initiated using *Cr*HydA1, utilising the reactions of Eu(II) as a supply of very low potential electrons (Scheme 22). A chelating ligand EGTA (ethylene glycol tetraacetic acid) has been shown to have an extremely high affinity for Eu(III), meaning that introduction of this ligand to Eu(II) results in the formation of a Eu(II)-EGTA complex that readily donates an electron at very low potential (-0.88 V at pH 8) to produce the Eu(III)-EGTA complex.[192]

Scheme 22: The Eu(III)/Eu(II) reduction potential and the effect of the addition of EGTA on the reduction potential.[192]

$$Eu^{III} \xrightleftharpoons{-0.4\ V} Eu^{II}$$

$$Eu^{III}{-}EGTA \xrightleftharpoons{-0.88\ V} Eu^{II}{-}EGTA$$

Cyclic voltammograms recorded in HEPES buffer are shown in Figure 92, left. The red trace was performed with $EuCl_2$ in the buffer solution, and a clear downward shift in the potential of the Eu(II)/Eu(III) couple is visible after addition of the EGTA ligand (blue trace). The voltammograms on the right show the same experiments recorded in phosphate buffer; the europium oxidation and reduction peaks are not visible as the potential of the Eu(II)/Eu(III) couple is shifted due to coordination of phosphate to the europium. The phosphate buffer system that has already been established for [FeFe]-hydrogenase EPR experiments in this chapter (section 6.2.2) is therefore incompatible with the europium/EGTA system. The enzyme samples for the EPR experiments in this chapter were supplied in a solution of phosphate buffer (section 2.2.10), to avoid the use of tris buffer salts, the amine group of which would react with formaldehyde (Scheme 11). EPR experiments using the europium system as a reducing agent for *Cr*HydA1 are ongoing using a HEPES buffer system.

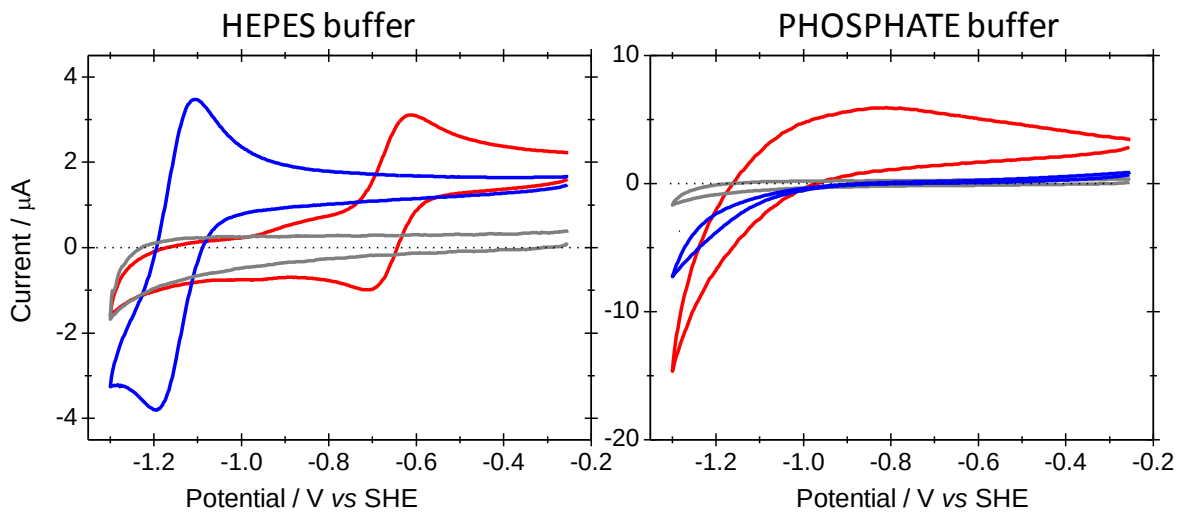

Figure 92: Cyclic voltammograms of $EuCl_2$ in different buffer solutions showing the effect of EGTA on the reduction potential of the Eu(III)/Eu(II) couple. Grey = buffer, red = $EuCl_2$ and blue = $EuCl_2$ + EGTA (1:1). Conditions: 25 °C, no rotation, 100% N_2, pH 8 HEPES (left) or pH 6 phosphate (right), 20 mV/s scan rate.

6.3.3 Nuclear Magnetic Resonance

The proposed reaction of acetaldehyde (CH_3CHO) with [FeFe]-hydrogenase is outlined in Scheme 23 for a system in a deuterated buffer solution. Although the reaction of enzyme with formaldehyde is faster and more extensive than with acetaldehyde,[164] the former is supplied in a water solution which makes it unsuitable for this study,[i] the water signal would overwhelm the ^{1}H-NMR spectrum.

At low potential, in deuterated buffer, the enzyme forms a state with a deuteride (D^-) bound at the Fe_d site of the H-cluster (from Scheme 18). Upon addition of acetaldehyde, this deuteride is transferred to the carbonyl carbon of acetaldehyde and an Fe_d-O bond is formed. Scheme 23 shows that once this aldehyde-bound state forms there are two possibilities:

(1) the corresponding deuterated alcohol (ethanol) is released

[i] It should be noted that a solution of formaldehyde in deuterated solution could be prepared by hydration of formaldehyde supplied as a solid polymer.

(2) the reaction reverses and the aldehyde is released from the enzyme. In this case there is a 50/50 chance that the released aldehyde will contain the deuteron instead of the original proton.

Scheme 23: Proposed scheme for the reaction of acetaldehyde with [FeFe]-hydrogenase. Proton NMR shifts for each proton environment are given below in blue. Product (1) is the alcohol product, deuterated ethanol. Product (2) is the released aldehyde, deuterated acetaldehyde .

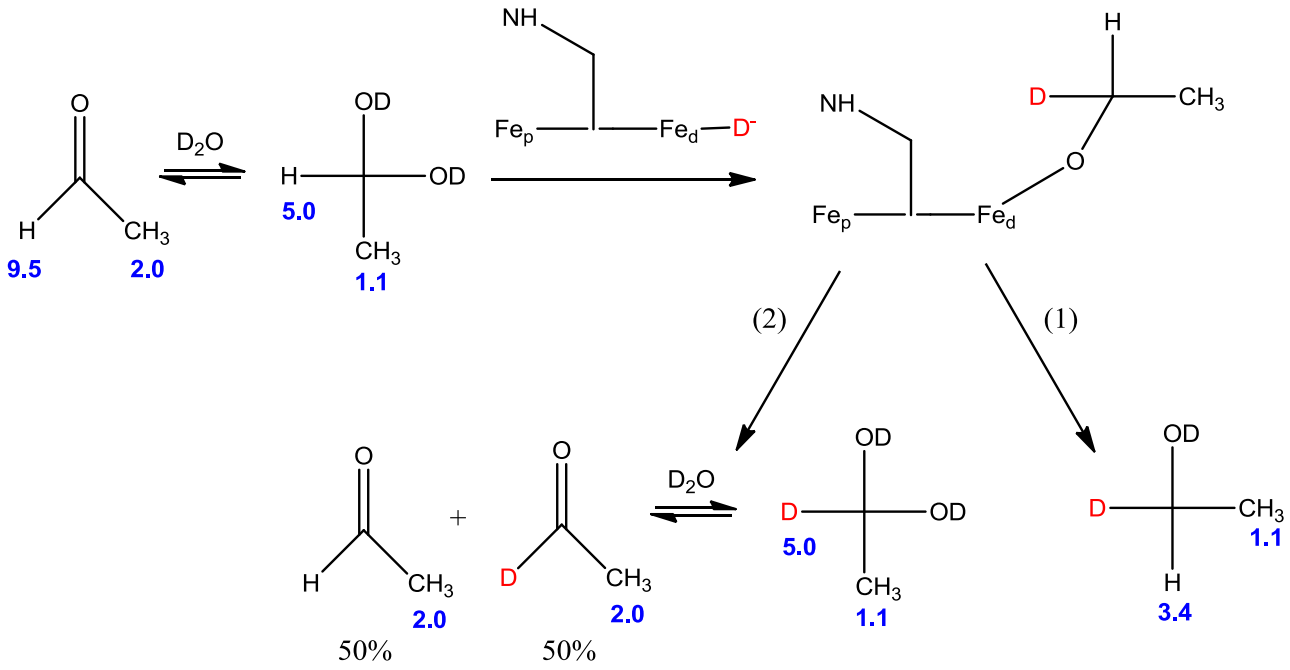

In either possible reaction it should be possible to detect the change using ^{1}H -NMR. In the first case, ethanol production (Scheme 23, path (1)), a new signal should appear around 3.4 ppm and the intensity of the original CH_3CHO peaks should diminish. In the second case (Scheme 23, path (2)), there should be both a loss of intensity of the CH_3CHO peaks and a change in the splitting pattern of the methyl group signals at 1.1 and 2.0 ppm. These signals are originally doublets, as the methyl group protons (in the aldehyde and hydrate) are coupled to the aldehyde proton (I= 1/2, 2nI+ 1=2), but exchange for a deuteron (I=1) affects the coupling, resulting in a triplet signal (2x1+1=3).

A ^{1}H-NMR spectrum of a solution of acetaldehyde in D_2O is shown in Figure 93, blue numbers represent the chemical shift and red numbers the peak integrals.

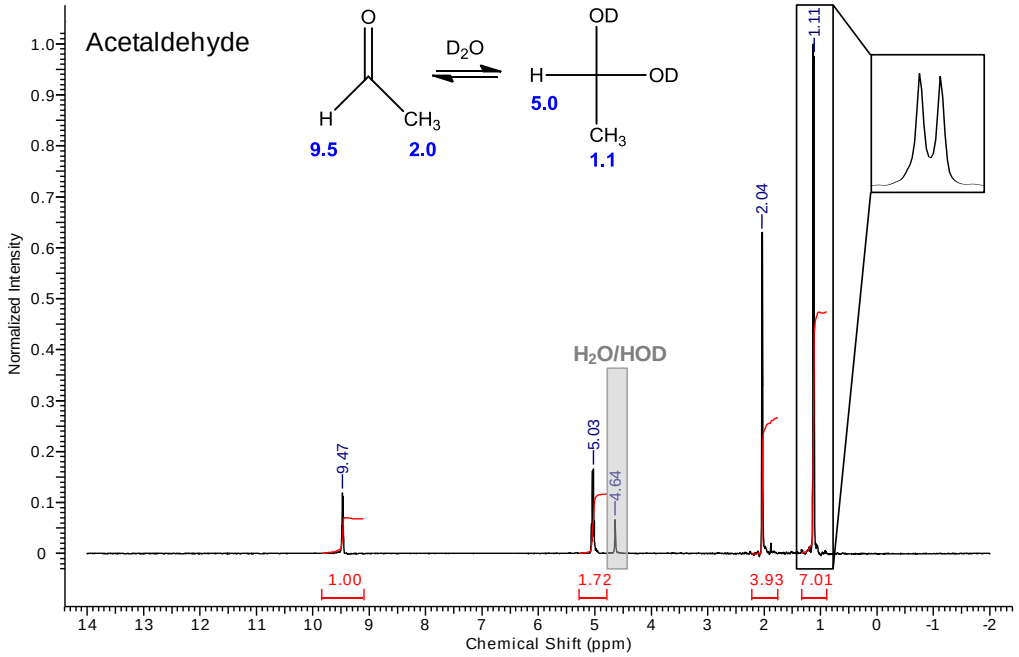

Figure 93: Proton NMR spectrum of acetaldehyde in D_2O. Peak positions of the multiplets are shown above in blue and the peak integrals in red beneath.

The peak at 9.5 ppm in Figure 93 corresponds to the aldehyde proton, and the integral of this peak (red numbers) has been set to 1. All other peak integrals are stated relative to this. It is expected that the peak at 2.0 ppm (CH_3 group of acetaldehyde) should integrate to three times that of the peak at 9.5 ppm, and that the peak at 1.1 ppm (CH_3 group of hydrate) should be three times greater than the peak at 5.0 ppm (proton in hydrate). This is however not the case, the integrals of the peaks at 2.0 and 1.1 ppm are more than three times greater than those at 9.5 and 5.0 ppm (respectively), resulting from polymerisation of the aldehyde in solution a shown in Chapter 4, Scheme 10.

The ^{1}H-NMR spectrum of the sample A from the experiment described in section 6.2.3 (Figure 87), is shown in Figure 94.

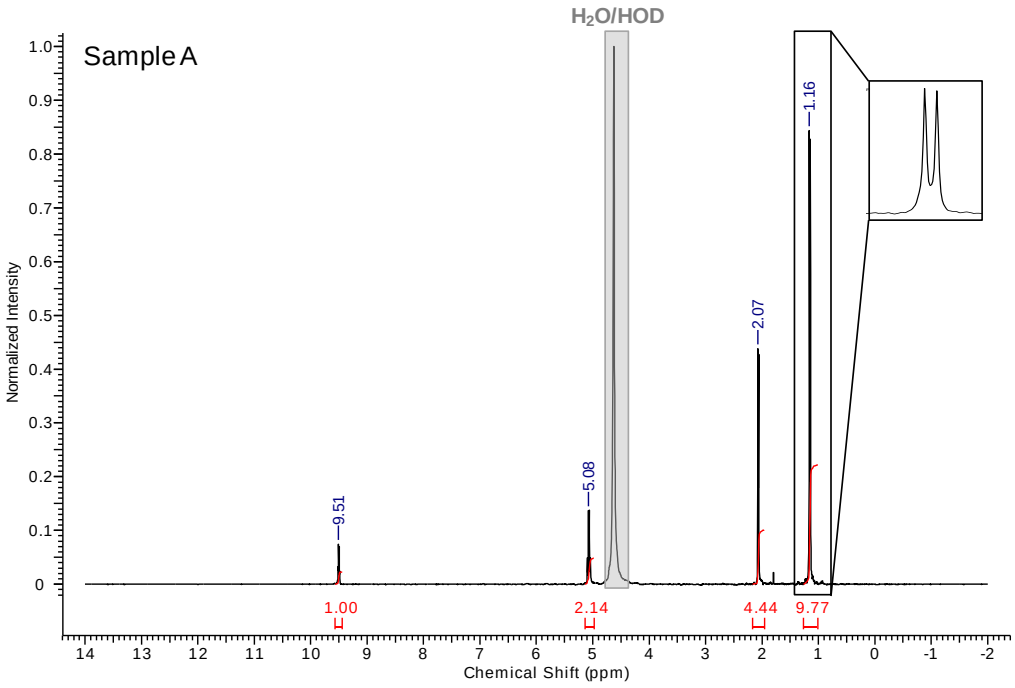

Figure 94: ^{1}H-NMR spectra of sample A. Peak positions of the multiplets are shown above in blue and the peak integrals in red beneath.

There is very little difference between the ^{1}H-NMR spectra in Figure 93 (acetaldehyde) and Figure 94 (experimental sample A). The only exception is the growth of the water peak at 4.6 ppm in the spectrum of sample A (Figure 94). The spectra recorded for samples B and C (not shown) were almost identical to that of sample A. The increase in the amount of water in the experimental sample is most likely due to contamination of the D_2O with water vapour during preparation of the deuterated buffer, and the H_2O introduced to the buffer by the salts (supplied in a hydrated form). There is no change to the splitting patterns in Figure 94 compared to Figure 93, and there are no peaks in the 3-4 ppm region which would indicate that ethanol has been produced. The ratio of the methyl peaks (at 1.1 and 2.0 ppm) to the proton peaks (at 5.0 and 9.5 ppm) is slightly higher for sample A (Figure 94) than the aldehyde (Figure 93), indicating a greater degree of polymerisation. This is not surprising given the length of the experiment (Figure 87, right).

The possible reactions of the labelled formaldehyde D^{13}CDO with [FeFe]-hydrogenase in a deuterated buffer solution are shown in Scheme 24.

Scheme 24: Proposed scheme for the reaction of deuterated formaldehyde with [FeFe]-hydrogenase in the presence of H_2 in deuterated buffer.

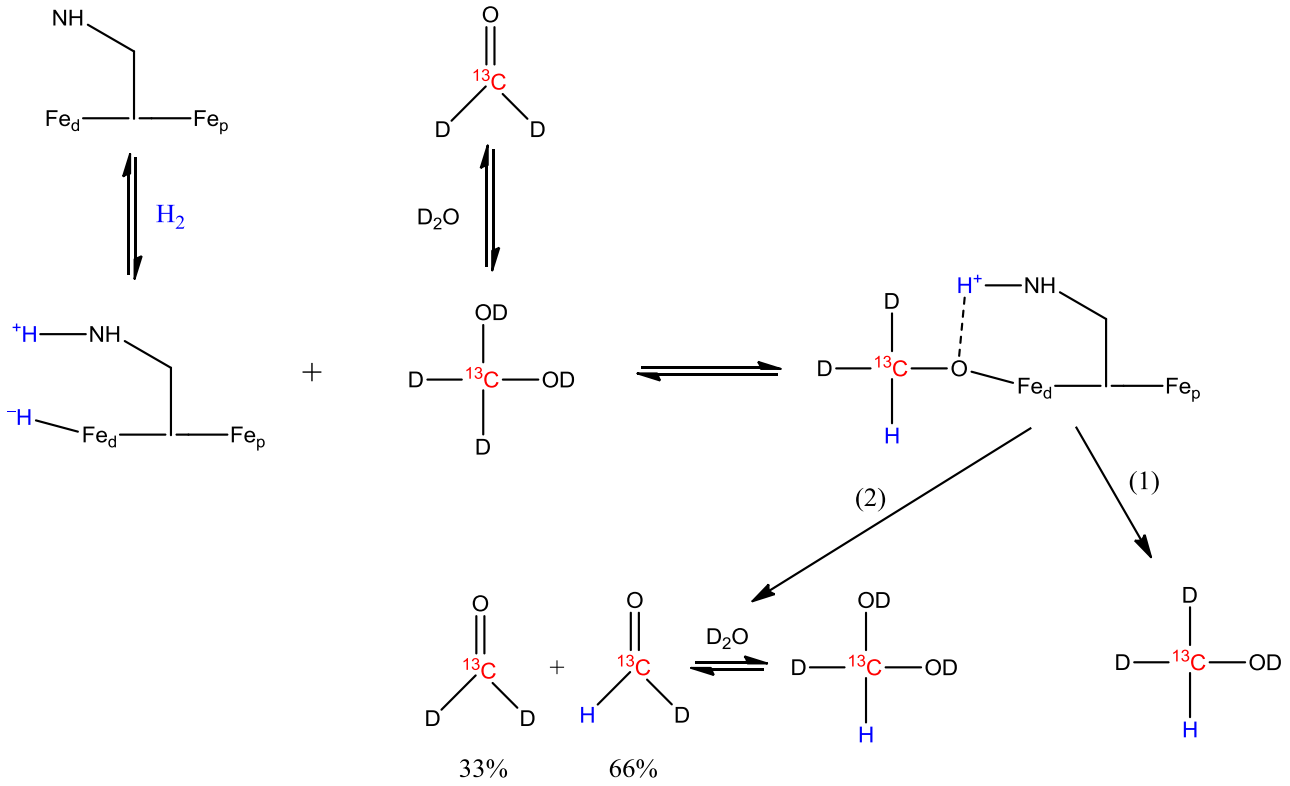

As shown in Scheme 24, under a H_2 atmosphere [FeFe]-hydrogenase is expected to be reduced to form a species with a hydride bound at the Fe_d site of the H-cluster (Scheme 18, Chapter 5). Upon addition of labelled formaldehyde (D^{13}CDO) the hydride is transferred to the carbonyl carbon and an Fe_d-O bond is formed. Once this aldehyde-bound state is formed there are two possibilities:

(1) the corresponding protonated alcohol (methanol) is released

(2) the reaction reverses and aldehyde is released. In this case there is a 66% chance that the released aldehyde will contain the transferred proton instead of the original deuteron.

In either of these cases it should be possible to detect the product using ^{13}C-NMR. The carbon in the original formaldehyde ($D^{13}CDO$) is coupled to two deuterons (I = 1), resulting in a quintet signal (2nI+1=5) at approximately 81 ppm. Both the possible products outlined above will exhibit a different ^{13}C-NMR spectrum to that of $D^{13}CDO$: in both products the carbon is coupled to a proton in addition to at least one deuteron, resulting in a more complicated splitting pattern. Additionally, in the alcohol product the chemical environment of the carbon is very different; the carbonyl (C=O) group in the aldehyde deshields the carbon atom from the magnetic field to a greater extent than the alcohol (C-OH) group, resulting in a smaller chemical shift in the methanol product (~47 ppm).

The ^{13}C-NMR spectra of the two samples from the experiment described in section 6.2.3 are shown in Figure 95. The experimental sample (hydrogenase + $D^{13}CDO$ + H_2) is shown at the top, and the control experiment ($D^{13}CDO$ + H_2) is shown at the bottom for comparison purposes.

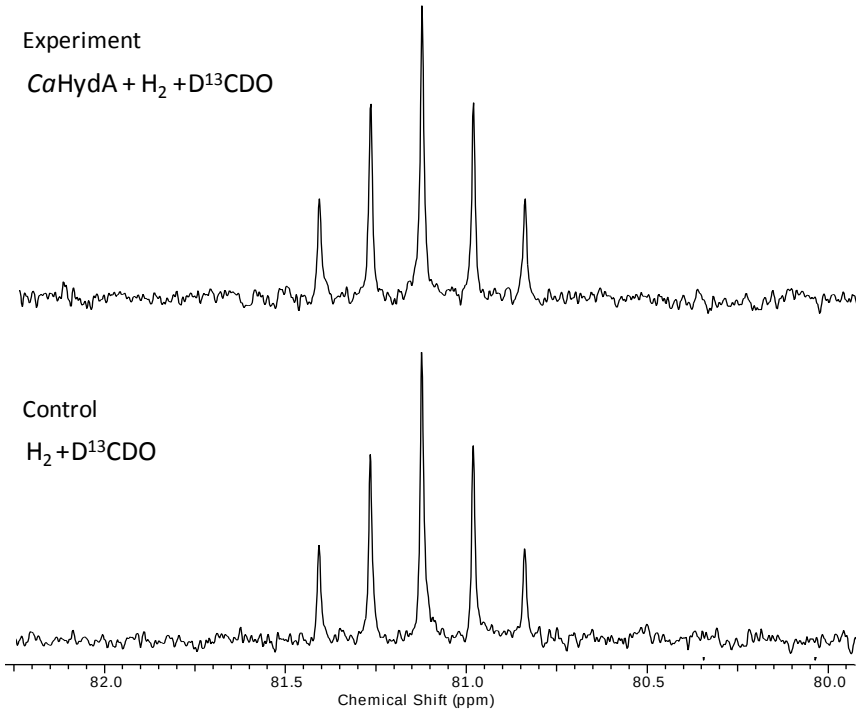

Figure 95: ^{13}C- NMR spectra of labelled formaldehyde (D^{13}CDO) in the experimental sample (top) compared with the control sample (bottom), both taken after 48 hours.

There is no difference between the two spectra in Figure 95, showing that neither H/D exchange or methanol production has occurred during the experiment. There was also no change in the ^{1}H-NMR spectrum (data not shown). After 48 hours 2 μL of the reaction solution was removed and studied using PFE to check that the enzyme had not been degraded by the prolonged exposure to aldehyde. A cyclic voltammogram (Figure 96, red) revealed that the enzyme was still active, however there was a change to the catalytic wave-shape compared to an uninhibited enzyme sample (black).

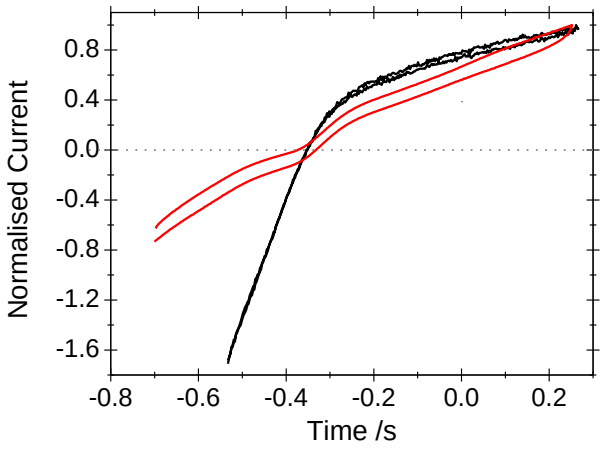

Figure 96: Cyclic voltammogram of *Ca*HydA, uninhibited enzyme sample (black) and after reaction with $D^{13}CDO$ for 48 hours (red). Conditions: 100% H_2, pH 6 phosphate buffer, ω = 3000 rpm, 5 °C, 20 mV/s scan rate.

The voltammogram no longer cuts the x-axis cleanly (Figure 96, red scan) compared to uninhibited enzyme (black scan) and resembles the voltammogram of *Cr*HydA1 in the potential region -0.5 to -0.3 V (Chapter 1, Figure 7). A larger overpotential is required to drive the reaction in either direction. It is likely that electron transfer between the electrode and the H-cluster has become less efficient, possibly due to damage to the FeS-cluster relay chain, or to the enzyme surface, resulting in poorer interaction with the electrode surface and slower electron transfer.

Given that the lack of reaction products cannot be explained by irreversible inactivation of the enzyme, the formaldehyde concentration was raised to ensure that it was not limiting the rate of reaction. Additional $D^{13}CDO$ was injected into the NMR solution to bring the concentration up to 20 mM, and the reaction left for a further 48 hours. Again there was no change in either the ^{1}H or ^{13}C-NMR spectrum (not shown).

6.4 Discussion

In this chapter IR, EPR and NMR spectroscopy were employed in an effort to either characterise the super-reduced state of [FeFe]-hydrogenase itself, or the reaction products of this state with formaldehyde. Although the existence of this state has been demonstrated using PFE (Chapters 4 and 5), as yet it still remains to be satisfactorily characterised spectroscopically. As described in the introduction to this chapter, IR studies of *Dd*HydAB and *Cr*HydA1 reveal the formation of a new state at very reducing potentials, however there are several stark differences between the state formed under these conditions for the two different hydrogenases.[82,85] In this chapter the development of both a transmission IR cell (Figure 86) and an ATR IR system (**Error! Reference source not found.**) for studying the states of [FeFe]-hydrogenases formed at very reducing potentials are described. The use of thin plates of silicon as a working electrode material was proven to be unsuitable for the study of hydrogenases in a transmission cell. Although potential control of a sample was made possible by the large working electrode surface area, the equilibration was very slow (>1000 s) and insufficient light, in the region 2170-2100 cm^{-1}, passes through this material, making it impossible to record the signals of the CN ligands at the active site of a hydrogenase. The ATR-IR cell, developed by Vincent *et al*,[187] has proven to be incompatible with [FeFe]-hydrogenases and no H-cluster signals were recorded. This may be related to the interaction of these hydrogenases with the Nafion network used to support the enzyme film on the ATR prism, although the exact reasons are unclear and experiments are ongoing.

Experiments to isolate the H_{sred} state of [FeFe]-hydrogenases in order to obtain an EPR spectrum of this (purported) paramagnetic state remain ongoing. EPR samples were prepared by reduction of the enzyme using methyl viologen in H_2, but no new (H_{sred}) reduced state

could be observed (Figure 91). Very low potentials are required to generate this state (< -0.5 V, Table 5, Chapter 5), a potential outside of the range of most electron mediators. The H_{sred} state is also extremely active at proton reduction, a substrate that cannot be removed from solution. For this reason aldehydes were identified as a method of trapping the enzyme in the super-reduced state. Aldehyde inhibited low-potential samples however also showed no evidence of a new paramagnetic species (Figure 91). The lack of H_{sred} generation in these experiments is likely to be due to the enzyme having been exposed to insufficient reduction potential. The possibility of using Eu(II)EGTA as a low-potential reductant is currently under investigation and preliminary experiments have established favourable conditions.

NMR experiments were carried out to detect the products of reaction of [FeFe]-hydrogenase with aldehydes (acetaldehyde, Figure 94 and formaldehyde, Figure 95). Several different methods were employed but none provided any evidence that alcohol (ethanol or methanol) is released after inhibition with aldehyde, or that reaction proceeds via the transfer of a hydride as proposed in

Scheme 15, Chapter 4. It is possible that the reaction of aldehyde with the H-cluster does not proceed exactly according to the proposed mechanism. DFT calculations (

Scheme 15, Chapter 4) show that reaction of formaldehyde with [FeFe]-hydrogenase in the H_{sre} state is barrier-less and strongly exothermic (ΔG = -34 kcal/mol), and results in the formation of a formaldehyde-bound state via a Fe-O bond. This mechanism supports the potential-dependent inhibition observed in PFE experiments (Chapter 4), but is not consistent with the observed reversibility of inhibition.[161] Such a thermodynamically favourable reaction is unlikely to be easily reversed. The DFT calculations only consider the 'naked' H-cluster and cannot predict the effect of the surrounding protein environment. The protein environment around the H-cluster must therefore play an important role in destabilising or hindering formation of the exothermic final products, thus moderating the actual potency of the formaldehyde as an enzyme inhibitor. It is possible that the formaldehyde-bound state is never actually fully formed; but that the transition state of this reaction is reached instead. Only partial hydride transfer occurs and the observed reactivation (either by raising the potential or removing aldehyde from the solution) is a straightforward reversal of the relevant steps (hydride transfer) in

Scheme 15. Reaction of [FeFe]-hydrogenase with formaldehyde would still inhibit H_2 production/oxidation activity, as formaldehyde would physically block the distal iron site, but as hydride transfer is not complete, alcohol would not be released, and the H/D exchange predicted for the NMR experiments in this chapter would not be possible.

References

References

(1) IEA *Key World Energy Statistics* **2010**.

(2) Barreto de Castro, L. A. *Braz. J. Med. Biol. Res.* **2010**, *43*, 230-233.

(3) Hoffert, M. I.; Caldeira, K.; Benford, G.; Criswell, D. R.; Green, C.; Herzog, H.; Jain, A. K.; Kheshgi, H. S.; Lackner, K. S.; Lewis, J. S.; Lightfoot, H. D.; Manheimer, W.; Mankins, J. C.; Mauel, M. E.; Perkins, L. J.; Schlesinger, M. E.; Volk, T.; Wigley, T. M. L. *Science (Washington, DC, U. S.)* **2002**, *298*, 981-987.

(4) Ball, M.; Wietschel, M. *Int. J. Hydrogen Energy* **2009**, *34*, 615-627.

(5) Bockris, J. O. *Science* **1972**, *176*, 1323.

(6) Schrope, M. *Nature (London, U. K.)* **2001**, *414*, 682-684.

(7) Sartbaeva, A.; Kuznetsov, V. L.; Wells, S. A.; Edwards, P. P. *Energy Environ. Sci.* **2008**, *1*, 79-85.

(8) Udengaard, N. R. *Abstracts of Papers, 228th ACS National Meeting, Philadelphia, PA, United States, August 22-26, 2004* **2004**, FUEL-197.

(9) Marban, G.; Valdes-Solis, T. *Int. J. Hydrogen Energy* **2007**, *32*, 1625-1637.

(10) http://news.bbc.co.uk/1/hi/business/7456141.stm 2008.

(11) http://www.fueleconomy.gov/feg/fuelcell.shtml 2012.

(12) Couper, A. M.; Pletcher, D.; Walsh, F. C. *Chem. Rev.* **1990**, *90*, 837-65.

(13) Hambourger, M.; Moore, G. F.; Kramer, D. M.; Gust, D.; Moore, A. L.; Moore, T. A. *Chem. Soc. Rev.* **2009**, *38*, 25-35.

(14) Gust, D.; Moore, T. A.; Moore, A. L. *Acc. Chem. Res.* **2009**, *42*, 1890-1898.

(15) Kalyanasundaram, K.; Graetzel, M. *Curr Opin Biotechnol* **2010**, *21*, 298-310.

(16) Reisner, E. *Eur. J. Inorg. Chem.* **2011**, 1005-1016.

(17) Noguera, D. R.; Brusseau, G. A.; Rittmann, B. E.; Stahl, D. A. *Biotechnol. Bioeng.* **1998**, *59*, 732-746.

(18) Dutta, D.; De, D.; Chaudhuri, S.; Bhattacharya Sanjoy, K. *Microb Cell Fact* **2005**, *4*, 36.

(19) Schuler, S.; Conrad, R. *Biol. Fertil. Soils* **1991**, *11*, 190-5.

(20) Cappelletti, B. M.; Reginatto, V.; Amante, E. R.; Antonio, R. V. *Renewable Energy* **2011**, *36*, 3367-3372.

(21) Thauer, R. K.; Klein, A. R.; Hartmann, G. C. *Chem. Rev. (Washington, D. C.)* **1996**, *96*, 3031-3042.

(22) Vincent, K. A.; Parkin, A.; Armstrong, F. A. *Chem. Rev. (Washington, DC, U. S.)* **2007**, *107*, 4366-4413.

(23) Ogata, H.; Kellers, P.; Lubitz, W. *J. Mol. Biol.* **2010**, *402*, 428-444.

(24) Volbeda, A.; Charon, M.-H.; Piras, C.; Hatchikian, E. C.; Frey, M.; Fontecilla-Camps, J. C. *Nature (London)* **1995**, *373*, 580-7.

(25) Page, C. C.; Moser, C. C.; Chen, X.; Dutton, P. L. *Nature (London)* **1999**, *402*, 47-52.

(26) Volbeda, A.; Martin, L.; Cavazza, C.; Matho, M.; Faber, B. W.; Roseboom, W.; Albracht, S. P. J.; Garcin, E.; Rousset, M.; Fontecilla-Camps, J. C. *JBIC, J. Biol. Inorg. Chem.* **2005**, *10*, 239-249.

(27) de Lacey, A. L.; Hatchikian, E. C.; Volbeda, A.; Frey, M.; Fontecilla-Camps, J. C.; Fernandez, V. M. *J. Am. Chem. Soc.* **1997**, *119*, 7181-7189.

(28) Happe, R.; Rosenboom, W.; Pierik, A. J.; Albracht, S. P. J.; Bagley, K. A. *Nature (London)* **1997**, *385*, 126.

(29) Gordon, J. C.; Kubas, G. J. *Organometallics* **2010**, *29*, 4682-4701.

(30) Pierik, A. J.; Roseboom, W.; Happe, R. P.; Bagley, K. A.; Albracht, S. P. J. *J. Biol. Chem.* **1999**, *274*, 3331-3337.

(31) Jensen, W. B. *J. Chem. Educ.* **2005**, *82*, 28.

(32) Volbeda, A.; Garcin, E.; Piras, C.; de Lacey, A. L.; Fernandez, V. M.; Hatchikian, E. C.; Frey, M.; Fontecilla-Camps, J. C. *J. Am. Chem. Soc.* **1996**, *118*, 12989-12996.

(33) Ogata, H.; Hirota, S.; Nakahara, A.; Komori, H.; Shibata, N.; Kato, T.; Kano, K.; Higuchi, Y. *Structure (Cambridge, MA, U. S.)* **2005**, *13*, 1635-1642.

(34) Peters, J. W.; Lanzilotta, W. N.; Lemon, B. J.; Seefeldt, L. C. *Science (Washington, D. C.)* **1998**, *282*, 1853-1858.

(35) Nicolet, Y.; Piras, C.; Legrand, P.; Hatchikian, C. E.; Fontecilla-Camps, J. C. *Structure (London)* **1999**, *7*, 13-23.

(36) Pieper, U.; Webb Benjamin, M.; Barkan David, T.; Schneidman-Duhovny, D.; Schlessinger, A.; Braberg, H.; Yang, Z.; Meng Elaine, C.; Pettersen Eric, F.; Huang Conrad, C.; Datta Ruchira, S.; Sampathkumar, P.; Madhusudhan Mallur, S.; Sjolander, K.; Ferrin Thomas, E.; Burley Stephen, K.; Sali, A. *Nucleic Acids Res* **2011**, *39*, D465-74.

(37) Fareleira, P.; Santos, B. S.; Antonio, C.; Moradas-Ferreira, P.; LeGall, J.; Xavier, A. V.; Santos, H. *Microbiology (Reading, U. K.)* **2003**, *149*, 1513-1522.

(38) Lobo, S. A. L.; Melo, A. M. P.; Carita, J. N.; Teixeira, M.; Saraiva, L. M. *FEBS Lett.* **2007**, *581*, 433-436.

(39) Hansen, T. A. *Antonie van Leeuwenhoek* **1994**, *66*, 165-85.

(40) Steenkamp, D. J.; Peck, H. D., Jr. *J. Biol. Chem.* **1981**, *256*, 5450-8.

(41) Pereira, I. A. C.; Romao, C. V.; Xavier, A. V.; LeGall, J.; Teixeira, M. *JBIC, J. Biol. Inorg. Chem.* **1998**, *3*, 494-498.

(42) Hatchikian, E. C.; Forget, N.; Fernandez, V. M.; Williams, R.; Cammack, R. *Eur. J. Biochem.* **1992**, *209*, 357-65.

(43) Jones, D. T.; Woods, D. R. *Microbiol Rev* **1986**, *50*, 484-524.

(44) Santangelo, J. D.; Duerre, P.; Woods, D. R. *Microbiology (Reading, U. K.)* **1995**, *141*, 171-80.

(45) Nolling, J.; Breton, G.; Omelchenko, M. V.; Makarova, K. S.; Zeng, Q.; Gibson, R.; Lee, H. M.; Dubois, J.; Qiu, D.; Hitti, J.; Wolf, Y. I.; Tatusov, R. L.; Sabathe, F.; Doucette-Stamm, L.; Soucaille, P.; Daly, M. J.; Bennett, G. N.; Koonin, E. V.; Smith, D. R.; Aldredge, T.; Ayers, M.; Bashirzadeh, R.; Bochner, H.; Boivin, M.; Bross, S.; Bush, D.; Butler, C.; Caron, A.; Caruso, A.; Cook, R.; Daggett, P.; Deloughery, C.; Egan, J.; Ellston, D.; Engelstein, M.; Ezedi, J.; Gilbert, K.; Goyal, A.; Guerin, J.; Ho, T.; Holtham, K.; Joseph, P.; Keagle, P.; Kozlovsky, J.; LaPlante, M.; LeBlanc, G.; Lumm, W.; Majeski, A.; McDougall, S.; Mank, P.; Mao, J.-I.; Nocco, D.; Patwell, D.; Phillips, J.; Pothier, B.; Prabhakar, S.; Richterich, P.; Rice, P.; Rosetti, D.; Rossetti, M.; Rubenfield, M.; Sachdeva, M.; Snell, P.; Spadafora, R.; Spitzer, L.; Shimer, G.; Thomann, H.-U.; Vicaire, R.; Wall, K.; Wang, Y.; Weinstock, K.; Wong, L. P.; Wonsey, A.; Xu, Q.; Zhang, L. *J. Bacteriol.* **2001**, *183*, 4823-4838.

(46) Kawasaki, S.; Watamura, Y.; Ono, M.; Watanabe, T.; Takeda, K.; Niimura, Y. *Appl. Environ. Microbiol.* **2005**, *71*, 8442-8450.

(47) von Abendroth, G.; Stripp, S.; Silakov, A.; Croux, C.; Soucaille, P.; Girbal, L.; Happe, T. *Int. J. Hydrogen Energy* **2008**, *33*, 6076-6081.

(48) Gorwa, M.-F.; Croux, C.; Soucaille, P. *J. Bacteriol.* **1996**, *178*, 2668-2675.

(49) Grossman, A. R.; Catalanotti, C.; Yang, W.; Dubini, A.; Magneschi, L.; Subramanian, V.; Posewitz, M. C.; Seibert, M. *New Phytol.* **2011**, *190*, 279-288.

(50) Happe, T.; Mosler, B.; Naber, J. D. *Eur. J. Biochem.* **1994**, *222*, 769-74.

(51) Florin, L.; Tsokoglou, A.; Happe, T. *J. Biol. Chem.* **2001**, *276*, 6125-6132.

(52) Melis, A.; Happe, T. *Plant Physiol.* **2001**, *127*, 740-748.

(53) Happe, T.; Naber, J. D. *Eur. J. Biochem.* **1993**, *214*, 475-81.

(54) Kamp, C.; Silakov, A.; Winkler, M.; Reijerse, E. J.; Lubitz, W.; Happe, T. *Biochim. Biophys. Acta, Bioenerg.* **2008**, *1777*, 410-416.

(55) Stripp, S.; Sanganas, O.; Happe, T.; Haumann, M. *Biochemistry* **2009**, *48*, 5042-5049.

(56) Nicolet, Y.; Cavazza, C.; Fontecilla-Camps, J. C. *J. Inorg. Biochem.* **2002**, *91*, 1-8.

(57) Nicolet, Y.; de Lacey, A. L.; Vernede, X.; Fernandez, V. M.; Hatchikian, E. C.; Fontecilla-Camps, J. C. *J. Am. Chem. Soc.* **2001**, *123*, 1596-1601.

(58) De Lacey, A. L.; Fernandez, V. M.; Rousset, M.; Cammack, R. *Chem. Rev. (Washington, DC, U. S.)* **2007**, *107*, 4304-4330.

(59) Lubitz, W.; Reijerse, E.; van Gastel, M. *Chem. Rev. (Washington, DC, U. S.)* **2007**, *107*, 4331-4365.

(60) Pandelia, M.-E.; Fourmond, V.; Tron-Infossi, P.; Lojou, E.; Bertrand, P.; Leger, C.; Giudici-Orticoni, M.-T.; Lubitz, W. *J. Am. Chem. Soc.* **2010**, *132*, 6991-7004.

(61) Huyett, J. E.; Carepo, M.; Pamplona, A.; Franco, R.; Moura, I.; Moura, J. J. G.; Hoffman, B. M. *J. Am. Chem. Soc.* **1997**, *119*, 9291-9292.

(62) Coremans, J. M. C. C.; Van der Zwaan, J. W.; Albracht, S. P. J. *Biochim. Biophys. Acta, Protein Struct. Mol. Enzymol.* **1992**, *1119*, 157-68.

(63) Cammack, R.; Patil, D. S.; Hatchikian, E. C.; Fernandez, V. M. *Biochim. Biophys. Acta, Protein Struct. Mol. Enzymol.* **1987**, *912*, 98-109.

(64) Lamle, S. E.; Albracht, S. P. J.; Armstrong, F. A. *J. Am. Chem. Soc.* **2004**, *126*, 14899-14909.

(65) Bagley, K. A.; Van Garderen, C. J.; Chen, M.; Woodruff, W. H.; Duin, E. C.; Albracht, S. P. J. *Biochemistry* **1994**, *33*, 9229-36.

(66) Stein, M.; van Lenthe, E.; Baerends, E. J.; Lubitz, W. *J. Am. Chem. Soc.* **2001**, *123*, 5839-5840.

(67) Fontecilla-Camps, J. C.; Volbeda, A.; Cavazza, C.; Nicolet, Y. *Chem. Rev. (Washington, DC, U. S.)* **2007**, *107*, 4273-4303.

(68) George, S. J.; Kurkin, S.; Thorneley, R. N. F.; Albracht, S. P. J. *Biochemistry* **2004**, *43*, 6808-6819.

(69) Kurkin, S.; George, S. J.; Thorneley, R. N. F.; Albracht, S. P. J. *Biochemistry* **2004**, *43*, 6820-6831.

(70) Keith, J. M.; Hall, M. B. *Inorg. Chem. (Washington, DC, U. S.)* **2010**, *49*, 6378-6380.

(71) Wu, H.; Hall, M. B. *C. R. Chim.* **2008**, *11*, 790-804.

(72) Siegbahn, P. E. M.; Tye, J. W.; Hall, M. B. *Chem. Rev. (Washington, DC, U. S.)* **2007**, *107*, 4414-4435.

(73) Siegbahn, P. E. M. *Adv. Inorg. Chem.* **2004**, *56*, 101-125.

(74) Stein, M.; Lubitz, W. *J. Inorg. Biochem.* **2004**, *98*, 862-877.

(75) Hagen, W. R.; Van Berkel-Arts, A.; Kruse-Wolters, K. M.; Voordouw, G.; Veeger, C. *FEBS Lett.* **1986**, *203*, 59-63.

(76) Goldet, G.; Brandmayr, C.; Stripp Sven, T.; Happe, T.; Cavazza, C.; Fontecilla-Camps Juan, C.; Armstrong Fraser, A. *J Am Chem Soc* **2009**, *131*, 14979-89.

(77) Parkin, A.; Cavazza, C.; Fontecilla-Camps, J. C.; Armstrong, F. A. *J. Am. Chem. Soc.* **2006**, *128*, 16808-16815.

(78) Van Dijk, C.; Van Berkel-Arts, A.; Veeger, C. *FEBS Lett.* **1983**, *156*, 340-4.

(79) Patil, D. S.; Moura, J. J. G.; He, S. H.; Teixeira, M.; Prickril, B. C.; DerVartanian, D. V.; Peck, H. D., Jr.; LeGall, J.; Huynh Boi, H. *J. Biol. Chem.* **1988**, *263*, 18732-8.

(80) Pierik, A. J.; Hagen, W. R.; Redeker, J. S.; Wolbert, R. B. G.; Boersma, M.; Verhagen, M. F. J. M.; Grande, H. J.; Veeger, C.; Mutsaers, P. H. A.; et al. *Eur. J. Biochem.* **1992**, *209*, 63-72.

(81) Pereira, A. S.; Tavares, P.; Moura, I.; Moura, J. J. G.; Huynh, B. H. *J. Am. Chem. Soc.* **2001**, *123*, 2771-2782.

(82) Roseboom, W.; Lacey, A. L.; Fernandez, V. M.; Hatchikian, E. C.; Albracht, S. P. J. *JBIC, J. Biol. Inorg. Chem.* **2006**, *11*, 102-118.

(83) De Lacey, A. L.; Stadler, C.; Cavazza, C.; Hatchikian, E. C.; Fernandez, V. M. *J. Am. Chem. Soc.* **2000**, *122*, 11232-11233.

(84) Silakov, A.; Reijerse, E. J.; Albracht, S. P. J.; Hatchikian, E. C.; Lubitz, W. *J. Am. Chem. Soc.* **2007**, *129*, 11447-11458.

(85) Silakov, A.; Kamp, C.; Reijerse, E.; Happe, T.; Lubitz, W. *Biochemistry* **2009**, *48*, 7780-6.

(86) Fernandez, V. M.; Munilla, R.; Ballesteros, A. *Arch. Biochem. Biophys.* **1982**, *215*, 129-35.

(87) Silakov, A.; Kamp, C.; Reijerse, E.; Happe, T.; Lubitz, W. *Biochemistry* **2009**, *48*, 7780-7786.

(88) Bruschi, M.; Fantucci, P.; De Gioia, L. *Inorg. Chem.* **2003**, *42*, 4773-4781.

(89) Wang, F.; Wang, M.; Liu, X.; Jin, K.; Dong, W.; Sun, L. *Dalton Trans.* **2007**, 3812-3819.

(90) Zhao, X.; Chiang, C.-Y.; Miller, M. L.; Rampersad, M. V.; Darensbourg, M. Y. *J. Am. Chem. Soc.* **2003**, *125*, 518-524.

(91) Zhao, X.; Georgakaki, I. P.; Miller, M. L.; Mejia-Rodriguez, R.; Chiang, C.-Y.; Darensbourg, M. Y. *Inorg. Chem.* **2002**, *41*, 3917-3928.

(92) Fan, H.-J.; Hall, M. B. *J. Am. Chem. Soc.* **2001**, *123*, 3828-3829.

(93) Bruschi, M.; Greco, C.; Fantucci, P.; De Gioia, L. *Inorg. Chem. (Washington, DC, U. S.)* **2008**, *47*, 6056-6071.

(94) Barton, B. E.; Rauchfuss, T. B. *Inorg. Chem. (Washington, DC, U. S.)* **2008**, *47*, 2261-2263.

(95) Thomas, C. M.; Liu, T.; Hall, M. B.; Darensbourg, M. Y. *Inorg. Chem. (Washington, DC, U. S.)* **2008**, *47*, 7009-7024.

(96) Hong, G.; Cornish, A. J.; Hegg, E. L.; Pachter, R. *Biochim. Biophys. Acta, Bioenerg.* **2011**, *1807*, 510-517.

(97) Hexter, S. V.; Grey, F.; Happe, T.; Climent, V.; Armstrong, F. A. *Proc. Natl. Acad. Sci. U. S. A.* **2011**, *109*, 11516-11521, S11516/1-S11516/2.

(98) Stripp, S. T.; Goldet, G.; Brandmayr, C.; Sanganas, O.; Vincent, K. A.; Haumann, M.; Armstrong, F. A.; Happe, T. *Proc. Natl. Acad. Sci. U. S. A.* **2009**, *106*, 17331-17336.

(99) Massanz, C.; Friedrich, B. *Biochemistry* **1999**, *38*, 14330-14337.

(100) Montet, Y.; Amara, P.; Volbeda, A.; Vernede, X.; Hatchikian, E. C.; Field, M. J.; Frey, M.; Fontecilla-Camps, J. C. *Nat. Struct. Biol.* **1997**, *4*, 523-526.

(101) Teixeira, V. H.; Baptista, A. M.; Soares, C. M. *Biophys. J.* **2006**, *91*, 2035-2045.

(102) Liebgott, P.-P.; de Lacey, A. L.; Burlat, B.; Cournac, L.; Richaud, P.; Brugna, M.; Fernandez, V. M.; Guigliarelli, B.; Rousset, M.; Leger, C.; Dementin, S. *J. Am. Chem. Soc.* **2011**, *133*, 986-997.

(103) Saggu, M.; Ludwig, M.; Friedrich, B.; Hildebrandt, P.; Bittl, R.; Lendzian, F.; Lenz, O.; Zebger, I. *ChemPhysChem* **2010**, *11*, 1215-1224.

(104) Cohen, J.; Kim, K.; King, P.; Seibert, M.; Schulten, K. *Structure (Cambridge, MA, U. S.)* **2005**, *13*, 1321-1329.

(105) King, P.; Ghirardi, M.; Seibert, M.; (Midwest Research Institute, USA). Application: WO

WO, 2004, p No pp given.

(106) Hong, G.; Pachter, R. *ACS Chem. Biol.* **2012**, *7*, 1268-1275.

(107) Lautier, T.; Ezanno, P.; Baffert, C.; Fourmond, V.; Cournac, L.; Fontecilla-Camps, J. C.; Soucaille, P.; Bertrand, P.; Meynial-Salles, I.; Leger, C. *Faraday Discuss.* **2011**, *148*, 385-407.

(108) Tard, C.; Pickett, C. J. *Chem. Rev. (Washington, DC, U. S.)* **2009**, *109*, 2245-2274.

(109) Kubas Gregory, J. *Acc. Chem. Res.* **1988**, *21*, 120-8.

(110) Camara, J. M.; Rauchfuss, T. B. *Nat. Chem.* **2012**, *4*, 26-30.

(111) Helm, M. L.; Stewart, M. P.; Bullock, R. M.; DuBois, M. R.; DuBois, D. L. *Science (Washington, DC, U. S.)* **2011**, *333*, 863-866.

(112) Kavanagh, P.; Leech, D. *Adv. Electrochem. Sci. Eng.* **2011**, *13*, 229-267.

(113) Cracknell, J. A.; Vincent, K. A.; Armstrong, F. A. *Chem. Rev. (Washington, DC, U. S.)* **2008**, *108*, 2439-2461.

(114) Brown, K. A.; Wilker, M. B.; Boehm, M.; Dukovic, G.; King, P. W. *J. Am. Chem. Soc.*, *134*, 5627-5636.

(115) Reisner, E.; Powell, D. J.; Cavazza, C.; Fontecilla-Camps, J. C.; Armstrong, F. A. *J. Am. Chem. Soc.* **2009**, *131*, 18457-18466.

(116) Wang, M.; Chen, L.; Li, X.; Sun, L. *Dalton Trans.* **2011**, *40*, 12793-12800.

(117) Zhang, X.; Veikko, U.; Mao, J.; Cai, P.; Peng, T. *Chem.--Eur. J.* **2012**, Ahead of Print.

(118) Reisner, E.; Armstrong, F. A. *Methods Mol. Biol. (N. Y., NY, U. S.)* **2011**, *743*, 107-117.

(119) Reeve, H. A.; Lauterbach, L.; Ash, P. A.; Lenz, O.; Vincent, K. A. *Chem. Commun. (Cambridge, U. K.)* **2012**, *48*, 1589-1591.

(120) Lazarus, O.; Woolerton, T. W.; Parkin, A.; Lukey, M. J.; Reisner, E.; Seravalli, J.; Pierce, E.; Ragsdale, S. W.; Sargent, F.; Armstrong, F. A. *J. Am. Chem. Soc.* **2009**, *131*, 14154-14155.

(121) Eddowes, M. J.; Hill, H. A. O. *J. Chem. Soc., Chem. Commun.* **1977**, 771-2.

(122) Yeh, P.; Kuwana, T. *Chem. Lett.* **1977**, 1145-8.

(123) Armstrong, F. A.; Butt, J. N.; George, S. J.; Hatchikian, E. C.; Thomson, A. J. *FEBS Lett.* **1989**, *259*, 15-18.

(124) Armstrong, F. A.; Cox, P. A.; Hill, H. A. O.; Lowe, V. J.; Oliver, B. N. *J. Electroanal. Chem. Interfacial Electrochem.* **1987**, *217*, 331-66.

(125) Leger, C.; Elliott, S. J.; Hoke, K. R.; Jeuken, L. J. C.; Jones, A. K.; Armstrong, F. A. *Biochemistry* **2003**, *42*, 8653-8662.

(126) McCreery, R. L. *Chem. Rev. (Washington, DC, U. S.)* **2008**, *108*, 2646-2687.

(127) Hirst, J. *Biochim. Biophys. Acta, Bioenerg.* **2006**, *1757*, 225-239.

(128) Bard, A.; Faulkner, R. *Electrochemical Methods: Fundamentals and Applications, New York: Wiley, 2001, 2nd ed*, 2002; Vol. 38.

(129) Fisher, A. C. *Electrode Dynamics*; Oxford Chemistry Primers.

(130) Fourmond, V.; Lautier, T.; Baffert, C.; Leroux, F.; Liebgott, P.-P.; Dementin, S.; Rousset, M.; Arnoux, P.; Pignol, D.; Meynial-Salles, I.; Soucaille, P.; Bertrand, P.; Leger, C. *Anal. Chem. (Washington, DC, U. S.)* **2009**, *81*, 2962-2968.

(131) Blanford, C. F.; Armstrong, F. A. *J. Solid State Electrochem.* **2006**, *10*, 826-832.

(132) Takahagi, T.; Ishitani, A. *Carbon* **1984**, *22*, 43-6.

(133) Leger, C.; Dementin, S.; Bertrand, P.; Rousset, M.; Guigliarelli, B. *J. Am. Chem. Soc.* **2004**, *126*, 12162-12172.

(134) Madden, C.; Vaughn Michael, D.; Diez-Perez, I.; Brown Katherine, A.; King Paul, W.; Gust, D.; Moore Ana, L.; Moore Thomas, A. *J Am Chem Soc* **2011**, *134*, 1577-82.

(135) Cao, Z.; Hall, M. B. *J. Am. Chem. Soc.* **2001**, *123*, 3734-3742.

(136) Liu, Z.-P.; Hu, P. *J. Am. Chem. Soc.* **2002**, *124*, 5175-5182.

(137) Bruschi, M.; Fantucci, P.; De Gioia, L. *Inorg. Chem.* **2002**, *41*, 1421-1429.

(138) Thauer, R. K.; Kaeufer, B.; Zaehringer, M.; Jungermann, K. *Eur. J. Biochem.* **1974**, *42*, 447-52.

(139) Goldet, G. *DPhil thesis: Electrochemical Investigations of Hydrogen-producing Enzymes*; University of Oxford, 2009.

(140) Goldet, G.; Wait Annemarie, F.; Cracknell James, A.; Vincent Kylie, A.; Ludwig, M.; Lenz, O.; Friedrich, B.; Armstrong Fraser, A. *J Am Chem Soc* **2008**, *130*, 11106-13.

(141) Lambertz, C.; Leidel, N.; Havelius Kajsa, G. V.; Noth, J.; Chernev, P.; Winkler, M.; Happe, T.; Haumann, M. *J Biol Chem* **2011**, *286*, 40614-23.

(142) Bruska, M. K.; Stiebritz, M. T.; Reiher, M. *J. Am. Chem. Soc.* **2011**, *133*, 20588-20603.

(143) Belsey, N. *DPhil thesis: Electrochemical Investigations of Hydrogenases : Small Molecule Inhibition and Novel Technological Applications*; Oxford University, 2009.

(144) Adams, M. W. W. *Biochim. Biophys. Acta, Bioenerg.* **1990**, *1020*, 115-45.

(145) Albracht, S. P. J.; Roseboom, W.; Hatchikian, E. C. *JBIC, J. Biol. Inorg. Chem.* **2006**, *11*, 88-101.

(146) Bennett, B.; Lemon, B. J.; Peters, J. W. *Biochemistry* **2000**, *39*, 7455-60.

(147) Lemon, B. J.; Peters, J. W. *Biochemistry* **1999**, *38*, 12969-12973.

(148) Lemon, B. J.; Peters, J. W. *J. Am. Chem. Soc.* **2000**, *122*, 3793-3794.

(149) Silakov, A.; Wenk, B.; Reijerse, E.; Albracht, S. P. J.; Lubitz, W. *JBIC, J. Biol. Inorg. Chem.* **2009**, *14*, 301-313.

(150) Telser, J.; Benecky, M. J.; Adams, M. W. W.; Mortenson, L. E.; Hoffman, B. M. *J. Biol. Chem.* **1986**, *261*, 13536-41.

(151) Chen, Z.; Lemon, B. J.; Huang, S.; Swartz, D. J.; Peters, J. W.; Bagley, K. A. *Biochemistry* **2002**, *41*, 2036-2043.

(152) Baffert, C.; Bertini, L.; Lautier, T.; Greco, C.; Sybirna, K.; Ezanno, P.; Etienne, E.; Soucaille, P.; Bertrand, P.; Bottin, H.; Meynial-Salles, I.; De Gioia, L.; Leger, C. *J. Am. Chem. Soc.* **2011**, *133*, 2096-2099.

(153) Adams, M. W. *Biochim Biophys Acta* **1990**, *1020*, 115-45.

(154) Patil, D. S.; Czechowski, M. H.; Huynh, B. H.; LeGall, J.; Peck, H. D., Jr.; DerVartanian, D. V. *Biochem Biophys Res Commun* **1986**, *137*, 1086-93.

(155) Silakov, A.; Reijerse, E. J.; Lubitz, W. *Eur. J. Inorg. Chem.* **2011**, 1056-1066.

(156) Compton, R. G.; Sanders, G. H. W.; Editors *Electrode Potentials*; Oxford University Press, 1996.

(157) Clayden, J.; Greeves, N.; Warren, S.; Wothers, P. *Organic Chemistry*; Oxford University Press, 2001.

(158) Hilal, S. H.; Bornander, L. L.; Carreira, L. A. *QSAR Comb. Sci.* **2005**, *24*, 631-637.

(159) Kiernan, J. A. *Microsc. Today* **2000**, 8, 10, 12.

(160) Means, G. E.; Feeney, R. E. *Biochemistry* **1968**, *7*, 2192-201.

(161) Wait, A. F.; Brandmayr, C.; Stripp, S. T.; Cavazza, C.; Fontecilla-Camps, J. C.; Happe, T.; Armstrong, F. A. *J. Am. Chem. Soc.* **2011**, *133*, 1282-1285.

(162) Slatyer, B.; Daday, A.; Smith, G. D. *Biochem J* **1983**, *212*, 755-8.

(163) Rao, K. K.; Hall, D. O. *Biochem. Soc. Trans.* **1985**, *13*, 631-2.

(164) Wait, A. *DPhil Thesis: Novel aspects of the reactions of hydrogenases with small molecule inhibitors*; University of Oxford, 2011.

(165) Fontecilla-Camps Juan, C.; Volbeda, A.; Cavazza, C.; Nicolet, Y. *Chem Rev* **2007**, *107*, 4273-303.

(166) Foster, C. E.; Kramer, T.; Wait, A. F.; Parkin, A.; Jennings, D. P.; Happe, T.; McGrady, J. E.; Armstrong, F. A. *J. Am. Chem. Soc.* **2012**, *134*, 7553-7557.

(167) Bruschi, M.; Greco, C.; Kaukonen, M.; Fantucci, P.; Ryde, U.; De Gioia, L. *Angew. Chem., Int. Ed.* **2009**, *48*, 3503-3506, S3503/1-S3503/20.

(168) Greco, C.; Bruschi, M.; Fantucci, P.; Ryde, U.; De Gioia, L. *J. Am. Chem. Soc.* **2011**, *133*, 18742-18749.

(169) Greco, C.; De Gioia, L. *Inorg. Chem. (Washington, DC, U. S.)* **2011**, *50*, 6987-6995.

(170) Ryde, U.; Greco, C.; De Gioia, L. *J. Am. Chem. Soc.* **2010**, *132*, 4512-4513.

(171) Zampella, G.; Greco, C.; Fantucci, P.; De Gioia, L. *Inorg Chem* **2006**, *45*, 4109-18.

(172) Noyori, R. *Angew. Chem., Int. Ed.* **2002**, *41*, 2008-2022.

(173) Yamakawa, M.; Ito, H.; Noyori, R. *J. Am. Chem. Soc.* **2000**, *122*, 1466-1478.

(174) Amara, P.; Mouesca, J.-M.; Volbeda, A.; Fontecilla-Camps, J. C. *Inorg. Chem. (Washington, DC, U. S.)* **2011**, *50*, 1868-1878.

(175) Burgess, B. K.; Lowe, D. J. *Chem. Rev. (Washington, D. C.)* **1996**, *96*, 2983-3011.

(176) Einsle, O.; Tezcan, F. A.; Andrade, S. L. A.; Schmid, B.; Yoshida, M.; Howard, J. B.; Rees, D. C. *Science (Washington, DC, U. S.)* **2002**, *297*, 1696-1700.

(177) Igarashi, R. Y.; Laryukhin, M.; Dos Santos, P. C.; Lee, H.-I.; Dean, D. R.; Seefeldt, L. C.; Hoffman, B. M. *J. Am. Chem. Soc.* **2005**, *127*, 6231-6241.

(178) Kumar, M.; Ragsdale, S. W. *Journal of the American Chemistry Society* **1992**, *114*, 8713-8715.

(179) Yang, Z.-Y.; Seefeldt, L. C.; Dean, D. R.; Cramer, S. P.; George, S. J. *Angew. Chem., Int. Ed.* **2010**, *50*, 272-275, S272/1-S272/2.

(180) Best, S. P. *Coord. Chem. Rev.* **2005**, *249*, 1536-1554.

(181) Murray, R. W.; Heineman, W. R.; O'Dom, G. W. *Anal. Chem.* **1967**, *39*, 1666-8.

(182) Stotter, J.; Zak, J.; Behler, Z.; Show, Y.; Swain, G. M. *Anal. Chem.* **2002**, *74*, 5924-5930.

(183) Moss, D.; Nabedryk, E.; Breton, J.; Maentele, W. *Eur. J. Biochem.* **1990**, *187*, 565-72.

(184) Borg, S. J.; Best, S. P. *J. Electroanal. Chem.* **2002**, *535*, 57-64.

(185) Silakov, A.; Wenk, B.; Reijerse, E.; Lubitz, W. *Phys. Chem. Chem. Phys.* **2009**, *11*, 6592-6599.

(186) Girbal, L.; von Abendroth, G.; Winkler, M.; Benton, P. M. C.; Meynial-Salles, I.; Croux, C.; Peters, J. W.; Happe, T.; Soucaille, P. *Appl. Environ. Microbiol.* **2005**, *71*, 2777-2781.

(187) Healy, A. J.; Reeve, H. A.; Vincent, K. A. *Faraday Discuss.* **2010**, *148*, 345-357.

(188) Hagen, W. R.; Van Berkel-Arts, A.; Kruese-Wolters, K. M.; Dunham, W. R.; Veeger, C. *FEBS Lett.* **1986**, *201*, 158-62.

(189) Bradford, M. M. *Anal. Biochem.* **1976**, *72*, 248-54.

(190) Jovic, V.; Lamovec, J.; Popovic, M.; Lazic, Z. *J. Serb. Chem. Soc.* **2007**, *72*, 1127-1138.

(191) Stombaugh, N. A.; Sundquist, J. E.; Burris, R. H.; Orme-Johnson, W. H. *Biochemistry* **1976**, *15*, 2633-41.

(192) Vincent, K. A.; Tilley, G. J.; Quammie, N. C.; Streeter, I.; Burgess, B. K.; Cheesman, M. R.; Armstrong, F. A. *Chem. Commun. (Cambridge, U. K.)* **2003**, 2590-2591.

Appendix 1

Density Function Theory Calculations

All electronic structure calculations presented in section 4.3 were carried out at the density functional level of theory as implemented in the Gaussian09 suite of programs.[A1.1] The BP86 GGA functional[A1.2] in conjunction with the TZVP triple-ζ basis set[A1.3] of Ahlrichs and co-workers on all H-cluster atoms (Fe, S, O, C, H, N) were used in all cases.

Geometry optimisations of the H-clusters in their respective broken-symmetry (M_s = 0 and M_s = 1/2) states were performed without any geometrical constraints (C_1 symmetry), using tight convergence criteria (Opt=tight, int=ultrafine). Stationary points were characterised by analysis of their second derivatives: the absence of imaginary frequencies is indicative of a true minimum, while exactly one imaginary frequency corresponds to a transition state structure. The H-clusters were embedded into a polarisable continuum model (PCM)[A1.4] with water as the solvent. The enzyme environment was approximated by adjusting the dielectric constant ε to a value of 4. Reported energies have been reported as electronic energies obtained from the self-consistent reaction field calculations. In this study we have considered a model which features dithiomethylamine (μ-dtma) as bridging ligand between the two iron centres of the $[2Fe]_H$ subcluster.

In order to model the complex electronic structure resulting from the open-shell character of the $[2Fe]_H$ and [4Fe4S] clusters domains we follow the computational protocol reported by Greco and co-workers. Full details are given in *Inorg. Chem.* **2008**, *47*, 6056.

In all cases the [4Fe4S] cubane is treated as diamagnetic by antiferromagnetic coupling of the Fe_1Fe_2 and Fe_3Fe_4 subunits (each containing a high-spin Fe^{2+} and Fe^{3+} ion, resulting in S_{loc} = 9/2) within this domain. We have considered two broken-symmetry determinants, one with a spin-down (β) / spin-up (α) arrangement within the Fe_1Fe_2 / Fe_2Fe_4 units (BS1), and *vice versa* (BS2). At the H_{ox-1} oxidation level these two solutions (M_S = 0) are energetically degenerate, due to the absence of a further electron residing on the vicinal $[2Fe]_H$ cluster. At the H_{ox-2} oxidation level their energies are split by additional antiferromagnetic (BS1) and ferromagnetic coupling (BS2) between the Fe_1Fe_2 subunit and the $[2Fe]_H$ cluster with S_{loc} = 1/2. Full details of the DFT calculations and optimised atomic coordinates for all relevant structures are available in the supporting information of reference A1.5.

[A1.1] Gaussian 09, Revision A.02, M. J. Frisch, G. W. Trucks, H. B. Schlegel, G. E. Scuseria, M. A. Robb, J. R. Cheeseman, G. Scalmani, V. Barone, B. Mennucci, G. A. Petersson, H. Nakatsuji, M. Caricato, X. Li, H. P. Hratchian, A. F. Izmaylov, J. Boino, G. Zheng, J. L. Sonnenberg, M. Hada, M. Ehara, K. Toyota, R. Fukuda, J. Hasegawa, M. Ishida, T. Nakajima, Y. Honda, O. Kitao, H. Nakai, T. Vreven, J. A. Montgomery, Jr., J. E. Peralta, F. Ogliaro, M. Bearpark, J. J. Heyd, E. Brothers, K. N. Kudin, V. N. Staroverov, R. Kobayashi, J. Normand, K. Raghavachari, A. Rendell, J. C. Burant, S. S. Iyengar, J. Tomasi, M. Cossi, N. Rega, J. M. Millam, M. Klene, J. E. Knox, J. B. Cross, V. Bakken, C. Adamo, J. Jaramillo, R. Gomperts, R. E. Stratmann, O. Yazyev, A. J. Austin, R. Cammi, C. Pomelli, J. W. Ochterski, R. L. Martin, K. Morokuma, V. G. Zakrzewski, G. A. Voth, P. Salvador, J. J. Dannenberg, S. Dapprich, A. D. Daniels, O. Farkas, J. B. Foresman, J. V. Ortiz, J. Cioslowski, and D. J. Fox, Gaussian, Inc., Wallingford CT, 2009.

[A1.2] (a) Becke, A. D. *Phys. Rev. A.* **1988**, *38*, 3098. (b) Perdew, J. P. *Phys. Rev. B* **1986**, *33*, 8822.

[A1.3] Schäfer, A.; Huber, C.; Ahlrichs, R. *J. Chem. Phys.*, 1994, **100**, 5829.

[A1.4] Tomasi, J.; Mennucci, B.; Cammi, R. *Chem. Rev*. **2005**, *105*, 2999.

[A1.5] Foster, C. E.; Kramer, T.; Wait, A. F.; Parkin, A.; Jennings, D. P.; Happe, T.; McGrady, J. E.; Armstrong, F. A. *J. Am. Chem. Soc.* **2012**, *134*, 7553-7557.

Appendix 2

Determination of Rate Constant

Consider the simple case of recovery of activity following inhibition of a hydrogenase as described by Reaction A2.1, where k_1 is the rate at which the enzyme reactivates and k_{-1} is the rate at which the enzyme is inactivated.

$$\text{Inactive} \underset{k_{-1}}{\overset{k_1}{\rightleftharpoons}} \text{Active} \qquad \text{Reaction A2.1}$$

The first order rate law is given by Equation A2.2 which integrates and is rearranged to Equation A2.3 in which [Inactive] is the concentration of the inactive species and $[\text{Inactive}]_0$ is the concentration of inactive species at $t = 0$.

$$\frac{d[\text{Inactive}]}{dt} = -k_1[\text{Inactive}] \qquad \text{Equation A2.1}$$

$$\text{Log}[\text{Inactive}] = -k_1 t + \text{Log}[\text{Inactive}]_0 \qquad \text{Equation A2.2}$$

The total concentration of enzyme at any time during the experiment is equal to the concentration of the "Inactive" species added to that of the "Active" species.

$$[\text{Total enzyme}] = [\text{Inactive}] + [\text{Active}] \qquad \text{Equation A2.3}$$

If all enzyme is inhibited at t = 0 the concentration of the "Inactive" species at $t = 0$, $[\text{Inactive}]_0$, is equal to the total concentration of enzyme. Throughout the experiment the current recorded is proportional to the concentration of active enzyme: $i_t \propto [\text{Active}]_t$.

When the reactivation process is complete a limiting current (i_{lim}) is reached, eg. at $t = \infty$, and [Active] at this point is proportional to the limiting current: $i_{lim} \propto [\text{Active}]_\infty$.

The $[Inactive]_0$ must equal the concentration of "Active" species when the reactivation process is complete and i_{lim} has been reached: $i_{lim} \alpha [Inactive]_0$.

As the concentration of the "Active" species throughout the reactivation process is proportional to the current, and throughout the reactivation process $[Inactive]_t = [Inactive]_0 - [Active]_t$, the $[Inactive]_t \alpha i_{lim}-i_t$.

Equation A2.2 can therefore be written:

$$\mathrm{Log}(i_{lim} - i_t) = -k_1 t + \mathrm{Log}(i_{lim}) \qquad \text{Equation A2.4}$$

and rearranges to:

$$\mathrm{Log}\left(\frac{i_{lim} - i_t}{i_{lim}}\right) = -k_1 t \qquad \text{Equation A2.5}$$

Thus, k_1 can be determined from the gradient of a $\mathrm{Log}[(i_{lim}-i_t)/i_{lim}]$ vs. t plot.